

In vitro and *in silico* simulations of femoral heads with avascular necrosis

James Anthony Anderson MEng

Submitted in accordance with the requirements for the degree of

Doctor of Philosophy

The University of Leeds

School of Mechanical Engineering

April 2015

The candidate confirms that the work submitted is his own and that appropriate credit has been given where reference has been made to the work of others.

This copy has been supplied on the understanding that it is copyright material and that no quotation from the thesis may be published without proper acknowledgement

© 2015 The University of Leeds and James Anthony Anderson

The right of James Anthony Anderson to be identified as Author of this work has been asserted by him in accordance with the Copyright, Designs and Patents Act 1988.

Acknowledgements

I would like to acknowledge and thank my supervisors Dr. Sophie Williams, Dr. Alison Jones, Professor John Fisher and Dr. Graham Isaac for their guidance throughout this project. Their guidance and ability to motivate has been invaluable.

The computational portion of this research would not have been possible without the contributions of Dr. Sami Tarsuslugil, Dr. Sebastian Sekora and Dr. Marlene Mengoni. They provided a great deal of practical advice as well as the tools required to make this research possible.

This research was funded by DePuy Synthes Joint Reconstruction. I am indebted to my managers and colleagues at DePuy Synthes for their unswerving support, encouragement and patience.

Abstract

Avascular necrosis of the femoral head (AVN) is a complex disease that is linked to multiple aetiologies including steroid use and alcohol abuse. Its pathology is characterised by localised ischemia leading to cell death followed by a period of partial repair during which a sclerotic boundary forms around the necrotic lesion. In many patients the pathology progresses to include involvement of the articular surface leading to arthritic degeneration of the joint.

Current classification systems for AVN evaluate lesion size and location and cannot accurately predict whether fracture will occur. There is a need for a prognostic tool to differentiate patients who would benefit from conservative therapies from those for whom arthroplasty is indicated. Previous research has indicated that lesion size and location affects disease progression and it was hypothesised that a morphology-based assessment would better quantify risk of progression.

In vitro experimental disease models were constructed by substituting a plug of bone from the central portion of porcine femoral heads with less stiff, weaker, bone from bovine lateral epicondyles. These models and control femoral heads were compressed to incrementally increasing displacements between flat platens. A parametric study using finite element analysis was used to demonstrate the sensitivity of the disease model to geometry and material properties and to develop a risk score that quantified stress discontinuities at the lesion boundary.

A more physiologically representative method of load application through a compliant and conforming surface was developed *in silico*. This was used to evaluate cone-shaped simulated lesions with varying size and orientation and a series of 47 organic lesion geometries derived directly from the proximal femoral anatomy of eight patients suffering from AVN, two of whom had subchondral fractures.

The experimental disease models were significantly less stiff than the control femoral heads and both were shown to behave linear-elastically at displacements below 1mm. This was beneficial as it allowed linear-elastic material properties to be used in the *in silico* simulations. These simulations confirmed that lesion properties and morphology significantly affected the stress distribution and highlighted that a physiologically representative method of load application is essential for future *in vitro* studies.

The risk score allowed patients to be ranked according to their fracture risk. The rank matched that obtained using the current gold standard grading system but with improved granularity as well as the opportunity to apply a threshold value for categorizing risk. This proved the potential for using a morphology-based risk analysis to better differentiate patients for whom early surgical intervention may be beneficial from patients who would benefit more from total hip arthroplasty.

Table of contents

Acknowledgements.....	3
Abstract.....	4
List of tables.....	8
List of figures.....	13
Abbreviations.....	24
Introduction.....	25
Chapter 1. Literature Review.....	27
1.1 Avascular necrosis of the femoral head.....	27
1.1.1 Occurrence in typically Caucasian populations.....	27
1.1.2 Occurrence in typically Asian populations.....	28
1.2 Etiology.....	28
1.2.1 Trauma.....	29
1.2.2 Alcohol abuse and steroid use.....	29
1.2.3 Systemic disease.....	29
1.2.4 Conclusion on etiology.....	30
1.3 Pathogenesis.....	30
1.3.1 Pre-radiologic phase.....	30
1.3.2 Limited repair.....	30
1.3.3 Destructive repair.....	32
1.3.4 Constructive repair.....	33
1.3.5 Asymptomatic AVN.....	33
1.3.6 Conclusion on pathogenesis.....	34
1.4 Classification and presentation of AVN.....	34
1.4.1 Grading systems.....	34
1.4.2 Presentation of patients with avascular necrosis.....	37
1.4.3 Lesion size and position.....	41
1.4.4 Conclusion on the classification and presentation of AVN.....	41
1.5 Treatment options.....	42
1.5.1 Core-decompression and conservative treatment.....	42
1.5.2 Bone grafting.....	44
1.5.3 Device-based treatments.....	44
1.5.4 Conclusion on treatments.....	45
1.6 Diagnostic imaging for avascular necrosis.....	45
1.6.1 Magnetic resonance imaging.....	47
1.6.2 Computed tomography.....	48
1.6.3 The gap between diagnostic grading systems and accurate prognosis.....	49
1.6.4 Conclusion on diagnostic imaging.....	50
1.7 The material properties of bone.....	51
1.7.1 Measures of bone density.....	52
1.7.2 Relationship between density and mechanical properties for healthy cancellous bone.....	53
1.7.3 The relationship between density and mechanical properties for diseased bone.....	54
1.7.4 Conclusion on the material properties of bone.....	55
1.8 Finite element analysis.....	56
1.8.1 Introduction to finite element analysis.....	56
1.8.1 Finite element models of AVN.....	56
1.8.2 Elements.....	58
1.8.3 Loading and constraint.....	59
1.8.4 Failure modelling.....	61
1.8.5 Two- and three-dimensional modelling.....	62
1.8.6 Conclusion on finite element analysis.....	63
1.9 Discussion.....	64
1.10 Objectives for experimental and computational studies.....	66
Chapter 2. Development of an <i>in vitro</i> disease model for AVN.....	69
2.1 Introduction.....	69

2.2	Benchmarking the properties of plugs taken from porcine femoral heads	72
2.2.1	Materials	72
2.2.2	Methods	73
2.2.3	Results of benchmarking bone from porcine femoral heads	75
2.3	Identifying a source of bone with “necrotic” bone properties	76
2.3.1	Identifying target properties for donor “necrotic” bone	76
2.3.2	Materials and methods	77
2.3.3	Results of identifying a source of bone with “necrotic” bone properties	79
2.3.4	Discussion	83
2.3.5	Conclusion	84
2.4	Assembling and testing disease model and native femoral heads	85
2.4.1	Introduction.....	85
2.4.2	Materials	86
2.4.3	Methods	90
2.4.4	Results of assembling and testing disease models and native femoral heads.....	93
2.4.5	Verification of the approach to derive elastic modulus	95
2.4.6	Inspection of experimental disease models	105
2.4.7	Discussion	106
2.4.8	Conclusion	109
Chapter 3.	Finite element simulation of experimental disease models	110
3.1	Introduction.....	110
3.2	Model Development	111
3.2.1	Standard methodologies.....	111
3.2.2	Mesh resolution optimisation.....	113
3.2.3	Interface study.....	116
3.2.4	Definition of measures and outputs	124
3.3	Parametric study	130
3.3.1	Parametric sweep	130
3.3.2	Multivariate analysis.....	133
3.3.3	Experimental disease model simulations.....	135
3.3.4	Results.....	138
3.3.5	Discussion.....	150
3.4	Conclusions.....	152
Chapter 4.	Finite element analysis based evaluation of lesion size, shape and orientation.....	154
4.1	Introduction.....	154
4.2	Standard methods for FE model generation	156
4.3	Development and evaluation of a conforming contact model	157
4.3.1	Introduction.....	157
4.3.2	Method	160
4.3.3	Results.....	162
4.3.4	Discussion	167
4.3.5	Conclusion	168
4.4	Simulation of experimental disease models using conforming contact.....	169
4.4.1	Introduction.....	169
4.4.2	Method	169
4.4.3	Results.....	170
4.4.4	Discussion	177
4.4.5	Conclusion	178
4.5	Simulation of cone shaped lesions.....	179
4.5.1	Introduction.....	179
4.5.2	Method	181
4.5.3	Results.....	182
4.5.4	Discussion	190
4.5.5	Conclusion	192
Chapter 5.	Image based tools for fracture risk prediction	193
5.1	Introduction.....	193
5.2	Image acquisition and processing	195

5.2.1	Patients	195
5.2.2	Method	195
5.2.3	Results for patient demographics and disease quantitation.....	204
5.3	Development of patient specific finite element simulations	205
5.3.1	Method	205
5.3.2	Results	214
5.4	Discussion	230
5.5	Conclusion.....	232
Chapter 6.	Summary review	234
6.1	Overall discussion	234
6.2	Overall conclusions	242
Appendix A: Method development.....		244
Appendix B: MicroCT scanning protocol.....		249
Appendix C: Design of experiments.....		250
Appendix D: Clinical scan parameters.....		253
Appendix E: Patient-specific cases.....		255

List of tables

Table 1. Ficat and Arlet classification system for femoral head AVN (Mont <i>et al.</i> , 2006).	34
Table 2. University of Pennsylvania (Steinberg) classification system for femoral head AVN (Steinberg <i>et al.</i> , 1995).	35
Table 3. ARCO classification system for femoral head AVN (Gardeniers, 1993)	36
Table 4. JOA classification system for femoral head AVN (Sugano <i>et al.</i> , 2002).....	36
Table 5. Grade at presentation and rate of progression for patients with femoral head AVN. The highlighted grades represent lesions without subchondral fracture or head flattening. Refer to tables 1 to 4 for a more detailed description of the Grading systems used. Core decompression is abbreviated to CD.	38
Table 6. Co-registered CT and MR slices through a femoral head with AVN. The rows represent adjacent slices through the femur. Variations in intensity within the MR image do not indicate variations in material properties. Variations in intensity within the CT image do not indicate the presence or absence of necrotic bone.	47
Table 7. Reported relationship between compressive strength (σ_b), elastic modulus (E) and density (ρ) for bone.....	54
Table 8. Summary of mechanical properties for bone samples taken from various locations on porcine and bovine femurs (Figures 13 and 14). The number of samples column indicates the total number of samples taken, with the number of samples used to generate the final statistics in parentheses. The target properties for the donor bone were a maximum elastic modulus of 130MPa (95% C.I. 89-172) and an ultimate compressive strength of 9MPa (95%C.I. 8-10).....	80
Table 9. Comparison between material properties derived experimentally for porcine femoral heads (healthy bone) and plugs taken from the lateral epicondyle of a bovine femur (necrotic bone) and those reported for human bone in the literature.	84
Table 10. Bone mineral density obtained for each of the femoral heads used as controls and experimental disease models and for the plug of bovine bone used as a simulated lesion. The location from which bone plugs were taken is identified: A was central on the lateral epicondyle; B was immediately superior to this location.	87
Table 11. Change in modulus between cycles three (compression to 1.5mm) and four (compression to 2.0mm). Negative values indicated a reduction in modulus.	94
Table 12. Parameters, derived modulus and actual work done four cases of Hertzian contact between a rigid, flat plate and a 30mm diameter sphere with differing degrees of non-linear elasticity.	97
Table 13. Load chosen as an endpoint for calculating work done for each disease model and control. This load equated to the largest load that had been applied to every disease model and control femoral head over that cycle.....	98
Table 14. Derived modulus and measured work done for the experimental samples and work done for a 34mm diameter, spherical, linear elastic body using the derived modulus and the difference between the two. Two cases where the absolute difference was close to one standard deviation of the measured work done were found (Femoral heads I and III). The case where the difference was more than 7 standard deviations away is highlighted in parentheses: This sample is an outlier and is not included in the calculated means and standard deviations.	102

Table 15. Distance between the top of the plug, eccentricity and nominal head diameter measured for each experimental disease model.	106
Table 16. Case list for mesh optimisation study. Five models with the same geometry (Figure 38) and material properties were generated.	114
Table 17. Qualitative and quantitative results of the two dimensional mesh convergence study using a 25mm diameter head. The boundary reaction force RF and peak von Mises stress in the head (VM peak) were extracted from the solved models.....	115
Table 18. Case list for the interface study. Four models were generated during the preliminary interface study. Sixteen models with varying head modulus, plug modulus, and interface conditions were generated.....	118
Table 19. The effect that the boundary conditions between the head and plug had on the stress and elastic modulus. In this table, a solid, homogenous model with E=300MPa was compared to a disease model where the head and plug both had E=300MPa. The tied constraint resulted in a very close approximation to the solid model. Replacing the tied constraint with a friction condition significantly reduced boundary reaction force and modulus. The peak von Mises stress increases slightly.	121
Table 20. Abbreviations used to identify the context of the relative risk value calculated	128
Table 21. Descriptive statistics showing the number of elements identified above the threshold value for each surface), and for the difference between each surface in the models constructed during the multivariate analysis (Section 3.3.2).....	129
Table 22. Case list for the single variable analysis study. Three separate evaluations were performed. In each case the geometry model was analysed with six different plug moduli and with both tied and friction head-plug interfaces.....	132
Table 23. Case list for multivariate analysis. The parameters for each case were dictated by a full factorial DoE matrix meaning that every possible combination of the four factors evaluated was tested.	134
Table 24. Levels for each factor in sensitivity analysis. The factors were chosen because they were likely to influence the response of the <i>in silico</i> disease model to an applied load. The levels for the head and plug moduli were chosen based upon the experimental results (Sections 2.2.3 and 2.3.3). Low levels were defined in each case as the level most likely to reduce the magnitude of the response.....	135
Table 25. Case list of experimental disease model-specific simulations. This list identifies the disease model subset from the full list of disease models and controls listed in table 2.....	136
Table 26. Plug and Head moduli derived from equations 10 and 11 for each disease model.	138
Table 27. Pearson product-moment correlation coefficients between each response.....	141
Table 28. von Mises stress distribution for the eight experimental disease model-specific FE simulations and the associated maximum stress in the outer surface, inner surface and the maximum difference.	149
Table 29. Young’s modulus assigned to the model components for each study using the conforming contact load configuration shown in Figure 64.	156
Table 30. Interactions for each interface in the conforming contact simulations (Figure 64) were consistent throughout the studies described in this chapter. The interfaces are described with the master surface listed first. All contact parameters are described in Section 3.2.1. Tied contact is	

defined as an interaction that restricts all relative motion at the interface between the two surfaces.	157
Table 31. List of parameters used in the study performed to develop a strategy for loading disease models through a conforming contact. The study was broken into three stages: a parametric sweep (n=25); a formalised Design of Experiments (n=8) and a final refinement stage (n=2).	160
Table 32. Factorial design used to evaluate the effect of platen radius, separation between apexes and filler modulus on the stress distribution and displacement in the femoral head.	162
Table 33. Design of experiments matrix used to investigate the effect of varying platen radius, separation between the platen and head and filler modulus on the peak von Mises stress in the head and the displacement of the most superior node in the head. The value attributed to each level is shown in Table 32.	162
Table 34. Results associated with each case described in Table 33. These results were used to identify the configuration that would be used in subsequent studies and to identify interactions between each factor.	163
Table 35. Number of elements identified as having stress above the threshold in the relative risk calculations for simulations of the experimental disease models using flat and conforming contact.	170
Table 36. Visual comparison of the von Mises stress distribution in the experimental disease model specific simulations loaded via a flat platen or through a conforming contact. Dark blue indicates areas of lowest stress; red indicates the areas of highest stress.	171
Table 37. Tests for correlation between the maximum von Mises stress values obtained at the outer and inner surfaces and the difference between the two obtained using two load conditions were performed by calculating a Pearson product-moment correlation co-efficient. The results for all three measures were highly correlated.	173
Table 38. Tests correlation between the three relative risk outcome measures obtained using two load conditions indicated that there was poor correlation in all three outcome measures.	175
Table 39. Displacements measured at the apex of the femoral head in the experimental disease models simulations. These displacements are the result of a displacement of 1.7mm being applied to the hemispherical platen during the simulation.	176
Table 40. Pearson product-moment correlation coefficients (r) for the relationship between displacement at the apex of the femoral head caused by applying a displacement of 1.7mm to the semi-circular platen in the conforming contact simulations and head modulus, plug modulus (Table 26), distance between the top of the plug and apex of the head and eccentricity (Table 15). Only head modulus showed a strong (negative) correlation.	176
Table 41. Comparing the relative risk scores obtained using flat and conforming contact simulations for cases IV, XVI and XVII highlighted the sensitivity of both the experimental disease model and relative risk score to the method of load application. The scores obtained using the conforming contact protocol were higher and the cases were ranked differently than when direct compression using a flat platen was used.	177
Table 42. Comparing relative risk scores for cases XIX and XX showed that there was a greater than two-fold difference between the cases using RR_O and RR_I , and a fourteen-fold difference using RR_D	178
Table 43. List of parameters for the cases evaluated in the conical lesion study. Five geometries were evaluated: 15°, 30° and 45° cones with radial boundary geometry, a 45° cone that flared	

outwards at the surface (acute boundary geometry) and a 45° cone that closed inwards at the surface (obtuse boundary geometry). The 45° variants were evaluated at different orientations relative to the load vector 180

Table 44. The maximum von Mises stress difference and number of elements identified both varied inversely with the included angle of the simulated lesion. 184

Table 45. Displacements caused at the apex of the head by displacing the platen by 1.7mm for different conical lesion sizes. Displacement varied directly with lesion size because more of the applied load was carried by the lower modulus lesion rather than the femoral head 184

Table 46. Displacements at the apex of the femoral head with a 45° lesion in caused by displacing the platen by 1.7mm for different orientations. No difference in displacement was measured suggesting that the elastic modulus of the femoral head was not affected by its orientation..... 186

Table 47. Anterior-posterior CT- and MR-derived views through a femoral head with AVN (patient 01_001) in ScanIP. The lesion boundary is visible as a low intensity band within the femoral head in the T1-weighted MR images. The boundary is marked with white arrows. It is noted that the high and low intensity bands in this image relate to fat content and are independent of material properties..... 201

Table 48. Demographics for the eight patients selected for the patient specific geometry model study. Patients 01_002 and 02_003 were identified as having suffered a subchondral fracture prior to image acquisition..... 204

Table 49. Lesion volume and ARCO classification for each patient included in the study. Head volume was estimated by calculating the volume of a sphere with the same diameter, lesion volume was calculated by multiplying the number of voxels in the lesion mask by the voxel volume. The ARCO grade was assigned based on the presence (Grade III) or Absence (Grade II) of fracture – note that all lesions were visible on radiographs and were by definition grade II or higher. The volume classification was dictated by the percentage involvement (<15% = A; 15%-30%=B; >30% = C). Location in the A-P and M-L planes was established by assessing whether the lesion was present in the Medial (M), Central (C) and Lateral (L) (Figure 97); Anterior (A), Central (C) and Posterior (P) quadrants respectively..... 205

Table 50. Six two-dimensional slices through the geometry models of each femoral head were generated from the three dimensional geometry model of each patient’s proximal femur, four with the femur in a neutral position and two with the femur oriented in 20° of flexion..... 208

Table 51. Schematic representation of the process of extracting and reorienting the 2D slice from the volume of interest (VoI). In this case a medio-lateral slice with the femur in a neutral orientation is shown. It was isolated from the 3D VoI (1) and re-oriented to lie on the X-Y plane (2). The VoI was cropped until it was 2 voxels thick in the Z-direction (3) and to leave 3-6mm of filler around the head remove the inferior 5mm from it. 209

Table 52. ScanFE settings used to generate an FE mesh to be exported into Abaqus..... 209

Table 53. General summary of relative risk (difference) scores for each case evaluated for each patient. The femur orientation and slice orientation columns describe the slices defined in Table 50. No score was calculated for patient 01_001 for the medio-lateral slice in 20° of flexion because the lesion was not present in this slice. Fracture cases are marked with an asterisk. 215

Table 54. The average revised score (using all cases for each patient) was used to rank the patients in ascending order. The ARCO grade and lesion volume are included for comparison. The patients marked with an asterisk constitute the fracture set. 221

Table 55. Average values for the cases from patients with and without a subchondral fracture and evaluation of the significance of the difference between the two sets for the components of the relative risk (difference) (RR_D), RR_D itself, percentage volume involvement and the product of the score and percentage volume involvement. A significant difference was found between sets for RR_D , percentage volume involvement (V) and the product of RR and V	222
Table 56. Number of cases with a revised score above a threshold of 360 for each patient. Thirteen cases from the no-fracture set were identified as having a revised score above 360. All cases came from four out of the six patients in that set.	223
Table 57. The patients were grouped according to revised relative risk score (relative risk (difference) x % volume involvement) and the presence or absence of fracture. Each patient was ranked in ascending order according to the average revised relative risk score (Table 52). Mid-head AP and ML images of the head and lesion are shown for reference.....	225
Table 58. Comparison between stance anterior-posterior slice statistics for patient 01_001 and patient 02_003. Patient 01_001 was identified as having the lowest risk of progression; patient 02_003 had the highest risk.	227
Table 59. Pearson product-moment correlation coefficients comparing the relative risk scores obtained for the medio-lateral, medial and lateral slices for each patient. The correlations were weak indicating that the three data sets were unrelated.....	229
Table 60. Comparison between previously reported material properties used in FE simulations of human femoral heads and the properties derived or used in the current studies.	236
Table 61. Maximum displacement for each cycle. These were calculated by adjusting the displacement values for each plot to originate at zero, then finding the highest value that was common across all data sets for a given cycle.	244
Table 62. Fields of view used for each cylinder diameter.	249
Table 63. Bilateral thresholds used to differentiate bone from tissue and air.	249
Table 64. Factors and levels for example Design of Experiments.	250
Table 65. The first three columns represent the experimental design. In this Full Factorial example, every permutation of levels is used. The last column is the response.	251
Table 66. Clinical CT scan parameters.....	253
Table 67. MR imaging sequences used in the clinical trial.....	254
Table 68. Geometric representations and von Mises stress plots for each slice generated for patient 01_001.....	255
Table 69. Geometric representations and von Mises stress plots for each slice generated for patient 01_002.....	256
Table 70. Geometric representations and von Mises stress plots for each slice generated for patient 01_003.....	257
Table 71. Geometric representations and von Mises stress plots for each slice generated for patient 01_004.....	258
Table 72. Geometric representations and von Mises stress plots for each slice generated for patient 01_005.....	259

Table 73. Geometric representations and von Mises stress plots for each slice generated for patient 01_006.....	260
Table 74. Geometric representations and von Mises stress plots for each slice generated for patient 02_001.....	261
Table 75. Geometric representations and von Mises stress plots for each slice generated for patient 02_003.....	262

List of figures

Figure 1. Flow chart summary of the studies performed in each chapter. The arrows represent the link between each one in terms of knowledge gained and the sequence in which each study was performed. It is repeated at the start of each chapter.....	26
Figure 2. A schematic representation of limited repair in femoral head AVN: A sclerotic band divides the distal living bone from the proximal necrotic segment. At this stage, the femoral head retains its spherical contour.....	31
Figure 3. Schematic representation of destructive repair in femoral head AVN: Peripheral osteolytic lesions provide an initiation site for subchondral fractures.....	32
Figure 4. Radiograph showing the crescent sign (arrows) (Steinberg <i>et al.</i> , 1995). <i>Reproduced with the permission of Dr. Steinberg</i>	32
Figure 5. Schematic representations of multi hole (left) and single hole (right) core decompression.....	43
Figure 6. Example cross-section of a femoral head generated using a T1-weighted MR scanning protocol. The lesion boundary is demarcated by the outer edge of the low intensity (black) band within the femoral head. High intensity indicates a region containing fat. Within the femoral head this indicates a region with viable bone marrow.....	46
Figure 7. Typical example of a CT image of a femoral head with pre-collapse AVN. This image corresponds to the MR image shown in Figure 6. The high intensity regions indicate areas of increased density but this does not relate to the boundary of the necrotic segment.....	46
Figure 8. Flow chart summary of the studies performed in each chapter.....	70
Figure 9. The PTX Universal plug cutter used to create a cylinder of bone with a nominal diameter of 9.8mm.....	73
Figure 10. Left: Photograph of the Instron materials testing machine. Right: detail view of the specimen mounted between two flat platens. The platens were wrapped in cellophane to reduce contamination of the machine.....	74
Figure 11. A typical stress-strain plot for a plug taken from a porcine femoral head. The location of automatically detected maximum elastic modulus is shown by a diagonal cross and the location of ultimate compressive strength is indicated by a horizontal cross.....	75
Figure 12. Stress-strain plots for samples taken from fourteen porcine femoral heads. The two samples that were identified as outliers are indicated by the broken lines.....	76
Figure 13. Schematic diagram showing the locations from which samples of bone were taken from porcine femurs.....	78

Figure 14. Schematic diagram showing the locations from which samples of bone were taken from bovine femurs.....	78
Figure 15. Box-whisker plot of maximum elastic modulus. The mean of the data set is represented by a diamond, the median by a bar. Mean maximum elastic modulus for donor bone (A) (Central on the lateral epicondyle, n=8) and B (Immediately superior to location H, n=10), both from the bovine lateral epicondyle. The error bars indicate 95% confidence interval. The target maximum and minimum are based on a nominal maximum elastic modulus that represents a 59% reduction in modulus compared to samples taken from porcine femoral heads with the same confidence interval as the original data.	81
Figure 16. Box-whisker plot of ultimate compressive strength. The mean of the data set is represented by a diamond, the median by a bar. Ultimate compressive strength for donor bone (A) and (B), both from the Bovine lateral epicondyle. The error bars indicate 95% confidence interval. The target maximum and minimum values represent a nominal strength that represents a 41% reduction in UCS compared to samples taken from porcine femoral heads with the range based on the same confidence interval as the original data.	81
Figure 17. Stress-strain plot for bovine sample J2. This sample was removed because of its atypical yield profile: a very short linear elastic region with a gradually reducing gradient (modulus) followed by a large stress plateau. The location of automatically detected maximum elastic modulus is indicated by the diagonal cross and the location of ultimate compressive strength is shown by the horizontal cross.	82
Figure 18. Preparation cuts for the first stage of generating the disease model. The broken lines represent the first cuts used to create the inferior flat, the solid line represents the final resection cut made through the isthmus after the hole has been cut and the donor bone inserted.	88
Figure 19. Photograph of the drill used to generate a hole within the porcine femoral heads. The shaft diameter of the drill was 9.5mm and it created a round-ended hole with an end radius of approximately 8.5mm	88
Figure 20. Photograph of the modified 12mm diameter wood auger used to prepare the domed end of the bone dowel. The end of the auger was reground to have a concave surface with a radius of 8.5mm	89
Figure 21. Example of a bone plug prepared using a PTX Universal No. 10 plug cutter (Figure 9). The end was domed to conform to the cavity created by the drill shown in Figure 18 using the modified wood auger (Figure 20)	89
Figure 22. Example of a porcine femoral head with a simulated lesion of donor bone which originated from the lateral epicondyle of a bovine femur. There is a theoretical line-to-line fit between the hole and plug. The arrows indicate the boundary of the plug. Note that the cartilage has been removed from the top of the sample.	89
Figure 23. Workflow for displacement controlled compressive loading of control and disease model femoral heads.....	91
Figure 24. Load-displacement plot for femoral head VI during its second cycle (compression to 1mm). The raw data (solid line) is overlaid with the best-fit Hertzian load-displacement curve (broken line). In this case, δ -adjustment factor is approximately 0.27mm. The best-fit algorithm was limited between 5N (0.25mm) and the yield point at 680N (0.72mm). The sum of the absolute error within these boundaries was 0.74mm (between 0.00 and 0.1mm per data point).....	93
Figure 25. Plot of load versus displacement for control femoral head XII. Each line represents a different load cycle.	94

Figure 26. Box-whisker plot showing the derived elastic modulus for disease models (n=8) and control femoral heads (n=11) over four cycles. The mean is represented by a diamond, the median by a bar. The bulk modulus was derived by minimising the error between an analytical Hertzian approach of centres and the measured compressive displacement.....	95
Figure 27. Load displacement relationship for four cases of Hertzian contact between a rigid, flat plate and a 30mm diameter sphere with differing degrees of non-linear elasticity.....	97
Figure 28. Plot of work done versus modulus for Hertzian contact between a rigid flat platen and a deformable spherical body comprised of increasingly nonlinear material. As the material becomes more nonlinear the work done reduces and the elastic modulus increases.	98
Figure 29. Analytical work-modulus relationship for a series of linear-elastic spheres with a 34mm diameter compressed by a rigid flat plate. The spheres had moduli between 90 and 550MPa	99
Figure 30. Two plots of work versus modulus for experimental data and the analytical solution. Top: n=18. The trend-line for the experimental data was flattened (the power is smaller) compared to the analytical solution. The R^2 value indicated a relatively worse fit to the data. Bottom: n=16. The experimental data followed the analytical solution almost exactly with a much higher R^2 . While the two data points that were excluded in the second plot detracted from the fit of the data, the difference in real terms was not sufficient to consider these points to be outliers.....	101
Figure 31. Work: Modulus relationship for cycle 3, during which the heads were compressed with a load of approximately 1180N. Top: experimental data compared to an analytical solution over the same load range. Bottom: experimental data compared to the analytical solution assuming a 5% reduction in load used in the analytical solution (1120N) compared to the experimental data (1179N).....	103
Figure 32. In cycle four the work-modulus relationship no longer resembled the analytical solution. The experimental results are significantly more varied: Work done to 1731N has a standard deviation of 192Nmm (excluding control sample XIII). The R^2 value for the experimental data trend line is 0.6 suggesting that the trend-line is no longer an accurate representation of the data.	104
Figure 33. Left: Schematic representation of the inferior surface of the disease models showing the equator of the head (solid circle), the periphery of the inferior cut (broken circle) and the centre of the head (cross). The plug is represented by a grey circle. The minimum distance from the plug centre to the equator (M) was estimated and used to orient the cut represented by the broken line. Right: Schematic representation of the cross-section obtained. The eccentricity (E) relative to the head centre and distance beneath the apex (D) were measured using a Vernier calliper.....	105
Figure 34. Cross section through <i>in vitro</i> disease model. The white arrows indicate the approximate area of load application; the black arrows show a crack propagating from the corner of the cavity. Note that in this image, the pin is significantly offset from the centre of load application. The crack has propagated from the geometric stress raiser closest to the mid-plane.	105
Figure 35. Displacement at inflection for disease model (n=8) and control (n=11) femoral heads. Although there was a large variation, the displacements at inflection were generally consistent across both data sets. The mean is indicated by a diamond, the median by a bar. The whiskers indicate the maximum and minimum for each set.	107
Figure 36. Force at inflection for disease model (n=8) and control (n=11) femoral heads. Although there was a large variation, there was a trend within each cycle for the control femoral	

heads to require a greater force to reach an inflection compared to the experimental disease model. The mean is indicated by a diamond, the median by a bar	108
Figure 37. Flow chart summary of the studies performed in each chapter.....	111
Figure 38. Schematic representation of the head and platen. The head was modelled as a 50mm diameter circular body with a chord located 10mm inferior to the equator. The platen was modelled as a 40mm x 10mm rectangle. The chord was pinned in the initial time step; a displacement of 0.5mm was applied to the upper surface of the platen during the first time step..	113
Figure 39. Plot of peak VM stress for each model described in table 16. Excluding the first model, the mean was 16.08MPa and (Range 15.6-16.4MPa, standard deviation 0.37MPa. Simulation parameters are described in Table 15 and Section 3.2.1.	116
Figure 40. Left: Disease model design. The dotted line represents the boundary between the plug and head. This was either represented as a friction interface or by a tied constraint. To evaluate the effect of the boundary condition, both the head and plug were assigned a modulus of 300MPa. Right: Control model design.....	119
Figure 41. Mesh detail at the interface between the plug and head at the top of the plug. The arrows point to the boundary. Left: the edge was seeded to align the nodes along the contact surface; Right, the nodes were misaligned.	120
Figure 42. Qualitative comparison of the effect of altering the boundary condition between the plug and head. Top left: A solid homogenous model used as a benchmark; Top right: A head-plug assembly with tied contact and an aligned mesh. Bottom left: a head-plug assembly with tied contact and a misaligned mesh; Bottom right: A head-plug assembly with a friction interface and misaligned mesh.....	121
Figure 43. Example of a simplified disease model with a friction interface in its deformed state (Case four in the interface study, Table 18). The black arrows indicate separation of the interface; the white arrows indicate areas that could fail in compression. The splitting effect extended along approximately 80% of the length of the plug.	122
Figure 44. Close up view of the superior corner of the head-plug boundary with a friction-based interaction after deformation. The element edge length is approximately 0.5mm and it is clear that approximately three elements (1.5mm) on each side of the superior surface are not in contact, reducing the effective width of the plug to 7mm (applying symmetry). This helped to explain the reduction in elastic modulus. The von Mises stress at the element indicated by the black arrow was approximately 8.5MPa; at the white arrow it was less than 0.1MPa.....	122
Figure 45. Plot of horizontal displacement caused by vertical compression of the head with a flat platen. The blue colour indicates displacement towards the left of the image; the red colour indicates displacement to the right of the image. Displacement was symmetrical and the head was displaced to a greater extent than the plug.	123
Figure 46. Schematic illustrating the path that values were taken from using of the Python script for one model. The Python script output a geometrically ordered array of VM stress values for each element in the inner and outer surface, starting at the bottom left element pair (white box) and following a clockwise path around the surfaces.	127
Figure 47. Examples of the variation in stress around the outer surface and inner surface, and the difference between the two surfaces. Top: an eccentric plug position; Bottom a concentric plug position. In the plots, the origin of the x-axis equates to the bottom left element at the interface with progression clockwise around the interface represented along the x-axis. Only the data to the right of the broken lines was included in the analysis. The region of stress above the threshold in the outer surface is identified using black circles; the region of stress above the threshold in the inner surface is identified using white circles and the region where the stress	

difference was above the threshold is identified using grey circles. Note that the location of maximum difference did not necessarily equate to the location of maximum stress in either surface.	129
Figure 48: Schematic representation of the three geometry models used to evaluate the effect of plug position. A: concentric plug 5mm below the apex, B: eccentric plug 5mm below the apex and C: concentric plug 2.5mm below the apex.	131
Figure 49. A plot of bone mineral density (BMD) versus Young's modulus for plugs of bone taken from bovine lateral epicondyles (triangles) and for plugs of bone taken from the central load bearing portion of porcine femoral heads (squares).	137
Figure 50. The relationship between plug modulus and the elastic modulus of the construct when the plug was concentric to the applied load and 5mm below the surface is shown. Using a friction boundary condition resulted in an elastic modulus that was lower than when a tied constraint was used at the interface between the plug and head.	139
Figure 51. Relationship between plug modulus and elastic modulus when the plug was positioned concentrically and 2.5mm below the apex of the head. Compared to when the plug was positioned 5mm below the apex (Figure 50), the empty plug condition was approximately half as stiff. When the friction interface was applied, the homogenous model was 16% less stiff than when the plug was 5mm below the surface.	139
Figure 52. The relationship between plug modulus and elastic modulus when the plug was lateralised by 2.5mm and positioned 5mm below the apex is shown. Compared to the results when the plug was concentric with the applied load (Figure 50), there was substantially less difference between the two boundary conditions, and the effect of changing plug modulus was also less.	140
Figure 53. Main effects plots showing change in elastic modulus in response to head modulus, plug modulus, eccentricity and depth beneath the apex.	142
Figure 54. Main effect plots for relative risk (difference) response.	143
Figure 55. Interaction plot showing change in elastic modulus in response to interactions between head modulus, plug modulus, eccentricity and depth beneath the apex.	144
Figure 56. Interaction plots for the relative risk (difference) response.	145
Figure 57. Bar chart of relative risk (difference) (RR_D) for each configuration, arranged in ascending order. The RR_D score for the first four configurations was negative indicating that the plug side of the surface was most highly stressed. The mean RR was 24 (standard deviation 43, range -37 to 126). This is indicated by the broken line on the plot.	145
Figure 58. Stress distribution plots for cases 5 and 6. The broken line in each plot indicates the approximate threshold (5.8MPa) above which elements were included in the relative risk calculation. The x-axis is the sequential element location, starting at the bottom left edge and moving clockwise around the surface.	145
Figure 59. Plot of elastic modulus derived from the FE simulations for each factorial design compared to the regression model derived from the same data.	146
Figure 60. Comparison between theoretical and experimentally derived moduli for porcine femoral heads and donor bone taken from the lateral epicondyle of bovine femurs.	147
Figure 61. Relative risk scores derived for each of the experimental disease model specific simulations (Section 3.3.3). The experimental disease models are identified by roman numerals; the three disease models that fractured are identified by an asterisk.	148

Figure 62. Peak von Mises stress in the outer and inner surface and the difference between each surface for each of the experimental disease model specific simulations. The experimental disease models are identified by roman numerals; the three disease models that fractured are identified by an asterisk	148
Figure 63. Flow chart summary of the studies performed in each chapter.....	155
Figure 64. Schematic diagram of the conforming contact concept assembly. The assembly consisted of a relatively stiff, hemispherical platen, a filler of relatively low modulus and a simulated femoral head. The simulated femoral head had a diameter of 50mm and extended 10mm beyond the hemisphere. In the design of experiments the diameter of the platen, the distance between the platen and head and the modulus of the filler were varied.....	158
Figure 65. Distribution of von Mises stress in the femoral head caused by loading the filler component using a flat platen until a displacement of 0.5mm at the apex of the femoral head was achieved. The concept geometry shown in Figure 63 was chosen because loading via a flat platen was found to generate near-uniform stress throughout the head.	159
Figure 66. Main effect plots for DoE evaluation of the effect of platen radius, separation and filler modulus on displacement at the apex of the head. Filler modulus had the largest effect on VM stress followed by separation. The responses to changes in platen radius and separation were of equal magnitude but inverted.....	164
Figure 67. Main effect plots for DoE evaluation of the effect of platen radius, separation and filler modulus on the peak VM stress at the apex of the head. Filler modulus had the largest effect on VM stress followed by separation. The effect of platen radius on VM stress was negligible compared to the other two factors.....	164
Figure 68. Interaction plots for DoE evaluation of the effect of platen radius, separation and filler modulus on the displacement at the apex of the head. The plots indicate that none of the factors interacted strongly but that the combination of high separation with high platen radius resulted in the same displacement as the combination of low separation with low platen radius. No other combination of the three factors resulted in the same confounded result.....	165
Figure 69. Interaction plots for DoE evaluation of the effect of platen radius, separation and filler modulus on the peak VM stress at the apex of the head. The plots indicate that none of the factors interacted strongly and that the combination of high platen radius, high filler modulus and low separation gave the highest peak VM stress. This equates to case three.	166
Figure 70. Left: Plot of von Mises stress distribution in a femoral head for the conforming contact methodology defined by this study. Right: Plot of von Mises stress distribution in the same head under direct compression using a flat platen. The stress under conforming contact was less concentrated at the apex and there was no flattening. However, it was noted that two areas of high stress, located at approximately 45° to the apex, were present in the left hand image.....	166
Figure 71. Left: Initial assembly for case three with white ovals indicating the undesirable stress concentrations; Right: Final model configuration showing the filler extended to encompass the entire head, thus moving the stress concentrations found in the initial design to the bottom edge of the simulated head. This location was outside the region considered in the RR evaluations. The platen had a radius of 20mm and was separated from the head by 10mm. This configuration exerted a surface load over an arc of approximately 140°.....	167
Figure 72. Maximum difference in von Mises stress measured between the inner and outer surfaces for the simulated experimental disease models under flat and conforming load cases. The results were highly correlated ($r=0.95$).....	172

Figure 73. Maximum von Mises stress measured in the outer surface for the simulated experimental disease models under flat and conforming load cases. The sets were highly correlated ($r=0.95$).....	172
Figure 74 Maximum von Mises stress measured in the inner surface for the simulated experimental disease models under flat and conforming load cases. The results were poorly correlated ($r=0.36$).....	173
Figure 75. Relative risk score calculated for the difference between the inner and outer surfaces for the simulated experimental disease models under flat and conforming load cases. The experimental disease models marked with an asterisk were found to have fractured during the test. The results for the flat and conforming load cases were not correlated ($r=0.3$).....	174
Figure 76. Relative risk score calculated for the outer surface for the simulated experimental disease models under flat and conforming load cases. The experimental disease models marked with an asterisk were found to have fractured during the test. The results for the flat and conforming load cases were not correlated ($r= -0.01$).	174
Figure 77. Relative risk score calculated for the inner surface for the simulated experimental disease models under flat and conforming load cases. The experimental disease models marked with an asterisk were found to have fractured during the test. The results for the flat and conforming load cases were not correlated ($r=0.18$).....	175
Figure 78. The relationship between the modulus of the femoral head in the simulated experimental disease model and the displacement at the apex of the femoral head caused by applying a displacement of 1.7mm to the semi-circular platen in the conforming contact simulations was shown to have a strong negative correlation ($r=-0.96$).....	176
Figure 79. Representations of conical lesions with (A) 15°, (B) 30° and (C) 45° included angles. The straight edges were aligned radially and the depth to which they extended below the surface of the head was maintained at 15mm below the apex. Note that the semi-circular rigid platen has been cropped from these images.....	180
Figure 80. Left: A simulated lesion with a 45° included angle (indicated by the broken lines and intersecting at the head centre) and an acute angle between the internal surface and the circumference (indicated by the solid line). Right: A simulated lesion with a 45° included angle and an obtuse angle between the internal surface and circumference.....	181
Figure 81. Cross-sections through the simulations using conforming contact with conical lesion models. The lesion was simulated with a 45° included angle. It was oriented neutrally (A) and rotated by 7.5° (B), 15° (C) and 22.5° (D) respectively.....	182
Figure 82. Variation in peak von Mises stress associated with the difference between the surfaces for the three cone angles considered. The diagrams in the chart show the lesion size and orientation for each case considered.....	183
Figure 83. Variation in relative risk (difference) associated with the difference between the surfaces for the three cone angles considered. The diagrams in the chart show the lesion size and orientation for each case considered.....	184
Figure 84. The peak difference in von Mises stress between the inner and outer surfaces increased as the angle between the edge of the lesion and vertical reduced. The results for the rotated 45° lesion were within 2.5% of the symmetrical case for the 15° and 30° centre-vertical angles.....	185
Figure 85. RR_D values calculated for symmetrical lesions with included angles of 45°, 30° and 15° compared to the results for a 45° lesion rotated to achieve the same centre-edge angle. The diagrams show the size and orientation of the simulated lesion in each case.....	186

Figure 86. Left: Acute edged lesion; Right: Obtuse edged lesion. The magnitude of the stress was similar to the baseline (a 45° lesion with the edges aligned radially) in both cases. However, the length of the surface identified in the relative risk calculation was significantly shorter in the obtuse case.	188
Figure 87. Peak von Mises stress in the inner surface, outer surface and the peak difference between the two surfaces for a radial-edged 45° lesion, an acute lesion at various angles relative to the load vector and an obtuse lesion at various angles relative to the load vector. The diagrams in the plot indicate the geometry used in each case.	188
Figure 88: Plots of von Mises stress for the acute and obtuse lesions in three orientations. When the acute lesion was rotated from neutral (A) to 7.5° (B) and 15°(C) the peak von Mises stress increased because both sections of the lesion boundary became more vertical and moved closer to the centre of the applied load. When the obtuse lesion was rotated from neutral (D) to 7.5° (E) the peak von Mises stress increased because the boundary moved closer to the applied load but reduced when it was rotated to 15° (F) because the lesion was shielded by the stiffer material above it.....	189
Figure 89. Relative risk (difference) associated a radial-edged 45° lesion, an acute lesion oriented neutrally, at 7.5° and at 15° relative to the load vector and an obtuse lesion oriented neutrally, at 7.5° and at 15° relative to the load vector. The relative risk (difference) score increased linearly with rotation for the acute case because both the magnitude and length of the stress discontinuity increased. It was substantially lower and varied less in the obtuse cases because of the limiting effect that the geometry had on the number of elements identified in the algorithm used to calculate relative risk.	189
Figure 90. Flow chart summary of the studies performed in each chapter.....	194
Figure 91. Schematic diagram of a neutrally oriented right femur with a lesion in the anterior-medial quadrant. The diaphysis was aligned to the global Y axis; the medial direction was aligned to the X axis. Approximately 20° of femoral anteversion (external rotation) was applied.....	196
Figure 92. Summary of process used to develop head, lesion and filler masks for patient 01_001. Note that the process is shown in two dimensions for simplicity but the steps were carried out in 3D.	197
Figure 93. Schematic representation of the workflow used to segment the femur geometry from the CT scan (in this case of patient 01_001) using ScanIP. The process was based on that presented in an earlier study (Buie <i>et al.</i> , 2007) and had six key steps: Importing the image and cropping it to establish a volume of interest; thresholding to identify the bone region; manually deselecting voxels (un-painting) associated with the acetabulum; using a closing function to solidify the construct; manually painting any gaps in the external surface that remained after the close function was used and smoothing the final surface.	198
Figure 94. Schematic representation of the completed femur and filler masks in the X-Y and Y-Z orientations. The filler occupied the entire volume of interest.....	199
Figure 95. Alignment of the MR scan to the CT derived mask for patient 01_001. Left: the high intensity region of the MR image representing the proximal femur is misaligned relative to the (purple) filler mask; Right: final alignment of the MR image relative to the filler mask. This was obtained by rotating and translating the MR image relative to the filler mask.	200
Figure 96. The process of generating a lesion mask: A. The lesion was identified as a low intensity band or region; B. The outer boundary was traced and extended beyond the surface of the femoral head; C. The mask was flood filled and smoothed using recursive Gaussian smoothing and D. Boolean subtraction was used to generate a conforming external surface.	

Only the anterior-posterior view is shown in this example (from patient 01_001) but the process was repeated in all three orientations	202
Figure 97. The CT slice is shown in image A. The equivalent MR slice is shown in image B. The lesion boundary is shown overlaid on the CT scan in image C and a schematic representation of the femoral head and lesion is shown in image D. All images are from patient 01_001 in the A-P view. Lesion location was quantified according to the ARCO grading system: The lesion was present in the central (C) and lateral (L) quadrants but not in the medial (M) quadrant)	203
Figure 98. Anterior and posterior views of the original mask (A, shown in red) generated for patient 01_001 overlaid with the mask representing the difference (C, shown in yellow) between the original and blind repeat. The difference in number of elements between the two masks was less than 0.27%.....	204
Figure 99. Anterior, medial, posterior and superior views of the femur and lesion geometry models for patient 01_002.....	206
Figure 100. Plots of von Mises stress over the lesion boundary. Left: the boundary when lesion was simulated with half the stiffness of the healthy bone; Right: the same surface from a simulation where the same material properties were used throughout.	207
Figure 101. Left: Typical example of the boundary between the head, lesion and filler portions in the model imported from ScanIP. Middle: Manually repaired mesh. Care was taken to maintain an equal element edge length at the surface where possible. Right: Revised mesh generated using the boundary nodes and the method developed by Dr. Marlene Mengoni. The mean element edge length in the original mesh was 1mm. It was 0.5mm in the revised mesh.....	211
Figure 102. Schematic diagram showing a typical example of the final construct. Left: Labelled by part; Right: Labelled by elastic modulus. The platen radius (20mm), separation between the platen and head/lesion construct (10mm) and filler modulus were defined in the study recorded in Section 4.3.....	211
Figure 103. Average relative risk (difference) score calculated for each patient using all slices for each patient. The two patients in the fracture set are shown red; patients in the no-fracture set are shown in blue.	217
Figure 104. Comparison between average relative risk (difference) scores obtained using only the stance cases (hatched bars) and using slices taken in both stance and 20° of flexion (solid bars). The two patients in the fracture set are shown in red. The patients in the no-fracture set are shown in blue.....	217
Figure 105. Average relative risk (difference) score multiplied by volume involvement for each patient. The two patients in the fracture set are shown in red and the patients in the no-fracture set are shown in blue. The volume (in mm ³) of each lesion was two orders of magnitude higher than the average relative risk score, masking its effect.....	219
Figure 106. Average relative risk (difference) score multiplied by percentage involvement (v/v %) for each patient. The two patients in the fracture set are shown in red. The patients in the no-fracture set are shown in blue. Describing the volume involvement as a percentage rather than a magnitude reduced the coefficient to the same order of magnitude as the relative risk (difference) scores.	219
Figure 107. Comparison between average RR _D x volume involvement scores obtained using only the stance cases (Hatched bars) and using slices taken in both stance and 20° of flexion (solid bars). The two patients in the fracture set are shown in red. The patients in the no-fracture set are shown in blue. The volume (in mm ³) of each lesion was several orders of magnitude higher than the average relative risk score, masking its effect.....	220

Figure 108. Comparison between average relative risk (difference) multiplied by percentage volume involvement scores obtained using only the stance cases (hatched bars) and using slices taken in both stance and 20° of flexion (solid bars). The two patients in the fracture set are shown in red and patients in the no-fracture set are shown in blue. Describing the volume involvement as a percentage rather than a magnitude reduced the volumetric component of the revised score to the same order of magnitude as the relative risk (difference) scores. 220

Figure 109. Plot of the revised relative risk scores for each case (n=47 from 8 patients) ranked in ascending order. The solid points represent cases from patients in the fracture set (12 cases from 2 patients). All cases from the fracture set had a revised score of more than 360..... 222

Figure 110. Scatter plot of patient rank according to the revised relative risk score (Table 52) against the number of cases per patient above a threshold value for the revised score of 360 (Table 56). Two patients (01_001 and 01_006) had no cases above the threshold. All six cases from each patient in the fracture set (01_002 and 02_003) were above the threshold. 223

Figure 111. Plot of von Mises stress around the lesion in the stance AP case from patient 01_001. This patient was identified as having the lowest risk of progression according to their revised relative risk score. The x-axis indicates the element index in the ordered set starting at the left-most element in the two dimensional plot. The surface was approximately 80 elements shorter than the equivalent case in the highest risk patient (Figure 108). 226

Figure 112. Plot of von Mises stress around the lesion in the stance AP case from patient 02_003. This patient was categorised as having a high risk of progression according to their revised relative risk score. The x-axis indicates the element index in the ordered set starting at the left-most element in the two dimensional plot..... 226

Figure 113. Comparison between relative risk scores derived from anterior-posterior slices taken in stance and 20° of flexion showing the mean, highest and lowest scores obtained for each patient. The bar represents the average of the two values (denoted by the solid circles)..... 228

Figure 114. Comparison between relative risk scores derived from medio-lateral slices taken in stance and 20° of flexion. The bar represents the average of the two values (denoted by the solid circles) No ML slice was taken for P01_001 in 20° of flexion as the lesion did not pass through this slice. The score was highest in stance for patients P01_003, P02_001 and P02_003; it was highest in flexion for the other cases. 228

Figure 115. Comparison of relative risk scores obtained for each patient from the central medio-lateral slice and slices taken 2mm medial and lateral to this slice. No trend was established and the intra-patient variation ranged from 44% to 144% 229

Figure 116. Evaluation of the sensitivity to slice selection using three medio-lateral slices, each 0.5mm apart. The plot shows maximum, minimum and mean scores obtained for each patient. ... 230

Figure 117. Flow chart summary of the studies performed in each chapter..... 234

Figure 118. Box-whisker plot of the work to a consistent displacement for disease model and control femoral heads across all repeats of the same cycle. The results were significantly different for the fourth cycle. The mean work done on the disease models is between 45% and 58% lower than was done on the controls 245

Figure 119. Box-Whisper plot comparing the work done on disease model and control femoral heads to achieve a consistent force. The mean work done on the disease model femoral heads was between 15% and 32% higher in all cases but the difference was not significant. 246

Figure 120. Displacement required to achieve a consistent displacement for disease model and control femoral heads. The displacement for the disease model femoral heads was between 14% and 23% higher but was only significantly different for the fourth load cycle. 246

Figure 121. Measured and analytically derived contact radii for femoral head VI (control). The underestimation of contact radius is typical of the results of attempts to derive the bulk modulus by minimising the error between the measured displacement and Hertzian approach of centres. ...	247
Figure 122. Elastic modulus derived using a single-modulus based approach.....	248
Figure 124. Main effect plots for DoE of the force generated by a lever. These show that the force generated varies inversely with the overall length of the lever; directly with the applied force and directly with the pivot location. The first plot shows the change in response when the Applied Force is 100N versus 300N, the second when the lever is 2m long versus 3m long and the third when the pivot location is 1m from the applied force and 1.5m from the applied force....	252
Figure 125. Interaction plots for the DoE example. Two important observations can be made: 1. In some interactions it is possible that one factor will invert the response to another. However, in this case the response varies directly regardless of the interaction; 2. One line in each plot has a steeper slope. This means that there is a different response to the factor considered in the X-axis depending on the factor considered in the legend: the factors are interacting to cause a response that is greater than the effect of any one factor on its own.	252
Figure 126. Relative risk scores for each case generated from Patient 01_001.....	255
Figure 127. Relative risk scores for each case generated from Patient 01_002.....	256
Figure 128. Relative risk scores for each case generated from Patient 01_003.....	257
Figure 129. Relative risk scores for each case generated from Patient 01_004.....	258
Figure 130. Relative risk scores for each case generated from Patient 01_005.....	259
Figure 131. Relative risk scores for each case generated from Patient 01_006.....	260
Figure 132. Relative risk scores for each case generated from Patient 02_001.....	261
Figure 133. Relative risk scores for each case generated from Patient 02_003.....	262

Abbreviations

ARCO – Association of Research Circulation Osseous

AVN – Avascular necrosis

BMD – Bone mineral density

BW – Body weight

CI – Confidence interval

CPS4R - continuous plain strain four node reduced integration

CT – Computed tomography

FEA – Finite element analysis

JOA – Japanese orthopaedic association

JRF – Joint reaction force

MRI – Magnetic resonance imaging

RR – Relative risk

RR_D – Relative risk (difference)

RR_I – Relative risk (inner)

RR_O – Relative risk (outer)

SARS – Severe acute respiratory system

UCS – Ultimate compressive stress

VM – Von Mises stress

VoI – Volume of interest

Introduction

Avascular necrosis (AVN) of the femoral head is a rapidly destructive disease that typically affects patients in their third to fifth decade of life (Mont and Hungerford, 1995). AVN is more prevalent in Asian populations than in Caucasian populations and has been reported as an indication for total hip arthroplasty in several national joint registries and epidemiological studies. Causes of AVN include trauma, alcohol abuse, steroid use and systemic diseases such as systemic lupus erythematosus. However, disease progression tends to follow a common pathway regardless of etiology. Pathogenesis is typically described as localised ischaemia leading to formation of a lesion of necrotic bone within the femoral head. Subsequent progression is characterised by formation of a sclerotic lesion boundary followed by incremental collapse or fracture of the bone underlying the articular surface.

Although total hip arthroplasty has been shown to be a successful treatment for AVN it is not an ideal solution because of the relatively short expected lifetime of the implant compared to that of the patient at the time of index surgery. In an attempt to avoid or delay the need for joint arthroplasty, several joint preserving treatment options have been developed with varying degrees of success.

When attempting to identify the best choice of treatment for an individual patient the surgeon must evaluate whether the welfare cost of a joint preserving treatment is outweighed by the likelihood of its success. Semi-quantitative disease classification systems have been developed to help the surgeon to monitor and develop a prognosis for their patients. However, these systems have been shown have poor prognostic ability and there is an unmet need for a more effective means of assessing the risk of progression.

Two- and three-dimensional diagnostic imaging techniques for AVN are well established and provide the information required to generate *in silico* experimental disease models that could help to develop and evaluate new prognostic measures. However, validation of *in silico* simulations of AVN would be challenging because the poor prognosis of conservatively treated AVN means that the default treatment for most patients is surgical intervention and altering this standard of care would be unethical.

This thesis records the development and evaluation of an experimental disease model for AVN; it's recreation *in silico* and the evolution from simplified simulation into a series of patient-specific computational models of femoral heads with AVN. While this incremental approach (Figure 1) did not obviate the need for clinical validation of such simulations, each increment allowed the development of logical rules against which the results of the next increment could be judged.

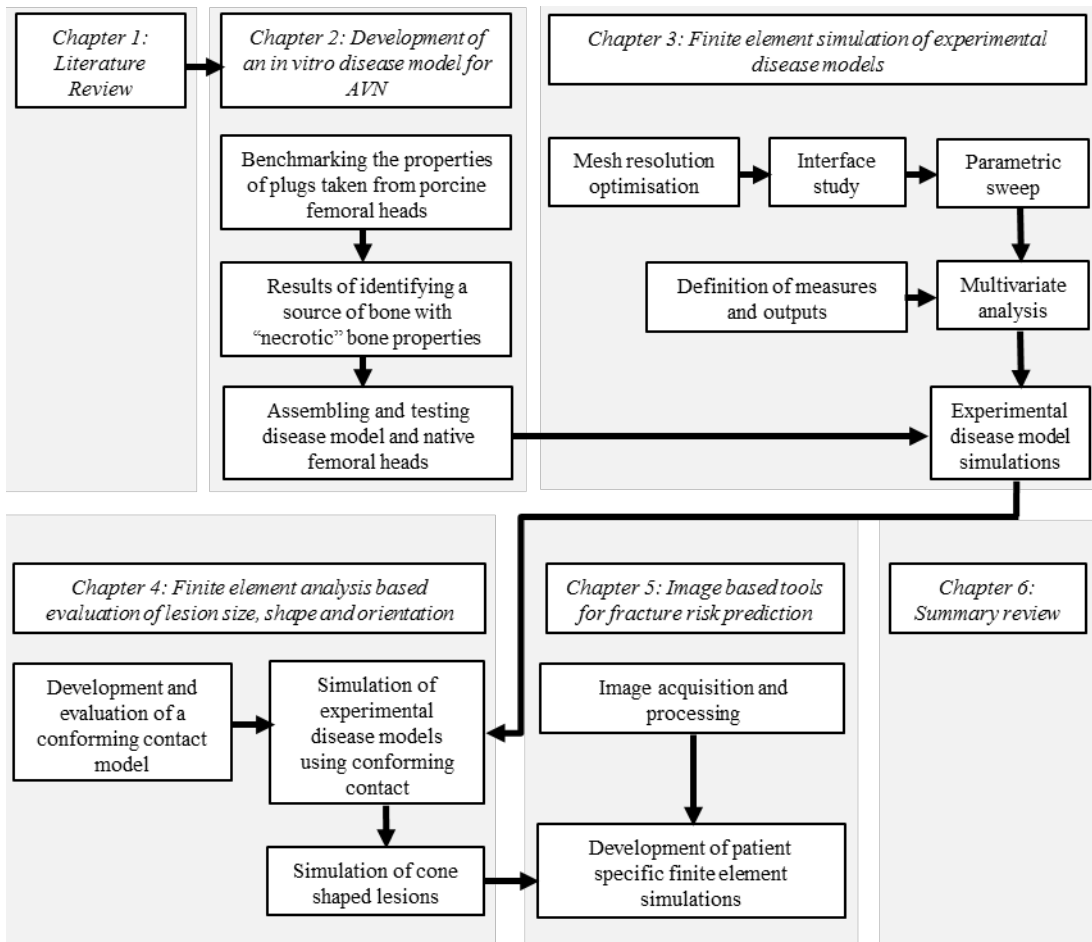


Figure 1. Flow chart summary of the studies performed in each chapter. The arrows represent the link between each one in terms of knowledge gained and the sequence in which each study was performed. It is repeated at the start of each chapter.

Chapter 1. Literature Review

1.1 Avascular necrosis of the femoral head

The term “avascular necrosis” is often used interchangeably with “osteonecrosis” within the clinical literature. Both terms refer to death of bone and the pathology of the end-stage disease described for both is characterised by gross fracture and collapse of the bone within the femoral head. The term “avascular necrosis” best describes the presence of an ischaemic lesion where in the early stages of the disease the lesion maintains a bone-like structure. The term “osteonecrosis” covers the entire spectrum of necrotic bone pathologies and can also be used to define cystic lesions that manifest as a region where the bone has been replaced by a cartilaginous cyst. The distinction is not well defined in the statistics available from clinical literature and national joint registries. Therefore the broader term will be used to discuss the incidence of disease where ambiguity exists. If source material provides unambiguous context such as reference diagnostic imaging, then the more specific term will be used.

Avascular necrosis can occur in multiple locations through the body but is most frequently detected in the hip joint (Mont and Group, 1999; Lv *et al.*, 2009). All statistics in this section relate specifically to the femoral head. This pathology is typically associated with younger patients with an Asian ethnicity. Hence the majority of epidemiological analysis focuses on Asian populations. There are however several national joint registries from predominantly Caucasian nations that list osteonecrosis as a potential reason for total hip arthroplasty, allowing comparison between the two ethnic groups. This comparison must be treated with caution because the country from which the data was obtained does not necessarily reflect the ethnicity of the patients affected.

1.1.1 Occurrence in typically Caucasian populations

Avascular necrosis of the femoral head generally affects younger people, with one American centre stating that 25% of their patients were under 25 (Hungerford and Jones, 2004). The reported rate varies geographically: analysis of the 2007 Canadian Joint Replacement Registry, the 2007 Australian National Joint Replacement Registry and the 2007 Swedish Hip Arthroplasty Register show that osteonecrosis accounts for between 2.8% and 6% of all primary total hip replacements in these countries (Seyler *et al.*, 2008). The 2009 National Joint Registry for England, Wales and Northern Ireland indicated a slightly lower incidence than for the other countries listed, reporting that 2% of total hip arthroplasties could be attributed to the disease in both 2008 (Emsley *et al.*, 2009) and 2012 (Porter *et al.*, 2013). However, when stratified by age, 18% of 30-39 year olds and 7% of 40-49 year olds who received a THA were diagnosed as having AVN. An analysis of the Nordic Arthroplasty Register Association indicated that 2.2% of THRs performed between 1995 and 2011 were associated with avascular necrosis (Bergh *et*

al., 2014). Lai et al., (2008) cite data from the Swedish (1992-2002) and Norwegian (1987-1999) registers: 2.9% and 0.8% respectively.

1.1.2 Occurrence in typically Asian populations

A nationwide survey in Japan found that 11,400 patients sought medical care for idiopathic osteonecrosis of the femoral head in 2005. Patients tended to be in their 40s, with 27% of males and 18% of female patients in this range, and the main potential causative factors were systemic steroid administration (51%) and habitual alcohol use (31%) (Fukushima *et al.*, 2010). In Korea, the incidence appears to be increasing over time: from 20.53 occurrences per 100,000 people in 2002 to 37.96 occurrences per 100,000 people in 2006. These cases account for between 50% and 60% of primary total hip replacements in this five year period (Kang *et al.*, 2009).

Although there is no national joint registry in Taiwan, Lai et al., (2008), were able to interrogate the National Health Insurance Database (1996-2004) to establish the variation of survival rates for total hip arthroplasty with disease. Avascular necrosis accounted for 46% of all total hip replacements. Of these, 79% were male, with a mean age of 50 years. The authors propose that their epidemiological results could be transferred to China as the majority of their subjects were Han Chinese. Tien et al., (2009), reported very similar statistics for Taiwan, but with the added detail that the proportion is increasing with time.

1.2 Etiology

Musso *et al.*, 1986 evaluated the effectiveness of conservative management of 36 patients aged between 13 and 76 years who presented with 50 osteonecrotic hips. The diagnoses included idiopathic AVN, acute or chronic steroid use, alcoholism and sickle cell anaemia. By a mean follow-up of 16 months, 76% of the hips had progressed sufficiently to require total hip arthroplasty. These results were shown to be similar to previous studies and it is concluded that the likelihood of progression was unrelated to the etiology (Musso *et al.*, 1986). Therefore only a short summary of the established risk factors is provided as background information.

The hypothesis that the final common pathway for the development of AVN involves an ischemic infarction is generally accepted, but the events leading to this infarction are not always clear (Assouline-Dayana *et al.*, 2002). In addition to the more established risk factors such as alcohol and steroid use, trauma and chronic metabolic disorders, theories exist around direct cellular toxicity and impaired mesenchymal cellular differentiation as potential mechanisms (Petrigliano and Lieberman, 2007). It should be noted however, that these manifestations may be co-morbidities of the true root cause.

1.2.1 Trauma

Avascular necrosis due to interruption of the blood supply due to trauma occurs within 8 hours from the time of injury. It is a complication of around 80% of displaced, and 15%-25% of undisplaced fractures of the femoral neck. It is believed that ischemic infarction caused by trauma is a likely root cause of the AVN, but mechanical damage at the time of injury may also contribute to the incidence of necrosis (Meyers, 1988).

1.2.2 Alcohol abuse and steroid use

Despite the lack of radiographic evidence to support the link between excessive alcohol consumption and AVN (Gold and Cangemi, 1979), alcohol and steroid use are the most frequently cited risk factors for developing AVN (Marker, Seyler, Ulrich, *et al.*, 2008).

It has been reported that between 10% and 74% of patients with non-traumatic AVN have excessive alcohol intake (Suh *et al.*, 2005). Possible causes include inhibition of the ability of mesenchymal stem cells to differentiate towards an osteogenic lineage (Suh *et al.*, 2005; Petrigliano and Lieberman, 2007) and a “Charcot-like” diminution of the normally protective pain responses (Gold and Cangemi, 1979) that could allow damage to accumulate where normally the initial insult would induce protective weight bearing (Meyers, 1988; Zinn, 1971).

The incidence of osteonecrosis in patients treated with steroids ranges from 5% to 58% depending on study (Chang *et al.*, 2006; Lv *et al.*, 2009). From a cohort of 71 patients treated with high doses of corticosteroids for Severe Acute Respiratory Syndrome (SARS), 39% developed AVN within 3-4 months of starting treatment. In total, 58% of the cohort developed AVN within 3 years and a significant proportion of patients were diagnosed with AVN in other joints (Lv *et al.*, 2009). A larger study (Guo *et al.*, 2014) reported similar results with 39.5% of 129 males and 19.3% of 410 females developing osteonecrosis. This study also indicated that the incidence of osteonecrosis varied depending on the type of steroid administered.

The association between steroid use and AVN may be clear but the exact mechanism remains unclear, with different study designs indicating different potential pathologies (Petrigliano and Lieberman, 2007; Chang *et al.*, 2006).

1.2.3 Systemic disease

Avascular necrosis is closely associated with Systemic Lupus Erythematosus (Kang *et al.*, 2009; Mont and Group, 1999; Hernigou *et al.*, 2006) and Sickle-cell anaemia (Hernigou *et al.*, 2006; Hernigou and Beaujean, 2002; Arlet, 1992). In the former, it may be a result of the disease or the cortico-steroid-based treatment regime. There is a more direct association with the disease in the latter. These cases are complex because the underlying systemic disease and the effect it has on the patients’ potential to recover from any intervention must also be considered.

1.2.4 Conclusion on etiology

Bone death may occur because of a number of different factors, from direct damage to the bone or interruption of the blood supply, to increased sensitivity to external stimulus or inhibition of the normal pain response, which allows un-heeded damage to occur. Although the true root cause may be variable, there is consensus that an ischemic infarction is the common pre-cursor to the formation of the necrotic lesion.

1.3 Pathogenesis

The true etiology of AVN is unclear and is likely to be multi-factorial. However, Musso *et al.*, (1986), suggested that there is no link between etiology and pathogenesis. They also failed to link pathogenic stage to the degree of disability: patients with a radiologically advanced disease may have few symptoms, but radiologically normal hips may be extremely painful.

The way in which the degenerative effect of the disease manifests is a principle factor in developing or choosing treatment options. In the broadest terms, AVN can be subdivided into symptomatic and asymptomatic disease. Symptomatic hips have a high likelihood of progression and a more direct correlation can be made between the stage and size of the lesion and outcome (Belmar *et al.*, 2004). This section presents a generalised description of the pathogenesis for symptomatic AVN followed by a short discussion of asymptomatic cases. This may be broken down into different stages: pre-radiologic, limited repair, destructive repair and constructive repair. It is the manifestation of the last two stages that dictates whether the joint becomes affected.

1.3.1 Pre-radiologic phase

In the pre-radiologic phase, cell necrosis occurs: marrow cells and osteoblasts die relatively quickly; osteoclasts are the last cells to die. The living cartilage above the lesion appears to be unaffected. Loss of bone cells does not affect the radiographic density; hence the femoral head will appear normal on X-ray but changes may be detectable using magnetic resonance (MR) imaging because unlike x-ray this imaging modality is capable of identifying regions of bone that lack viable bone marrow before structural changes occur (Arlet, 1992; Mont and Group, 1999; Hernigou and Lambotte, 2000).

1.3.2 Limited repair

Limited repair consists of bone metabolism in coarse cancellous bone and is limited to the reactive interface at the periphery of the lesion (Hernigou and Beaujean, 2002; Motomura *et al.*, 2011). There is controversy over whether the term “creeping substitution” applies to this stage: Glimcher and Kenzora, 1979a) refuted the application of this term arguing that the repair is limited to the reactive interface and does not continue to “creep”; Sugano *et al.*, (2002), supported the term in 2001.

This phase produces a characteristic sclerotic rim with adjacent hyper-vascularity. In a post-mortem examination of osteonecrotic femoral heads, repair was found to be limited to the reactive interface for up to 63 months; only rarely did the repair process extend into the necrotic lesion (Plenk Jr *et al.*, 2001). The replacement of dead marrow cells and capillaries by large, stellate, undifferentiated mesenchymal cells and capillary buds containing live endothelial cells is a consistent pathological finding during limited repair. However, the extent of proliferation and number of cells differentiating to fibroblasts varies hugely.

There is a difference in the formation of new bone between non-traumatic AVN and AVN due to femoral neck fracture (Glimcher and Kenzora, 1979a). In the former, new bone formation occurs on the surfaces of dead trabeculae, and never extends out as randomly into the intertrabecular space as it does in the latter. Bone formation in traumatic AVN is more rapid, affects a greater volume, and usually involves more of the femoral head distally: at the fracture site.

In both cases, the process of repair tends to cease after a period of time leaving totally necrotic lesions within the bone. In non-traumatic AVN, this is due to two distinct biological mechanisms: failure of the mesenchymal cells to differentiate to osteoblasts (which interrupts bone formation), and failure of the capillaries and mesenchymal cells of the repair tissue to proliferate and spread to areas adjacent to the dead portions of the femoral head. It is proposed that whereas in non-traumatic AVN this is a “turning off” of the cells, in traumatic avascular necrosis the process is physically inhibited by secondary phenomena such as intra-capital fractures, possibly with formation of fibrous layers between fragments, and the development of subchondral cysts.

An increase in the total mass of bone per unit volume occurs during limited repair, resulting in a relative increase in radiographic density and loss of fine structure. It is noted that changes in bone structure indicate living, not necrotic, bone. In non-traumatic AVN, the repair phase is manifested as a patchy area or band of increased radio-density. The portion proximal to this line represents the dead (sclerotic) segment as shown in Figure 2. During this phase the head retains its spherical contour and the joint-space is also retained (Glimcher and Kenzora, 1979b).

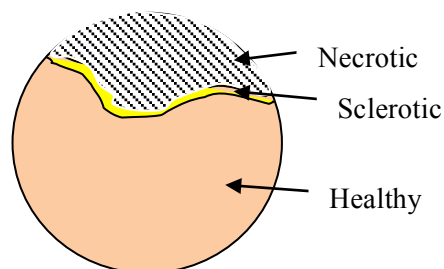


Figure 2. A schematic representation of limited repair in femoral head AVN: A sclerotic band divides the distal living bone from the proximal necrotic segment. At this stage, the femoral head retains its spherical contour.

1.3.3 Destructive repair

Destructive repair is an extension of the repair process into the lesion. Predominant resorption of the necrotic bone leads to femoral head breakdown within 2 to 50 months. This may occur through incremental fracture of the trabeculae within the lesion in the absence of the repair mechanisms associated with normal bone homeostasis leading to compressive failure. An alternative failure mode is the formation of fractures originating from resorptive cavities and fatigue fractures in the subchondral bone (Plenk Jr *et al.*, 2001; Motomura *et al.*, 2011) (shown schematically in Figure 3) which tend to originate at the lateral boundary of the necrotic lesion (Motomura *et al.*, 2011). In this phase, changes to the compact subchondral bone and articular cartilage begins to occur. At the end of this stage, the cartilage is likely to be only loosely connected to the underlying bone. Thus the presence and extent of collapse is a major prognostic indicator of disease progression (Mont *et al.*, 2006). Subchondral fractures are rarely found in the posterior of the femoral head (Atsumi *et al.*, 1989).

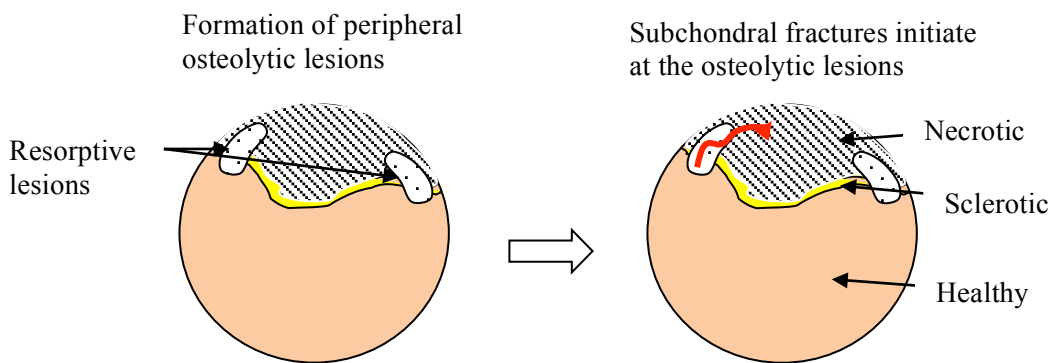


Figure 3. Schematic representation of destructive repair in femoral head AVN: Peripheral osteolytic lesions provide an initiation site for subchondral fractures.

The “crescent sign” is a significant radiographic feature of advanced AVN. It is an area of radiolucency beneath the subchondral bone in the shape of an arc, or crescent. An example radiograph displaying the crescent sign is shown in Figure 4.

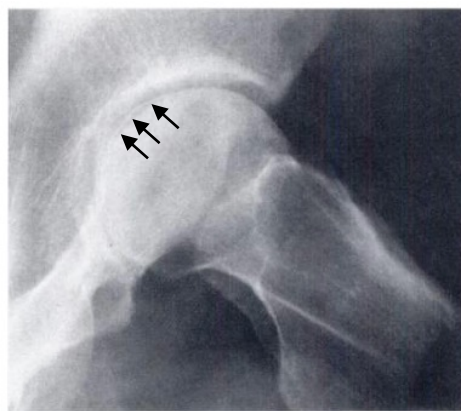


Figure 4. Radiograph showing the crescent sign (arrows) (Steinberg *et al.*, 1995). *Reproduced with the permission of Dr. Steinberg.*

It can often be seen prior to initial collapse of the articular surface, and hence is a useful indication of imminent failure. Because of this, it features in several of the key grading systems discussed in section 1.4.1. The pathogenesis of the crescent sign is described in detail in the third of a series of papers (Glimcher and Kenzora, 1979b). They support the findings of Catto, (1965), who proposes that subchondral fracture occurs after the onset of AVN and initiation of the repair process. It was concluded that the subchondral lucency is not the result of active bone resorption along the entire fracture site, but is the radiographic manifestation of a fracture that originates in an area of focal resorption and travels through dead bone (Glimcher and Kenzora, 1979b; Arlet, 1992 and Motomura *et al.*, 2011). Regardless of mechanism, these authors agree that the site of fracture initiation is in subchondral bone superior to the lesion.

Plenk Jr *et al.*, (2001), suggest that there is a benefit to treatments that modify the destructive repair process to creeping substitution rather than resorption-dominated. This is substantiated by Aaron *et al.*, (1989) who, along with Meyers, (1988) and Glimcher and Kenzora, (1979a) state that it is not the disease but the repair process or imposition of mechanical factors on the necrotic segment that leads to loss of mechanical integrity, collapse of the articular surface and eventual destruction of the joint.

1.3.4 Constructive repair

Constructive repair originates at subchondral fracture sites or the reactive interface and may reduce the volume of the necrotic lesion. In cases where constructive repair occurs, the disease progresses more slowly (Plenk Jr *et al.*, 2001). It is noted that by this stage, permanent deformation of the femoral head is present: any repair that occurs limited to the re-constitution of the material, not the structure.

1.3.5 Asymptomatic AVN

Magnetic resonance imaging makes it possible to diagnose AVN before symptoms or radiographic evidence appears. In this way, AVN is often diagnosed in asymptomatic hips when the patient presents with a symptomatic contra-lateral hip. The fate of asymptomatic AVN is not broadly studied, but it is clear that the pathogenesis does not necessarily follow that of symptomatic disease. Furthermore, there is a significant relationship between the onset of pain and the occurrence of femoral head collapse, and a significant relationship between lesion size and collapse (Nam *et al.*, 2008), with 72%-91% of hips with lesions occupying less than 15% of the femoral head surviving (Belmar *et al.*, 2004). Overall, however, 73%-100% of hips with asymptomatic AVN can be expected to progress without treatment (Belmar *et al.*, 2004), indicating that lack of pain cannot be used as a predictor for successful conservative management.

1.3.6 Conclusion on pathogenesis

When discussing AVN, it is important to understand two key principles: progression is a manifestation of the *repair* process in reaction to a specific injury to the bone rather the spreading of a “disease”; Remodelling of the inorganic portion of bone indicates the presence of living cells, not necrotic tissue.

The general phases, from cell death, through generation of a sclerotic band, weakening and eventual collapse of the subchondral bone are driven by a combination of mechanical and biological events. The duration between stages is ill-defined and also influenced by these events.

1.4 Classification and presentation of AVN

1.4.1 Grading systems

Classification of pathology is important as it allows surgeon to quantify changes to a patient’s condition that occur between serial consultations and also helps to inform them of the best treatment option for a particular patient. At least seventeen different methods have been proposed for evaluating the extent of a necrotic lesion within the femoral head. In general, they use identifiable changes in the bone morphology from imaging to quantify the severity of involvement at a given time but, although there is a general trend between the severity of the classification and the risk of failure, they do not quantify this relationship.

Of the grading systems available, only four are commonly used (Marker, Seyler, Ulrich, *et al.*, 2008; Mont *et al.*, 2006; Marker, Seyler, McGrath, *et al.*, 2008): Ficat and Arlet (Mont *et al.*, 2006) (Table 1), The University of Pennsylvania (Steinberg) grading system (Steinberg *et al.*, 1995) (Table 2), the ARCO grading system (Gardeniers, 1993) (Table 3) and the Japanese Orthopaedic Association grading system (Sugano *et al.*, 2002) (Table 4). The University of Pennsylvania and ARCO systems are the most comprehensive (Cui and Saleh, 2008). The latter quantifies area, location and involvement of the articular surface to give a detailed description of the case.

Table 1. Ficat and Arlet classification system for femoral head AVN (Mont *et al.*, 2006).

Stage	Radiographic findings
1	None (Only evident on MRI)
2	Diffuse sclerosis, cysts (Visible on radiographs)
3	Subchondral fracture (Crescent sign, with, or without head collapse)
4	Femoral head collapse, acetabular involvement, osteoarthritic degeneration

Table 2. University of Pennsylvania (Steinberg) classification system for femoral head AVN (Steinberg *et al.*, 1995).

Stage	Radiographic findings	Sub-classification		Involvement
0	Normal or non-diagnostic radiograph, bone scan and MRI	Not applicable		
I	Normal radiograph. Abnormal bone scan and / or MRI	A	Mild	<15% of head involvement as seen on radiograph or MRI
		B	Moderate	15% to 30%
		C	Severe	>30%
II	Abnormal radiograph showing "cystic" and sclerotic changes in the femoral head. Head remains spherical	A	Mild	<15% of head involvement as seen on radiograph or MRI
		B	Moderate	15% to 30%
		C	Severe	>30%
III	Subchondral collapse producing a crescent sign below subchondral layer.	A	Mild	Subchondral collapse (crescent) beneath <15% of the articular surface
		B	Moderate	Crescent beneath 15% to 30%
		C	Severe	Crescent beneath >30%
IV	Flattening of the femoral head	A	Mild	<15% of surface has collapsed and depression is <2mm
		B	Moderate	15% to 30% collapsed or 2-4mm depression
		C	Severe	>30% collapsed or >4mm depression

Table 3. ARCO classification system for femoral head AVN (Gardeniers, 1993)


Stage	0	I	II	III	IV
Findings	All present techniques show normal or non-diagnostic results	X-ray, CT are normal, at least one of the techniques below is positive	No crescent sign, x-ray abnormal: showing sclerosis, osteolysis, local porosis	Crescent sign on x-ray and/or flattening of the articular surface of the femoral head	Osteoarthritis, joint space narrowing, acetabular changes, joint destruction
Techniques	X-ray CT Scintigraph MRI	Scintigraph MRI Quantitate using MRI	X-ray CT Scintigraph MRI Quantitate using MRI	X-ray CT Quantitate on X-ray	X-ray only
Quantitation	No	% Area involvement Minimal A <15% Moderate B 15% to 30% Extensive C >30%		Length of crescent A <15% B 15% to 30% C >30% % Surface collapse and dome depression A <15%, <2mm B 15% to 30%, 2mm-4mm C >30%, >4mm	No
Sub-classification	No				No

Table 4. JOA classification system for femoral head AVN (Sugano *et al.*, 2002).

Stage	Finding	Quantitation	Location
1	Demarcation line, subdivided by relationship to weight-bearing area	1A	Medial
		1B	Central
		1C	Lateral
2	Early flattening WITHOUT demarcation line around necrotic area		
3	Cystic lesions, subdivided by site in the femoral head	3A	Medial
		3B	Lateral

Both the Ficat and ARCO systems have been found to have poor inter-observer reliability and only fair intra-observer variability, thus the value of comparison between studies is diminished; “the Ficat and ARCO systems are still not sufficient to reliably assess the status of AVN alone” (Schmitt-Sody *et al.*, 2008). As the JOA and Steinberg systems use largely the same staging rationale as the aforementioned systems, doubt must also be cast on the reliability of comparisons between studies that use these systems.

The ARCO system was first published in 1991. It was revised in 1993 and is the most recent of the popular systems (Gardeniers, 1993). At the time it was first released, computed tomography (CT) and MR imaging were already established as superior in both sensitivity and specificity than plane radiographs (Cherian et al., 2003; Mont et al., 1998; Ohzono et al., 1992; Sugano et al., 2002), making them the mode of choice for early diagnosis. However, their use was limited to qualitative estimates of the percentage of area of the femoral head occupied by the lesion.

Angular classification systems are also worth noting (Steinberg *et al.*, 2006; Koo and Kim, 1995). They are quicker but coarser than more involved methods that attempt to classify the implant based upon volume and pathology (Steinberg *et al.*, 1995; Gardeniers, 1993). Of the angular estimates, the index of necrotic extent presented by Cherian et al., (2003), demonstrates the latest iteration. The index of necrotic extent is calculated by making two angular measurements of the extent of the lesion, calculated on the sagittal and coronal MRI slices that show the maximum lesion size. The calculation assumes that the load bearing surface approximates to the upper 180° of the femoral head and the affected arcs are divided by 180°, multiplied together and then by 100 to derive a “percentage” of the articular surface involved. Steinberg et al., (2006), evaluated this method against a volumetric estimate, based upon the percentage area involvement in coronal and sagittal radiographs, and found good correlation. This suggests that, as a simple diagnosis tool, the index of necrotic extent is a viable option where resource for more involved methods is unavailable. However, volumetric estimates based on either plane radiographs or orthogonal CT or MR images may offer improved quantitation of the lesion on survivorship of the femoral head than angular estimates (Hernigou and Lambotte, 2001; Mont *et al.*, 2006) but there remains a need for a truly quantitative approach.

1.4.2 Presentation of patients with avascular necrosis

It is generally accepted that patient selection is the single most important factor for a successful joint preserving procedure. The volume of dead bone, the extent of the deformation of the articular surface and involvement of the acetabulum dictate the outcome of the treatment (Cui and Saleh, 2008). There is great value in identifying patients who can benefit from joint preserving procedures when their disease is in its early stage (Nishii, Sugano, Ohzono, Takahashi Sakai, *et al.*, 2002) but this is hampered by the fact that patients often become symptomatic and are diagnosed only after considerable collapse is already present (Musso *et al.*, 1986; Belmar *et al.*, 2004). A caveat to this generalisation is that, depending on etiology, between 30% and 98% of patients are reported to present with bilateral involvement (Schmitt-Sody *et al.*, 2008) and while a significant number of these patients will present with pain in only one hip (Hungerford and Jones, 2004), investigation of the contralateral joint gives the opportunity for early diagnosis.

Although highly variable, the rate of progression of AVN is well documented. A summary of data presented in eight papers that included conservative treatment or core decompression (refer to Section 1.5.1) in their analysis is provided in Table 5. These papers stratify the patient cohorts by lesion grade using different systems and give an indication of the risk of progression for different severities of AVN.

Considering the reported unreliability of the grading systems (Schmitt-Sody *et al.*, 2008), two conclusions can be reached without relying on grading systems. In all studies, the majority of untreated femurs collapsed within 2 years, with larger lesions more likely to collapse. Where size is reported, the lesions tended to be “large” (occupying more than 30% of the head). It is noted that around 80% of the cases were “pre-collapse” at presentation. However, this cannot be taken as an indication of typical disease state at presentation as these studies focus on treatments that are known to be ineffective in cases where the articular surface is involved.

Table 5. Grade at presentation and rate of progression for patients with femoral head AVN. The highlighted grades represent lesions without subchondral fracture or head flattening. Refer to tables 1 to 4 for a more detailed description of the Grading systems used. Core decompression is abbreviated to CD.

Paper	Treatment	Grade at presentation	N	Follow up (FU) criterion	Result	Mean time to collapse for CD group (Mo)	Mean time to collapse for conservative treatment group (Mo)	Conclusion
Koo <i>et al.</i> , 1995	Conservative treatment versus CD	Steinberg I	22	FU 2 Years	15/22 collapsed	12	15	Of the 33 pre-collapse hips 75% collapsed in <2 years regardless of treatment
		Steinberg II	11		10/11 collapsed	6	6	
		Steinberg III	4		4/4 collapsed	6	6	

Steinberg I: Normal radiograph, abnormal MRI; Steinberg II: Sclerosis visible on radiograph; Steinberg III: Crescent sign (Steinberg *et al.*, 1995).

Paper	Treatment	Grade at presentation	N	Follow up (FU) criterion	Result	Conclusion
Musso <i>et al.</i> , 1986	Conservative treatment	Ficat II	7	Mean FU 18 Months	6/7 progressed from II to III	Of the 7 pre-collapse hips, 85% collapsed at a mean of 18 months. Note: the average duration of the disease before intervention was 28 months from initial diagnosis
		Ficat III	26		12/26 progressed from III to IV	
		Ficat IV	2		both remained at IV	

Ficat I: Normal radiograph, abnormal MRI; Ficat II Sclerosis visible on radiographs; Ficat III Crescent sign (Mont *et al.*, 2006).

Table 5 continued.

Paper	Treatment	Grade at presentation	N	Follow up (FU) criterion	Required THA	Conclusion
Steinberg <i>et al.</i> , 1999	CD with bone grafting	Steinberg IA	3	Mean FU 39 Months (range 24-72)	3	21% required THA after first intervention
		Steinberg IB	4		1	
		Steinberg IC	4		2	
		Steinberg IIA	11		1	
		Steinberg IIB	9		3	
		Steinberg IIC	42		13	

Steinberg I: Normal radiograph, abnormal MRI; Steinberg II: Sclerosis visible on radiograph; Steinberg III: Crescent sign; A: <15% involvement; B: 15%-30% involvement; C: >30% involvement. (Steinberg *et al.*, 1995).

Paper	Treatment	Grade at presentation	N	Follow up (FU) criterion	Collapsed	Conclusions
Nishii, Sugano, Ohzono, T. Sakai, <i>et al.</i> , 2002	Conservative	ARCO IIA	16	Minimum FU 2 years	1	The risk of collapse increases with lesion size, Lesions tended to be larger. Overall, of the 65 pre-collapse hips, 50% collapsed, the majority of these had a lesion occupying >30% of the femoral head - 80% of IIC hips collapsed
		ARCO IIB	19		8	
		ARCO IIC	30		24	

ARCO = Association Research Circulation Osseous. ARCO II: No crescent sign, x-ray abnormal showing sclerosis, osteolysis, local porosis. A: <15% involvement; B: 15%-30% involvement; C: >30% involvement (Gardeniers, 1993).

Paper	Treatment	Grade at presentation	N	Follow up (FU) criterion	Collapsed	Conclusions
Ohzono <i>et al.</i> , 1992	Conservative	JOA 1A	6	Mean FU 5 years (2-18)	0	The majority of large lesions collapsed - the IC lesions collapsed at a mean of 16 months (2-36).
		JOA 1B	16		2	
		JOA 1C	68		64	
		JOA 2	4		4	
		JOA 3A	17		2	
		JOA 3B	5		5	

JOA = Japanese Orthopaedic Association. JOA 1: Presence of a sclerotic line; A=Media involvement, B=Medial and central, C=Medial, central and lateral. JOA 2: Early flattening without demarcation line around necrotic area. JOA 3:

Cystic Lesions: A = Medial, B=Lateral.

Table 5 continued.

Paper	Treatment	Grade at presentation	N	Follow up (FU) criterion	Number at last Follow up	Conclusions
Iorio <i>et al.</i> , 1998	CD	Ficat I	7	Mean 5 years (1-13)	3	The majority of lesions progressed, the majority of lesions presented before the crescent sign was visible, most progressed from IIA to collapse between FU
		Ficat IIA	20		11	
		Ficat IIB	6		2	
		Ficat III	0		12	
		Ficat IV	0		5	

Ficat I: Normal radiograph, abnormal MRI; Ficat II Sclerosis visible on radiographs; Ficat III Crescent sign; Ficat IV: Femoral head collapse (Mont *et al.*, 2006). IIA - no crescent, IIB – crescent (Iorio *et al.*, 1998).

Paper	Treatment	Grade at presentation	N	Follow up (FU) criterion	Grade at last Follow up	Conclusions
Plenk Jr <i>et al.</i> , 2001	CD and conservative	ARCO IIB	4	Mean FU 21 months (0-63)	0	7 CD, 7 conservative, no difference between groups.
		ARCO IIC	5		2	
		ARCO IIIA	0		0	
		ARCO IIIB	0		1	
		ARCO IIIC	2		3	
		ARCO IVA	0		0	
		ARCO IVB	0		3	
		ARCO IVC	3		5	

ARCO I: Normal radiograph, abnormal MRI; ARCO II: No crescent sign, x-ray abnormal showing sclerosis, osteolysis, local porosis; ARCO III Crescent sign on x-ray and / or flattening of the articular surface; ARCO IV: Osteoarthritis. A: <15% involvement; B: 15%-30% involvement; C: >30% involvement (Gardeniers, 1993)

Paper	Treatment	Grade at presentation	N	Follow up (FU) criterion	Revised at last follow-up	Conclusions
Aigner <i>et al.</i> , 2002	CD	ARCO I	30	Mean FU 68.9 Months (31-120)	1	CD appears to be effective at ARCO I, less so at II and III.
		ARCO II	9		5	
		ARCO III	6		3	

ARCO I: Normal radiograph, abnormal MRI; ARCO II: No crescent sign, x-ray abnormal showing sclerosis, osteolysis, local porosis; ARCO III Crescent sign on x-ray and / or flattening of the articular surface; ARCO IV: Osteoarthritis. A: <15% involvement; B: 15%-30% involvement; C: >30% involvement

Only two studies have quantified the change in lesion volume over time. Takao *et al.*, (2006), and Zhao *et al.*, (2009), both used contiguous MR images to assess whether lesion morphology changed over time. In the former study no significant change was seen between images taken 1 year apart. Conversely, Zhao *et al.*, (2009), showed spontaneous reduction in volume. There are key differences between these studies: Takao *et al.*, (2006), used a general sample of the AVN patient population, their baseline measurements were often taken a significant time after initial onset and the follow-up period was relatively short. Zhao *et al.*, (2009) specifically included patients treated with high dose steroids for severe acute respiratory syndrome (SARS). The mean time between initial steroid administration and baseline image acquisition was shorter and the mean follow-up time was significantly longer than the other study. The studies are in

partial agreement as although the latter study showed significant differences between baseline and subsequent lesion measurements, they failed to show a significant difference between later measurements. This suggests that reduction in lesion size occurs in the short term, but does not continue to progress. What is not clear, however, is whether the reduction in lesion volume is associated with healing within the bone or collapse of the articular surface.

1.4.3 Lesion size and position

Lesion volume (Steinberg *et al.*, 1999) and location (Nishii, Sugano, Ohzono, Takahashi Sakai, *et al.*, 2002) are two of the most important factors affecting the prognosis for a particular patient. Numerous studies have demonstrated that large lesions in the weight bearing area have a far greater chance of progressing than small lesions. There is some consensus that “large” in this context refers to lesions occupying more than 30% of the volume of the femoral head; Nishii *et al.*, (2002b), found that lesions occupying more than 30% of the femoral head were at significant risk of collapse regardless of location. When the necrotic volume is less than 30% of the femoral head, location has a significant influence on survivorship with lesions in the anterior-superior portion of the femoral head being identified as more likely to collapse regardless of volume. The proposal that a lesion occupying 30% of the femoral head is a critical size is, to an extent, supported by Steinberg *et al.*, (1999), who found that radiographic progression occurred in hips with a lesion that occupied more than 15% of the cross-sectional area. It is noted that many papers make poor distinction between two and three-dimensional measurements.

The method of volume calculation or approximation has a large influence on the reported ability to correlate volume to survivorship (Nishii, Sugano, Ohzono, Takahashi Sakai, *et al.*, 2002). There is a trade-off between high accuracy and ease of calculation, with many surgeons preferring a coarser method for the sake of expediency (Steinberg *et al.*, 2006).

1.4.4 Conclusion on the classification and presentation of AVN

Lesion size and position are risk factors for progression, as is the presence of pain, but they cannot fully explain whether collapse will occur. Biological factors such as systemic disease or chronic treatments are also factors that must be considered. From a biomechanical perspective, lesion shape may be significant but there is currently no data to support this hypothesis.

In terms of quantifying the lesion, general agreement is found in the literature that <15%, 15-30% and >30% of head volume constitute “small”, “medium” and “large”. Used in isolation, current classification systems are insufficient to accurately predict progression to collapse, possibly due to the fact that shape and patient demographics are not considered. Another potential problem is the subjectivity of such systems. Although the best solution for many patients will be clear, there exists a sub-set for whom the ideal treatment remains controversial. In these cases there is an unmet clinical need for robust stratification into those who would

benefit from early intervention and those for whom this would represent an unnecessary welfare and fiscal cost.

When quantifying the rate of progression, both time from onset of pain, and time from initial diagnosis are useful statistics to include in future studies. Lesions do appear to change in volume over time, but this appears to be a short-term phenomenon and if morphological changes are to be quantified, early time points and regular measurement intervals are required.

Many patients will only present once the opportunity to preserve the articular surface has been lost. However, in a significant number of cases the contralateral hip will be affected to a lesser degree and the possibility of avoiding bilateral total hip arthroplasty remains.

1.5 Treatment options

The most immediate requirement for treatment is the reduction in pain. Second to that is restoration and preservation of joint function. It is known that the prognosis for small asymptomatic lesions is better than for moderate to large lesions (Belmar *et al.*, 2004), but their survivorship potential drops significantly if they become symptomatic. The surgeon's dilemma therefore, is to decide whether to intervene early hoping to save the joint, but at the risk of performing unnecessary treatment that could be detrimental to future total hip arthroplasty (Hungerford and Jones, 2004). The alternative is to monitor the hip at the risk of missing the critical change from a salvageable joint to one that has already begun to degenerate arthritically. Attempts have been made to assist the surgeon by correlating lesion size and position to probability of collapse (Nishii, Sugano, Ohzono, T. Sakai, *et al.*, 2002; Mazières *et al.*, 1997). However, although these studies gave promising results, the authors acknowledge the limited study size, and limitation of the input to only anatomical predictors.

1.5.1 Core-decompression and conservative treatment

Core decompression was originally described in 1964 (Parsons and Steele, 2008), and remains one of the most prevalent treatments for AVN (Lieberman, 2004) because of its immediate palliative effect (Bejar *et al.*, 2005). It can be broadly subdivided into single hole, which uses a biopsy trephine in the range of 5-15mm diameter, or multi-hole, where a Steinman or Kirshner-type pin is used to create multiple small holes that penetrate the lesion (Marker, Seyler, Ulrich, *et al.*, 2008). Schematic representations of these are shown in Figure 5. The latter is generally preferred as it reduces the complications associated with weakening the femoral head or neck using a large diameter trephine (Mont *et al.*, 2004).

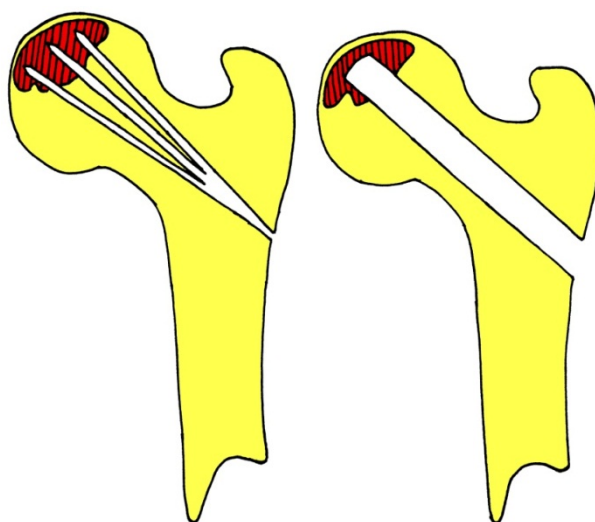


Figure 5. Schematic representations of multi hole (left) and single hole (right) core decompression

Core decompression can be augmented with bone grafting, injection of bone marrow, or use of adjunct therapies such as electrical stimulation (Steinberg *et al.*, 1990) or pharmacological therapies. Augmentation with bone marrow has been studied by a number of researchers. There is evidence to suggest improved revascularisation and repair of the bone structure (Edgar and Einhorn, 2011) but there is still an average duration between diagnosis and conversion to THA of approximately 1 year (Lau *et al.*, 2014). In all cases the goals are to reduce the intraosseous pressure and restore or improve vascular flow to prevent further ischemic episodes (Parsons and Steele, 2008). As core decompression does not mechanically augment the femoral head, this treatment modality is only indicated prior to collapse of the articular surface (Lieberman, 2004).

Four authors (Yoon *et al.*, 2001) performed a retrospective review of 42 reports regarding 2025 hips treated by either core decompression (1206 hips) or conservative management (819 hips). Although various joint loading regimes such as “toe-touch”, assisted, or non-weight bearing were evaluated as non-operative treatments, no difference between them could be measured, with an overall “satisfactory clinical result” in only 22.7% of cases. This compares to survivorship of between 53% and 70% depending on whether high-volume (and therefore highly experienced) centres are included. These results correlate with earlier and later studies (Parsons and Steele, 2008, Marker, Seyler, Ulrich, *et al.*, 2008, Hungerford and Jones, 2004 and Musso *et al.*, 1986). The latter expounding on the general futility of conservative treatments and quoting Glimcher and Kenzora, (1979b): “the underlying pathologic process proceeds clinically and radiologically whether the patient uses crutches or not”. When survivorship is stratified by diagnostic grade (bearing in mind the limited inter-observer reproducibility of the grading systems) rather than treatment versus conservative management, a distinct trend emerges: Radiographically normal hips have a far greater chance of survival than those that display sclerotic changes, which in turn are more likely to survive than hips with subchondral

fracture (Musso *et al.*, 1986; Ohzono *et al.*, 1992; Koo and Kim, 1995; Steinberg *et al.*, 1999; Nishii, Sugano, Ohzono, T. Sakai, *et al.*, 2002; Aigner *et al.*, 2002). This goes some way to supporting the proposal that conservative treatment has a role to play in the management of hips with AVN, as long as the lesion is sufficiently small (Nam *et al.*, 2008; Parsons and Steele, 2008). It should be noted that the treatments generally defined as core-decompression have evolved over time, and there is evidence to suggest that survivorship in patients treated after 1992 has improved compared to those treated before this time (Marker, Seyler, Ulrich, *et al.*, 2008).

1.5.2 Bone grafting

Morsellised bone grafting is often used to augment large diameter core decompression. Depending on the approach, it may remove more necrotic bone than standard core decompression with the potential to re-position and mechanically support the articular surface (Parsons and Steele, 2008). The survivorship for non-vascularised grafting varies drastically, with clinical success rates between 36% (Seyler *et al.*, 2008) and 90% (Johnson *et al.*, 2010) reported. There is some controversy about whether the necrotic portion should be comprehensively removed or, on the basis that even necrotic bone is stronger than morselized graft, only partially removed to provide a cavity into which a structural augment can be placed (Matsusaki *et al.*, 2005).

Free vascularised fibular grafting is another option to structurally augment the core-decompression tract. It is an extremely skilled and resource intensive procedure, requiring up to six hours of surgery (Aldridge *et al.*, 2003). The technique has evolved from using non-vascularised fibular struts to fill a large core-decompression tract. In the latest incarnation of the technique, a tract is created through the femoral neck into the affected region within the femoral head and the necrotic lesion is debrided. The surgically created cavity is then filled with morselized bone graft and a section of the fibula including a vascular pedicle is excised. The fibular strut is impacted into the tract and an anastomosis of the vascular pedicle is performed. The aim is to promote osteogenesis and vascularisation as well as mechanically supporting the femoral head. Reported survivorship varies from 70% to 80% at 2-5 years (Parsons and Steele, 2008; Chen *et al.*, 2006; Dean *et al.*, 2001).

1.5.3 Device-based treatments

The only true solution for end-stage AVN is total hip arthroplasty. This has been shown to be generally successful, with 97% (95% confidence interval (CI): 96-97%) survivorship at 2 years and 77% (95% CI: 74%-80%) at 16 years. However, this survivorship is lower than patients from the same cohort from the Nordic Arthroplasty Register Association database (n=427,806) treated for primary osteoarthritis (98% (95% CI: 98%-98%) at two years and 86% (95% CI: 86%-86%)) (Bergh *et al.*, 2014).

However, a number of devices are currently marketed specifically for the treatment of pre-collapse AVN. Of these, only the Osteonecrosis Intervention Implant (Zimmer Inc., Warsaw, IN) has been written about by independent authors. This is a porous tantalum pin and the implantation procedure aims to provide the benefits of core decompression coupled with provision of mechanical support. The clinical results are mixed, with reports that, although the device offers a “safe ‘buy time’ technique” (Varitimidis *et al.*, 2009) little bone in-growth occurred at an average of 13 months and the device is unable to prevent disease progression (Tanzer *et al.*, 2008).

1.5.4 Conclusion on treatments

Controversy exists over the efficacy of conservative treatment, but there is a general acceptance that it is not viable in advanced cases. Mechanical interventions such as bone grafting may act to strengthen the femoral head or weaken it, but this can be characterised as a compound engineering structure, thus modelled using established principles. Estimating the effect on the strength of the femoral head that biological (with or without mechanical effect) treatments may have is a more complex proposal. In both cases, a “four-dimensional” simulation is required: analysing three spatial measurements over time.

1.6 Diagnostic imaging for avascular necrosis

The ARCO grading system (Section 1.4.1) is the current gold standard for classification of AVN. It utilises plane x-ray, CT and MR imaging depending on the disease state. It was concluded in Section 1.4 that both lesion size and shape are likely risk factors for disease progression and there is a need to establish methods to exploit these modalities to improve evaluation of the risk of disease progression. Image analysis software such as ScanIP (Simpleware Ltd., Exeter, UK) provides a means of identifying the lesion boundary in three dimensions allowing the user to accurately quantify lesion volume as a percentage of the femoral head meaning that quantification is technically feasible (Zoroofi *et al.*, 2001).

Example images from MR and CT scans of a femoral head with AVN are shown in Figures 6 and 7 respectively. It is clear from these images that estimation of percentage involvement within a particular slice is subjective and depends on the imaging modality. Another source of variation is the user’s choice of slice. Three pairs of co-registered CT and MR images are shown in Table 6. The pairs of images represent the central-anterior region of the femoral head and are spaced approximately 2.5mm apart. The proportion of the head occupied by the lesion is significantly different between adjacent slices and between image modalities.



Figure 6. Example cross-section of a femoral head generated using a T1-weighted MR scanning protocol. The lesion boundary is demarcated by the outer edge of the low intensity (black) band within the femoral head. High intensity indicates a region containing fat. Within the femoral head this indicates a region with viable bone marrow.

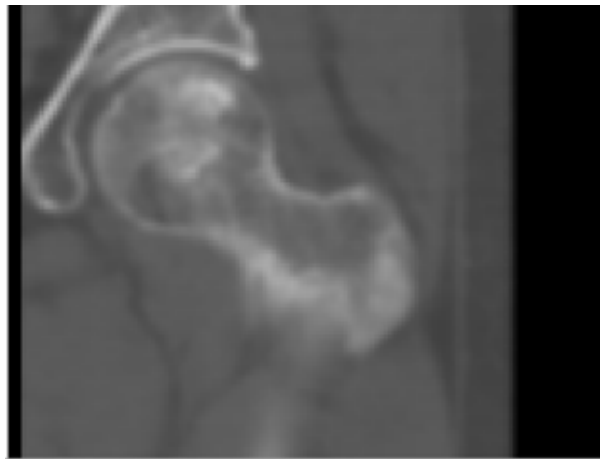


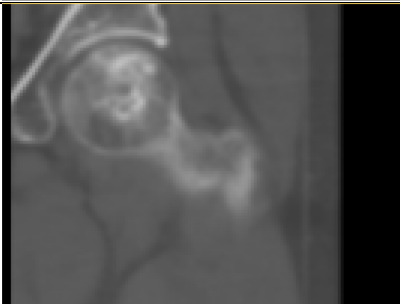





Figure 7. Typical example of a CT image of a femoral head with pre-collapse AVN. This image corresponds to the MR image shown in Figure 6. The high intensity regions indicate areas of increased density but this does not relate to the boundary of the necrotic segment.

Table 6. Co-registered CT and MR slices through a femoral head with AVN. The rows represent adjacent slices through the femur. Variations in intensity within the MR image do not indicate variations in material properties. Variations in intensity within the CT image do not indicate the presence or absence of necrotic bone.

Computed Tomography	Magnetic Resonance Imaging
	
	
	

1.6.1 Magnetic resonance imaging

Magnetic resonance imaging is recognised as the standard for confirming suspected AVN because it is often possible to distinguish small lesions or subchondral fractures that are invisible on plane radiographs (Calder *et al.*, 2008). It has been demonstrated to be both sensitive (sensitivity 88%-94%) and specific (specificity 71% to 100%) (Barille *et al.*, 2014).

AVN is identified by the presence of low-intensity (black) bands on T1-weighted MR images (Marker, Seyler, McGrath, *et al.*, 2008; Sakamoto *et al.*, 1997; Takao *et al.*, 2010) (Figure 6). These bands are an indication of the fibrovascular reactive interface, osteolysis, cysts, reparative tissue or subchondral fracture (Gardeniers, 1993; Kim *et al.*, 2003) and correlate to areas that lack hydrogen-rich marrow fat (Fordyce and Solomon, 1993). Increasing the magnetic field strength increases image clarity and scanning speeds (Alvarez-Linera, 2008; Schmitt *et al.*, 2004). Until the year 2000 MR scanners typically had an output of 0.5 Tesla (T) to 1.5T, but 3T scanners are now established in clinical use. Their increased sensitivity and specificity has been demonstrated in several applications (Alvarez-Linera, 2008; Schmitt *et al.*, 2004; Anderson *et al.*, 2008). However, clinical papers on the use of MRI for diagnosis of AVN published since

2000 either cite the use of 1-1.5 T scanners or do not include the field strength as a variable (Tien *et al.*, 2009; Anderson *et al.*, 2008; Popovic and Kocar, 2010; Schmitt *et al.*, 2004). At the time of review, only one paper (Popovic and Kocar, 2010) explicitly cites the use of a 3T scanner for diagnosis of AVN, but it does not discuss whether the field strength was of benefit. It must be noted that MRI is insensitive to necrotic changes outside the femoral head, suggesting that it must be used with caution when assessing patients with extensive involvement (Calder *et al.*, 2008).

Zoroofi *et al.*, (2001) and Zoroofi *et al.*, (2004) presented a means of segmenting AVN lesions using T1-weighted MRI data sets. The technique allowed quantitative assessment of lesion geometry, determining bone viability and perhaps most crucially, defining the relationship between the risk of collapse and lesion morphology. They found experimentally that semi-automated techniques for defining the lesion boundary such as snakes and active contours were not appropriate for segmenting lesions and observed that it is very difficult to express the shape of pathological or necrotic lesions with mathematical functions. The algorithmic technique described in 2001 demonstrated excellent effectiveness in segmenting femoral heads with small lesions, but moderate to poor effectiveness when lesions occupied 25% or more of the femoral head. The later methodology showed improved rate of achieving a satisfactory segmentation outcome with “good” results in 90% of the cases evaluated but this was still subject to algorithmic failures introduced by extremes of pathology and anatomy. The study was benchmarked against a manual segmentation method where the outer edge of the low intensity band was painted by three experts. This manual approach was shown to be reproducible, with over 95% agreement between the experts.

1.6.2 Computed tomography

Computed tomography (CT) provides better delineation of osseous structures than MRI (Lang *et al.*, 1992; Poelert *et al.*, 2013) making it the modality of choice if the goal is to generate *in silico* mechanical simulations (Mahfouz *et al.*, 2007; Yosibash, Padan, *et al.*, 2007; Viceconti *et al.*, 2004; Lobos *et al.*, 2009; Bucki *et al.*, 2010; Radcliffe and Taylor, 2007; Bryan *et al.*, 2010; Bryan *et al.*, 2009) or statistical models (Golland *et al.*, 1999). It is also a more sensitive means of estimating lesion grade and location compared to plain radiographs (Cherian *et al.*, 2003; Ohzono *et al.*, 1992). Similar to MRI, CT technology has advanced significantly since its inception with a transition from single detector to multi-detector arrays offering significant benefits in terms of speed, image quality and reduced radiation exposure (Rubin *et al.*, 1999; Rubin, 2003; Rubin *et al.*, 1999; Rubin, 2003). Sixteen and sixty-four detector CT scanners are now used in orthopaedics (Fayad *et al.*, 2009), from which highly accurate and repeatable images can be obtained (Markel and Chao, 1993). However, it remains inferior to MR as a means of detecting AVN, with one study showing that only 81% of MR-confirmed cases of AVN were identified during consensus review of concurrent CT scans (Barille *et al.*, 2014). A

typical CT derived image of a femoral head with AVN is shown in Figure 7. This image corresponds directly with the MR image shown in Figure 6, indicating the very different distribution of material density (indicated by CT) and bone viability (indicated by MR).

One challenge associated with deriving a patient-specific geometry model from CT scans is obtaining consistent results. Manual approaches where the surface of the bone is outlined are time consuming and subject to user variability and the excellent contrast between bone and soft tissue lends itself to an approach where threshold values are applied to isolate regions of the image. An automated method of segmenting cortical and trabecular compartments of a long bone using two thresholds and a closing function to generate a mask was developed by Buie *et al.*, 2007. Using this approach, a large proportion of the bone surface can be identified in a single step by applying a grayscale intensity threshold. In cases where there is a mixed density trabecular structure such as in the subchondral region of the femoral head this step may fail to create a complete mask. Adding a second step that used a closing function to grow the existing mask by a defined number of voxels before shrinking it again will tend to close up pores to provide a solid mask representing the trabecular regions. In regions where the trabecular structure is particularly open or the cortical structure is particularly thin it may be necessary to revert to a manual painting operation but the opportunity for user induced variability will be substantially reduced because the proportion of the surface that must be manually defined surface will tend to be small.

The automated method presented by Buie *et al.*, 2007 was shown to be at least as accurate as manual segmentation with a tendency towards less user bias. Although the need for an automated process will be dictated by the number of samples in the data set, the method can be executed manually with the same expected outcome. Despite the opportunity to reduce the user input required, segmentation of CT scans to generate 3D geometry models is time consuming and it is not reasonable to expect that this would be undertaken routinely in a clinical setting. A more user-centred approach would be to define a method that used a small number of representative 2D cross-sections to characterize the lesion. This has the advantage of allowing quick segmentation of a user-selected 2D cross-sectional image and also allows intuitive reference back from the geometry model to the original image for verification purposes.

1.6.3 The gap between diagnostic grading systems and accurate prognosis

To a large extent, the requirements for diagnosis and prognosis are similar: it must be possible to estimate the extent of the infarction and the degree of physiological changes. For diagnosis, comparison to a set of schematic images is sufficient to allow a clinician to identify and record the presence of AVN semi-quantitatively. All the commonly used grading systems rely on size, shape and presence or absence of subchondral fracture to quantify the extent of a lesion. While

predicting collapse of the femoral head when fractures are already present may be reliable, it is also futile if the goal is to preserve the articulation. Prognosis in the earlier stages is far less reliable. The link between progression and lesion size has been established (Hernigou *et al.*, 2006; Koo and Kim, 1995; Nishii, Sugano, Ohzono, T. Sakai, *et al.*, 2002; Mazières *et al.*, 1997; Cui and Saleh, 2008), and while there is consensus that small lesions are unlikely to progress, this factor may provide only a 50% chance of predicting collapse of small lesions within two years (Hernigou and Lambotte, 2001). The predictive power increases slightly when position is included (Nishii, Sugano, Ohzono, Takahashi Sakai, *et al.*, 2002) but it is clear that factors beyond lesion size and location are critical for accurate prognosis.

Identifiable gaps in the current systems include the effect of shape: two lesions with the same volume but different shapes will logically cause different stress distributions within the femoral head. In addition, patient weight and activity level, the presence of systemic disease (Mont *et al.*, 2010), concomitant treatments and other demographics such as age, sex and ethnicity. When attempting to incorporate such factors it is important to consider the diversity and potential ambiguity of scales and units.

1.6.4 Conclusion on diagnostic imaging

Magnetic resonance imaging is the modality of choice for detecting and defining the morphology of AVN lesions. The use of more powerful scanners with improved resolution will become more common in the future and image-based diagnosis of AVN using MRI should become correspondingly easier. Automated methods of segmenting lesions will also improve with time but the effort required to develop and validate such methods may be outweighed by their potential inability to cope with complex lesion geometries.

Manual segmentation of lesions from T1-weighted MR data is an established method and may be a more appropriate short-term approach, especially if the lesions in question are large or have complex morphology.

Computed tomography offers the ability to generate high resolution images of the bone architecture and can be used to produce geometry models through a threshold-based approach that, although still manual, will have a lower tendency towards selection bias than methods that rely on contour painting.

There is little visual correlation between the lesion boundary identified using MR and the bone mineral density characterized by CT. Therefore the contribution that each modality makes to the final model must be clearly understood. An example set of co-registered CT and MR slices is shown in Table 6. It is important to note that variations in intensity within the MR image do not indicate variations in material properties and that variation in intensity within the CT image does not indicate the presence or absence of necrotic bone.

Three dimensional segmentation of CT and MR images to generate geometry models is time consuming and unlikely to be satisfactory in a clinical setting. Generation of 2D geometry models directly from user-identified slices is a potentially faster approach that allows intuitive reference back from the geometry model to the original image for verification purposes.

It is concluded that using a combination of CT and MR images may provide the best method of defining both the necrotic lesion bone geometry. MR data should be used to generate lesion geometry by manually painting the outside edge of the low intensity band in T1-weighted MR images. Computed tomography data should be used to define the geometry of the femur itself. The methodology used to evaluate lesion geometry should be compatible with an approach that uses 2D cross-sections through the femur as a surrogate for a more detailed 3D process.

1.7 The material properties of bone

Bone is a mixture of a fibrous organic framework within an inorganic mineral matrix. The mineral portion of bone, which constitutes around 75% of the dry weight, is principally composed of Calcium Phosphates and Calcium Carbonate, generally in the form of crystalline Hydroxyl Apatite, $\text{Ca}_{10}(\text{PO}_4)_6(\text{OH})_2$, and amorphous Calcium Phosphates. The organic portion is principally type 1 collagen (Seeman and Delmas, 2006; Carter and Spengler, 1978).

Long bones, for example the femur, tibia and fibula are divided anatomically into three zones. The diaphysis is the central portion; the metaphysis is the transition from the diaphysis to the epiphysis, which describes the ends of the bone proximal to an articulation.

The diaphyses of long bones are composed of dense cortical bone that forms an approximately cylindrical shaft. The centre of the shaft, or medulla, is filled with bone marrow. The metaphyses and epiphyses have a cortical shell that is continuous with that of the diaphysis, but is filled with cancellous bone that forms a three-dimensional network of bony plates and columns. The long bones of the body are arranged in this way in response to mechanical stimulus: Hollow, cortical bone is present where the load is largely axial; cancellous bone is found at the ends where multi-directional loads must be distributed and re-aligned to the axis of the bone.

The distinction between cancellous and cortical bone is based on porosity, with cancellous bone generally exhibiting between 30%-90% porosity, and cortical bone exhibiting around 5%-30%. Differentiation between very dense cancellous bone and very porous cortical bone is arbitrary (Carter and Spengler, 1978). The trabeculae in human bone are typically 100 μm to 150 μm thick; cortical bone thickness varies between 1mm and 5mm (Wehrli *et al.*, 2006).

Bone is a relatively stiff biological structure. It is a viscoelastic material which several investigators have compared to fluid-filled porous engineering materials (Ciarelli *et al.*, 1991; Goldstein, 1987) and the stiffness and strength of a sample will vary with the rate of load

application. Under sustained loads, the structure will tend to creep, reducing the stress for a given strain. In constrained compression of human cancellous bone, viscous flow of marrow from the trabecular pores leads to strengthening of the bone only at strain rates of 10 sec^{-1} or higher (Carter and Hayes, (1976). There is no difference in response when the strain rate is 0.01 sec^{-1} or lower indicating that this rate can be considered quasi-static.

It is also generally accepted as transversely anisotropic, being stronger and stiffer longitudinally than in the transverse direction. Under both monotonic and cyclic loading, cortical bone failure is governed more by strain magnitude than stress magnitude (Carter and Spengler, 1978; Currey, 1970), meaning that loading under displacement control results in a change in load-bearing capacity faster than testing under load-control.

The strain-rate dependency of bone material properties must be considered when developing both test protocols and material models based on the results. Using a quasi-static strain rate for *in vitro* testing will reduce the influence of bone marrow. This is important because the viscoelastic behaviour of necrotic bone has not been characterised. If a surrogate material is used then steps should be taken to reduce the influence of this property. The disadvantage of using a quasi-static approach is that it does not represent the highly dynamic nature of joint loading. Under high strain rates the marrow within the trabecular bone may act to stiffen the structure but it must also be recognised that the bone marrow in necrotic lesions may be missing or have different viscosity to healthy marrow.

1.7.1 Measures of bone density

The term “true density” is used to describe the density of the material at a microscopic level. Although their apparent densities may be vastly different, the true density of cancellous bone is only around 3% lower than that of cortical bone. “Apparent density” refers to the density of the structure as a tissue and is also known as bone mineral density (BMD). This may be either the three-dimensional mass of mineral per unit volume (Carter and Hayes, 1976), if measured by CT, or planar mass of mineral per unit area if measured by Dual Energy X-ray Analysis (DEXA) (Wehrli *et al.*, 2006; Wehrli, 2007).

Carter and Hayes, (1976) report the apparent densities for cancellous bone from the tibial plateau to be in the range of 0.07g/cm^3 to 0.97g/cm^3 . Changes in the apparent density of cancellous bone may be caused by either a change in mineralisation or a change in porosity and it should be noted that two samples with the same apparent density could have different degrees of porosity and mineralisation that cancel each other out.

1.7.2 Relationship between density and mechanical properties for healthy cancellous bone

It has been shown that the compressive strength and elasticity of cancellous bone can be directly linked to apparent density (Carter and Spengler, 1978; Wirtz *et al.*, 2000) and ash weight (Brown and Ferguson, 1980). Bone is an anisotropic material and its properties vary widely with anatomic location. An example of the variability in reported results is shown in Table 7. The differences are a function of the orientation and location from which the bone was taken, the shape of the sample and the rate at which the sample was tested. It is clear that reported relationships must be used with caution unless the specific location and orientation are identical to that of the current study.

Subchondral bone density varies around the surface of the femoral head. The superior-medial portion is the most dense location: 180%-198% higher than the lowest density regions found in the lateral portion of the femoral head (Wright *et al.*, 2012).

At a material level, Poisson's ratio may be considered an isotropic material property. Turner *et al.*, (1999) compared Young's modulus derived by nano-indentation to that obtained using acoustic microscopy for cancellous bone from a human distal femoral condyle. They varied the Poisson's ratio assumed in their nano-indentation technique from 0.2 to 0.4 and found that it changed the measured value of Young's modulus by no more than 8%. Based on this result they concluded that the results were not greatly affected by the chosen values for Poisson's ratio. Therefore, when calculating the Young's modulus for trabecular bone using acoustic microscopy, they assumed an isotropic value for Poisson's ratio of 0.3.

At a structural level however, Poisson's ratio is an anisotropic property with ratios reported for bovine cancellous bone in different orientations ranging from 0.222-0.422 (Ashman and Rho, 1988). Ulrich *et al.*, (1999) used a material Poisson's ratio of 0.3 to derive structural anisotropic elastic stiffness constants from finite element analysis based on micro-CT images. They reported similar variation in orthogonal Poisson's ratios for samples taken from the lumbar spine, iliac crest and calcaneus. However, for samples of cancellous bone taken from human femoral heads, the lowest orthogonal Poisson's ratio was 0.310 ± 0.031 and the highest was 0.333 ± 0.042 . This suggests that in the specific case of femoral head cancellous bone, an isotropic Poisson's ratio of 0.3 is satisfactorily representative.

Table 7. Reported relationship between compressive strength (σ_b), elastic modulus (E) and density (ρ) for bone

Data extract from Wirtz <i>et al.</i> , 2000	Compressive strength, σ_b (MPa)		Elastic modulus, E (MPa)	
Load direction	Axial	Transverse	Axial	Transverse
Cortical Bone	$\sigma_b=72.4\rho^{1.88}$	$\sigma_b=27\rho^{1.51}$	$E=2065\rho^{3.09}$	$E=2314\rho^{1.57}$
Cancellous bone	$\sigma_b=40.8\rho^{1.89}$	$\sigma_b=27\rho^{1.37}$	$E=1904\rho^{1.64}$	$E=1157\rho^{1.78}$
Data extracted from Lotz, Gerhart, and Hayes 1990	Aligned to neck axis		Aligned to neck axis	
Cancellous bone	$25\rho^{1.8}$		$1310\rho^{1.4}$	
Isotropic elastic modulus				
Data extracted from Yosibash, Trabelsi, and Milgrom 2007	Carter and Hayes 1976 (Cortical)		$2875\rho^3$	
	Carter and Hayes 1976 (Cancellous)		$2003\rho^{1.56}$	
	Cody et al. 2000 (Cortical)		$1684\rho^{3.3}$	
	Cody et al. 2000 (Cancellous)		$1949\rho^{2.5}$	
	Keyak and Falkinstein 2003 (Cortical)		$10200\rho^{2.01}$	Ash density
	Keyak and Falkinstein 2003 (Cancellous)		$5307\rho+469$	Ash density
	Keller 1994		$10500\rho^{2.3}$	Ash density
Data extracted from Dopico-González, New, and Browne 2010			$10+2875\rho^3$	
Data extracted from Gupta, New, and Taylor 2006			$7281\rho^{1.52}$	
ρ = Apparent density (g/cm^3) unless otherwise stated				

1.7.3 The relationship between density and mechanical properties for diseased bone

Wehrli et al., (2006), proposed that the power relationship remains valid when considering osteoporotic bone: that there is no difference in the ultra-structural and chemical makeup of osteoporotic bone compared to normal bone, and it is the relative reduction in bone mineral density caused by increased porosity that drives increased brittleness. It is likely that this theory holds true for the areas of focal osteolysis that form during destructive repair. However, the earlier stage of limited repair may lead to a denser and therefore stronger band of bone peripheral to the lesion with an associated loss of anisotropy.

Only limited data on the material properties of necrotic bone is available and no data on whether the bone continues to exhibit isotropic material properties has been found. Brown et al., (1981), tested nine femoral heads with AVN retrieved at primary arthroplasty to derive their strength and elastic and plastic moduli. They compressed cubic test samples at a constant rate of 0.004 sec^{-1} and used a finite element analysis derived compensation factor to correct for apparent stiffening caused by the sample shape when interpreting the results. The location within the femoral head from which the cubic samples were taken was recorded and the results compared to spatially matched controls. Absolute values reported for the healthy controls ($n=3$, absolute

average stiffness's 445MPa, 458MPa and 421MPa and strengths 19.1MPa, 19.7MPa and 19.4MPa) were presented. The values for necrotic bone were presented as a percentage reduction in both strength and modulus relative to the controls.

For the single pre-collapse femoral head used in the study, bone samples taken from the necrotic region demonstrated a 41% reduction in UCS and a 59% reduction in elastic modulus when compared to healthy bone from an equivalent location.

Looking specifically at the only pre-collapse head, they report a statistically significant 41% reduction in strength and a 59% reduction in modulus when compared to healthy bone from an equivalent location. In terms of elastic and plastic behaviour; most necrotic bone reached an elastic limit, after which there was a rapid decrease in stress. Continued loading, however, caused the stress to build again. This is characteristic of the failure pattern for a porous structure. Using a porcine model of juvenile ischemic necrosis, Aruwajoye et al., (2013) found that the nano-indentation-derived modulus of ischemic bone was higher and that this bone was more susceptible to micro-cracking. This suggests that the reduced macro-scale modulus is actually the result of embrittlement at a micro-scale.

A dilemma faced by the Brown et al., (1981), is the fact that the dry, defatted mass density of necrotic bone increased by around 51% compared to healthy bone. Although this correlates to radiographic findings, it makes estimates of structural properties based upon the well-established power relationships discussed in the previous section impossible. This represents a significant gap in the scientific knowledge surrounding avascular necrosis.

Haba et al., (2012), evaluated the structural properties of severely osteoarthritic femoral heads by extracting a 12mm diameter core from the central portion of excised femoral heads, aligned to the neck axis. They obtained values for the structural modulus and ultimate compressive strength of 232 ± 130 MPa and 6.1 ± 3.3 MPa respectively but these values must be used with caution as the values relate to a single orientation and the properties are likely to be anisotropic.

1.7.4 Conclusion on the material properties of bone

Bone is a complex material that, although analogous in many ways to other engineering materials, has its own distinct set of properties. The compressive strength and elastic modulus can be related to apparent density using a power-law relationship but one must be careful to consider the location and orientation of the samples when applying such power laws.

It may not be necessary to correlate mechanical properties to physical density: Hounsfield or radio-density may be sufficient. When referring to density, it is important to distinguish between true and apparent density. Although there is only around a 3% difference in the true densities of cancellous and cortical bone, there is a significant difference in apparent densities because of the increased porosity of cancellous bone. The porosity of cortical bone may be up to 30%;

cancellous bone may be up to 90% porous. The transition from cortical to cancellous bone is ill defined in terms of apparent bone density.

It is also important to note that measures of apparent density can be represented in different ways depending on the measurement method: CT gives a three-dimensional estimate; DEXA gives two-dimensional results. Bone mineral density and bone mineral content are distinct, although often confused, units of measure.

Changes in apparent density may be caused by a change in the mineral content of the bone or the porosity. Thus two samples with the same apparent density may have a different mineral content or porosity: it is not clear from the literature whether this distinction has an effect on the mechanical properties but it is the opinion of the author that dense bone with a low mineral content is likely to be less stiff and fail in a more ductile manner than porous bone with a high mineral content.

Only limited data describing the material properties of femoral heads with AVN exists. However, the available literature suggests that, based on a sample size of one, pre-collapse necrotic bone demonstrates a 59% reduction in elastic modulus and 41% reduction in strength related to healthy bone from an equivalent location. Attempts to apply density-based models for strength and modulus may be confounded by the increase in apparent density associated with collapse of the necrotic segment. No information exists on the anisotropic behaviour of necrotic bone and, given the structural changes that occur such properties cannot be assumed to remain valid.

1.8 Finite element analysis

1.8.1 Introduction to finite element analysis

Finite element (FE) analysis is an engineering tool that provides a method of solving structurally indeterminate problems by reducing the continuous structure into a mesh of simple elements connected by nodes. The force and displacement applied to each node can be established by defining the energy associated with each element as a series of differential equations and solving them by assuming that the minimum potential energy within a system occurs when the system is in equilibrium

1.8.1 Finite element models of AVN

Brown et al., (1993), investigated the effect of core decompression on the mechanical integrity of necrotic femoral heads using a linear elastic finite element model. To model the lesion, they created a typical volume within a femoral head based on MRI data and uniformly attenuated the modulus of this volume by 75%, and the strength by 50%, citing an earlier *in vitro* study with the same principal author (Brown et al., 1981). They were able to show the benefit of stopping a large-diameter core decompression tract short of the lesion, thus maintaining the mechanical

support provided by the necrotic bone. They were also able to demonstrate that it was the loss of mechanical strength in the cancellous bone beneath the subchondral layer rather than involvement of the subchondral layer itself that caused the highest concentrated stresses, and hence the greatest likelihood of subchondral fracture.

In their analysis of the mechanics of femoral head AVN, Yang et al., (2002), cited Brown et al., (1981) to define the material properties of healthy and necrotic bone. They used moduli of 445MPa and 218MPa, and yield strengths of 19.4 and 5.5MPa respectively, assumed isotropy and ignored the effects of cortical bone. A Poisson's ratio of 0.3 was used throughout and neither cartilage nor cortical bone was modelled. Lesion shape and location were based on MRI scans of 55 patients with AVN and approximated as a cone, the axis of which was aligned to the head centroid. They evaluated the stress index, defined as the ratio of measured stress to yield strength, and compared the location of highest stress index to the location of fracture sites in osteonecrotic femoral heads. Although static failure is likely to occur at a stress index greater than unity, fatigue fracture could occur at significantly lower loads. In a normal femoral head the stress index was limited to 0.1. The same stress index was found in necrotic femoral heads when the conical angle of the lesion was less than 110° . The authors concluded that lesions of this size are unlikely to result in fracture because the maximum stress index was comparable to healthy bone. For lesions with an angle between 110° and 150° , the maximum stress index ranged from 0.15 and 0.3 in regions equivalent to physiological fracture sites. The fact that the stress index is significantly below unity in these sites suggests that fractures associated with AVN lesions are fatigue induced rather than a result of static over-load. The reduced strength reported by Brown et al., (1981) and hyper-calcification (sclerosis) leading to loss of trabecular structure and embrittlement at the periphery of the necrotic lesions may contribute to this.

Daniel et al., (2006), evaluated contact stress in the articular surface of a femoral head with a simulated osteonecrotic lesion. They found that contact stress increased with reducing lesion stiffness and was sensitive to orientation of the load vector.

A more recent study by Zhou et al., (2014), compared the stress distribution in femoral heads with necrotic lesions to simulations run with the same bone geometry but without a lesion present. They also used data from Brown et al., (1981) as a source for necrotic bone properties when they simulated one ARCO IIB and one ARCO IIC lesion. Femur geometry was derived from co-registered CT and MRI. Their results show that the presence of a lesion interrupted the normal stress distribution (Normal distribution being characterised by a pillar of elevated stress running superior-inferior from the load bearing portion). Similar material properties were used by Bae et al., (2013), who again cited the previous work by Brown et al., (1981). In this study, simplified lesion geometry was constructed by generating a cone with a 100° included angle. It is noted however, that their analysis did not evaluate the effect of the lesion on their outcome measure (stress in the lateral diaphysis).

All studies of the osteonecrotic femur published to date have used homogenous material properties for both the femoral head and lesion. This may be appropriate given the lack of data regarding the material properties of necrotic bone and the complexity of the microstructure of a femoral head with a necrotic lesion. Vaughan *et al.*, (2012) discussed the development of a multi-scale FE modelling approach. In this approach, the tissue fibres would be modelled at a microscopic scale within a macro structure. The concept of using a multi-scale finite element model to predict tissue level elastic properties as a function of radiographic parameters could be considered for future work because it offers improved simulation of the highly anisotropic properties of bone.

1.8.2 Elements

The size and configuration of elements has a significant effect on the veracity of a finite element model. If the elements are too large, varying the edge length slightly will result in a significant change in the reported stress and strain magnitudes. This is especially true in simulations of contact between two bodies where the change in contact area caused by the inclusion or exclusion of one element may be significant. It is therefore necessary to reduce the average edge length until the results converge. Polagar *et al.*, (2003), performed a convergence study when evaluating strain distribution in a human femur under physiological and simplified loading using ten-node tetrahedral elements. They found that using a 4mm average edge length gave a converged solution, with differences in strain energy values and principal stress magnitudes in a reference position below 2%. Using a larger mesh has the advantage of allowing a continuum approach to modelling bone where one element represents the structural material properties of several trabeculae (Jones and Wilcox, 2007). An inherent advantage of this approach is that using larger elements reduces the risk of artificial stiffening of the structure associated with a very fine mesh.

Bryan *et al.*, (2009), Bryan *et al.*, (2010) and Koivumäki *et al.*, (2012) used tetrahedral elements in their simulations of native human femurs, as did Dopico-González *et al.*, (2010) when they simulated a femur with a total hip prosthesis. Hernandez *et al.*, (2007) opted for 8-node brick elements when simulating the effect of resorption cavities on cancellous bone strength, as did Turner *et al.*, (2005) when they evaluated strain-mediated peri-prosthetic bone remodelling in the proximal femur. In general, the elements used in the aforementioned studies appear to have been linear. However Bevill and Keaveny, (2009), showed a benefit to using non-linear elements for micro-FE evaluations of trabecular bone strength when using models derived from CT scans with voxels greater than 80 μ m, highlighting the fact that image resolution must be considered during element selection. It is noted that linear elements offer sufficient resolution for a continuum approach.

1.8.3 Loading and constraint

Load transfer within the hip joint is achieved through the largely conforming articular surfaces of the acetabulum and femoral head. The conformance and relative compliance of cartilage serves to distribute the joint reaction force over the surface of the femur, reducing the stress within the bone itself. It is therefore necessary to understand this loading pattern and to define a practical analogue for use in testing disease models for AVN.

The musculo-skeletal system has a high degree of mechanical redundancy, making determination of the forces transmitted by the structural members complex (Polagar *et al.*, 2003). During the gait cycle, the femur experiences a wide range of forces. Bergmann *et al.*, (2001), defined the *in vivo* joint reaction force (JRF) vector for the femoral head during various activities. This work of this research group has become a gold standard in defining the loading regime for *in vitro* studies because the data is obtained in live patients directly from the hip joint for a wide range of activities. Other solutions, such as deriving the JRF from force-plate data using reverse kinematics is limited to a small number of activities and is subject to uncertainties because of the assumptions made in the analysis.

The region of contact between the cartilage of the femoral head and that of the acetabulum *in vivo* varies with age and pathology with a tendency towards increasing congruity with age (Dorr *et al.*, 2000). This makes it difficult to predict the exact contact conditions between the acetabulum and a necrotic femoral head. In their simulation of a femoral head with osteonecrosis, Yang *et al.*, (2002) applied load via a cartilage layer attached to a rigid concave surface conforming to the femoral head and with a contact region of 130°. Their simulation evaluated the effect of different lesion positions with respect to the centre of the applied load. Although the load vector was medialised by 15° to vertical, the authors do not claim to represent a specific activity. Rather the load represents a physiologically representative but generic loading condition allowing the results to be interpreted qualitatively for different load vectors.

Approximations are usually made by considering only the main muscle groups active at a particular point in the gait cycle. For example, peak loading during normal gait includes components from the gluteus minimus and medius, the iliopsoas and vastus medialis, but generally only body weight and abductor tension are considered when the investigation focuses on the proximal femur (Radcliffe and Taylor, 2007; Yang *et al.*, 2002; Brown *et al.*, 1993).

Wei *et al.*, (2005) evaluated the influence of mechanical properties of the subchondral plate, femoral head and neck on the dynamic stress distribution of the articular cartilage. They used a three dimensional model of the acetabulum and proximal femur and simulated body weight, abductor and adductor muscle forces. The resultant plot of von Mises stress indicated a region of elevated stress occupying approximately 90° of the articular surface with an approximately

parabolic distribution. The authors concluded that the stress distribution aligned well to the region of high density trabecular bone within the femoral head.

Various studies have chosen their load configuration to represent an instant at 10% of the gait cycle (Polagar *et al.*, 2003): the point just after heel-strike, but before the contralateral foot has been lifted off. The JRF at this point is a fraction of body weight (BW) but is contributed to by both the abductors and adductors which may effectively stiffen the femur by counteracting the bending moment. Peak JRF may be more appropriate where damage accumulation or ultimate strength is considered (Dopico-González *et al.*, 2010). Another alternative is provided by Turner *et al.*, (2005), who chose to use the load representing 45% of the gait cycle as this was the instant of highest load.

An alternative to using a single load condition would be to simultaneously simulate the loads applied to the femoral head during the entire gait cycle. This approach may address the main drawback of the other methods: That they only represent a single point within the duty cycle of the hip. However, the approach remains an approximation of what is in reality a highly dynamic kinematic environment. It also removes the ability to identify whether specific activities or joint positions cause the greatest risk of fracture.

Each node within a 2D or 3D FE model can potentially move in 3 or 6 degrees of linear and rotational freedom. Constraining the number of degrees of freedom in which the nodes at the boundary of the simulation can move is critical to developing a realistic model that will solve. The method of identifying and constraining these nodes should ideally represent the real-world constraints applied to the body being analysed. Over-constraining a model or applying constraint too close to the region of interest can result in stress concentrations that would not manifest in a physical specimen. Under-constraining a model will allow it to move in an unrealistic way.

Interactions between the surfaces of the components in an FE model assembly must also be defined so that one body cannot occupy the same physical volume as another. Two interaction cases are important to consider: A tied case and one governed by friction.

In the tied case the nodes of the two bodies in contact are constrained to move together. This is appropriate in cases where the two bodies are physically connected such as the continuum between the native bone and necrotic bone at the lesion boundary *in vivo*. In cases where the surfaces are able to move relative to each other a friction constraint is more appropriate. The co-efficient of friction controls the shear force transferred between the two bodies and can be optimised to replicate experimental values. One advantage of a friction interface is that it can be allowed to separate after contact. This is particularly useful in cases where deformation of one body could alter the proportion of one surface in contact with the other.

1.8.4 Failure modelling

Bone failure may occur *in vivo* because of static overload in tension, compression or shear as a result of a traumatic event such as a fall. It may also occur because of a fatigue failure under repeated application of sub-critical loads. In both cases failure may manifest as a macro-scale crack or as a region of crushed trabeculae.

There are several different ways of modelling bone failure. One method is to apply a failure criterion such as critical stress or critical strain, and assess where elements exceed this value. This is useful when comparing a series of scenarios. For example, Dopico-González et al., (2010) used the percentage of bone exceeding 0.8% strain to compare the effect of different implants in different femurs.

A more explicit method of modelling bone failure is to use fracture mechanics theory to simulate progressive damage within the micro-structure, with the option of introducing physiological repair mechanisms too, as described by Taylor and Lee, (2003). Kosmopoulos and Keller, (2008), assessed bone micro-damage initiation and accumulation beyond the pre-yield scenario. They combined a generalised plasticity stress-strain law with measurement of strain intensity to simulate crack propagation under increasing load. Micro-damage (cracking) was simulated as an element-by-element reduction in trabecular modulus. A scalar damage parameter calculated from the initial and reduced trabecular modulus was used to define the critical element damage level at which the load bearing capacity of trabecular bone is lost.

Taylor et al., (1999), used continuum damage mechanics, a discipline described in great detail by Ambroziak and Kłosowski, (2006), and finite element analysis to simulate the fatigue behaviour of cortical bone. From experimental fatigue data they were able to derive a formula for the number of cycles to failure as a function of stress and initial elastic modulus. This was calculated for each element.

It is noted that the initial elastic modulus cannot necessarily be explicitly measured from the first cycle in a tensile fatigue test, it may be necessary to derive it using linear regression from either the first ten cycles, or the first 10% of the fatigue life, whichever is lower (Cotton *et al.*, 2005). This should be differentiated from the undamaged tangent modulus, measured using a low stress static compression test prior to fatigue testing, which is used to normalise input stress between samples rather than to interpret damage. Damage, defined by a phenomenological damage parameter, was assumed to accumulate in each element as a linear function of the life fraction: number of loading cycles divided by the number of cycles to failure. Once the life fraction reached one, the element was removed from subsequent cycles. To model cumulative damage, the modulus and permanent strain for a given number of cycles were calculated using empirical formulae as a function of the damage parameter. The bone was assumed to have failed once a band of contiguous elements through the cross section had failed. Cotton et al.,

(2005) noted that damage, expressed as loss of stiffness, is approximately linear between 10% and 90% of a sample's fatigue life.

Strain-adaptive bone remodelling in peri-prosthetic bone has been numerically simulated in a number of studies (Behrens *et al.*, 2009). Such studies have been shown to produce realistic patterns of stress-shielding-induced osteolysis but are very sensitive to boundary and loading conditions. Similarly, a study on predicting fracture in osteoporotic femurs showed that the fracture site was sensitive to load orientation (Bessho *et al.*, 2009).

All of the methods described above relied on experimentally derived material models and require extensive method development to implement successfully. As there is no detailed material model for necrotic bone, comparing absolute measures of stress and strain to a material failure threshold would be inappropriate. A better approach would be to evaluate the risk of failure by quantifying the magnitude and physical extent of stress concentrations caused by the presence of a lesion within the femoral head. It was highlighted by Motomura *et al.*, (2011) that fractures may occur as a result of stress concentrations at the lesion boundary suggesting that this region should be a focus for the investigation. It is important to consider both the magnitude and physical size of stress concentrations within the bone structure when assessing the impact that they will have. Small regions of high stress could indicate regions where individual trabeculae are most likely to yield or be subjected to strain adaptive remodelling but the effect would be limited to a small region because failure of a small number of trabeculae will restore equilibrium in the surrounding bone (Prendergast and Taylor, 1994). In comparison, a region of high stress that also affects a large area represents a higher risk of gross structural failure.

The mechanical reasons for failure are likely to be confounded by other clinical factors and the concept of an "absolute risk score" in an orthopaedic context was introduced by Fardellone, (2008). Such a score considers both clinical factors (etiology) and measurements of disease pathology and in this paper, the author proposes a cut-off score above which surgical intervention is recommended. They caution that any such score must be validated by therapeutic trials. While inclusion of etiological factors is beyond the scope of this thesis, the development of a pathology-based risk score that considers the physical size and magnitude of stress discontinuities within the femoral head is viable and is an important first step towards a holistic risk assessment.

1.8.5 Two- and three-dimensional modelling

It is important to consider the compromises associated with using two-dimensional or three-dimensional models. While three-dimensional models have the advantage of fully characterising a complex structure, they take longer to develop and require a three dimensional geometry model to be created.

Two-dimensional simulations could be generated from 3D models or directly from 2D images. The latter would significantly reduce the time and complexity required to generate geometry models, especially if manual segmentation was required.

There are two approaches to generating 2D FE models: Plane strain and plane stress (Bathe, 1996). The plane strain approach assumes that the 2D model represents a section through body with a continuous cross-section. The third dimension is assumed to be sufficiently large that the strain in that dimension approximates to zero. The plane stress approach assumes that the third dimension is small compared to the other two so that the resultant out-of-plane stress is negligible. Although still a compromise compared to a 3D approach, the plane stress approach is more appropriate than the plane strain approach for simulations of anatomic structures where the cross-section varies rapidly.

1.8.6 Conclusion on finite element analysis

Finite element analysis offers a powerful means of evaluating the impact that lesion shape could have on prognosis. This methodology is theoretically capable of simulating complex mechanical systems in 3D to give detailed information about the likelihood of mechanical failure or remodelling. However, for such a method to be viable, a balance must be found between using complex methods that have the potential to allow detailed classification based on 3D assessments and 2D methods that offer a more basic insight but require significantly less time to develop. One must also consider the need for non-engineers to be able to interpret the results in a meaningful way and to transpose their findings onto a typically two-dimensional representation of the bone architecture. On balance, a 2D approach using linear plane stress elements that are large compared to the trabecular structure appears to offer a viable solution. A balance between using small enough elements to represent the structure and large enough elements to allow a continuum approach to be used must be found.

In terms of implementing a finite element model of the femur, there are a large number of predicate examples with different loading, meshing and material modelling strategies. This reflects the diversity of the unanswered questions and future studies must ensure that these parameters are controlled not only in consideration of the particular analysis, but also of whether comparison to predicate studies is required.

FE analysis of necrotic lesions has also been implemented previously, but so far appears to have focussed on generic or patient specific models with simplified lesion geometries. The lesions are typically modelled as having reduced modulus and strength but this is based upon limited *in vitro* data. To date, no studies have compared the effect that real lesion geometries have on the stress distribution within the femoral head. The definition of failure within a model varies between studies. Strategies such as defining a stress index, risk score or threshold values may be relatively simple to execute, but may not represent true failure to the extent that methods

such as continuum damage mechanics might. Again, the failure-modelling strategy must be driven by the particular requirements of a study.

Sensitivity of simulations to loading and boundary conditions must be evaluated as these factors have been shown to significantly influence outcome. Many studies have applied complex loading regimes intended to replicate physiological joint loads. A more simplistic approach is likely to render similar quality of information within a comparative study but may not be sufficient to make a clinical diagnosis. Sensitivity to load vector orientation may also indicate whether the risk of subchondral fracture for a particular patient varies depending on the activity they are engaged in; depending on lesion shape and location, the risk of fracture during normal walking could be low but higher in deep flexion or vice versa.

Although there is a trend for necrotic lesions to be found in the superior-anterior quadrant of the femoral head, their size, shape and location remains highly variable. Even with significant anatomic data available, attempting to accurately reproduce a single joint load condition is likely to be based on several assumptions. If anatomic data is limited then more assumptions must be made and it is unlikely that the added complexity will add to the value of the conclusions drawn from the simulation.

It is also noted that no study to date has been validated clinically. Validation of FE simulations of AVN is challenging because the poor prognosis of conservatively treated AVN means that the default treatment for most patients is surgical intervention and altering the standard of care would be unethical.

1.9 Discussion

Avascular necrosis of the femoral head predominantly occurs in Asian populations but also contributes significantly to the number of patients treated with total hip arthroplasty in Caucasian populations. It is associated with a number of systemic diseases and with alcohol and steroid use. The hip joint is the most frequently involved joint and there is a large volume of data relating to the incidence, etiology and pathogenesis available relating to this anatomic location. One of the aims of this thesis was to develop a morphology-based means of assessing the risk of loss of mechanical integrity in femoral heads AVN. To achieve this, *in vitro* and *in silico* simulations of femoral heads with avascular necrosis were generated. The anatomy and anticipated loading in these simulations is highly specific to the femoral head and therefore the literature review has focussed on literature relating specifically to AVN in the femoral head.

Regardless of etiology, the disease is characterised by a high probability of collapse of the articular surface of the femur and rapid destruction of the joint. The affected patients tend to be younger than those typically associated with joint arthroplasty and it is desirable to be able to identify those for whom a joint preserving treatment could delay or even prevent the need for

joint replacement. Conversely, joint replacement may offer the best chance of a positive outcome some patients. If these patients could be identified earlier, it might be possible to avoid the fiscal and welfare cost of a failed joint preserving treatment.

Current grading systems are based on semi-quantitative evaluation of lesion size and location. While they may offer a pragmatic means of classifying the disease state, they have been shown to be of limited benefit in developing an accurate prognosis for patients with pre-collapse AVN. There remains therefore, an unmet clinical need for robust stratification of this patient group into those who would benefit from early intervention and those for whom this would represent an unnecessary welfare and fiscal cost.

Computed tomography and MR imaging offer the potential to define bone and lesion geometry. They have both been established as valuable diagnostic tools for detecting AVN and methods of deriving bone and lesion geometry from these image modalities have been developed. With the exception of Nishii *et al.*, (2002), these studies have focussed on image processing rather than assessing the risk of progression. Nishii *et al.* advanced the state of the art by quantifying lesion volume and location within the femoral head using an image-based approach but did not consider the morphology or mechanical properties of the lesion. There remains a need for a means of translating the qualitative information provided by CT and MR into a quantitative assessment of the risk of disease progression. Both modalities will be required to fully characterize a necrotic lesion: While CT images provide detailed information on the bone geometry and potential for deriving material properties, they provide only ambiguous information on the lesion morphology. In contrast, MR images provide a clear indication of the boundary of the lesion but cannot be used to derive material properties or the geometry of the femur.

There is limited data on the material properties of bone found within a femoral head with avascular necrosis. However, there is consensus that the lesion represents a region of proportionally weaker and less stiff bone compared to the surrounding healthy bone. Depending on the shape of the lesion and its location relative to the applied load, failure could occur through compression of the necrotic bone itself: incremental micro-fracture of the trabeculae in the absence of the repair mechanisms associated with normal bone homeostasis resulting in cumulative collapse (Pugh *et al.*, 1973; Arlot *et al.*, 1983), or through a shear mechanism initiated at stress concentrations around the periphery of the lesion (Motomura *et al.*, 2011). The likelihood of both scenarios will vary with the location of the lesion and the shape of its boundary relative to the joint load vector.

Previous studies have demonstrated that FE analysis offers a means of evaluating the effect that the presence of a lesion has on the stress distribution within the femoral head but have not evaluated how the stress distribution changes according to lesion morphology. It has been

shown that CT and MR data can be used to derive the geometry of the femur and lesion respectively and from this it would be possible to develop an FE simulation capable of performing such an evaluation. In the long term it may prove possible to develop automated methods of generating an FE model from CT and MR data but manual methods currently remain the gold standard. The great advantage of an automated approach would be the reduction in time required to generate the geometry models. This would facilitate the use of 3D simulations that offer the best chance of identifying the location within the femoral head at greatest risk of failure. Generation of 3D models using a manual approach would be prohibitively time consuming in a clinical setting. Isolation and segmentation of a small number of 2D images would require significantly less time and expertise and are therefore more likely to be implemented. One must also consider the need for the results of a 3D FE simulation to be translated back in to the native CT and MR images, which are most usefully presented as a series of two-dimensional cross-sections.

Therefore, if FEA can improve the accuracy with which a prognosis can be developed, then a strategy that utilises 2D geometry and simulations appears to be most viable. This offers the advantage of allowing a more efficient workflow from image acquisition to providing a solution. However, it increases the risk that the most severely affected region of the femoral head is missed either because of the user's choice of 2D cross-section or because of variation in the orientation of the femoral head within the simulation.

The location and magnitude of the joint reaction force has been well characterised for different activities (Bergmann *et al.*, 2001) and the likelihood of failure will change depending on the activity undertaken. While it would be possible to assess the risk associated with specific lesion geometries for specific activities, this potentially limits the overall assessment of risk, especially as the size, shape and location of lesions is highly variable. A better approach may be to develop a risk assessment methodology that is based on the position of the lesion relative to the joint vector. This would allow a qualitative assessment of which activity is most likely to be associated with failure.

1.10 Objectives for experimental and computational studies

The overall aim of this thesis is to develop a morphology-based means of assessing the risk of disease progression through an engineering analysis of the stress distribution within the femoral head.

Patient-specific FE simulations of femoral heads with avascular necrosis can be developed with existing techniques. However, because of the poor prognosis associated with conservative treatment, the development of clinical follow-up data to validate them is challenging and beyond the scope of this thesis. Therefore an incremental approach to developing and evaluating FE simulations is required. The approach is summarised as follows:

1. Development of *in vitro* and *in silico* experimental disease models for AVN (Chapters 2 and 3)

The first objective will be to develop *in vitro* and *in silico* experimental disease models that can be used to demonstrate the effect that introducing a region of relatively less stiff bone into the femoral head has on the overall stiffness of the construct. The ability of the experimental disease model to recreate the organic lesion shapes and loading observed clinically will be limited by the means available to generate the model. The outcome of this experiment will be largely predictable as reducing the stiffness of a component of the construct will logically reduce the overall stiffness and will have limited clinical relevance. However, it is an important first step as it allows comparison of FE simulations to experimental results.

These FE simulations will provide limited novel information in terms of the effect on the overall stiffness of the construct and their morphology will not represent the clinical scenario. However, they will allow a sensitivity analysis that characterises the effect that variation within the experimental disease model has on the stress at the interface between the healthy bone and lesion to be performed. This is fundamental to the overall aim because it facilitates development and evaluation of an interface-based scoring algorithm for quantifying the severity of the effect of this variation. This is a novel approach to assessing the risk of disease progression and it is important to fully characterise its sensitivity.

2. Increasing the clinical relevance of the *in silico* simulation (Chapter 4)

The second objective will be to reduce the magnitude of the gap between the simulated experimental disease models and the physiological scenario. They will be achieved by developing FE simulations that include more clinically relevant lesion shapes and by developing a more physiologically representative method of applying load. The literature review highlighted a range of potential methods of load application. It also highlighted the fact that the joint reaction force vector varies substantially depending on activity. The aim of the improved method of physiological loading will therefore not be to recreate a specific activity, but to generate an understanding of how the inter-relationship between the force vector and the lesion location affects the risk score. The key outcome from this objective will be an understanding of the sensitivity of the scoring algorithm developed in Chapter 3 to variations in method of load application as well as lesion shape, volume and position. This will enable the hypothesis that the failure mode, either direct compressive failure of the necrotic bone or development of fractures originating at stress concentrations in the healthy bone-lesion interface, varies depending on the position of the lesion relative to the load vector. This is an important outcome because it may help to identify specific activities that increase the risk of fracture on a patient-specific basis.

3. Evaluation of an image-based tool for fracture risk prediction (Chapter 5)

The final objective will be to use the scoring algorithm on organic lesion geometries derived from patient-specific imaging. This will enable an evaluation of whether it provides improved prognostic information compared to current clinical grading systems. To achieve this, FE simulations must be generated using CT data to derive the geometry of the femur and MR data to define the lesion boundary. Generating three dimensional geometry models from CT and MR data using manual segmentation methods gives the greatest flexibility during FE method development. However, in a clinical setting, the speed with which a 2D geometry model could be generated from a single CT and MR slice is far greater, especially if manual segmentation processes are used. Therefore a strategy that uses 2D FE simulations is desirable.

This strategy potentially increases the sensitivity of the assessment to the choices the user makes when setting up the simulations. Therefore, a key outcome will be to quantify this sensitivity and to reach a conclusion as to whether the benefits associated with this approach are outweighed by the potential for misrepresenting the risk of progression.

Chapter 2. Development of an *in vitro* disease model for AVN

2.1 Introduction

Current options for testing mechanical treatments for femoral head AVN are limited to the use of either *in vivo* pre-clinical animal models or human femoral heads recovered during joint replacement surgery. The welfare cost of both options must be carefully considered as they produce limited samples with highly variable pathologies. This makes them unsuitable for *in vitro* evaluations of surgical treatments. There is an unmet need for an experimental disease model that accurately and repeatably recreates AVN.

Studies have demonstrated that the bone inside a necrotic lesion is less stiff and less strong than healthy bone from an equivalent location. Generating an experimental disease model that recreates the material properties consistently while also recreating lesion morphology is challenging. The main objectives of this study were to develop a novel *in vitro* experimental disease model that approximated the properties, but not necessarily the morphology, of a femoral head with an avascular necrotic lesion and to assess its overall stiffness in a consistent manner. A secondary objective was to establish the load and displacement range over which the materials behaved in a linear elastic way in order to establish a strategy for defining material properties in future *in silico* disease models.

Methods used to construct an *in vitro* experimental disease model for AVN are described in Chapter 2. The first stage in developing the disease model was to identify suitable material to represent the necrotic lesion. This was achieved by benchmarking bone taken from porcine femoral heads and then identifying a source of substitute bone with properties analogous to necrotic bone. Although AVN and its treatment have been studied since the 1960s, clinical data in English-language literature on the material properties of necrotic bone is limited to that produced by Brown *et al.*, (1981) who reported a 41% reduction in UCS and a 59% reduction in elastic modulus for necrotic bone in a pre-collapse lesion compared to healthy bone taken from the same location. These reductions defined the target for the properties of the substitute bone in the current study.

Experimental disease models then were constructed and tested to establish the effect of the simulated lesion on the biomechanics of the femoral head. The workflow and link to Chapter 3, where the experimental disease models were recreated *in silico* is summarized in Figure 8.

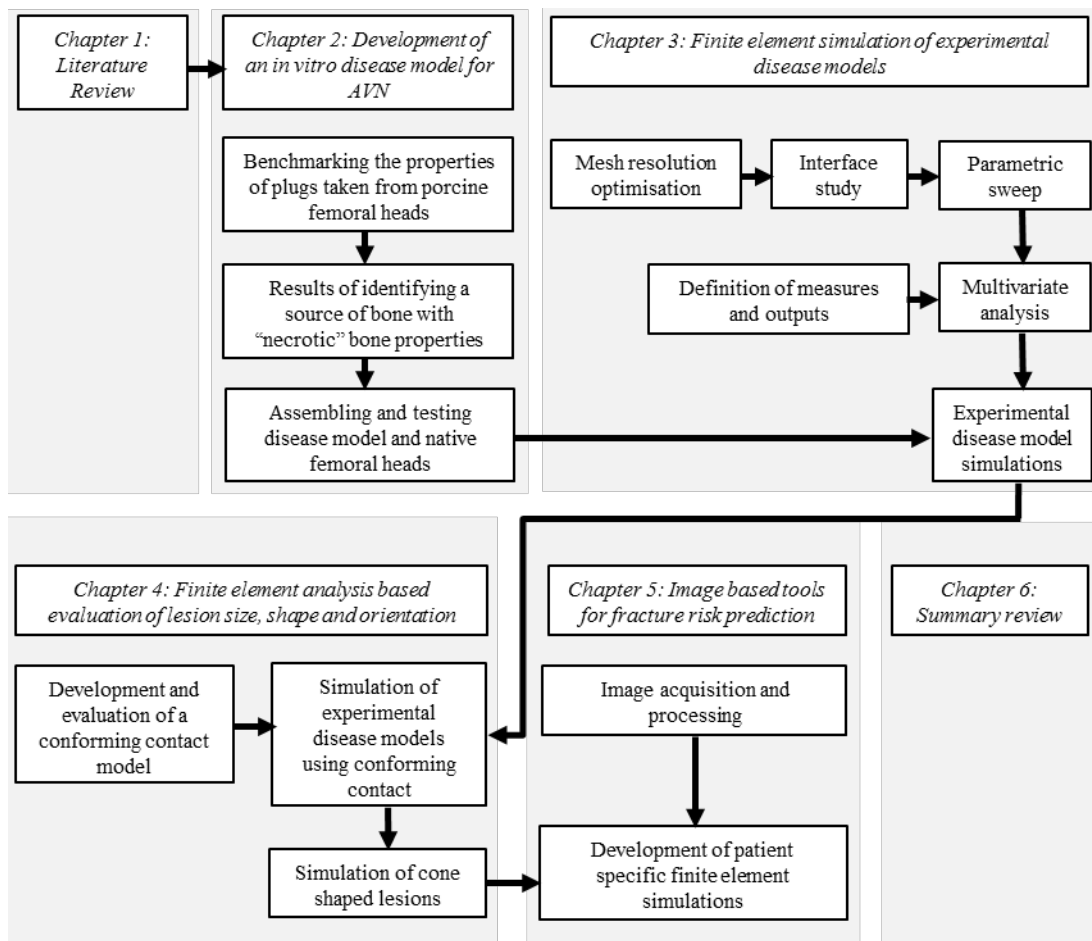


Figure 8. Flow chart summary of the studies performed in each chapter.

While the etiology of AVN remains unclear and is likely to be multi-factorial, the pathogenesis appears to be generally consistent (Musso *et al.*, 1986): Cell death initiates a healing response which manifests first as a sclerotic band around the lesion followed by focal resorption at the lateral periphery. These areas of low density bone may act as stress raisers and be the origin of subchondral fractures (Motomura *et al.*, 2011). The strength of the bone within the lesion itself is also reduced (Brown *et al.*, 1981).

End-stage AVN manifests as subchondral collapse followed by degeneration of the joint itself (Motomura *et al.*, 2011; Arlet, 1992; Mont and Group, 1999; Hernigou and Lambotte, 2000; Glimcher and Kenzora, 1977). Lesion size and location within the femoral head have been established as risk factors for pathological progression, with large, anterior-superior lesions identified as having the highest risk (Nishii *et al.*, 2002).

The effect that the altered material properties have on the gross properties of the femoral head has only been investigated using un-validated finite element simulations (Brown *et al.*, 1992). This presents difficulties when attempting to develop new treatments for AVN and in verifying their effectiveness. There is a need therefore, for *in vitro* and *in silico* biomechanical simulations that can be used to evaluate the effect of altered material properties and structural discontinuities within the femoral head.

An experimental disease model that accurately characterises both the mechanical and morphological characteristics of a necrotic femoral head is an aspirational target that was beyond the scope of the current investigation. The first step towards this target was to answer the following scientific questions:

1. Can a disease model with material properties that are representative of healthy and necrotic bone be constructed using porcine bone?
2. What effect does the change in material properties within a simulated lesion have on the bulk material properties of the disease model?
3. Can a linear-elastic material model be used to simulate experimental disease models *in silico*

This chapter presents an experimental methodology and the results of an *in vitro* disease model for AVN. A proof-of-concept disease model was constructed by substituting a dome-ended cylinder of bone from the centre of a porcine femoral head with a conforming plug of bone taken from the lateral epicondyle of a bovine femur. No attempt was made to accurately represent lesion shapes, but the relative volume and absence of a subchondral collapse mean that they could be most closely compared to a clinical grade of ARCO IIB or C (Table 3).

The disease models were tested alongside native porcine femoral head controls. Each construct was compressed between flat platens under displacement control to obtain load-displacement data. Elastic modulus was derived from this by using least-squares regression to fit an analytical Hertzian contact load-displacement plot to the experimental result. This approach assumed linear elastic behaviour and was validated by comparing the derived work-modulus relationship to an analytical solution. Limits to the applicability of the linear elastic behaviour were identified and used as a basis for subsequent Finite element (FE) analysis.

The study is presented in four stages:

1. Benchmarking the properties of plugs taken from porcine femoral heads.
2. Identifying a source of bone with “necrotic” bone properties.
3. Assembling and testing disease model and native femoral heads.
4. Validation of the assumed linear-elastic Hertzian model.

The Hertzian contact mechanics approach was more involved than simpler work-based comparisons but was the only approach that allowed the bulk modulus of the materials to be derived. Other approaches were evaluated and are summarised in appendix A: Method development.

2.2 Benchmarking the properties of plugs taken from porcine femoral heads

2.2.1 Materials

Sample source

Porcine femoral heads were used as a surrogate for human tissue because such heads were large enough to make testing interventions designed for human anatomy feasible and because, in the author's experience, they have mechanical properties that are closer to human bone than other large animal models such as bovine or equine bone.

Fresh whole porcine legs were obtained from an abattoir (Penny and Sons, Rawdon, Leeds, UK) where the age of slaughter was between 6 and 8 months. All samples were prepared within 12 hours of sacrifice.

Gross dissection

The whole femur was excised using a lateral approach intended to prevent unintended damage to the femoral head. The entire lateral aspect of the femur was exposed first, followed by the knee. Sharp dissection was used to remove the majority of the soft tissue from the diaphysis until the capsule was visible. The abductors were separated from the greater trochanter and tissue superior to the femoral neck was split in a lateral to medial direction until the capsule was completely exposed. The capsule was split around the entire neck to expose the head-neck junction. The Teres ligament was then separated using a stab incision originating in the region of the transverse acetabular ligament and directed superiorly.

As much of the remaining soft tissue was removed from the excised femurs as practicable before the femoral head was inspected for inclusion in the experiment. Exclusion criteria were: gross deformities of the proximal femur or cartilage, or subchondral bone defects caused either by blunt trauma or during dissection. However, no samples were excluded for these reasons.

Sample preparation

All test samples were taken using a PTX universal #10 plug-cutter (B&Q Plc. Hampshire, England) (Figure 9). This created a cylinder of material with a 9.8mm nominal diameter and up to 25mm in length. The plug-cutter had a chisel-like cutting face with clearance at all sides and was designed for rapid material removal at low speeds. Preliminary testing indicated that heating effects were minimal and that aspiration during plug manufacture was unnecessary. Bone samples were taken from the central core of porcine femoral heads, on an axis through the head centre and patellar groove, and orthogonal to the surface.



Figure 9. The PTX Universal plug cutter used to create a cylinder of bone with a nominal diameter of 9.8mm

Approximately 5mm of bone was cut from the outer surface to remove cartilage and give a flat, uniformly cancellous test sample. Both ends were flattened and made parallel using a hand file and Vernier callipers prior to testing. In the final stage of preparation, samples were rinsed in water to remove debris from the cut surfaces.

Storage

All samples were stored in individually identified vials until they were tested. All samples were tested within 100 days of preparation. Samples that were not immediately tested were frozen at -18°C . Frozen samples were defrosted at room temperature prior to testing. This storage protocol has been previously shown not to significantly affect the material properties of trabecular bone (Pelker *et al.*, 1984; Linde *et al.*, 1993).

2.2.2 Methods

Fourteen test pieces were compressed between flat platens at a constant strain rate of 0.01s^{-1} based on a previously published protocol (Carter and Hayes, 1976). The literature review indicated that quasi-static strain rate for *in vitro* testing was most appropriate because the viscoelastic behaviour of necrotic bone has not been characterised and this approach reduced the influence that this property would have on the outcome. The disadvantage of using a quasi-static approach is that it does not represent the dynamic nature of joint loading that may be the cause of brittle fracture.

Load was applied using an Instron 3366 materials testing machine (Instron, Norwood, MA) fitted with a 10kN load cell (product code 2530-443, Instron, Norwood, MA) (Figure 10) and data collected at a sampling rate of 1Hz.

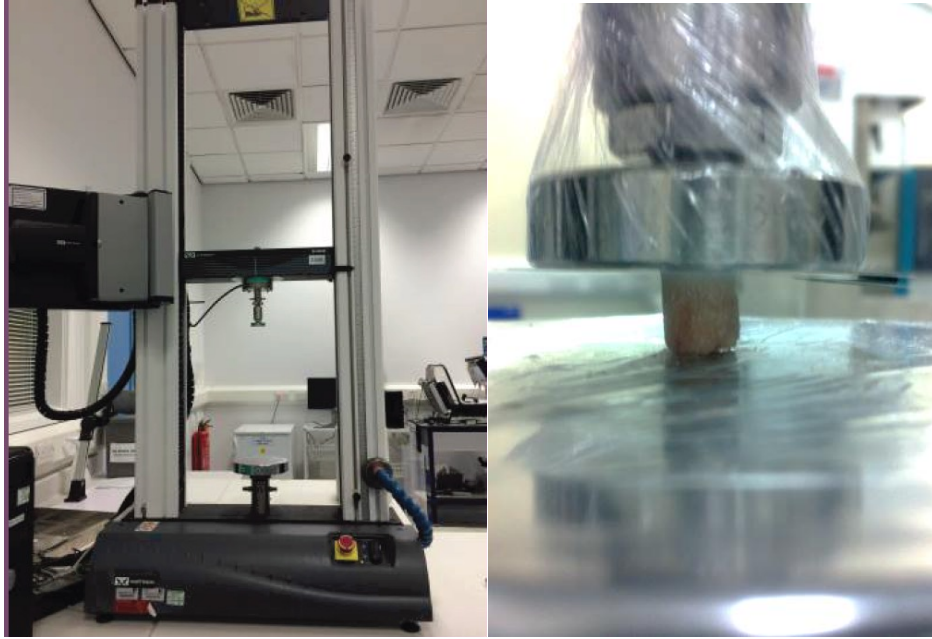


Figure 10. Left: Photograph of the Instron materials testing machine. Right: detail view of the specimen mounted between two flat platens. The platens were wrapped in cellophane to reduce contamination of the machine.

Compression was continued for several seconds after an inflection in the load-displacement plot occurred. The load-displacement coordinates were converted to stress and strain using the sample geometry. The maximum positive slope on each stress-strain plot, equating to maximum elastic modulus of the sample was calculated for each sample.

Compressive engineering strain (ϵ) was calculated by dividing the displacement of the platen by the original length of the test specimen, which was measured using Vernier callipers. Compressive stress (σ) was calculated by dividing the applied load (Newtons) by the cross-sectional area (mm^2). Thus the derived modulus has units N/mm^2 , or Mega-Pascals (MPa).

The maximum elastic modulus was calculated automatically by identifying the maxima of a moving linear regression of the stress-strain data over 10 data points using Excel™ (Microsoft). The ultimate compressive strength (UCS) was defined as the apex of the stress-strain plot. This was defined algorithmically as the apogee in the data set. A typical plot of the locations for maximum elastic modulus (EMax) and UCS is shown in Figure 11. The mean and 95% confidence interval for the maximum elastic modulus and UCS were derived for the data set.

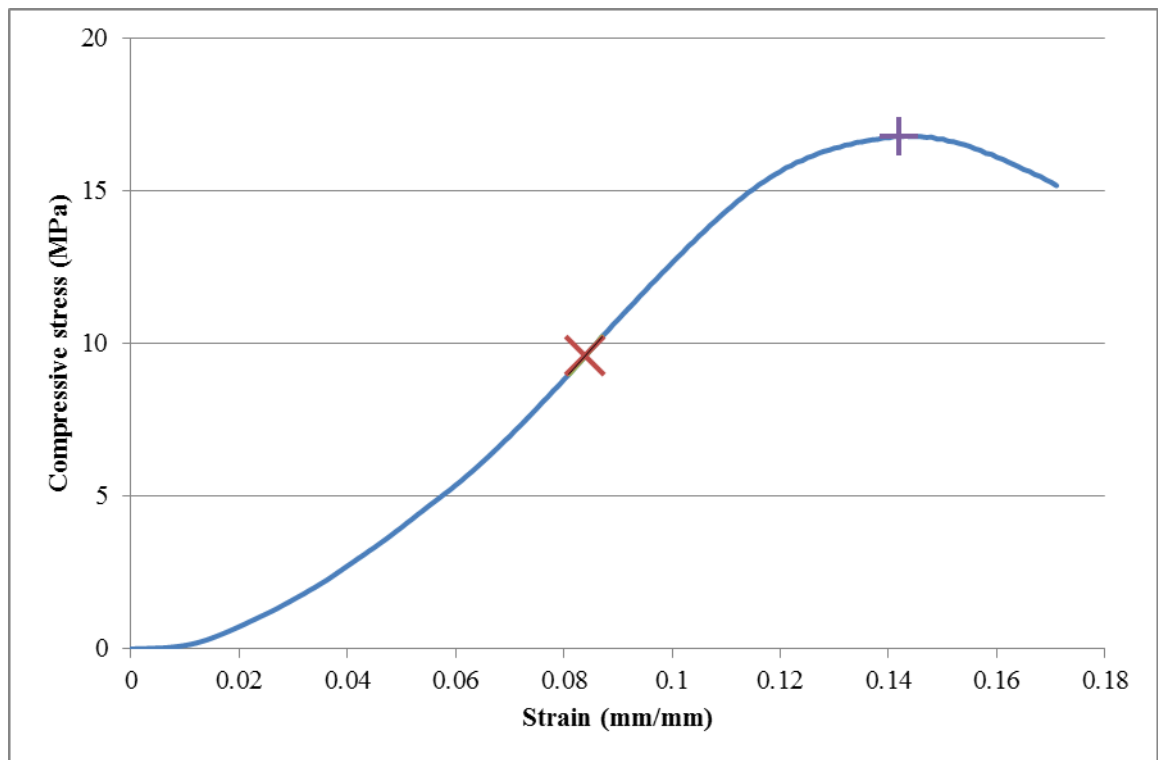


Figure 11. A typical stress-strain plot for a plug taken from a porcine femoral head. The location of automatically detected maximum elastic modulus is shown by a diagonal cross and the location of ultimate compressive strength is indicated by a horizontal cross.

2.2.3 Results of benchmarking bone from porcine femoral heads

This experiment was designed to characterise bone taken from the central core of porcine femoral heads. Ten millimetre diameter bone plugs were removed from fresh porcine femoral heads and compressed at a constant strain rate of 0.01s^{-1} .

Maximum elastic modulus and UCS were calculated from the load-displacement data for each sample. The mean Maximum elastic modulus was 318MPa (n=12, 95%C.I: 38.56MPa). The mean UCS was -15.19MPa (n=12, 95% C.I: 0.87MPa).

Two samples were removed from the set because they had a low length to width ratio. Their yield behaviour was significantly different (Figure 12) to the rest of the set and was more characteristic of incremental shear failure within the material associated with short, wide samples than an acute compressive failure.

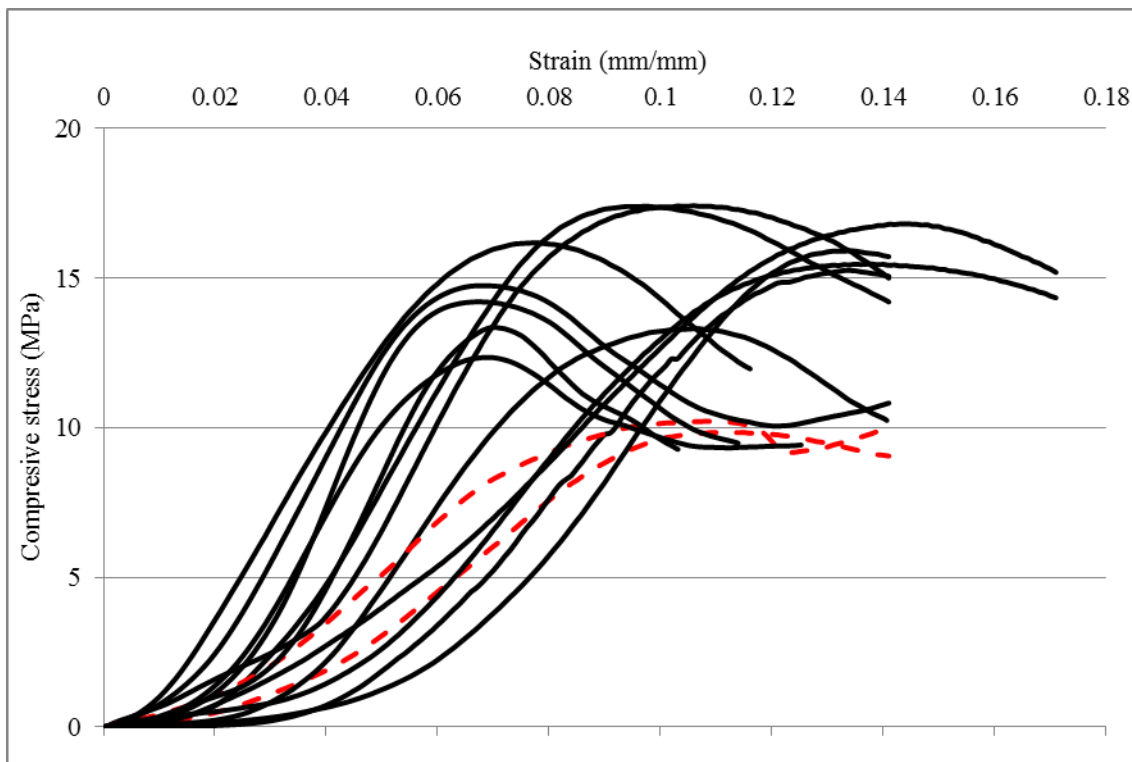


Figure 12. Stress-strain plots for samples taken from fourteen porcine femoral heads. The two samples that were identified as outliers are indicated by the broken lines

2.3 Identifying a source of bone with “necrotic” bone properties

2.3.1 Identifying target properties for donor “necrotic” bone

Brown *et al.*, (1981) characterised the material properties of bone samples from multiple locations within femoral heads with avascular necrosis. Nine necrotic femoral heads were evaluated in total but only one of these was in a pre-collapse condition. In each case, the entire femoral head was cut into uniform cubes and each cube oriented such that compression occurred in the anatomic superior-inferior direction between flat plates at a strain rate of $0.004s^{-1}$. The elastic modulus was calculated as the slope of the initial positive curve in the stress-strain plot. Although not explicitly stated, the diagram indicates that the initial toe region was ignored.

It is noted that the strain rate used by Brown *et al.* is significantly lower than the strain rate used in the experiment described in this chapter ($0.01s^{-1}$). However, this difference has been shown to have no significant effect on apparent material properties (Carter and Hayes, 1976).

The absolute values obtained for the necrotic femoral heads were compared to spatially corresponding control cubes from healthy femoral heads ($n=3$, absolute average stiffness’s 445MPa, 458MPa and 421MPa and strengths 19.1MPa, 19.7MPa and 19.4MPa) and the overall result for necrotic bone presented as a percentage reduction in both strength and modulus.

For the single pre-collapse femoral head, bone samples taken from the necrotic region demonstrated a 41% reduction in UCS and a 59% reduction in elastic modulus when compared

to healthy bone from an equivalent location. This is the most relevant target for the current experiment as the intention is to identify pre-collapse patients that are at risk of pathological progression.

These values were used to develop a target elastic modulus and UCS for bone that would be used to represent necrotic bone in the simulation by applying the same ratio to the benchmark results for plugs taken from porcine femoral heads: A 41% reduction in UCS from 15.19MPa = 9MPa; a 59% reduction in elastic modulus from 318MPa = 130MPa.

2.3.2 Materials and methods

Plugs of bone taken from different locations on porcine and bovine femurs were evaluated against the target elastic modulus and UCS determined in Section 2.2.3. Fresh whole porcine legs were obtained from an abattoir (Penny and Sons, Rawdon, Leeds, UK) where the age of slaughter was between 6 and 8 months. Bovine femurs, aged 24-28 months, were sourced from the same location. These were provided with the majority of the soft tissue already removed. To establish anatomic locations accurately, any remaining soft tissue was removed using a scalpel and forceps. All samples were prepared within 12 hours of sacrifice.

The same protocol for harvesting plugs of bone as was described in Section 2.2.1 was used with the exception of the alignment of the tool axis when the plugs were harvested. Previously this was aligned approximately to the standing load vector through the femoral head. As samples were taken from various positions around the femur, this was impossible so alignment of the tool axis normal to the surface was adopted in all cases. The locations from which each sample was taken are shown in Figure 13 and Figure 14.

In total, 111 samples of bone from 14 different locations and two species (porcine and bovine) were evaluated using the same compression test protocol as was described in Section 2.2.2.

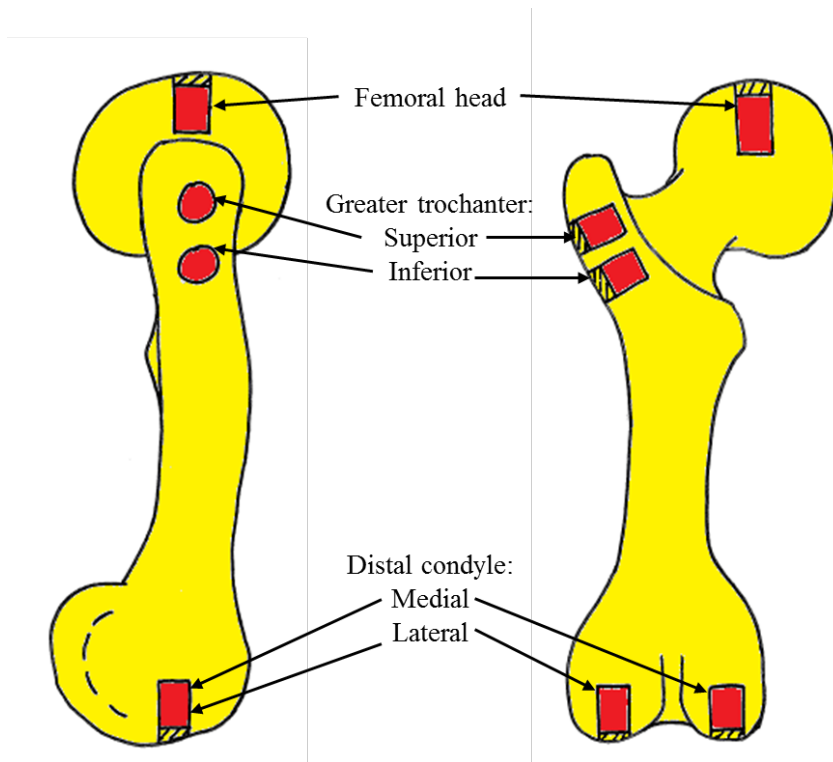


Figure 13. Schematic diagram showing the locations from which samples of bone were taken from porcine femurs.

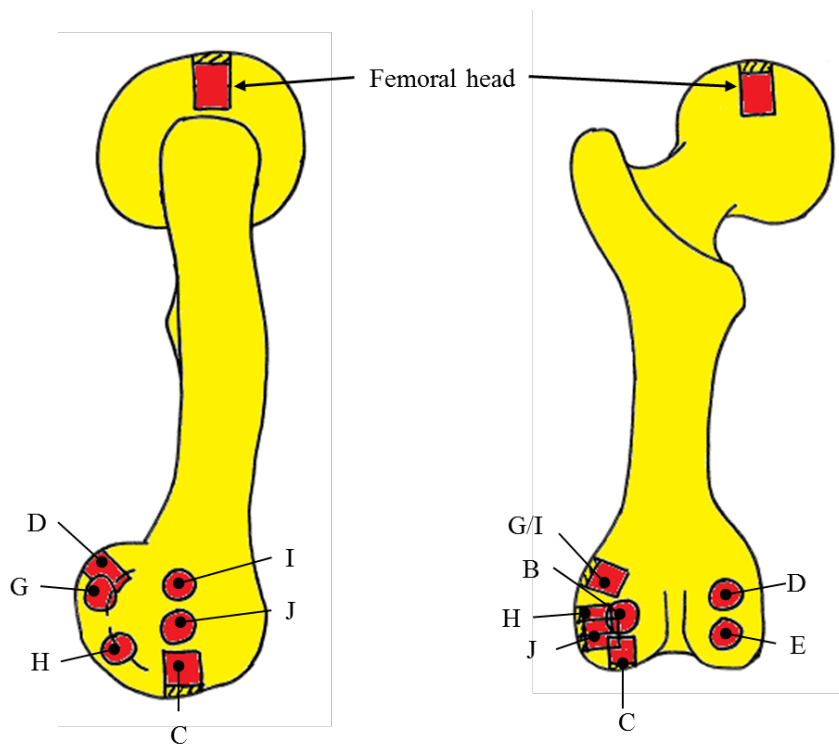


Figure 14. Schematic diagram showing the locations from which samples of bone were taken from bovine femurs

2.3.3 Results of identifying a source of bone with “necrotic” bone properties

In this study, samples of bone from a number of different locations on porcine and bovine femurs were tested in uniaxial compression. The aim was to identify a source of bone that would provide a 41% reduction in UCS and a 59% reduction in elastic modulus when compared to bone from the central portion of porcine femoral heads (Section 2.2). A source of bone was identified that gave a 42%-51% lower mean stiffness and a 44%-63% lower mean UCS.

The locations from which bone samples were taken with properties closest to the target values for maximum elastic modulus and UCS were samples from the bovine lateral epicondyle: central on the lateral epicondyle and immediately superior to the central point. Henceforth these samples are referred to as donor bone A and B. The results for all locations are summarised in Table 8.

Box-whisker plots of the results are shown in Figure 15 and Figure 16. Although the modulus for both donor locations closely matched the target, the ultimate compressive strength was approximately 30%-40% lower. Comparing the properties of the donor bone to the properties of bone taken from the central portion of porcine femoral heads, samples from the donor locations had a 42%-51% lower stiffness and a 44%-63% lower UCS. The box-whisker plots indicated that there was large variation and that, for maximum elastic modulus especially; the properties of the donor bone chosen may be significantly closer to the host value than the target relationship.

Table 8. Summary of mechanical properties for bone samples taken from various locations on porcine and bovine femurs (Figures 13 and 14). The number of samples column indicates the total number of samples taken, with the number of samples used to generate the final statistics in parentheses. The target properties for the donor bone were a maximum elastic modulus of 130MPa (95% C.I. 89-172) and an ultimate compressive strength of 9MPa (95%C.I. 8-10).

Location	No. of samples	Maximum elastic modulus (MPa)			Ultimate compressive strength (MPa)		
		Mean	95% Confidence	As % of target	Mean	95% Confidence	As % of target
Porcine femoral head	14 (12)	318.19	41.65	100	15.19	0.94	100
Porcine greater trochanter, inferior	4 (4)	57.36	35.78	18	3.85	1.59	25
Porcine greater trochanter, superior	4 (4)	59.68	18.19	19	3.13	1.21	21
Porcine distal lateral condyle	5 (5)	259.6	48.54	82	8.05	0.89	53
Porcine distal medial condyle	5 (5)	335.94	32.53	106	12.46	0.5	82
Bovine_B	5 (5)	553.96	113.42	174	21.34	1.2	140
Bovine_C	5 (5)	255.51	77.24	80	10.32	1.59	68
Bovine_D	5 (5)	753.73	158.6	237	26.7	4.55	176
Bovine_E	5 (5)	602.22	200.85	189	29.92	6.3	197
Bovine femoral head	11 (11)	869.84	119.8	273	38.83	3.33	256
Bovine_G	12 (12)	94.73	29.49	30	4.9	1.21	32
Bovine_H (Donor bone A)	12 (8)	182.73	25.48	57	8.27	0.71	54
Bovine_I	11 (11)	80.69	22.75	25	3.5	0.75	23
Bovine_J (Donor bone B)	11 (10)	155.28	26.22	49	5.53	0.53	36

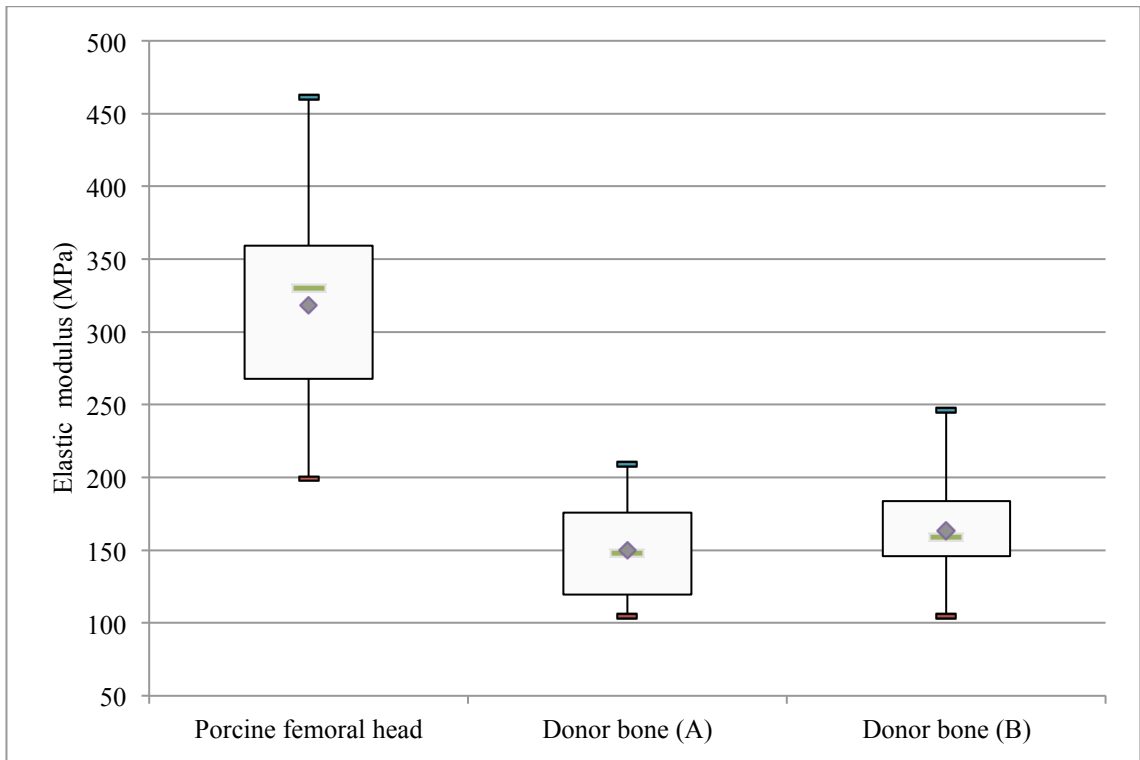


Figure 15. Box-whisker plot of maximum elastic modulus. The mean of the data set is represented by a diamond, the median by a bar. Mean maximum elastic modulus for donor bone (A) (Central on the lateral epicondyle, n=8) and B (Immediately superior to location H, n=10), both from the bovine lateral epicondyle. The error bars indicate 95% confidence interval. The target maximum and minimum are based on a nominal maximum elastic modulus that represents a 59% reduction in modulus compared to samples taken from porcine femoral heads with the same confidence interval as the original data.

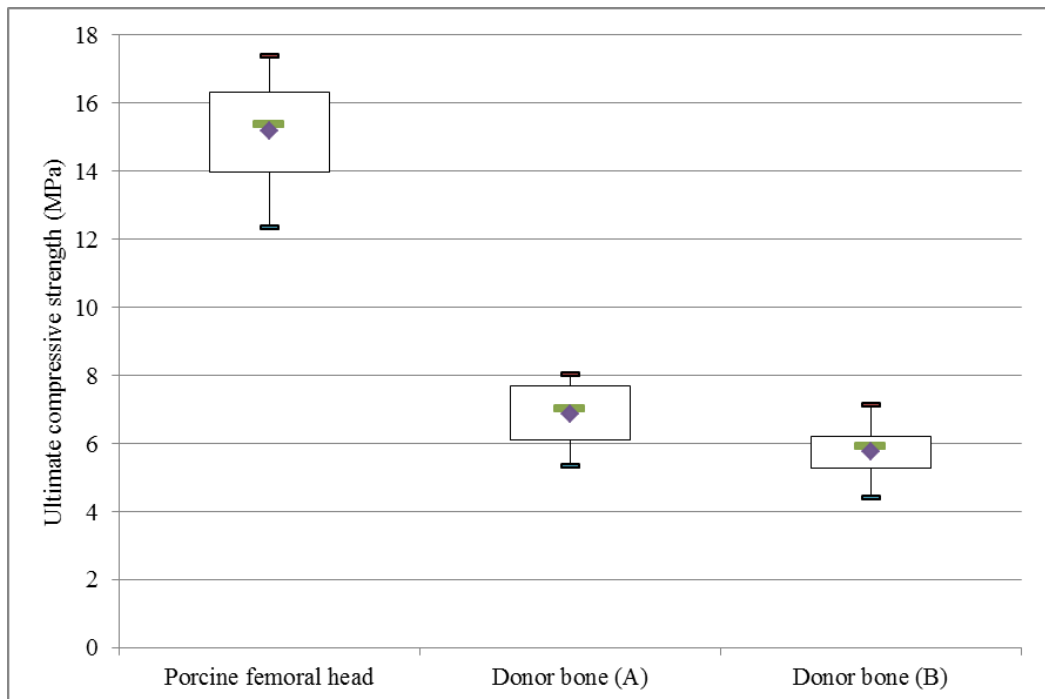


Figure 16. Box-whisker plot of ultimate compressive strength. The mean of the data set is represented by a diamond, the median by a bar. Ultimate compressive strength for donor bone (A) and (B), both from the Bovine lateral epicondyle. The error bars indicate 95% confidence interval. The target maximum and minimum values represent a nominal strength that represents a 41% reduction in UCS compared to samples taken from porcine femoral heads with the range based on the same confidence interval as the original data.

Several samples were removed:

- Porcine femoral head samples: two were removed for reasons described in Section 2.2.3
- Donor bone A: Four samples (2, 3, 4 and 5) were removed: Two failed at the growth plate rather than through material failure; the experimental setup was incorrect for the other two.
- Donor bone B: One sample (sample 2) was removed for the same reason as previously described in Section 2.2.3. The stress-strain plot for this sample is shown in Figure 17. Again, the plot is characterised by a short region of linear-elastic behaviour followed by a gradual decrease in modulus and large stress plateau that is atypical of acute compressive failure. The UCS was approximately 50% lower than the other samples

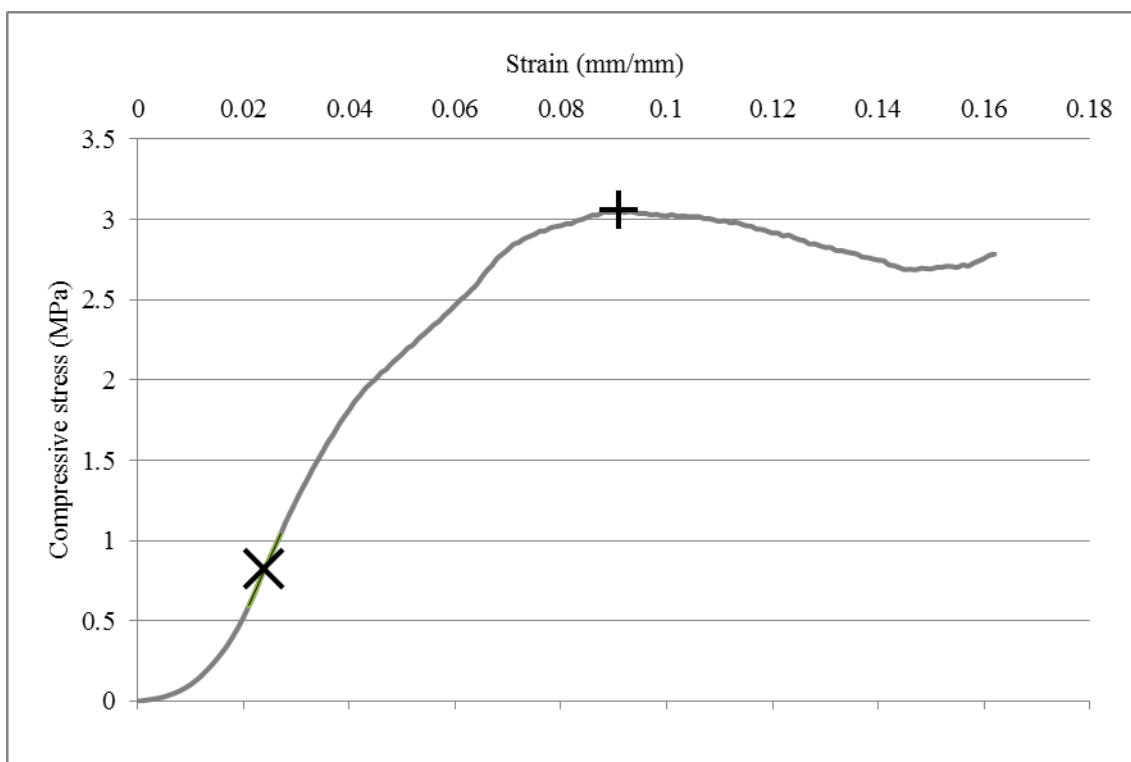


Figure 17. Stress-strain plot for bovine sample J2. This sample was removed because of its atypical yield profile: a very short linear elastic region with a gradually reducing gradient (modulus) followed by a large stress plateau. The location of automatically detected maximum elastic modulus is indicated by the diagonal cross and the location of ultimate compressive strength is shown by the horizontal cross.

2.3.4 Discussion

The purpose of this investigation was to find an appropriate source of bone that could be used to simulate necrotic bone in a femoral head based disease model. Overall, the inter-quartile ranges for the bone properties were consistent between bone taken from porcine femoral heads and that taken from the bovine lateral epicondyle. This suggests that properties could be matched to give a consistent ratio. However, given the lack of data regarding the variation in necrotic bone properties, a better approach is to randomise the allocation of “necrotic” bone samples and include this as a variable within the analysis of the disease model.

Mechanical testing of biological specimens is subject to a number of sources of variation. Differences in activity level and maturity between individual animals can lead to variation in trabecular structure and bone mineral density, which have a direct impact on the mechanical properties of the sample.

Sample preparation can also have a significant impact. Where possible the magnitude of this impact was reduced by using a consistent plug diameter and standardised protocol for sample preparation. However, samples were harvested from locations identified relative to anatomic landmarks such as the Greater Trochanter, insertion of ligaments and the articular surfaces. These vary from sample to sample, so slight variation in the exact sample location is expected.

The test methodology potentially introduced additional variability. To reduce this potential, care was taken to remove a consistent thickness of superficial bone to maintain as much homogeneity in the samples as possible. A constant strain rate of 0.01s^{-1} was used throughout to reduce the influence of viscoelasticity (Carter and Hayes, 1976) and all samples were stored in a way that had minimal effect on their material properties of the calcified portion of bone (Pelker *et al.*, 1984; Linde *et al.*, 1993).

Combining results from both locations, the donor bone had a mean modulus of 157 MPa (Range 105-228 MPa) and a mean UCS of 6.3 MPa (Range 4.9-7.6 MPa). The mean elastic modulus was comparable to that reported for necrotic human bone. The ultimate compressive strength for the simulated necrotic bone was lower than that reported for pre-collapse necrotic bone but was comparable to the strength of both osteoporotic and osteoarthritic femoral heads. (Table 9).

Table 9. Comparison between material properties derived experimentally for porcine femoral heads (healthy bone) and plugs taken from the lateral epicondyle of a bovine femur (necrotic bone) and those reported for human bone in the literature.

Author	Healthy bone		Diseased bone		
	Elastic modulus (MPa)	Ultimate compressive strength (MPa)	Disease	Elastic modulus (MPa)	Ultimate compressive strength (MPa)
Experimental results	318±119	15.2±2.85	Simulated AVN	157±52	6.3±1.4
Brown <i>et al.</i> , 1981 (Femoral head)	439±19	19.4±0.3	Pre-collapse AVN	Mean 180	Mean 11.4
Li and Aspden, 1997 (Femoral head)	Median 310	Not reported	Osteoarthritis	Median 356	Median 4.3
			Osteoporosis	Median 247	Median 2.5
Haba <i>et al.</i> , 2012 (Femoral head)	Not reported	Not reported	Osteoarthritis	232±130	6.1±3.0
Steinhauser <i>et al.</i> , 2006 (Femoral neck)	385.7±SD189.4 361.7±SD300.6	8.5±6.0 6.6±5.2	Not reported	Not reported	Not reported
Öhman <i>et al.</i> , 2007 (Femoral head)	273±1.06	18.0±6.4	Not reported	Not reported	Not reported

Variation in the region of 50% of the mean was found for ultimate compressive strength. The definition of ultimate compressive strength was less ambiguous than that of maximum stiffness because there was always an apogee: a single data point that signified the transition from a positive (increasing compressive stress with strain) to negative (decreasing stress with strain) modulus, whereas the maximum slope could occur over a relatively large section of the data. Variation in the region of 100% of the mean was found in the modulus derived for these samples. A qualitative comparison of the stress-strain plots in Figure 12 suggests that this variation was a true representation of the spread within the data.

2.3.5 Conclusion

Uniform plugs of bone were extracted from the central portion of porcine femoral heads. When tested in unconstrained compression they were found to have a mean maximum elastic modulus was 318MPa (n=12, 95%C.I: 38.56MPa). The mean UCS was -15.19MPa (n=12, 95% C.I: 0.87MPa). In seeking a location from which proportionally weaker and less stiff bone could be harvested to provide a surrogate for necrotic bone, the central and superior regions of bovine lateral epicondyles were found to provide the closest match to a target of 41% reduction in UCS and a 59% reduction in elastic modulus when compared to native bone from an equivalent location. Comparing means, samples from these locations had a 42%-51% lower stiffness and a 44%-63% lower UCS.

2.4 Assembling and testing disease model and native femoral heads

2.4.1 Introduction

This section describes the construction and testing of experimental disease models for femoral heads with avascular necrosis. Disease models were created by substituting a portion of bone subjacent to the subchondral bone in a porcine femoral head with a plug of donor bone taken from a bovine epicondyle.

Avascular necrosis of the femoral head is a complex disease from both a biological and mechanical perspective. The experimental disease model evaluated in this chapter was purely mechanical and was designed to allow specific variables, for example the moduli of the native and donor bone and the location of the simulated lesion within the femoral head to be evaluated while removing sources of variability such as load orientation and lesion shape where possible.

The mechanical integrity of a femoral head with a necrotic lesion is affected by regions of focal sclerosis and osteolysis, the presence of cumulative micro-fractures and, perhaps most importantly, the volume, shape and location of the lesion within the femoral head. For the purpose of this disease model, lesions were assumed to be homogenic (without focal osteolysis or sclerosis) and have a consistent shape and volume. Focal osteolysis in the subchondral region of necrotic femoral heads may act as a stress raiser and site of fracture initiation (Motomura *et al.*, 2011). Although low density regions were not recreated experimentally, the geometry of the simulated lesion included a geometric stress concentration at the superior edge of the simulated lesion.

The properties of the femoral head and lesion surrogate bone, the proximity of the lesion to the bearing surface and its location relative to the load vector were variables inherent in the construction of the model and were considered in the analysis of the results.

In a patient the femoral head will be subject to loading from multiple orientations as the patient carries out their activities of daily living. Load transfer will be through the conforming surfaces of the acetabulum and femoral head. This was beyond the scope of the disease model as it introduced more variables than could be reasonably evaluated. In the disease model a single load was applied vertically through the femoral head using a flat platen.

It is logical that altering the material properties in the centre of the femoral head would have a proportional effect on the elastic modulus of the construct. To confirm this, experimental disease models and control femoral heads were constructed and loaded in compression. The resulting load-displacement plots were analysed to derive the apparent moduli and the difference between the experimental disease models and controls was evaluated.

These results provided the basis for developing *in silico* simulations of the experimental disease models in Chapter 3.

2.4.2 Materials

Fresh whole porcine legs were obtained from an abattoir (Penny and Sons, Rawdon, Leeds, UK) where the age of slaughter was between 6 and 8 months. Excised bovine femurs, aged 24-28 months at slaughter, were sourced from the same location. All samples were prepared within 12 hours of sacrifice using the method described in Section 2.3.

To quantify the relationship between the native and donor bone, and with the intention of developing BMD-derived material properties for use in *in silico* simulations, both the femoral heads and donor plugs were CT scanned using a MicroCT100 scanner. The CT scanning protocol is described in Appendix B. Porcine femoral heads were randomly assigned to be disease models or controls; one bone plug taken from the bovine lateral epicondyles was randomly assigned to each disease model femoral head. On average the BMD of the donor bone was approximately 20% lower than that of the native femoral heads in the same location (range 13%-33%) (Table 10). This data was used in Chapters 3 and 4 to develop experimental disease model specific FE simulations. Note that the measured Maximum elastic modulus and ultimate compressive strength of the donor bone were 44%-63% and 42%-51% lower respectively (Section 2.3).

Table 10. Bone mineral density obtained for each of the femoral heads used as controls and experimental disease models and for the plug of bovine bone used as a simulated lesion. The location from which bone plugs were taken is identified: A was central on the lateral epicondyle; B was immediately superior to this location.

	Femoral head	BMD	Bone plug	BMD
		mgHA/ccm		mgHA/ccm
Experimental Disease Models	I	265	A-I	221
	IV	297	A-III	230
	X	269	B-VIII	204
	XI	300	B-IV	262
	XVI	265	B-I	186
	XVII	259	B-V	174
	XIX	251	B-IX	216
	XX	241	B-VII	209
Controls	II	260	-	-
	III	268	-	-
	V	246	-	-
	VI	232	-	-
	VII	266	-	-
	VIII	298	-	-
	IX	248	-	-
	XII	257	-	-
	XIII	272	-	-
	XIV	294	-	-
	XV	232	-	-

Porcine femurs were excised using the same protocol described in Section 2.2.2. The proximal and distal halves were separated and as much soft tissue as possible was removed.

The porcine femoral heads to be used as controls and disease models were prepared by creating a flat surface inferiorly using a hacksaw and removing the cartilage superiorly using a scalpel.

The flat surface was extended laterally (Figure 18) to facilitate preparation of the hole without the need to clamp the femoral head itself and to create clearance to allow correct alignment of the drill. The inferior flat provided a consistent alignment plane to allow repeatable orientation of the specimen during physical testing and for this orientation to be recreated *in Silico*.

Cartilage is unaffected in the early stages of the disease (Mont *et al.*, 2006) so the superior cartilage was removed from the disease model and control femoral heads to reduce the potential variability that it would introduce. The majority of the cartilage was removed using a cutting action, taking care not to cut the subchondral bone. Once only a thin layer of cartilage remained, the scalpel was orientated normal to the surface and used to gently scrape the remnant from the bone surface until a smooth surface with no ridges of cartilage remained. The final

stage of preparation of the control femoral heads was to cut through the remaining femoral neck, approximately in the location of the isthmus.

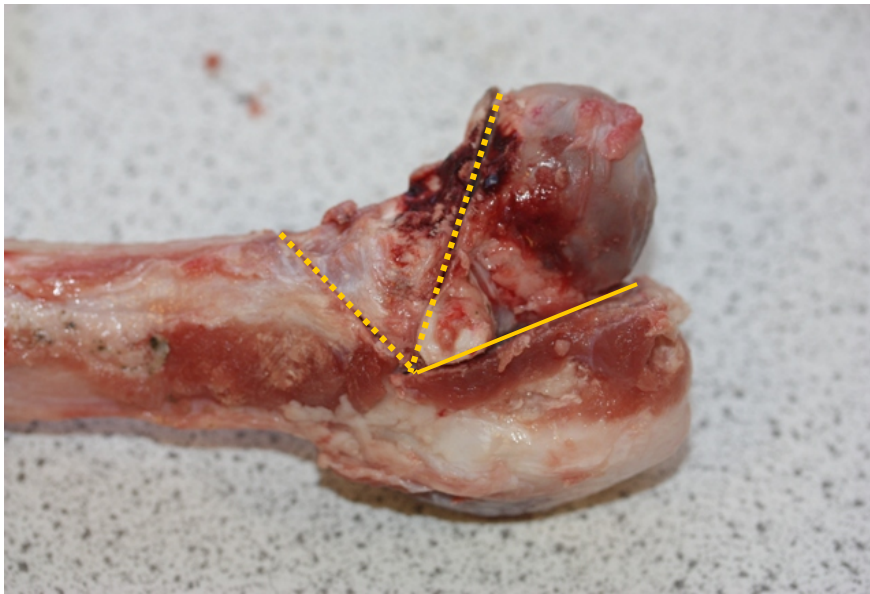


Figure 18. Preparation cuts for the first stage of generating the disease model. The broken lines represent the first cuts used to create the inferior flat, the solid line represents the final resection cut made through the isthmus after the hole has been cut and the donor bone inserted.

For disease models, a round-ended hole (nominal spherical radius approximately 8.5mm), of nominal diameter 9.5mm was made using a single-fluted cancellous bone drill (Prototype drill provided by DePuy-Synthes Joint Reconstruction (Figure 19). The drill was rotated at low speed and used without irrigation. It was centred on and aligned orthogonally to the inferior cut surface of the femoral head. The end of the hole was positioned approximately 5mm from the subchondral surface (Figure 22). This was achieved iteratively by drilling a short distance, measuring the depth of the hole with a Vernier calliper and comparing it to the height of the resected femoral head. Once the desired depth had been reached the cavity was cleaned of debris using fresh water.



Figure 19. Photograph of the drill used to generate a hole within the porcine femoral heads. The shaft diameter of the drill was 9.5mm and it created a round-ended hole with an end radius of approximately 8.5mm

A close-fitting plug of donor bone from the lateral epicondyle of bovine femurs was extracted using a PTX Universal number 10 plug cutter, which created a cylindrical plug with a 9.8mm nominal diameter. The end of the plug was domed using a hand-powered 12mm wood auger (Figure 20). The cutting face of the auger was reground into a concave form with a 9mm radius by the author using a Dremel (Robert Bosch Tool Co., Illinois). The plug was rinsed in fresh water to remove debris. A prepared plug is shown in Figure 21.

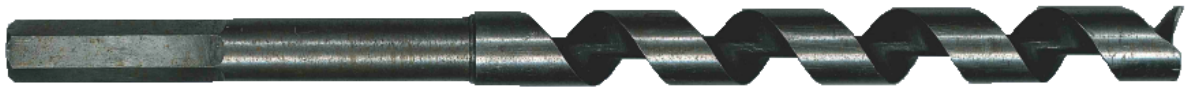


Figure 20. Photograph of the modified 12mm diameter wood auger used to prepare the domed end of the bone dowel. The end of the auger was reground to have a concave surface with a radius of 8.5mm

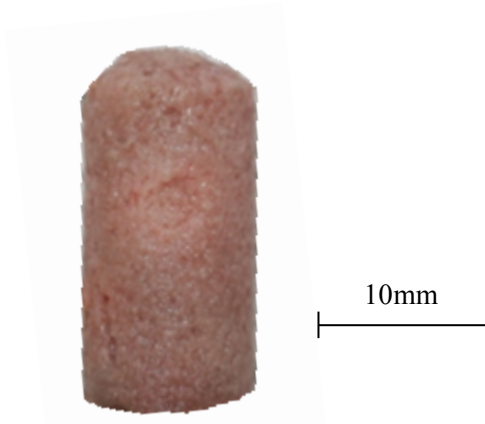


Figure 21. Example of a bone plug prepared using a PTX Universal No. 10 plug cutter (Figure 9). The end was domed to conform to the cavity created by the drill shown in Figure 18 using the modified wood auger (Figure 20)

The length of the prepared plug and depth of the hole were measured using a Vernier calliper then the plug was inserted into the hole using light impaction. The depth of the hole and the length of the plug were compared to ensure that full seating had occurred. The plug was then trimmed flush to the inferior surface of the femoral heads. The inferior surface of the construct was potted in a thin layer of PMMA resin to provide a flat datum prior to testing. A cross-section of an actual sample is shown in Figure 22.

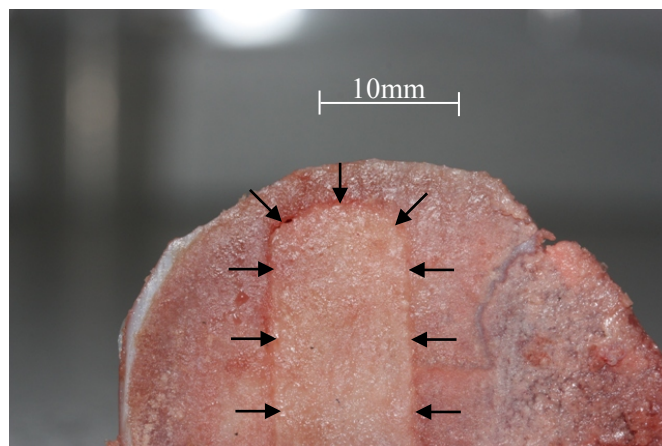


Figure 22. Example of a porcine femoral head with a simulated lesion of donor bone which originated from the lateral epicondyle of a bovine femur. There is a theoretical line-to-line fit between the hole and plug. The arrows indicate the boundary of the plug. Note that the cartilage has been removed from the top of the sample.

In total, 9 experimental disease models and 11 controls were prepared for testing. One experimental disease model was lost due to a programming error that resulted in it being compressed by more than 2mm in the first cycle. Its results are not included in the following sections. In cases where the disease models could not be tested immediately they were rinsed

with fresh water and frozen at -18°C and thoroughly defrosted in room temperature air prior to testing. This storage protocol has been shown to have insignificant effect on the mechanical properties of the calcified portion of bone (Pelker *et al.*, 1984; Linde *et al.*, 1993).

2.4.3 Methods

Experimental disease models and control femoral heads were compressed between flat platens and the structural moduli were calculated using a Hertzian contact approach. The work:modulus relationship for individual femoral heads and for the entire data set were compared to an analytical solution to confirm whether the materials approximated to linear-elastic behaviour.

Samples were tested on an Instron 3366 materials testing machine (Norwood, MA) fitted with a 10kN load cell (product code 2530-443, Instron, Norwood MA) and data collected at a sampling rate of 1Hz. The PMMA-mounted heads were placed centrally under the load-cell on a flat platen. The load cell was attached to the load frame and a 40mm diameter flat platen was attached to the load cell (Figure 10, right).

Control and disease model femoral heads were thoroughly thawed at room temperature before being compressed to incrementally greater displacements at a constant rate of $0.01\text{mm}\text{s}^{-1}$ in accordance with the recommendation made by Carter and Hayes, (1976).

One pair of femoral heads, comprising of a control and experimental disease model, was compressed to 0.25mm, 0.5mm, 0.75mm, 1mm, 1.5mm and 2mm, however, the contact area associated with 0.25mm compression was extremely small and there was very little difference between the 0.5mm and 0.75mm samples. The remainder of the samples were compressed in sequence to 0.5mm, 1mm, 1.5mm and 2mm. The loading workflow is shown schematically in Figure 23.

In order to record the contact area between the femoral head and platen, 30mm x 30mm sections of Pressurex medium (measurement range $100\text{-}500\text{kg}/\text{cm}^2$, spatial resolution $5\text{-}15\mu\text{m}$) film (Sensor Products LLC, USA) were positioned between the top of the femoral head and the compression platen prior to the start of each load cycle and removed after the cycle had completed. No calibration of the film was required as its role was only to record the size of the contact area, not the applied load.

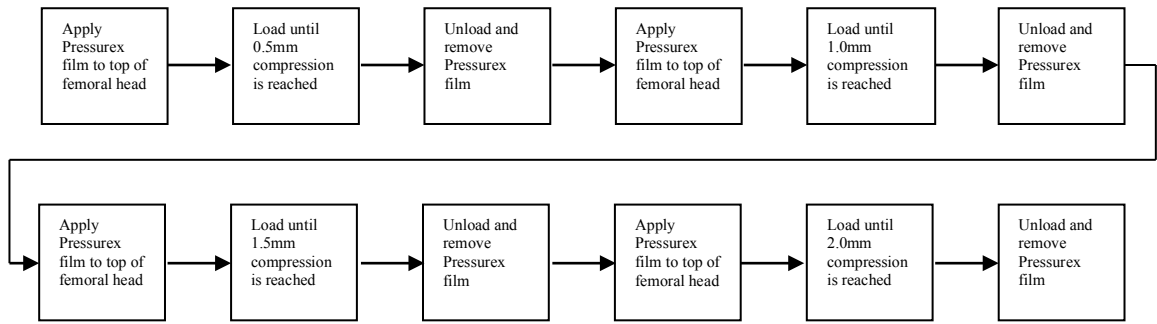


Figure 23. Workflow for displacement controlled compressive loading of control and disease model femoral heads

In several cases during the final load cycle (loading to a displacement of 2mm), a clear inflection point was observed on the real-time load-displacement plot or a cracking sound associated with bone fracturing was heard and the test was stopped early to avoid gross damage to the construct. All femoral heads were (re-)frozen at -18°C upon completion of the test cycles.

The load-displacement data generated for each control and disease model femoral head were analysed using an approach based on Hertzian contact analysis. The motivation for using such an approach was that it provides an estimate of the bulk modulus of both the disease model and control the femoral heads.

In 1895 Hertz published volume 1 of his book, “Gesammelte Werke”. His work still provides the foundation of the analysis of surface stresses and deformations produced by pressure between curved bodies. Formulas based on Hertzian theory give the maximum compressive stresses, which occur at the centre of the contact surfaces, but not the maximum shear or tensile stresses. The maximum shear stress occurs in the interiors of the mating parts. The maximum tensile stress occurs at the boundary of, and is normal to the contact area (Young and Budynas, 2002).

The fundamental contact equations are:

Equation 1: Contact modulus E^* . E_1 is the Young’s modulus and ν_1 is the Poisson’s ratio of the femoral head; E_2 is the Young’s modulus and ν_2 is the Poisson’s ratio of the platen. E_1 is in the 100’s of Mega-Pascal range and E_2 is in the 100’s of Giga Pascal range thus the second component tends towards zero. This introduces an error of between 0.15% and 0.2%.

$$\frac{1}{E^*} = \frac{1 - \nu_1^2}{E_1} + \frac{1 - \nu_2^2}{E_2}$$

Equation 2. Assuming a Poisson’s ratio of 0.3 for both materials and approximating the second component to zero simplifies this equation to:

$$E_1 = 0.91 * E^*$$

Equation 3: Effective curvature R . R_1 is the measured radius of the femoral head and R_2 is the radius of the platen. The platen is a flat surface, therefore the second component tends to zero and R tends to R_1 .

$$\frac{1}{R} = \frac{1}{R_1} + \frac{1}{R_2}$$

Equation 4: Semi contact width a . P is the applied load, R is the effective radius and E^* is the effective modulus. The contact modelled here is between a femoral head (modulus in the region of 300MPa) and a flat steel platen (modulus in the region of 190GPa). In this instance, P and R are known; a and E^* are unknown.

$$a = \left(\frac{3PR}{4E^*} \right)^{\frac{1}{3}}$$

Equation 5: Approach of centres, δ , based upon the semi-contact radius and the radius of the femoral head. R and δ are known, again, a is unknown.

$$\delta = \frac{a^2}{R}$$

Equation 6: Combining equations 2, 4 and 5 allows the known approach of centres to be linked directly to the unknown modulus of the femoral head.

$$\delta = \frac{\left(\frac{0.824PR}{E^*} \right)^{\frac{2}{3}}}{R}$$

Hertzian contact mechanics provides a theoretical description of the interaction between the platen and the femoral heads in compression with a number of caveats:

1. The femoral heads are not perfectly spherical.
2. The contact radius is relatively large.
3. The interaction is not perfectly elastic.
4. Bone is not isotropic or known to have a constant Poisson's ratio.

Two approaches to comparing the results to a Hertzian contact model were used with the intention of reverse-engineering the bulk modulus. The first was to best-fit a Hertzian load-displacement plot to the test data using Equation 6. The second was to use the contact area measured from the Pressurex film to derive an elastic modulus that minimised the absolute error between the measured and theoretical contact radius (Equation 4) over the cumulative test cycles. The second approach is described in appendix A.

To fit a Hertzian contact model to the test data, Equation 6 was used to derive the theoretical approach of centres for the applied load. An adjustment factor was introduced to the approach of centres equation to accommodate the toe-region associated with the platen not being in full contact with the sample at the start of the case and with the slight warping of the PMMA base.

The steps for this analysis were:

1. Calculate the slope over an approximately 80 μ m (9 data points) displacement.
2. Identify the first reduction in slope (an indication of yield).
3. Calculate the instantaneous contact radius and approach of centres.
4. Minimise the error between the calculated approach of centres and the measured compression; bounding the calculation between 5N and the point of inflection by varying the modulus and adjustment factor.

2.4.4 Results of assembling and testing disease models and native femoral heads

A typical example of the result of this approach is shown in Figure 24. The majority of the deviation between the experimental and analytical solution was toward the end of the load cycle. This apparent increase in stiffness followed by a reduction was an indication of plastic deformation.

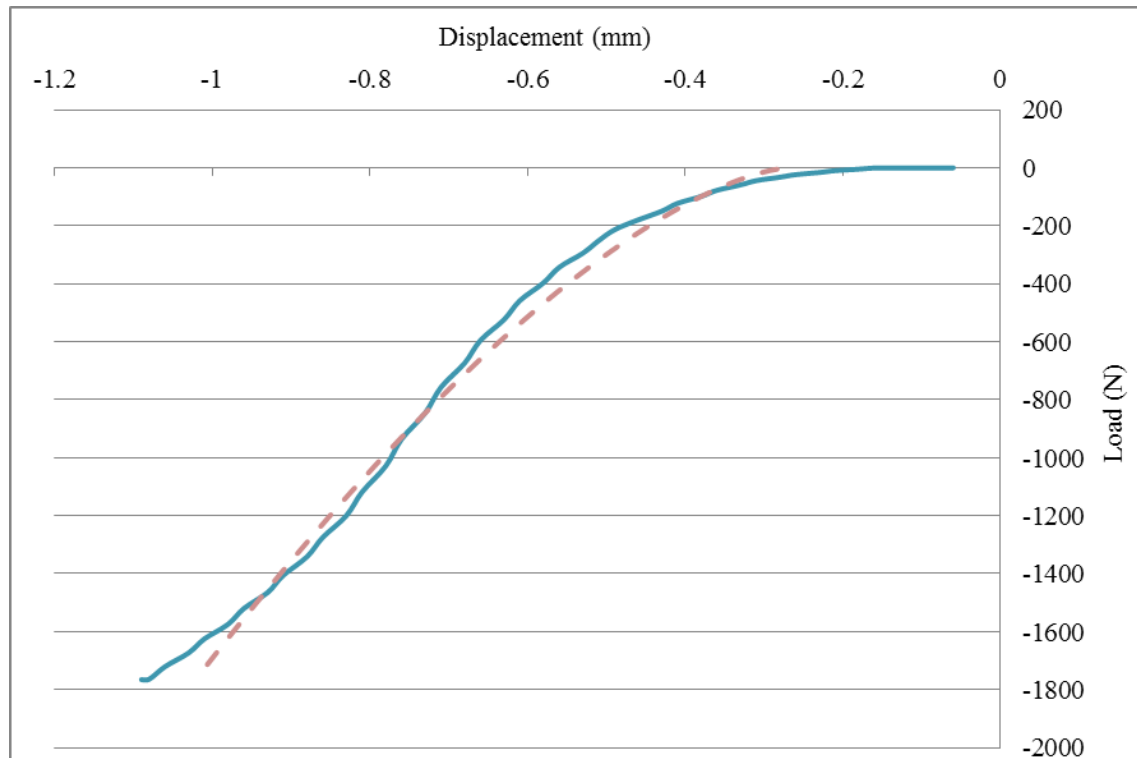


Figure 24. Load-displacement plot for femoral head VI during its second cycle (compression to 1mm). The raw data (solid line) is overlaid with the best-fit Hertzian load-displacement curve (broken line). In this case, δ -adjustment factor is approximately 0.27mm. The best-fit algorithm was limited between 5N (0.25mm) and the yield point at 680N (0.72mm). The sum of the absolute error within these boundaries was 0.74mm (between 0.00 and 0.1mm per data point).

An example plot of all four cycles for a control femoral head is shown in Figure 25. Although the results for individual control and disease models were variable, several general trends were evident: the disease model femoral heads were less stiff and tended to have an extended toe-region of high strain (displacement) but low stress (load). This toe-region was present in all plots and was due in part to slight warping of the PMMA potting medium and to small variations in the initial pre-load. Also, the cumulative results for the control femoral heads tended to be more closely grouped between 0mm and 1mm suggesting that less plastic deformation was taking place compared to the disease models.

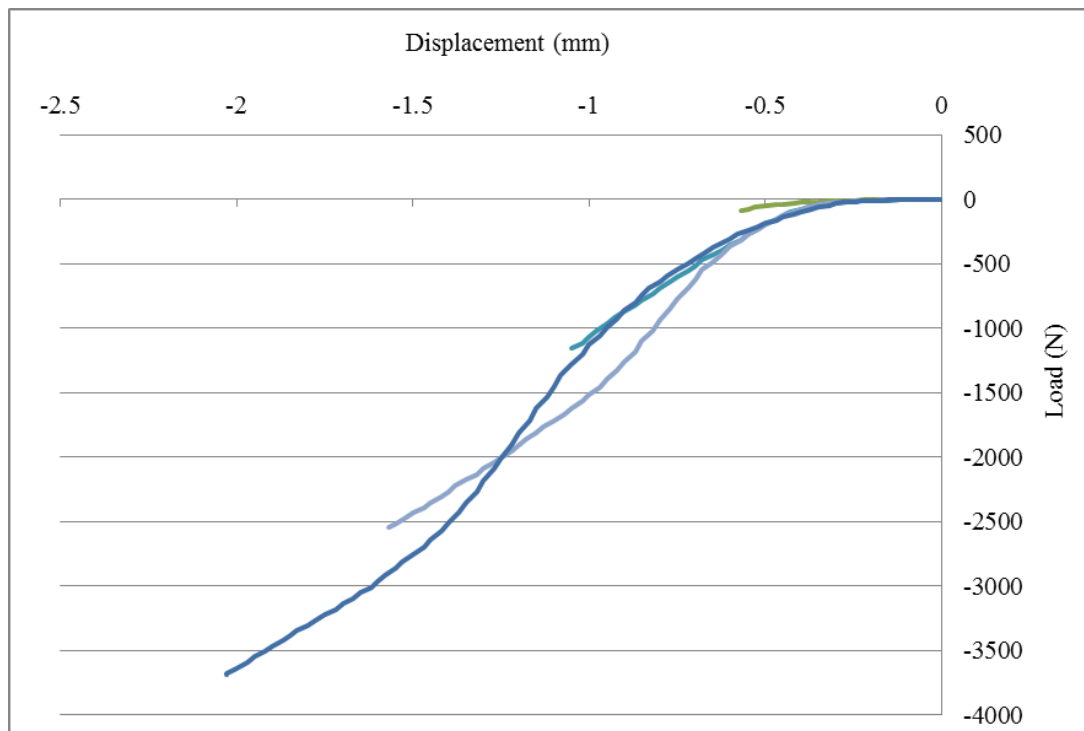


Figure 25. Plot of load versus displacement for control femoral head XII. Each line represents a different load cycle.

When native femoral heads were tested, there was a general trend of increasing modulus that was consistent with cumulative damage in a porous structure (Carter and Hayes, 1977) without gross failure. In some cases there was a slight reduction in modulus between the third (compression to 1.5mm) and fourth (compression to 2mm) cycles indicating that a gross failure event had occurred. Although not consistent, the reduction in modulus was more distinct in the evaluation of disease model femoral heads. A summary of the change in modulus between cycles three and four is shown in Table 11.

Table 11. Change in modulus between cycles three (compression to 1.5mm) and four (compression to 2.0mm). Negative values indicated a reduction in modulus.

Disease Model		Control	
I	-7%	II	17%
IV	17%	III	22%
X	18%	V	-2%
XI	-26%	VI	6%
XVI	-14%	VII	16%
XVII	-32%	VIII	4%
XIX	-23%	IX	-14%
XX	-18%	XII	5%
-	-	XIII	6%
-	-	XIV	8%
-	-	XV	-41%

A box-whisker plot of the moduli calculated for disease model and native femoral heads for each cycle is shown in Figure 26. After the first cycle the mean modulus for the control femoral heads was approximately 250-300MPa (range 130MPa to 512MPa). The modulus for the disease model femoral heads was again consistent after the first cycle: approximately 200MPa (range 92MPa to 397MPa).

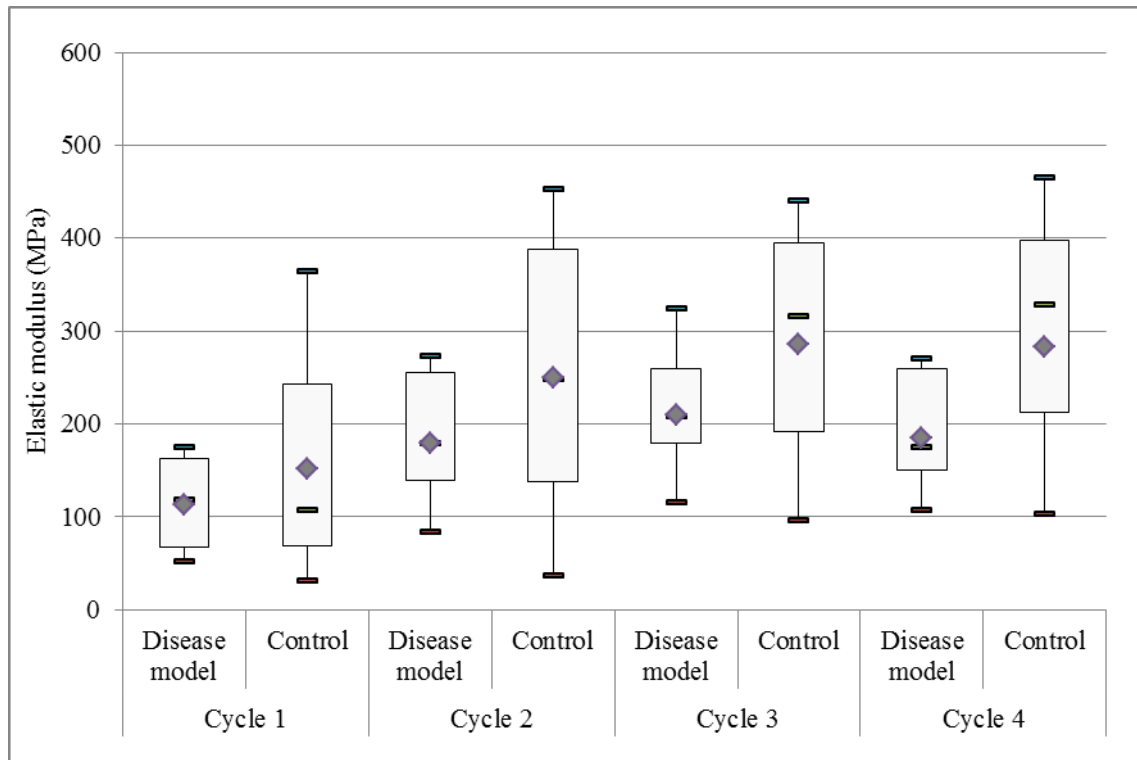


Figure 26. Box-whisker plot showing the derived elastic modulus for disease models (n=8) and control femoral heads (n=11) over four cycles. The mean is represented by a diamond, the median by a bar. The bulk modulus was derived by minimising the error between an analytical Hertzian approach of centres and the measured compressive displacement.

2.4.5 Verification of the approach to derive elastic modulus

As trabecular bone is compressed, the intra-trabecular spaces close and the modulus increases (Carter and Hayes, 1977). Hence the experimental load-displacement relationship can increase exponentially because of both geometry and material non-linearity. In Hertzian contact, the force increases because the contact area increases and there is more material in contact to resist incremental displacement. In a non-linear material, the stiffness increases with displacement or force. The extent of the non-linearity was unknown so it was necessary to ascertain the validity of the assumed linear-elastic material model.

The approach described in Section 2.4.3 used least-squares regression to fit an analytical load-displacement relationship to experimental data. The theoretical relationship assumed a constant elastic modulus. This approach will produce an elastic modulus value for any data with a positive slope even if the relationship between load and displacement was non-Hertzian.

Work done, calculated as the integral of a load-displacement plot, is independent of the shape of the data and so can be calculated exactly for any given load-displacement data set. If the data represented a linear-elastic material in Hertzian contact then the relationship between work done and elastic modulus would correlate to an analytical solution. As the non-linearity increased, the deviation from the analytical solution would also increase.

As an example, the work-modulus relationship was compared for four theoretical cases (Figure 27). In all cases the data represented a 30mm diameter sphere compressed to a force of 500N. In case 1, the material was linear-elastic with a Contact modulus E^* of 250MPa. In cases 2-4, the mean modulus over the load range was the same but the stiffness increased at a rate of 0.1% per Newton, 0.5% per Newton and 1% per Newton. The defining functions are:

Case 1: Modulus constant; $E^* = 250\text{MPa}$.

Case 2: Modulus defined by the function: $E^*_{n+1} = 1.001E_n$ | $E_0 = 244\text{MPa}$. $E^*_{\text{mean}} = 250\text{MPa}$.

Case 3: Modulus defined by the function: $E^*_{n+1} = 1.005E_n$ | $E_0 = 221\text{MPa}$. $E^*_{\text{mean}} = 250\text{MPa}$.

Case 4: Modulus defined by the function: $E^*_{n+1} = 1.010E_n$ | $E_0 = 194\text{MPa}$. $E^*_{\text{mean}} = 250\text{MPa}$.

The load-displacement relationship for these cases is shown in Figure 27. As the non-linearity increased, the area under the curve was reduced. A qualitative comparison to the plot for displacement to 1.5mm shown in Figure 23 suggested that the material was indeed behaving slightly non-linearly.

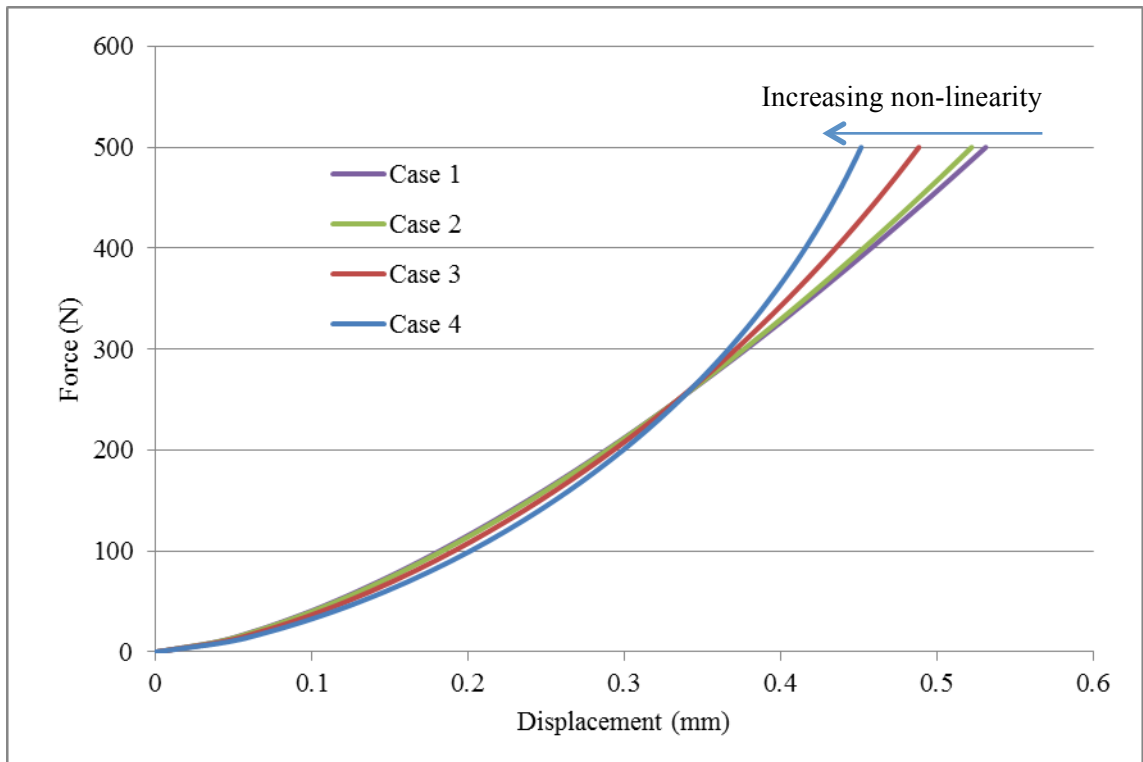


Figure 27. Load displacement relationship for four cases of Hertzian contact between a rigid, flat plate and a 30mm diameter sphere with differing degrees of non-linear elasticity.

Actual work done for each case was calculated by integrating the load-displacement data to a consistent maximum load for each cycle.

A single effective modulus (E^*_{derived}) was derived for each case using the same protocol as was used for the experimental data (N.B. for case 1 the residual error was zero, verifying the equations used). The modulus and work done for each case is shown in Table 12. The same data is shown as an x-y plot in Figure 28. As the non-linearity increased, the error increased in both parameters: The ratio of work to modulus reduced. If the data represents a non-linear system, then the work done will be lower than predicted, and the modulus will be higher than predicted. The closer the material is to a linear-elastic condition, the lower the error between the analytical and derived solutions.

Table 12. Parameters, derived modulus and actual work done four cases of Hertzian contact between a rigid, flat plate and a 30mm diameter sphere with differing degrees of non-linear elasticity.

Case	Description	E^*_0 (MPa)	E^*_{Derived} (MPa)	Residual error (mm)	Actual work done (Nmm)
1	$E^*=250\text{MPa}$	250	250	0	106
2	0.1% stiffening factor	244	252	0.11	102
3	0.5% stiffening factor	221	260	0.56	88
4	1% stiffening factor	194	269	1.1	72

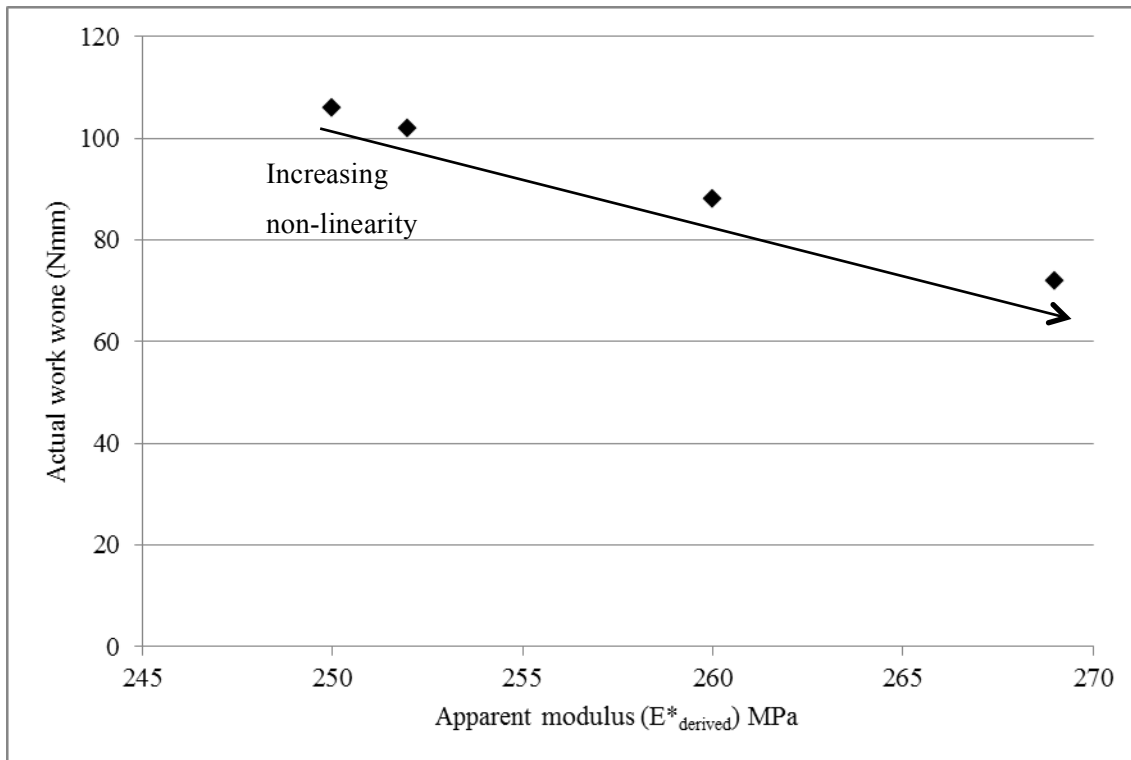


Figure 28. Plot of work done versus modulus for Hertzian contact between a rigid flat platen and a deformable spherical body comprised of increasingly nonlinear material. As the material becomes more nonlinear the work done reduces and the elastic modulus increases.

While it was possible to calculate an error for a single data point, the analytical solution was dependent on the input so it was not possible to verify whether the error is due to the experimental results or the choice of input in the analytical solution. To differentiate between these, both the individual error and the data trend were analysed.

The work-modulus relationship for a number of linear-elastic spheres with moduli between 90 and 550MPa¹, a Poisson's ratio of 0.3 and a diameter of 34mm compressed by a rigid flat platen is plotted in Figure 29. This diameter is equal to the mean diameter of the porcine femoral heads used in the experiment. The work done equates to a maximum applied load of 513 N, equivalent to the maximum load that was applied to every head during the second load cycle (Table 13). This exercise was repeated for cycles three and four; data from cycle 1 was not used as the applied load was so low that the variability in the data made establishing a trend impossible.

Table 13. Load chosen as an endpoint for calculating work done for each disease model and control. This load equated to the largest load that had been applied to every disease model and control femoral head over that cycle.

Cycle	Load (N)
1	88
2	513
3	1179
4	1731

¹ The moduli used in this example equate to a Hertz effective modulus of 100MPa to 600MPa

The work-modulus relationship for a series of 34mm diameter spheres with moduli between 90MPa and 550MPa in contact with a flat surface, compressed up to a load of 513N is described by the function: $Work = 3927.8 \times (modulus)^{-0.667}$ and shown graphically in Figure 29.

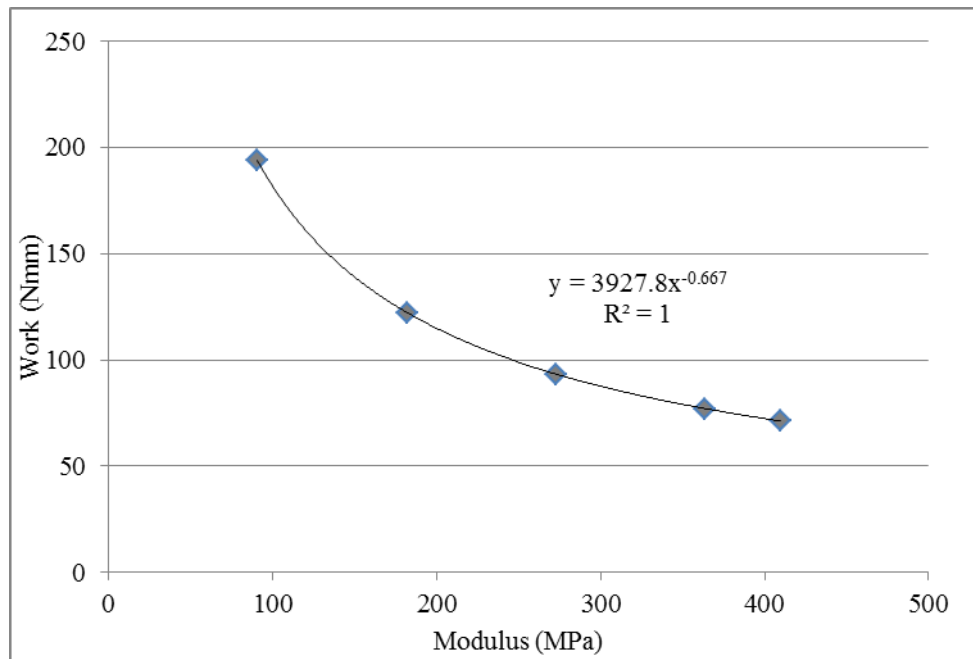


Figure 29. Analytical work-modulus relationship for a series of linear-elastic spheres with a 34mm diameter compressed by a rigid flat plate. The spheres had moduli between 90 and 550MPa

The mean work done (calculated as the area under the recorded load-displacement curve) for all disease models and controls (n=18, one outlier removed) for the second load cycle was 116 Nmm with a standard deviation of 38Nmm.

Using the function derived previously and the modulus derived for each femoral head, the work that would have been done if the head were perfectly elastic was calculated. On an individual basis the work-modulus relationships for 15 out of 18 samples were within $\pm 9\%$ of the analytical solution. This magnitude of error equated to approximately 4 data points, less than half the number of data points used to calculate the slope in the steps for establishing the elastic modulus described in Section 2.4.3 suggesting that the error was within the resolution of the analysis method.

Of the remaining three samples, one disease model result was within 15% and the remaining samples (one disease model, one control) differed by 22% and 39% respectively. These errors cannot be solely attributed to the resolution of the analysis method so it is reasonable to conclude that some non-linearity had occurred.

The two samples with the largest error were approximately 1 standard deviation from the analytical solution and it was concluded that they had exhibited a degree of non-linear behaviour but this was insufficient to exclude them from the data set. The third data point (control, femoral head XIII) was so far from the trend line that it was considered an outlier.

The entire data set is presented in Table 15. The experimental results represent femoral heads of various diameters (mean 34mm, Range 31-37). The analytical solution assumed a single diameter of 34mm. Thus a small residual error associated with differences in head diameter is inherent in the results.

A plot of work versus modulus for both the disease model and control experimental results from cycle 2 is shown in Figure 30. The theoretical relationship reproduced from Figure 29 is overlaid. Two versions are presented: One version contains the 16 heads that behaved in the most linear-elastic manner and the other with all data points except the outlier. While the fit to the analytical solution was improved by reducing the number of data points, there was insufficient evidence to exclude them from the data set.

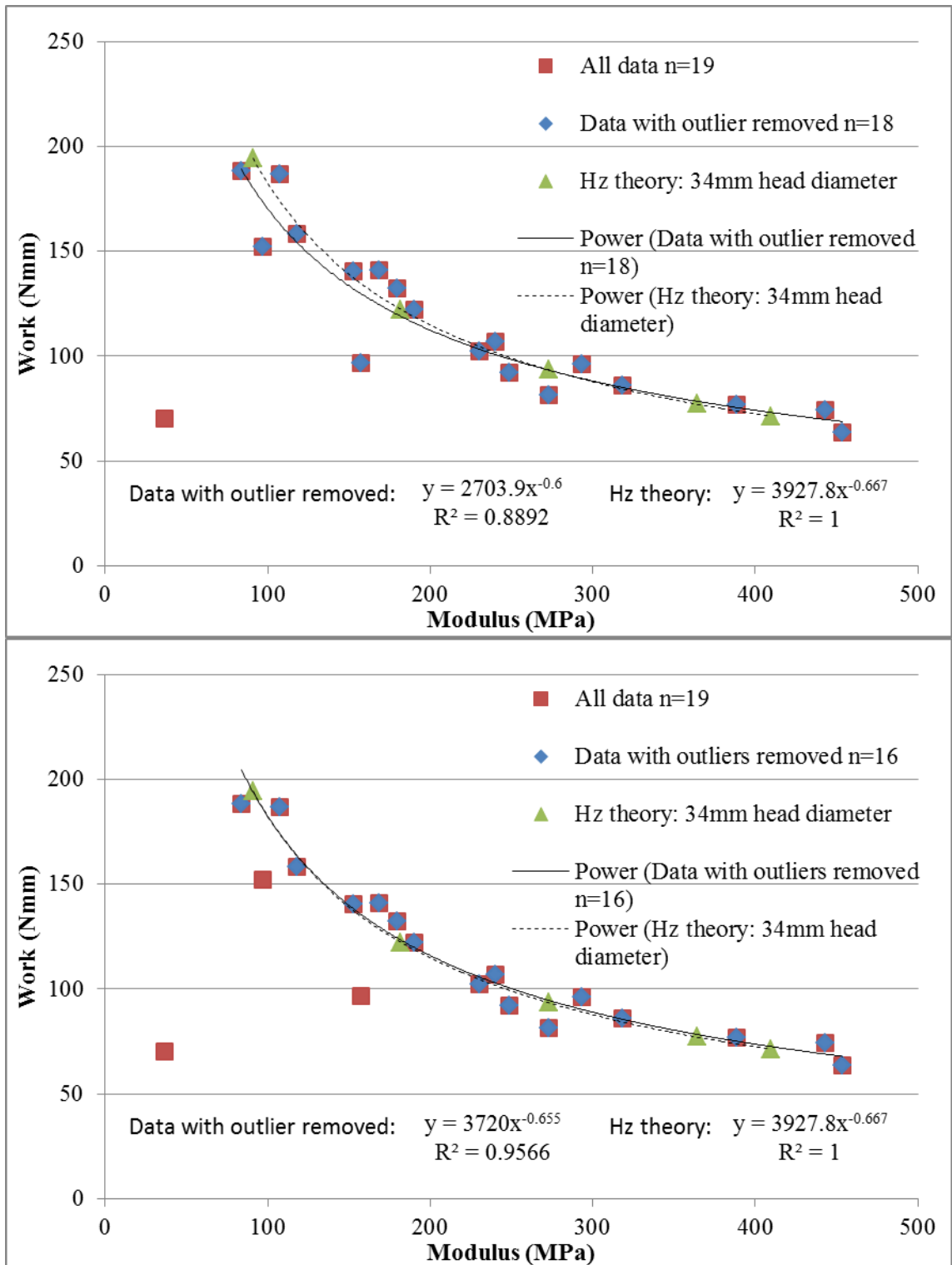


Figure 30. Two plots of work versus modulus for experimental data and the analytical solution. Top: n=18. The trend-line for the experimental data was flattened (the power is smaller) compared to the analytical solution. The R^2 value indicated a relatively worse fit to the data. Bottom: n=16. The experimental data followed the analytical solution almost exactly with a much higher R^2 . While the two data points that were excluded in the second plot detracted from the fit of the data, the difference in real terms was not sufficient to consider these points to be outliers.

Table 14. Derived modulus and measured work done for the experimental samples and work done for a 34mm diameter, spherical, linear elastic body using the derived modulus and the difference between the two. Two cases where the absolute difference was close to one standard deviation of the measured work done were found (Femoral heads I and III). The case where the difference was more than 7 standard deviations away is highlighted in parentheses: This sample is an outlier and is not included in the calculated means and standard deviations.

	Femoral head	Experimental results		Work derived using $W=3927.8E^{-0.667}$	Error (Nmm)
		Elastic modulus for cycle 2 (MPa)	Work done to 513N (Nmm)		
Disease model	I	97	152	186	34
	IV	240	107	102	-5
	X	153	141	137	-4
	XI	84	188	205	17
	XVI	169	141	128	-13
	XVII	190	122	118	-4
	XIX	273	81	93	12
	XX	230	102	104	2
Control	II	118	158	163	5
	III	157	97	135	38
	V	318	86	84	-2
	VI	443	74	67	-7
	VII	388	77	74	-3
	VIII	180	132	123	-9
	IX	453	63	66	3
	XII	248	92	99	7
	XIII	[37]	[70]	[356]	[286]
	XIV	107	186	174	-13
	XV	293	96	89	-7
Mean		230	117	119	2
Std. deviation		114	38	41	14

The results from cycles three and four (using a load of 1179N and 1731N as end points respectively) were evaluated using the same process. The resulting plot for cycle three is shown in Figure 31. The experimental results had a lower ratio of work to modulus than the analytical solution and had a larger spread. Reducing the maximum force to which the work done was calculated from the analytical solution by 5% (60N) re-aligned the experimental and analytical results almost perfectly. This equated to an 8% reduction in work done for the same modulus.

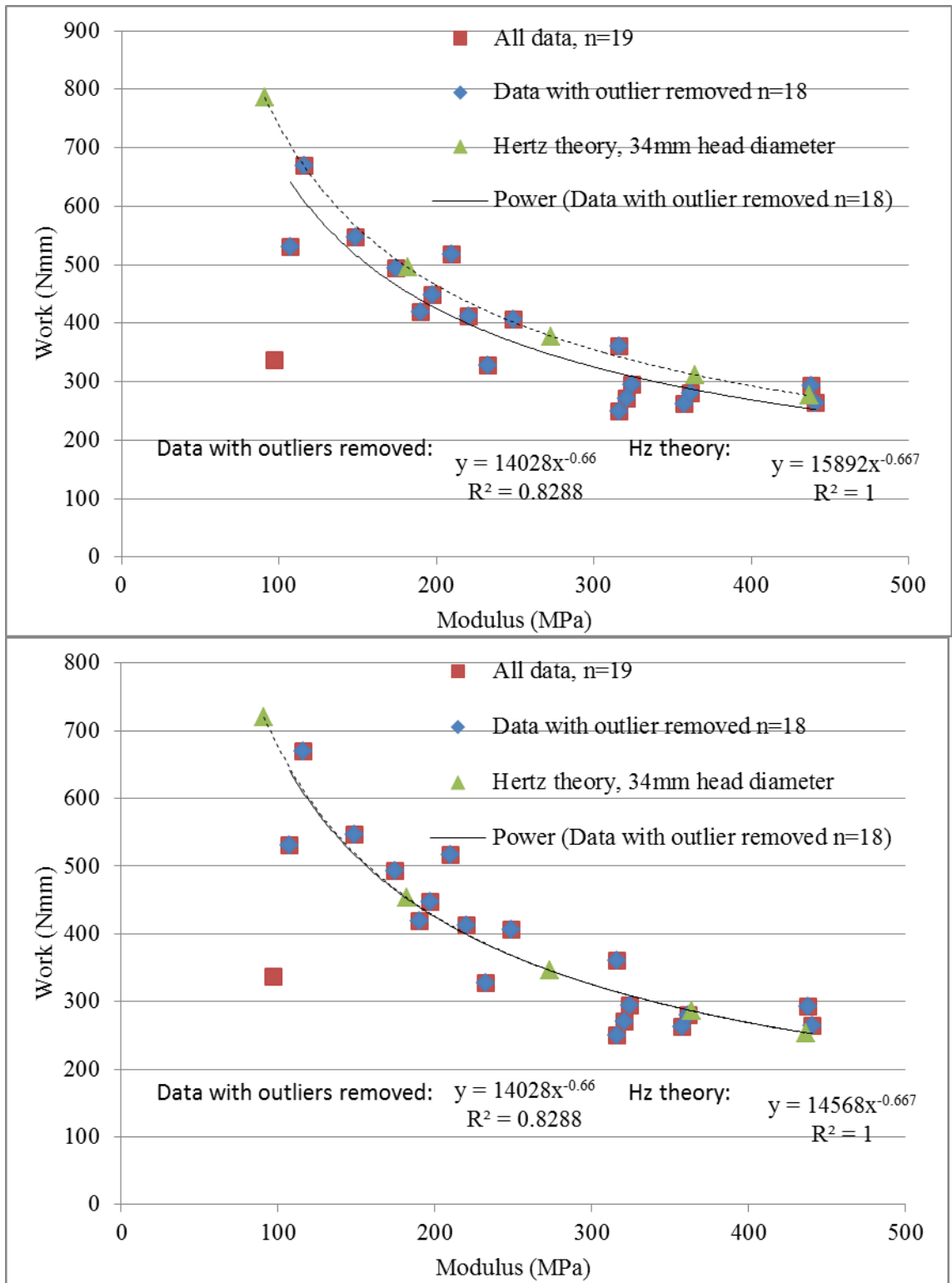


Figure 31. Work: Modulus relationship for cycle 3, during which the heads were compressed with a load of approximately 1180N. Top: experimental data compared to an analytical solution over the same load range. Bottom: experimental data compared to the analytical solution assuming a 5% reduction in load used in the analytical solution (1120N) compared to the experimental data (1179N).

To put this deviation into context, 60N equates to 2-3 data points or 20-60 μ m. Excluding control sample XIII, the mean difference between the analytical and experimental work done during the third cycle was 45Nmm with a standard deviation of 43Nmm. Given that the exponent for the experimental data trend line still approximates to (-2/3) it is likely that the

heads are still behaving as a linear-elastic body. However, with an R^2 value of 0.83 this assumption must be treated with caution.

The apparent reduction in work done is associated with plastic failure of the most superficial trabeculae. This would increase the contact area (and therefore reaction force) compared to the analytical solution.

In cycle four the work-modulus relationship no longer resembled the analytical solution. The experimental results were significantly more varied: Work done to 1731N had a standard deviation of 192Nmm (excluding control sample XIII). The R^2 value for the experimental data trend line (Figure 32) was 0.6 suggesting that the trend-line is no longer an accurate representation of the data. The five stiffest samples (all controls) may have retained a linear behaviour but as both work and elastic modulus are affected by non-linearity, it is difficult to conclude this with certainty. The six least stiff (five disease models and one control) were also the furthest from the analytical solution.

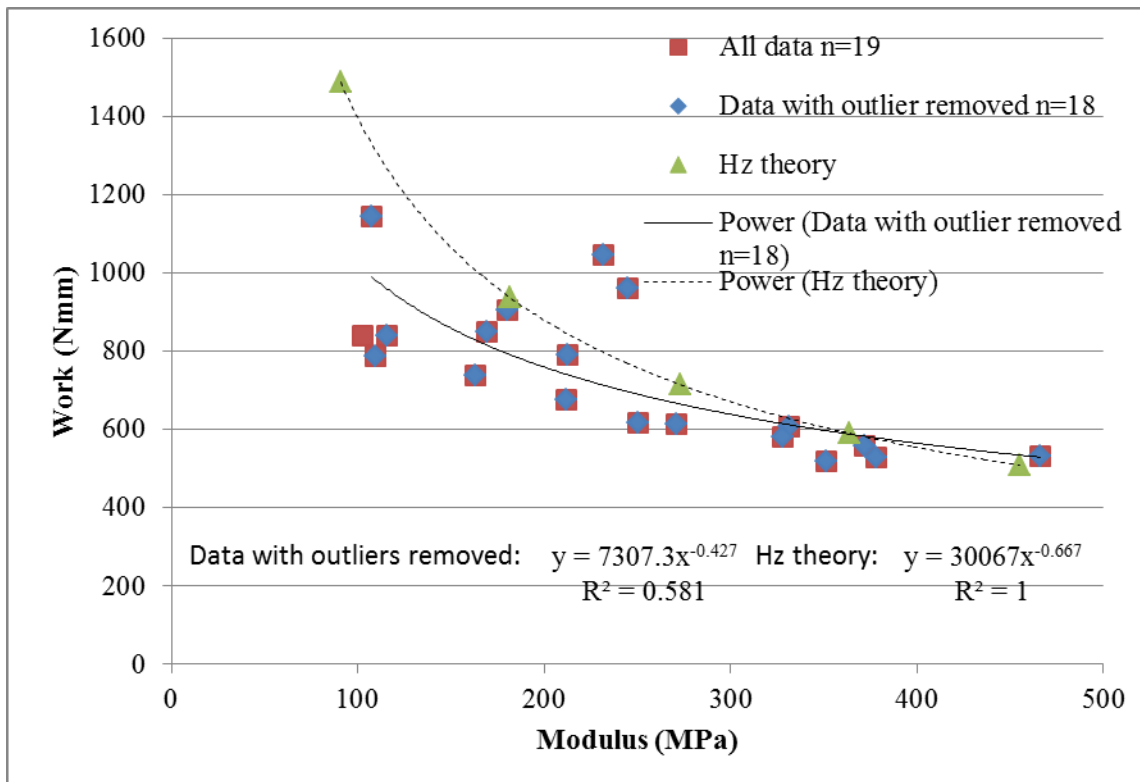


Figure 32. In cycle four the work-modulus relationship no longer resembled the analytical solution. The experimental results are significantly more varied: Work done to 1731N has a standard deviation of 192Nmm (excluding control sample XIII). The R^2 value for the experimental data trend line is 0.6 suggesting that the trend-line is no longer an accurate representation of the data.

It was concluded from this verification that the experimental disease model and control femoral heads approximated to linear-elastic behaviour at loads lower than below 1200N and displacements below 1mm.

2.4.6 Inspection of experimental disease models

To evaluate the position of the plug each disease model was inspected to establish the orientation of maximum eccentricity. This was achieved by measuring the approximate distance between the centre of the inferior surface of the plug and the equator of the femoral head using an analogue Vernier calliper. These locations were not planar but by holding the calliper against the inferior flat and rotating the head in a set position and distance from the eye, it was possible to identify the orientation of maximum eccentricity. Once this orientation was identified the disease models were sectioned in line with the plane of maximum eccentricity using a junior hacksaw through the centre of the plug. A schematic of the orientation of the cut is shown in Figure 34. An example of the cross-section obtained is shown in Figure 34. In this example, the plug was eccentric and a crack originating from the corner of the plug and traversing the subchondral bone was evident.

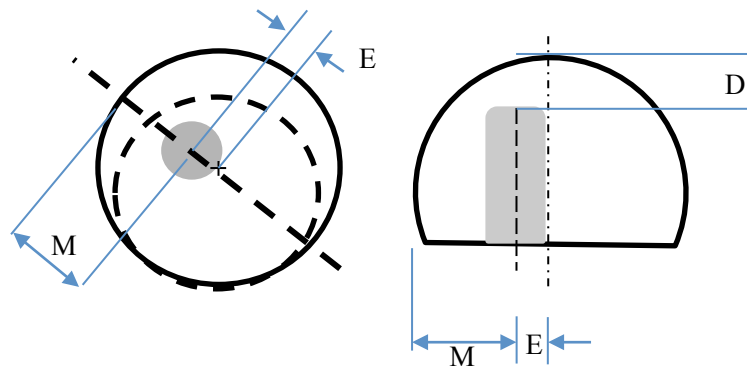


Figure 33. Left: Schematic representation of the inferior surface of the disease models showing the equator of the head (solid circle), the periphery of the inferior cut (broken circle) and the centre of the head (cross). The plug is represented by a grey circle. The minimum distance from the plug centre to the equator (M) was estimated and used to orient the cut represented by the broken line. Right: Schematic representation of the cross-section obtained. The eccentricity (E) relative to the head centre and distance beneath the apex (D) were measured using a Vernier calliper.

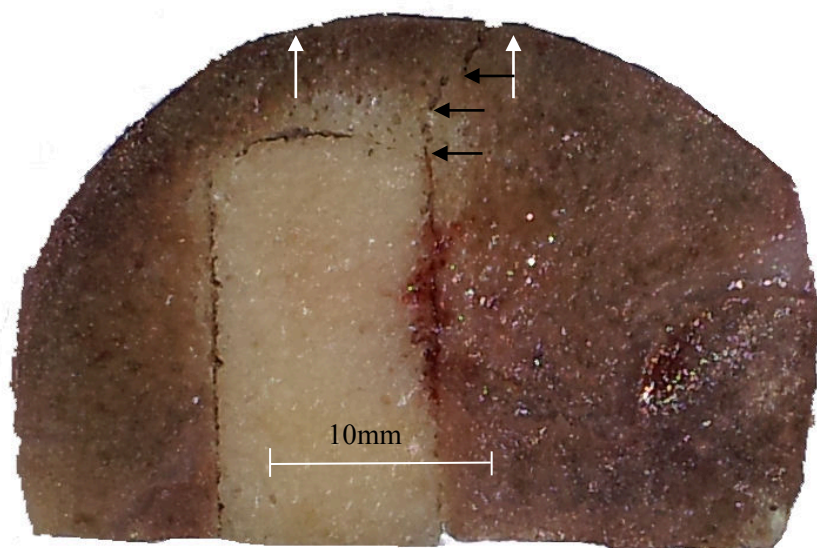


Figure 34. Cross section through *in vitro* disease model. The white arrows indicate the approximate area of load application; the black arrows show a crack propagating from the corner of the cavity. Note that in this image, the pin is significantly offset from the centre of load application. The crack has propagated from the geometric stress raiser closest to the mid-plane.

The diameter of each femoral head was measured using a set of Vernier callipers. The mean diameter was 34mm (range 31mm to 37mm). All heads displayed a degree of flattening during the test. The eccentricity, distance beneath the apex and nominal head diameters are recorded in Table 15.

Table 15. Distance between the top of the plug, eccentricity and nominal head diameter measured for each experimental disease model.

Disease Model	Distance between top of plug and apex of head (mm)	Eccentricity (mm)	Nominal head diameter (mm)
I	4	0	31
IV	6	4	32
X	6	4	34
XI	3	0	37
XVI	4	0	32
XVII	5	0	24
XIX	4	3	33
XX	5	0	36

2.4.7 Discussion

The strength and stiffness of the native porcine bone were characterised and the results used to identify a source of bone to simulate the lesion. The test methodology used to evaluate the disease model benchmarked the mechanical properties of the disease model compared to native femoral heads. It could also be used to assess the impact that mechanical interventions intended to reduce the effect of the necrotic lesion would have on the disease model.

It was expected prior to conducting these studies was that disease model femoral heads would have a lower elastic modulus because of the introduction of both a stress-raising geometry and a body of lower modulus within the femoral head.

The elastic modulus of the control and disease model femoral heads was derived using a Hertzian contact-based approach to best-fit an analytical solution to the experimental data by varying the length of the toe region and the Young's modulus used in the Hertzian equation. This approach had the principal benefit that plasticity was taken into account when the stiffness was calculated for each cycle. The progressive stiffening associated with collapse of the intra-trabecular spaces could therefore be identified by comparing the modulus derived for consecutive cycles. Although there was no significant difference between the results of the experimental disease model and control over the first three cycles, the disease models were more distinctly less stiff than the controls in the final cycle suggesting that damage accumulated more rapidly.

The variability in the results was partly attributable to differences in bone density: the individual bone mineral densities (BMD) for both the native and disease model femoral heads

varied by up to 13% from their mean. Normalising the modulus against BMD reduced the interquartile range and the maximum-minimum range but was insufficient to explain the variation.

A more significant contribution came from the definition of the upper limit chosen for each data set. The displacement at the point of inflection (bounding the data over which the approach of centres was compared to the analytical solution when minimising the error between the test data and Hertzian model) varied by around 60%. This equated to around 25 data points. It is notable that the range of displacements at inflection was approximately consistent for both data sets (Figure 35).

The force at the inflection point varied between data sets (Figure 36). This accounted for a significant proportion of the variation as the calculated approach of centres was based on this value.

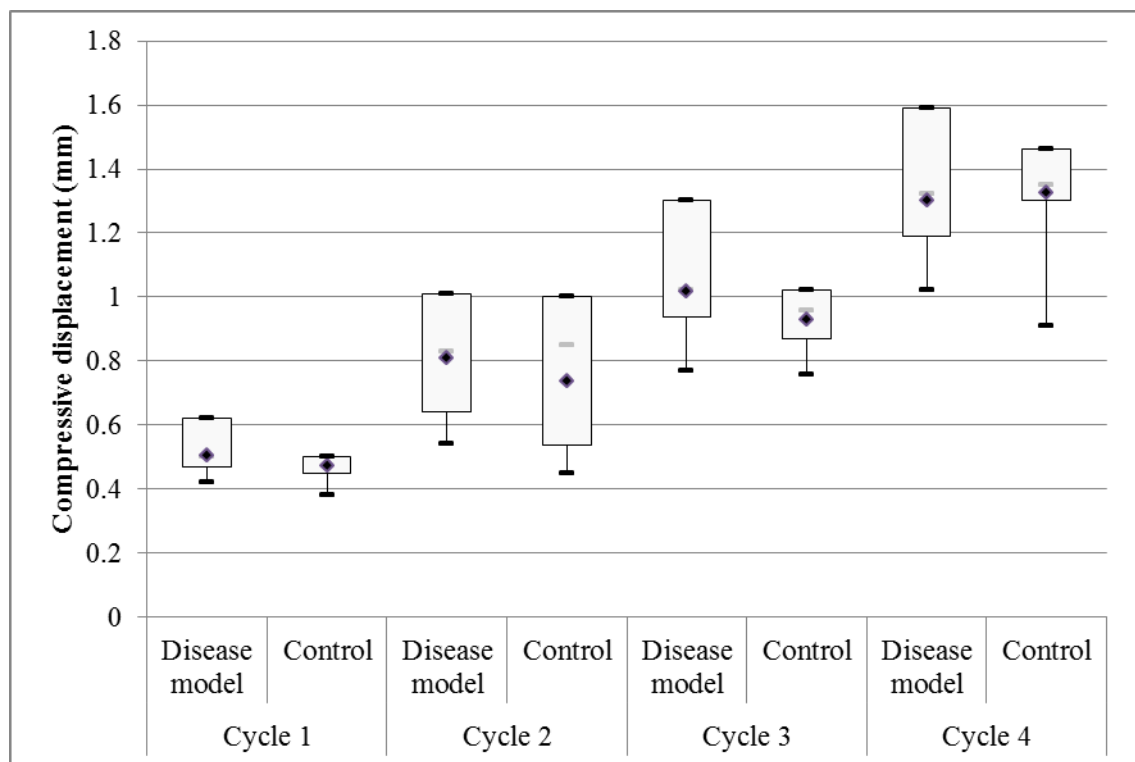


Figure 35. Displacement at inflection for disease model (n=8) and control (n=11) femoral heads. Although there was a large variation, the displacements at inflection were generally consistent across both data sets. The mean is indicated by a diamond, the median by a bar. The whiskers indicate the maximum and minimum for each set.

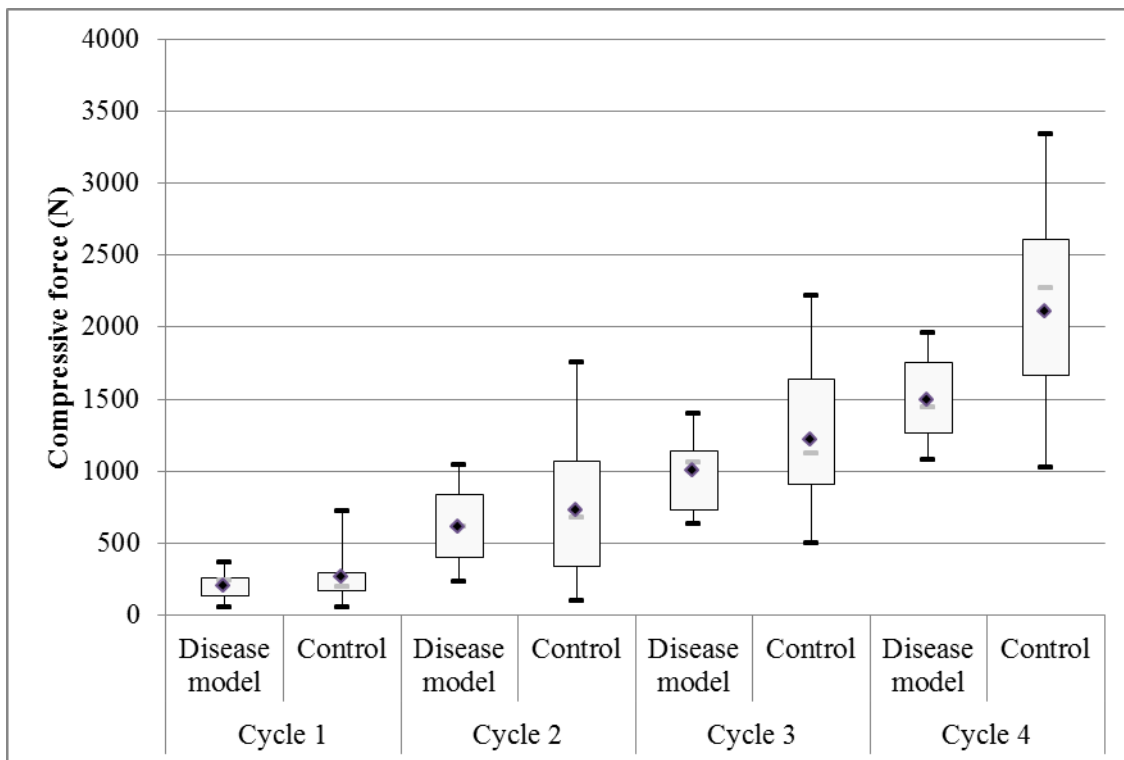


Figure 36. Force at inflection for disease model (n=8) and control (n=11) femoral heads. Although there was a large variation, there was a trend within each cycle for the control femoral heads to require a greater force to reach an inflection compared to the experimental disease model. The mean is indicated by a diamond, the median by a bar

The proof of concept disease models constructed from porcine femoral heads with a plug of weaker bone substituted for the central load bearing native bone were less stiff and weaker than the native controls. The results for both control and disease models were consistent with the results of the single-modulus based approach described in Appendix A.

The derived elastic modulus of the control femoral heads (Mean 250MPa for cycle 2 and 280MPa for cycles 3 and 4) over consecutive load cycles) was lower than the elastic modulus derived for the material (Mean 318MPa (n=12, 95% C.I: 38.56MPa)).

The elastic modulus of the disease models was comparable to the mean of the moduli derived for the substituted and native bone plugs: The donor bone plugs were approximately 50% less stiff than the plugs taken from the centre of the porcine femoral heads and the disease model constructs were approximately 25% less stiff.

There was a trend for the disease model femoral heads to become less stiff over consecutive cycles. In contrast, the control femoral heads tended to become stiffer. This indicates a difference in failure mode: loss of mechanical integrity in the disease models versus cumulative compressive failure of the trabecular structure leading to stiffening of the local bone in the controls.

The work: modulus relationship for all experimental samples was compared to equivalent analytical solutions. At loads around 500N, the disease models and controls both behaved as a

linear-elastic material and conformed well to Hertzian theory. At 1200N, a Hertzian work-modulus relationship still existed as the work: modulus curve still had an exponent of $(-2/3)$. However there was evidence of some plastic deformation. This manifested as a consistent reduction in work done across the modulus range. Between 1200N and 1800N the degree of non-linearity increased significantly, especially when the elastic modulus was less than 300MPa. There were two possible explanations for this:

1. Macro-scale cracking in the disease models resulted in a non-Hertzian relationship between load and displacement.
2. The non-linearity is driven by plastic failure of the trabeculae: a strain based failure. The less stiff samples experienced the greatest deformation and were also the ones that exhibited the most non-linear behaviour.

The second explanation is supported by the apparent continued correlation of the stiffest components: at lower strains the degree of plastic deformation was lower.

Another source of variation was the physical location of the plug of donor bone within the femoral head in the experimental disease models and the interface between the plug and host bone, which allowed movement of the two components of the disease model relative to each other.

2.4.8 Conclusion

The purpose of this experiment was to establish whether an *in vitro* disease model for AVN could be constructed using a porcine femoral head. The effect of introducing a simulated lesion into a porcine femoral head would have on its bulk properties was quantified and the accuracy with which bone, which is known to be a non-linear inhomogeneous material, could be approximated to a linear-elastic homogenous material for the purposes of generating *in silico* disease models was evaluated.

The lateral epicondyle of a bovine femur was found to be a suitable source of donor bone with reduced material properties compared to a porcine femoral head. Introducing a simulated lesion using bone from this source into an otherwise healthy porcine femoral head reduced the strength and elastic modulus of the construct compared to native controls. Within limited force (less than 1200N) and displacement (less than 1mm) magnitudes, both disease models and control femoral heads behaved in a linear elastic manner. The effect of the elastic modulus of both the porcine femoral head and donor bone taken from the lateral epicondyle of a bovine femur, and the variation in physical location warrants further investigation. These results were predictable; however, they confirmed the effectiveness of the novel method of generating and testing experimental disease models.

Chapter 3. Finite element simulation of experimental disease models

3.1 Introduction

One of the aims of this thesis was to develop a morphology-based means of assessing the risk of loss of mechanical integrity in femoral heads with AVN. Current methodologies for classifying AVN use lesion size and location as quantitative measures. These methodologies have been shown to have limited prognostic ability and it is hypothesised that including lesion morphology will improve prognostic accuracy. Lesions can be visualised using MR to allow a qualitative assessment to be performed but a less ambiguous quantitative measure is desirable. There is histological evidence that fractures may originate at stress-concentrations in the lesion boundary but this has not yet been evaluated *in vitro* or *in silico*.

The overall aim of the finite element (FE) analysis investigation was to enable patient-specific lesions resulting from AVN to be compared and ranked according to severity. This is an important step towards identifying lesions that are likely to collapse. The experimental disease models highlighted the need to understand the influence of material properties, lesion position within the femoral head and its geometry. Given the limited data and uncertainty around the material properties and loading conditions in a natural femur with avascular necrosis, the focus of the studies in this chapter was on establishing basic rules to associate the change in stress distribution within the femoral head with changes in lesion size, material properties and location. As direct validation of the patient-specific simulations was impossible, the investigation was split into sequential studies, each of which informed the development of the next. This approach helped to define the sensitivity and validity of the simulations.

The variability in experimental disease model geometry (Table 15) and material properties (Table 9) in the experimental disease models were used to develop the following hypotheses.

1. The apparent stiffness of the disease model will reduce with proximity of the plug to the outer surface of the femoral head because more of the load will be carried by the lower stiffness material.
2. The apparent stiffness of the disease model will increase if the plug is translated away from the centre of load application because more of the load will be carried by the stiffer native material.
3. An increase in stiffness of the plug material will increase the apparent stiffness of the disease model.

Six studies will be reported on in this chapter, their interrelationship is shown schematically in Figure 37.

1. Model development:
 - a. Mesh resolution optimisation study.
 - b. Definition of measures and outputs.
 - c. Evaluation of different interfaces.
2. Parametric studies:
 - a. Parametric sweep.
 - b. Multi-variable analysis methods.
 - c. Experimental disease model specific study.

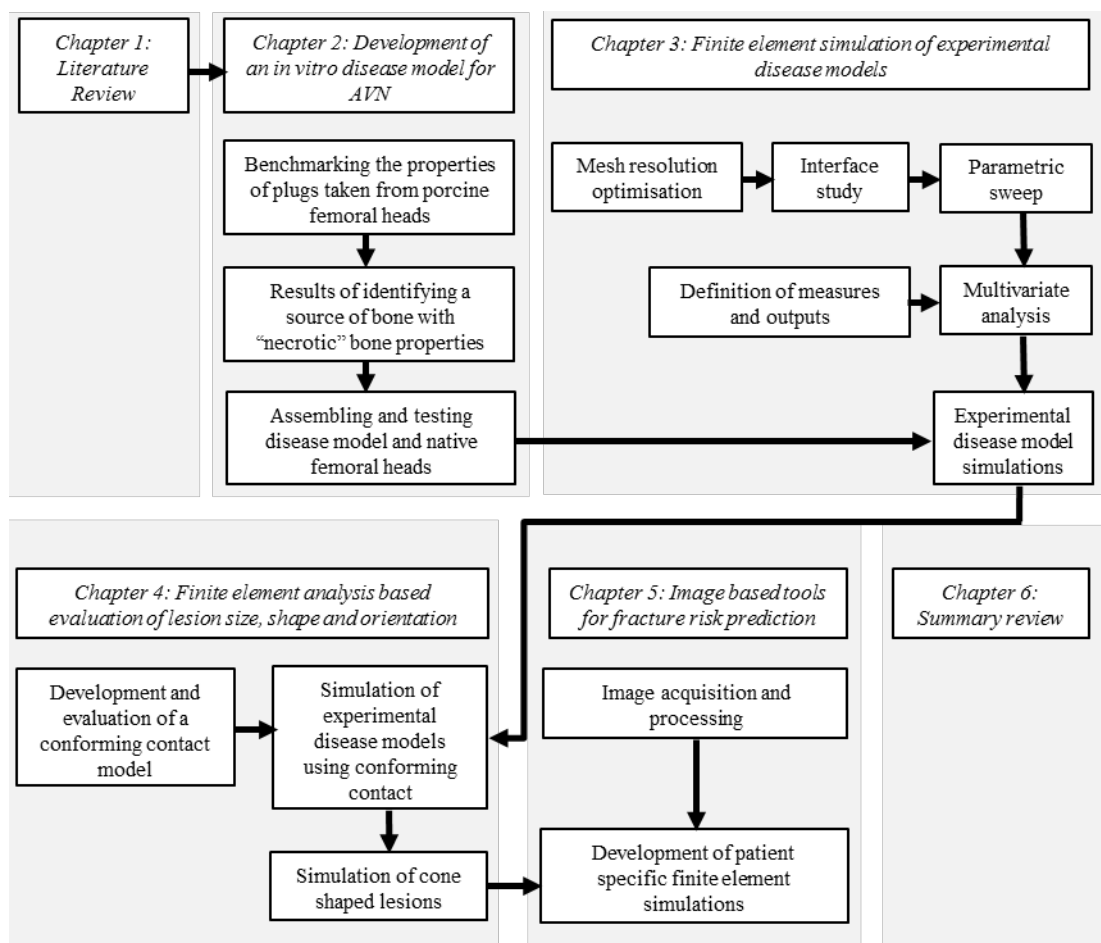


Figure 37. Flow chart summary of the studies performed in each chapter.

3.2 Model Development

3.2.1 Standard methodologies

Finite element simulation provides a means of quantifying the effect of lesion morphology on the stress distribution at the lesion boundary and therefore it can be used to facilitate development of a quantitative risk score. However, validation of the score is challenging because the poor prognosis of conservatively treated AVN means that the default treatment for

most patients is surgical intervention and altering the standard of care would be unethical. Therefore an incremental approach to developing and evaluating clinically relevant FE simulations was required. This chapter records the first stage, which was to investigate the effect that variation within the experimental disease model developed in Chapter 2 had on the stress at the interface between the native and simulated necrotic bone.

In addition to evaluating the stiffness of each construct, an interface-based risk-scoring algorithm for quantifying the severity of the effect of this variation was developed. This was a novel approach to assessing the risk of disease progression that characterised both the magnitude of the stress discontinuity at the lesion boundary and the size of the region most severely affected and has the potential to improve fracture prediction clinically.

Parametric studies were used to computationally characterise the effect of material properties, lesion location and the interface simulating the lesion boundary on the stiffness of the disease model construct. Two-dimensional models were used because the most efficient evaluation workflow in a clinical setting would be to derive the simulations directly from 2D image data rather than require segmentation of 3D medical images.

These studies provided a detailed understanding of the sensitivity of the risk score and supported the overall aim to develop 2D methodology for evaluating patient-specific simulations.

All models were constructed using continuous plane stress four node reduced integration (CPS4R) elements using Abaqus version 6.11-1 (Dassault Systemes Simulia Corp. Providence, RI, USA). These are four-node bilinear elements with reduced integration and hourglass-control. A plain stress approach was used as the 2D simulations represented a three dimensional body that did not have a uniform cross-section.

The head components were modelled as shown in Figure 38 and assigned a linear elastic modulus of 300MPa. No information exists on the anisotropic behaviour of necrotic bone and, given the structural changes that occur, the properties derived for healthy bone surrounding the lesion cannot be assumed to remain valid. An elastic modulus of 300MPa was chosen to have a similar magnitude to the experimental results for bone taken from porcine femoral heads. A linear-elastic material model that did not account for visco-elasticity was used because of the quasi-static test methodology used to generate the experimental data. The chord was pinned in the initial time step to represent contact with the lower platen to represent the constraint applied in the experimental disease model. A displacement of 0.5mm was applied to the upper surface of the platen during the first time step. This approach was intended to approximate the standing JRF as a load aligned to the long axis of the femur. While this may not represent the true load case for a particular pathology, the relationship between the JRF and lesion geometry remains feasible within the wider population.

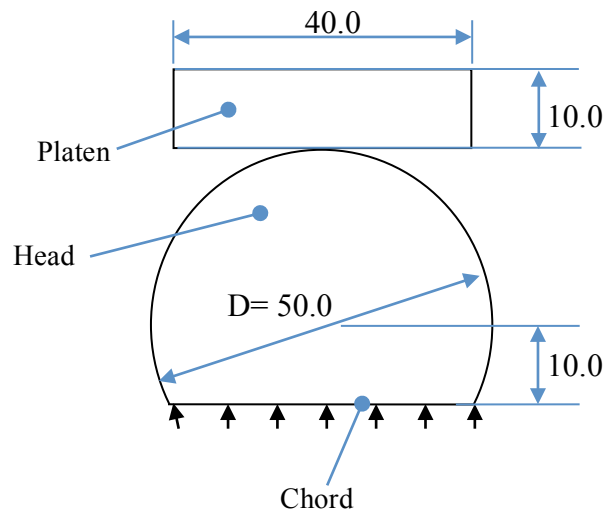


Figure 38. Schematic representation of the head and platen. The head was modelled as a 50mm diameter circular body with a chord located 10mm inferior to the equator. The platen was modelled as a 40mm x 10mm rectangle. The chord was pinned in the initial time step; a displacement of 0.5mm was applied to the upper surface of the platen during the first time step.

The interface between the head and platen was modelled as surface to surface contact with small sliding, hard normal contact and tangential movement governed by a penalty friction coefficient of 1.0. The platen was assigned as the master surfaces in the contact pair. Adjustment was allowed only to correct over closure but separation was allowed after contact. A high friction interface condition was chosen to replicate the physical test, representing contact between the dry subchondral bone and the matt-finished surface of the platen.

3.2.2 Mesh resolution optimisation

Introduction

The purpose of the mesh resolution study was to identify the effect of mesh density (or mean element edge length) on the outcome measures. The aim was to identify a mesh structure that was as coarse as possible to facilitate the use of a continuum material model but which provided a similar outcome to a finer mesh in terms of stress magnitude.

Method

No lesion was simulated in this study and the same geometry and material properties, representing a 50mm diameter femoral head with an elastic modulus of 300MPa were used throughout. The five cases evaluated are summarised in Table 17. The target element edge length was defined as the coarsest mesh that gave results within 5% of the more refined meshes.

Table 16. Case list for mesh optimisation study. Five models with the same geometry (Figure 38) and material properties were generated.

Study	Case name	Head diameter (mm)	Target element edge length (mm)		Elastic modulus (MPa)
			On head	On platen	
Mesh optimisation	Model 1	50	1.0	4.0	300
	Model 2		0.5	4.0	
	Model 3		0.25	4.0	
	Model 4		0.125	0.5	
	Model 5		0.125	0.125	

The peak von Mises (VM) stress and elastic modulus derived from the reaction force were used as outcome measures. The former was used to establish when the result was no longer significantly influenced by element size; the latter was not used to evaluate mesh convergence but allowed the difference between the input elastic modulus and the derived elastic modulus to be established.

The first three models evaluated the effect of reducing target element edge length in the head while maintaining a coarse mesh in the platen. Model convergence failed when the target element edge length in the head was reduced to 0.125 mm with a 4mm target edge length on the platen so the fourth and fifth models were run with more refined meshes on the platen.

The outcome of this study defined the target maximum element edge length for the head and platen for all subsequent studies.

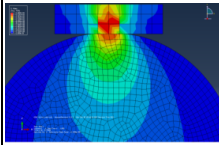
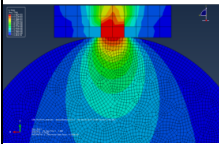
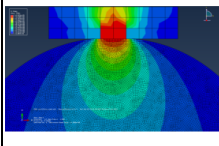
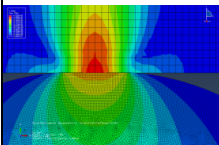
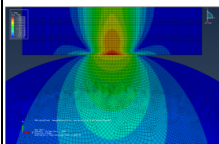
Results

The sum of the reaction force (RF) at the pinned boundary was equal to the force applied by the platen. The least refined mesh (Model 1) had a significantly higher reaction force than the other models indicating that the results of this model were skewed by the mesh parameters. The distribution of VM stress in each model is shown in Table 17; the peak VM stress is summarised in Figure 39.

The mean RF value of all cases (except model 1) was 74.71N with a total range, expressed as a percentage of the mean of 0.21%; the standard deviation was 0.07N (0.1%). The RF value was consistent over the range of mesh densities because it was a gross measure of the elasticity of the material and the effect of any anomalies in the contact region were averaged out. The peak VM stress in the head was more sensitive to element size as it was affected by local stress concentrations caused by element geometry. Excluding model 1, the mean peak VM stress was 16.1MPa with a total range, expressed as a percentage of the mean of 5%; the standard deviation was 0.36 (2.2%).

The mean elastic modulus of the head component in models 2 to 5 was calculated to be 264MPa: 35.6MPa or 12% lower than the input elastic modulus. They were all considered to provide suitable configurations for future model development.

Table 17. Qualitative and quantitative results of the two dimensional mesh convergence study using a 25mm diameter head. The boundary reaction force RF and peak von Mises stress in the head (VM peak) were extracted from the solved models.

Case			Data from model		Derived outputs		Elastic modulus (MPa)
	Target element edge length (mm)	Qualitative	RF (N)	VM peak (MPa)	Contact radius (mm)	Approach of centers (mm)	
1	1 (platen edge length 4mm)		75.4	15.5	2.83	0.5	265
2	0.5 (platen edge length 4mm)		74.6	15.6	2.73	0.5	281
3	0.25 (platen edge length 4mm)		74.8	16.0	2.75	0.5	278
4	0.125 (platen edge length 0.5mm)		74.8	16.4	2.76	0.5	276
5	0.125 (platen edge length 0.125mm)		74.7	16.3	2.75	0.5	277

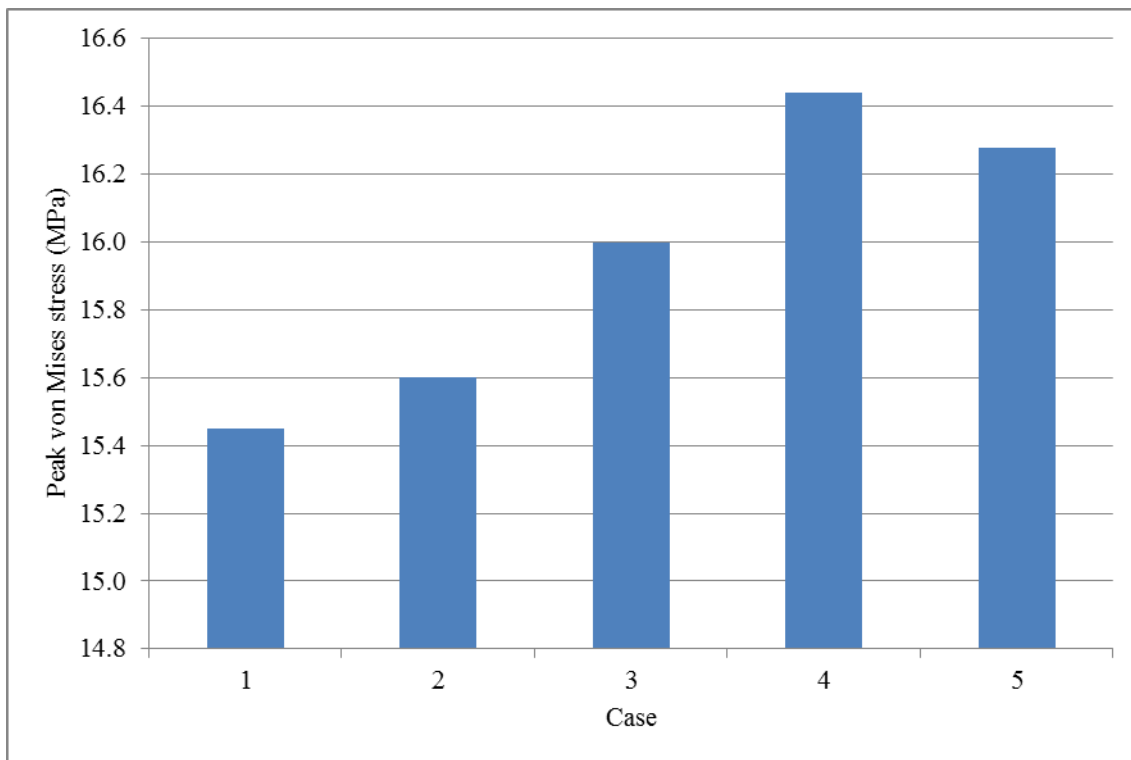


Figure 39. Plot of peak VM stress for each model described in table 16. Excluding the first model, the mean was 16.08MPa and (Range 15.6-16.4MPa, standard deviation 0.37MPa. Simulation parameters are described in Table 15 and Section 3.2.1.

Discussion

Choosing an element length was a compromise between achieving sufficient accuracy and using computational resource efficiently. The peak VM stress in the model using a 0.5mm average element length (model 2) was less than 5% lower than in the higher resolution models that used a 0.25mm or 0.125mm average element length (models 3-5). The differences between them are attributable to the relatively coarse mesh used for the platen: The addition of one or two elements to the contact region represents a significant change in the contact area. The difference between the coarse and fine meshes could also be a function of the stiffening effect of using a very fine mesh on a relatively large structure. Using a relatively coarse mesh facilitated the use of continuum material properties and the avoidance of the potential stiffening effect attributed to very fine meshes.

3.2.3 Interface study

Introduction

One aim of this study was to establish a standard approach to defining the interface between the two bodies in subsequent studies. The second aim was to identify the impact that the interface conditions had on the construct. This helped to define the simulation strategy but also provided an insight into the difference in behaviour between the experimental disease model where a friction interface existed and the clinical scenario where a continuum between the two bodies exists.

In the experimental disease model there was an interference fit between the plug and native bone. This held the plug of bone inside the femoral head securely but the coefficient of friction was not quantified experimentally. Therefore it was necessary to evaluate a range of friction coefficients to understand the sensitivity of the simulation to this parameter.

Once the effect of mesh density had been established, the model was adapted to include a plug of material with properties defined independently from the head component. Further mesh convergence was not required as the strains at the boundary were less than the strains in the contact region. As the model was loaded under displacement control, the strains in the contact region were the same as those evaluated in the original mesh convergence study.

The same boundary conditions were used as in the previous study (Section 3.2.2) when the design of the interface between the plug and head was investigated. Nodal alignment and the difference between using a tied interface and a friction interface were evaluated. The former was representative of the continuum between healthy bone and the necrotic lesion in patients' femoral heads. The latter was more representative of the experimental disease model where an interference fit existed between the native and substituted bone. Two material property combinations were evaluated: one where the head and plug had the same modulus and one where the materials were defined separately.

The first three cases in this study isolated the effect of the interface on the outcome measures by maintaining homogeneity between the head and plug bodies while varying the interface conditions as described in Table 18. The hypothesis that a tied interface would give the same outcome as a solid model and that a reduction in friction coefficient at the interface between the head and plug would reduce the overall stiffness was posed. The remaining cases varied the friction coefficient to gauge its influence on outcome.

This study identified the influence that the characteristics of the interface had on the outcome. This was investigated further in the parametric study (Section 3.3).

Table 18. Case list for the interface study. Four models were generated during the preliminary interface study. Sixteen models with varying head modulus, plug modulus, and interface conditions were generated

Study	Case name	Head modulus (MPa)	Plug modulus (MPa)	Interface conditions	Plug eccentricity	Plug depth beneath apex (mm)
Preliminary interface study	Solid	300		n/a	n/a	n/a
	Tied / Aligned nodes			Tied	Central	5mm
	Tied / Misaligned nodes			Tied		
	Homogenous, friction interface $\mu=1.0$ / misaligned nodes			Friction $\mu=1.0$		
Friction interface study	Homogenous, friction interface $\mu=0.8$	300		Friction $\mu=0.8$		
	Homogenous, friction interface $\mu=0.6$			Friction $\mu=0.6$		
	Homogenous, friction interface $\mu=0.4$			Friction $\mu=0.4$		
	Homogenous, friction interface $\mu=0.2$			Friction $\mu=0.2$		
	Homogenous, friction interface $\mu=0.01$			Friction $\mu=0.01$		
	Inhomogenous, friction interface $\mu=1.0$			300	150	Friction $\mu=1.0$
Friction interface study (continued)	Inhomogenous, friction interface $\mu=0.8$			Friction $\mu=0.8$		
	Inhomogenous, friction interface $\mu=0.6$			Friction $\mu=0.6$		
	Inhomogenous, friction interface $\mu=0.4$			Friction $\mu=0.4$		
	Inhomogenous, friction interface $\mu=0.2$			Friction $\mu=0.2$		
	Inhomogenous, friction interface $\mu=0.01$			Friction $\mu=0.01$		

Table 18 continued.

Study	Case name	Head modulus (MPa)	Plug modulus (MPa)	Interface conditions	Plug eccentricity	Plug depth beneath apex (mm)
Friction interface study (continued)	Inhomogenous, friction interface $\mu=0.8$	300	150	Friction $\mu=0.8$	Central	5mm
	Inhomogenous, friction interface $\mu=0.6$			Friction $\mu=0.6$		
	Inhomogenous, friction interface $\mu=0.4$			Friction $\mu=0.4$		
	Inhomogenous, friction interface $\mu=0.2$			Friction $\mu=0.2$		
	Inhomogenous, friction interface $\mu=0.01$			Friction $\mu=0.01$		

Method

The design for the disease model and control are shown in Figure 40. The head and platen were modelled in the same way as described in Section 3.2.2 including assignment of boundary conditions and loading under displacement control. The plug was modelled with a diameter of 10mm and a domed superior end with a radius of 8.5mm. The head and plug were both assigned a modulus of 300MPa in the initial phase of the study. This allowed direct comparison to the results reported in the mesh optimisation study (Section 3.2.2). The plug modulus was then reduced to 150MPa to make the construct more representative of the experimental disease model.

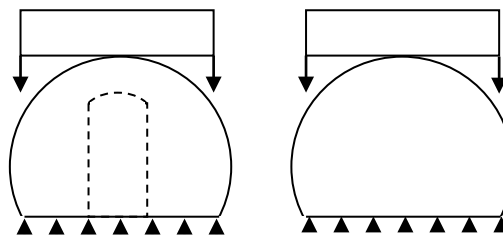


Figure 40. Left: Disease model design. The dotted line represents the boundary between the plug and head. This was either represented as a friction interface or by a tied constraint. To evaluate the effect of the boundary condition, both the head and plug were assigned a modulus of 300MPa. Right: Control model design.

A 0.5mm mesh was used in both models and the inferior edge was pinned to represent the experimental model and allow direct comparison to the results reported previously. For the preliminary interface study, the tied constraint model and friction model were constructed with two mesh orientations: one with nodes aligned at the top of the plug and one with nodes misaligned as shown in Figure 41. In the friction model, tangential movement at the boundary

was governed by penalty friction with a co-efficient of 1.0; normal behaviour was defined as hard contact.

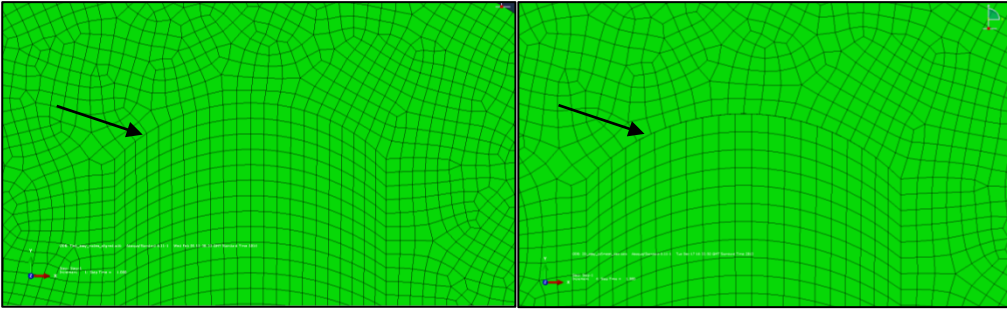


Figure 41. Mesh detail at the interface between the plug and head at the top of the plug. The arrows point to the boundary. Left: the edge was seeded to align the nodes along the contact surface; Right, the nodes were misaligned.

Results

The results are summarised in Table 20 and presented qualitatively in Figure 42. The tied model closely matched the results of the solid model regardless of mesh alignment at the interface. Comparing the tied interface model to the solid model, the reaction force and modulus increased by 1.8%; peak von Mises stress increased by 2.5%. Small discontinuities caused by nodal misalignment in the stress field were evident in the superior surface of the friction interface.

Changing the interface conditions from tied to friction resulted in a 13% reduction in reaction force and elastic modulus compared to a tied interface model. The peak VM stress increased by 4.3% in the friction model compared to the tied model.

Altering the coefficient of friction made no difference to the elastic modulus or peak VM stress therefore only one value for the friction interface is reported.

A friction constraint allowed separation of the two surfaces in contact caused by bending of the material above the plug. This provided an indication of where both tensile (splitting the interface) and compressive failure may occur. This splitting effect along the boundary extended approximately 80% down the edge of the plug (Figure 43). The actual magnitude, which was a function of the applied Poisson's ratio, was small. The absolute separation of nodes along the interface was 0.1mm or less.

The reduction in elastic modulus was attributed to the fact that the friction interface did not allow generation of tensile stress at the plug-head interface: the surfaces were allowed to separate after contact. Deformation of the material superior to the plug also reduced the width of the plug in direct contact with the head, reducing the width over which load was transferred from 10mm to approximately 7mm.

Perhaps the most relevant outcome of this study was identification of a (compressive) stress concentration and large stress gradient at the superior corners of the interface in the friction constraint model. The area of peak compression in the head corresponded to the location of cracks found in gross sections of the *in vitro* disease models (Figure 34). The outer surface of the interface was in compression with a VM stress of around 8.5MPa. The inner surface was under negligible stress (Figure 44).

Table 19. The effect that the boundary conditions between the head and plug had on the stress and elastic modulus. In this table, a solid, homogenous model with $E=300\text{MPa}$ was compared to a disease model where the head and plug both had $E=300\text{MPa}$. The tied constraint resulted in a very close approximation to the solid model. Replacing the tied constraint with a friction condition significantly reduced boundary reaction force and modulus. The peak von Mises stress increases slightly.

Model	Reaction force (N)	von Mises peak stress (MPa)	Elastic modulus (MPa)
Solid	74.6	15.6	264
Tied / Aligned nodes	75.9	16.1	269
Tied / Misaligned nodes	76.0	16.1	269
Friction interface / Misaligned nodes	66.0	16.3	233

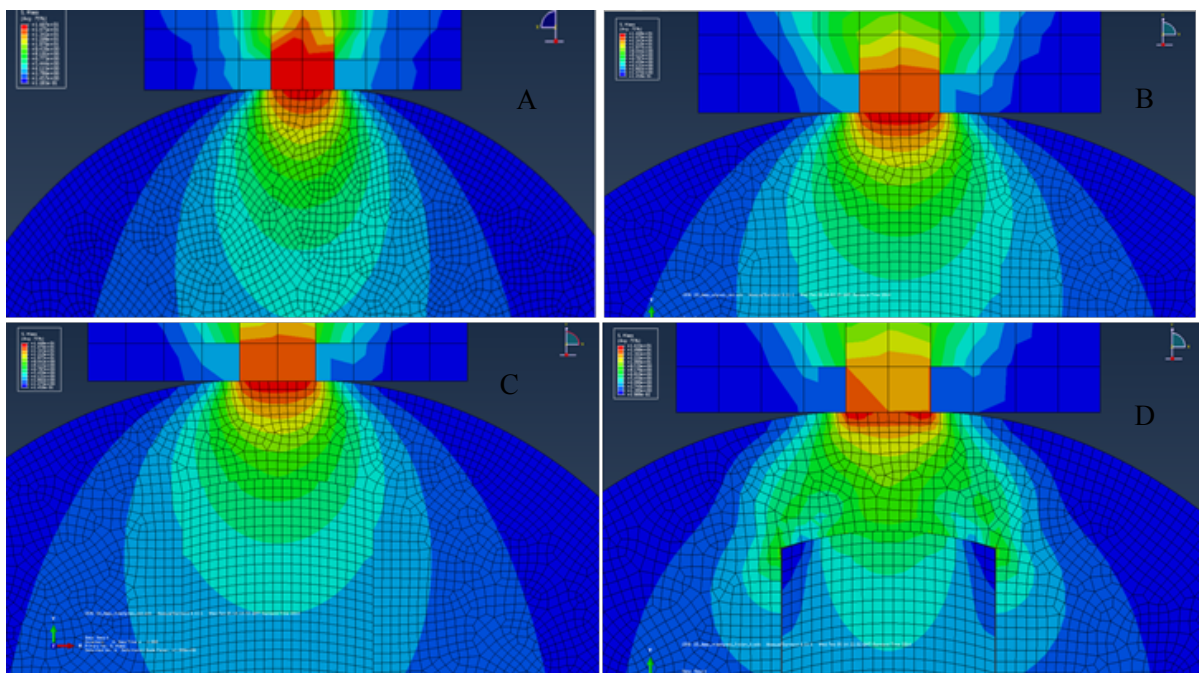


Figure 42. Qualitative comparison of the effect of altering the boundary condition between the plug and head. Top left: A solid homogenous model used as a benchmark; Top right: A head-plug assembly with tied contact and an aligned mesh. Bottom left: a head-plug assembly with tied contact and a misaligned mesh; Bottom right: A head-plug assembly with a friction interface and misaligned mesh.

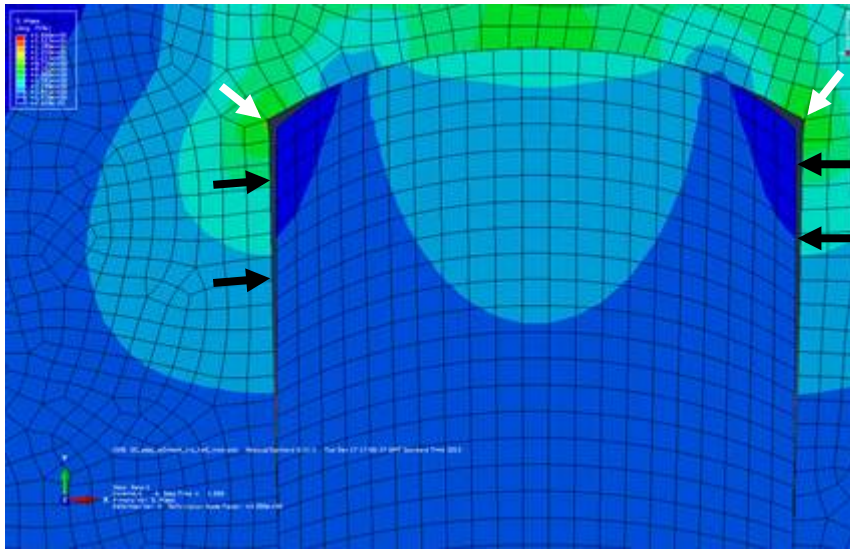


Figure 43. Example of a simplified disease model with a friction interface in its deformed state (Case four in the interface study, Table 18). The black arrows indicate separation of the interface; the white arrows indicate areas that could fail in compression. The splitting effect extended along approximately 80% of the length of the plug.

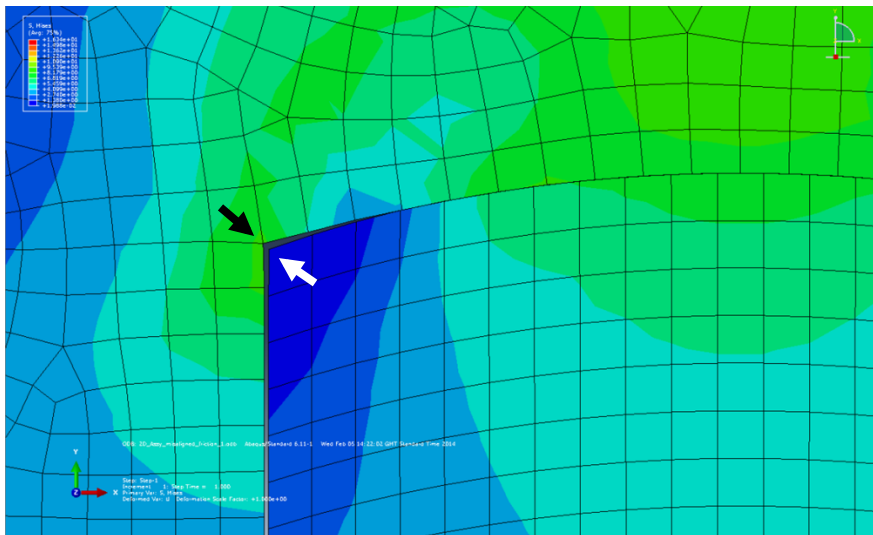


Figure 44. Close up view of the superior corner of the head-plug boundary with a friction-based interaction after deformation. The element edge length is approximately 0.5mm and it is clear that approximately three elements (1.5mm) on each side of the superior surface are not in contact, reducing the effective width of the plug to 7mm (applying symmetry). This helped to explain the reduction in elastic modulus. The von Mises stress at the element indicated by the black arrow was approximately 8.5MPa; at the white arrow it was less than 0.1MPa.

Discussion

A tied boundary was expected to give similar results to the solid model as the nodes at the boundary were constrained to move together and this was shown to be the case. A friction interface allowed the head and plug components to move independently: One surface deformed more than the other and also allowed the two surfaces to separate as demonstrated in Figure 45. Thus the elastic modulus of a construct that used a friction constraint was lower than the solid model.

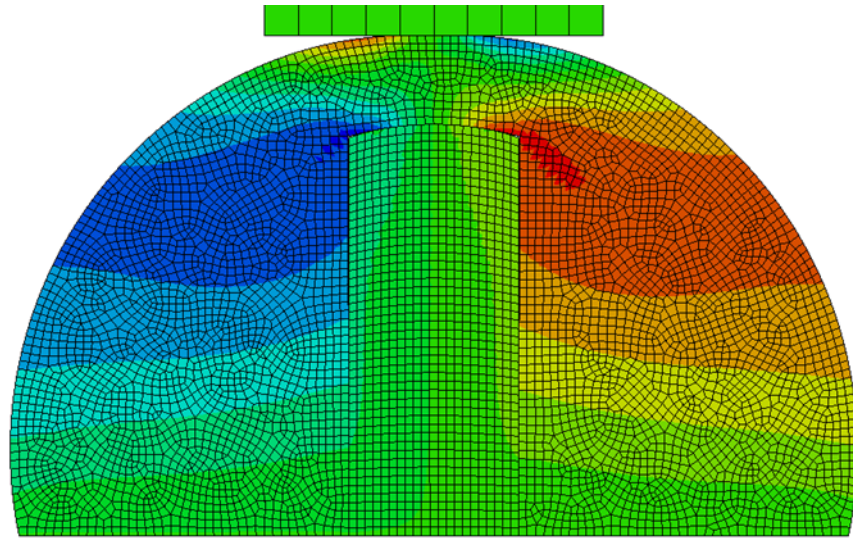


Figure 45. Plot of horizontal displacement caused by vertical compression of the head with a flat platen. The blue colour indicates displacement towards the left of the image; the red colour indicates displacement to the right of the image. Displacement was symmetrical and the head was displaced to a greater extent than the plug.

The difference in outcome measures between the tied models with aligned and misaligned meshes was negligible. However, some discontinuities were visible at the superior interface in the friction interface model with the misaligned mesh so an aligned mesh was used in all future models at the lesion-femur interface and platen-head interface. It was hypothesised that there would be no difference between a homogenous solid model and a homogenous head-plug assembly with a tied boundary constraint. The difference in elastic modulus between the tied and solid simulations was 1.8% compared to 11.7% when a friction interface was compared to the solid model.

3.2.4 Definition of measures and outputs

Introduction

During the experimental investigation described in Chapter 2, the elastic modulus of the experimental disease models and controls was calculated using a Hertzian analytical solution for linear elastic contact between the rigid platen and deformable femoral head. An approach based on the same principle was used during the first two studies described in this chapter (Sections 3.2.2 and 3.2.3) to establish an elastic modulus for the construct (as differentiated from the elastic modulus of the individual materials). The elastic modulus was calculated from the reaction force in the FE simulation and can thus be described as a secondary or derivative measure. The VM stress, a direct measure, was extracted directly from within the region of contact between the head and platen.

In Chapter 4, the transition from hard contact between a rigid platen and the femoral head to conforming contact between the two bodies is described. This was developed with the intention of transmitting a more distributed load onto the surface of the femoral head. This approach negated the use of a Hertzian contact-based measure and so another derivative outcome was developed to allow comparison between simulations. The aim during development of the new outcome measure was to quantify the impact that changes to lesion orientation, material properties and geometry had on stress distribution within the femoral head at the lesion boundary and by implication the risk of an adverse outcome such as fracture or remodelling for each case within a study. The term “relative risk” (RR) is used throughout the following chapters to reinforce the fact that this outcome allowed different cases within each study to be ranked, but was not intended to quantify absolute risk of failure.

It is important to consider the physical size of stress concentrations within the bone structure and the impact that they will have. Small regions of high stress could indicate regions where individual trabeculae are most likely to yield or be subjected to strain adaptive remodelling but the effect would be limited to a small region because failure of a small number of trabeculae will restore equilibrium in the surrounding bone (Prendergast and Taylor, 1994). In comparison, a region of high stress that also affects a large area represents a higher risk of gross structural failure. On this basis, the RR score was defined as the mean stress in the region identified multiplied by the number of elements. This produced a single number that quantified the physical size of the disrupted stress field as well as the magnitude of the stress. By considering both parameters, the score accommodated two possible failure scenarios:

1. Geometrically small but highly stressed regions where mechanical failure of individual trabeculae could manifest as cumulative fracture or local remodelling (Pugh *et al.*, 1973).

2. Relatively large areas of elevated stress or disruptions in the stress field are less likely to be subject to acute failures but are possible sites of bone remodelling.

The number of elements was used in the risk score as a measure of length because the element edge length was constant throughout each study and conversion to a unit of length offered no improvement to the resolution or understanding of the proposed outcome measure. While this approach was an efficient way to evaluate the concept, it is acknowledged that conversion to units of length would improve the usability of the measure if it proved viable.

The relationship between elastic modulus and the RR score was evaluated in the multivariate parametric study described introduced in Section 3.3. The RR score was used exclusively for all studies thereafter.

Method: Estimation of elastic modulus using a Hertzian contact approach

The contact radius and approach of centres were derived from the RF value which is equal to the force transferred from the platen to the top of the head and equates to the force per unit length used in the two dimensional Hertzian equations for line contact (Equation 7 and Equation 8).

Equation 7: Hertzian contact radius, a , for line contact where P' is the force per unit length, R is the effective curvature (Equation 3) and E^* is the contact modulus (Equation 1). Note that E^* was related back to E_1 using Equation 2.

$$a = 2 \left(\frac{P'R}{\pi E^*} \right)^{\frac{1}{2}}$$

Equation 8. Approach of centres for line contact. P' is the force per unit length, E was the Young's modulus for each body (the head was body 1, the platen was body 2), ν is Poisson's ratio for each body and R_x is the contact radius of each body. As E_2 was very large compared to E_1 the second half of the function tended to zero.

$$\delta = \frac{2P'}{E_1} \left[\frac{1 - \nu_1^2}{E_1} \left(\ln \frac{4R_1}{a} - \frac{1}{2} \right) + \frac{1 - \nu_2^2}{E_2} \left(\ln \frac{4R_2}{a} - \frac{1}{2} \right) \right]$$

As the models were loaded under displacement control, δ was a known constant of 0.5mm. P' was equated to the summed vertical RF and the value for E_1 that gave the correct relationship between δ and P' was derived iteratively by minimising the error between the applied δ and that derived from P' and E_1 using least-squares regression.

Method: Relative risk score

Development of this score was carried out in parallel with the multivariate analysis introduced in Section 3.3.2. Elastic modulus does not in isolation provide a useful measure of the risk of femoral head fracture. The experimental data showed that there was large variation in material properties between samples. Also, bone fracture occurred in specific locations within the femoral head and although these may be strain mediated (strain increases with reducing modulus for a consistent load); local geometry still played a significant role.

There was a need therefore to define a risk score that would allow simulations with different geometries and material properties to be evaluated. To fulfil this need, the risk score was required to meet two criteria:

1. It should be applicable to all geometries from the simple experimental disease model where the head was compressed by a flat platen (i.e. Hertzian contact) to patient-specific models where load was applied through a conforming contact and the surface of the lesion had an organic form.
2. Its magnitude should not be dictated by a single factor but should be affected by both material properties and geometry.

As there is no detailed material model for necrotic bone, comparing absolute measures of stress and strain to a material failure threshold would be unreliable. A more appropriate approach would be to evaluate the risk of failure by quantifying regions of elevated stress caused by the presence of a lesion within the femoral head. It was highlighted by Motomura *et al.*, 2011 that fractures may occur as a result of stress concentrations at the lesion boundary suggesting that these regions should be a focus for the investigation. It is important to consider both the magnitude and physical size of stress concentrations within the bone structure and the impact that they will have. Small regions of high stress could indicate regions where individual trabeculae are most likely to yield or be subjected to strain adaptive remodelling but the effect would be limited to a small region because failure of a small number of trabeculae will restore equilibrium in the surrounding bone (Prendergast and Taylor, 1994). In comparison, a region of high stress that also affects a large area represents a higher risk of gross structural failure.

Although elastic modulus fulfilled requirement two, it relied on an approximation to Hertzian contact and could not be used where load was applied through a conforming surface. In contrast, peak VM stress, which always occurred in the region of contact between the platen and femoral head, was governed predominantly by the head modulus so it failed the second requirement.

The magnitude of the stress at the head-plug interface was sensitive to both plug location and the material properties and, as clinical failure tends to occur in this region (Motomura *et al.*, 2011), it was also a physiologically relevant response.

To facilitate evaluation of the stress at the interface, the element values of VM stress for each element pair around the boundary were exported from Abaqus into Excel (Microsoft, Redmond, WA, USA) using a Python (Python Software Foundation, DE, USA) script². The purpose of the

² The requirements for the Python script were defined by the author; the script itself was written by Dr. Sebastian Sekora, University of Leeds, UK.

script was to order the element pairs in terms of their geometric location (Figure 46) rather than by element number or stress magnitude and export the VM stress values.

To achieve this, two element sets defining the inner and outer surfaces were created. The terms “inner” and “outer” will be used henceforth to describe these sets. Starting with the seeding element (by default, the element furthest to the left/bottom in the outer set, as shown in Figure 46) the Python script iteratively identified neighbouring elements within the outer set and converted their order from numerical by stress magnitude to a geometric sequence. It then identified the closest element from the inner set to each element in the outer set by searching for the element pair whose centres were closest. A tolerance of no greater than half the target element edge length was used to restrict the search and avoid multiple elements from the inner set being assigned to one element from the outer set. The script output a comma-separated variables table containing five columns: Outer element identity (ID), outer element VM stress (A), inner element ID, inner element VM stress (B) and stress difference (A-B). Stress difference was calculated for each element pair in sequence.

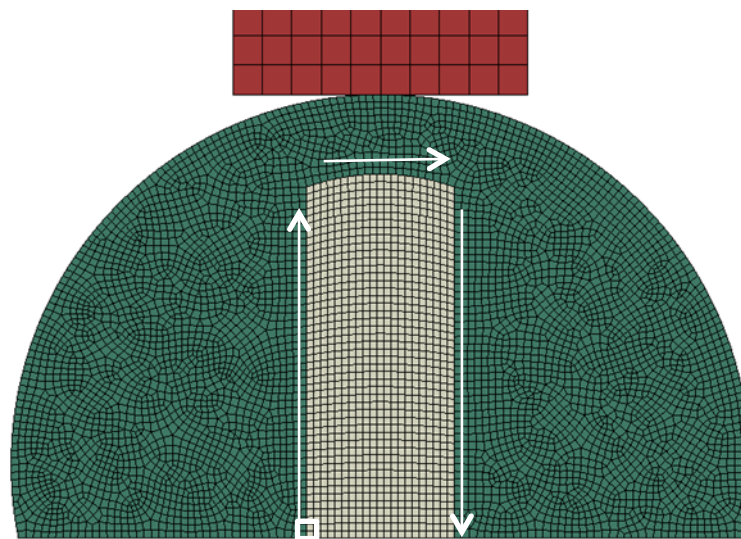


Figure 46. Schematic illustrating the path that values were taken from using of the Python script for one model. The Python script output a geometrically ordered array of VM stress values for each element in the inner and outer surface, starting at the bottom left element pair (white box) and following a clockwise path around the surfaces.

Once exported into Excel, the variation in stress magnitude around the inner and outer surfaces and the difference between the two surfaces at each location were plotted.

To quantify the physical length of the region of highest stress, a threshold value T , equating to 80% of the maximum stress value in each surface or 80% of the maximum difference was used to isolate a number of elements in the region of the highest stress or difference (Equation 9).

Equation 9: The model-specific threshold (T) was defined as 80% of the maximum stress in either the inner or outer surface of that model, or the maximum difference between element pairs.

$$T = 0.8 \times \text{Maximum stress (difference)}$$

The limit of 80% of the maximum stress was chosen by evaluating the results of the multivariate analysis (Section 3.3.2). This threshold identified a minimum of two elements (approximately 1mm) on each surface in the models generated as part of the multivariate analysis.

In models with symmetrical geometry, inclusion of the entire surface in the calculation identified two distinct regions of interest in symmetrical models. In the asymmetric models only one region of interest was ever identified. To remove the artificial doubling of the RR score in symmetrical models, only one side of each surface was included and by design the same number of elements was included in each analysis. The side included in the analysis was chosen to include the most highly stressed region of the surface.

Multiplying the number of elements above the model-specific threshold value by the mean VM stress magnitude for these elements quantified the magnitude and physical size of a stress concentration. This could be defined as a response in the context of the outer and inner surfaces, or the difference between the two.

The RR score for the difference between the two surfaces had greater versatility because it identified both the magnitude and which side of the surface was most the highly stressed: A negative value indicated that the stress on the plug side was higher than on the healthy bone side. The different definitions of relative risk are summarised in Table 20.

Table 20. Abbreviations used to identify the context of the relative risk value calculated .

Response	Abbreviation
Relative Risk calculated for the outer surface	RR _O
Relative Risk calculated for the inner surface	RR _I
Relative Risk calculated for difference between the two surfaces	RR _D

Results

Very distinct stress concentrations such as are apparent in the plot in Figure 47 (bottom) manifest as a small number of elements above the threshold. Flatter profiles were characterised by the identification of a larger number of elements above the threshold (Figure 47 (top)). The number of elements above the threshold value identified for each surface in the study described in Section 3.3.2 are summarised in Table 21.

Typical examples of the resultant plots and physical representation for symmetrical and asymmetrical models are shown in Figure 47. This method allows a comparison of the length of a discontinuity in the stress field but had to be used in conjunction with the magnitude of the stress in each model to give an estimate of relative risk.

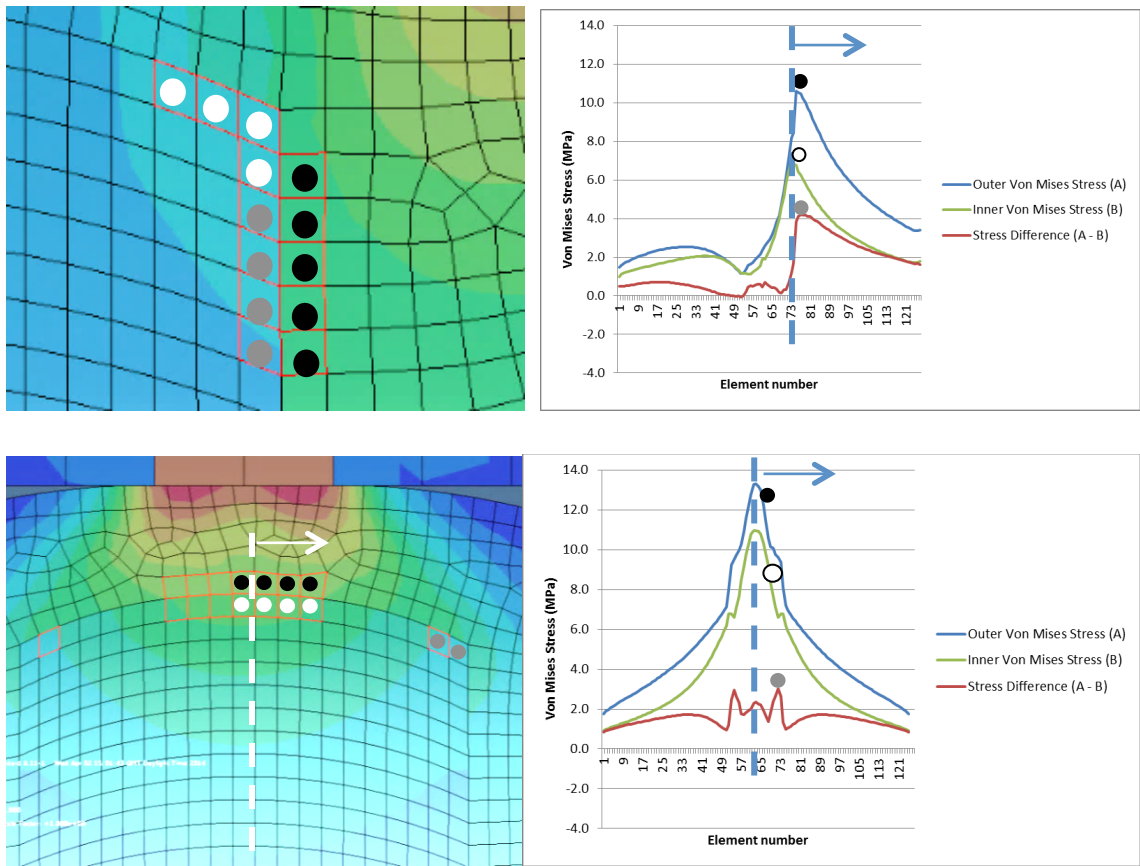


Figure 47. Examples of the variation in stress around the outer surface and inner surface, and the difference between the two surfaces. Top: an eccentric plug position; Bottom a concentric plug position. In the plots, the origin of the x-axis equates to the bottom left element at the interface with progression clockwise around the interface represented along the x-axis. Only the data to the right of the broken lines was included in the analysis. The region of stress above the threshold in the outer surface is identified using black circles; the region of stress above the threshold in the inner surface is identified using white circles and the region where the stress difference was above the threshold is identified using grey circles. Note that the location of maximum difference did not necessarily equate to the location of maximum stress in either surface.

Table 21. Descriptive statistics showing the number of elements identified above the threshold value for each surface), and for the difference between each surface in the models constructed during the multivariate analysis (Section 3.3.2).

Statistic	Number of elements		
	Outer surface	Inner surface	Difference between surfaces
Minimum	3	2	2
Mean	7.7	7	15.8
Median	7.5	7.5	15
Maximum	16	10	33

Discussion

Distinct stress concentrations were manifest in several model configurations. While such singularities could indicate regions where individual trabeculae were most likely to yield, or be subjected to strain adaptive remodelling, the effect would be limited to a small region because failure of a small number of trabeculae will restore equilibrium in the surrounding bone (Prendergast and Taylor, 1994). In comparison, a region of high stress that also affects a large area represents a higher risk of gross structural failure. It is noted that this phenomenon relates to healthy bone and the micro-structural properties of bone at the lesion boundary are less well defined. However, the same argument can be made for discontinuities in the stress field: very small discontinuities are unlikely to be physiologically relevant and large ones more are likely to represent regions where bone remodelling takes place. Therefore a response that was a function of both the stress magnitude and the physical length of the peak was developed. The proposed relative risk score used the number of elements as a surrogate for a unit of length. This was an acceptable approach in the current study as the same element edge length was maintained throughout each study. However, conversion to a unit of length would disambiguate the score and make it robust to the changes to modelling methodology that may become necessary if a multi-scale approach is developed in the future.

3.3 Parametric study

The purpose of this study was to evaluate the effect on the elastic modulus and relative risk scores of changing the stiffness of the plug and the location of the plug within the head.

Finite element simulations were created using simplified geometry that was representative of the experimental disease models. The target mesh densities for the head, plug and platen identified in the mesh optimisation study were used; both tied and friction interfaces were evaluated to build on the knowledge gained in the interface study.

The parametric study was split into two parts, a parametric sweep and a multivariate analysis. The purpose of the parametric sweep was to understand the direction of change induced by each variable and to identify boundaries for the factors used in the multivariate analysis. The multivariate analysis allowed interactions between the factors to be evaluated systematically.

3.3.1 Parametric sweep

Introduction

The plug modulus and interface conditions were varied for three different geometry cases (A, B and C, Figure 48). Simulations using all three geometry models were executed using tied boundary conditions and with different coefficients of friction at the interface between the head and plug. The case list is summarised in Table 22.

This study showed that there was a consistent relationship between the results derived for simulations with a tied interface and a friction interface meaning that only one interface need be used for subsequent studies. As the ultimate goal of the investigation was to evaluate patient-specific studies where the healthy bone – lesion boundary is a continuum, all subsequent studies employed a tied interface.

This study also confirmed that the modulus and position of the plug within the head influenced the outcome measure and that all three factors should be considered in the multivariate analysis.

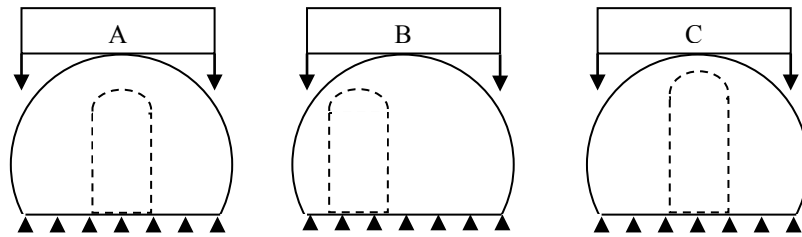


Figure 48: Schematic representation of the three geometry models used to evaluate the effect of plug position. A: concentric plug 5mm below the apex, B: eccentric plug 5mm below the apex and C: concentric plug 2.5mm below the apex.

Table 22. Case list for the single variable analysis study. Three separate evaluations were performed. In each case the geometry model was analysed with six different plug moduli and with both tied and friction head-plug interfaces.

Study	Case	Head modulus (MPa)	Plug Modulus (MPa)	Head-plug interface	Plug horizontal location	Plug depth beneath the apex
Single variable analysis: Concentric plug (Model A)	Tied interface	300	200; 150; 100; 50; 1. N.B. the 300MPa case was executed in the interface study	Tied	Central	5mm
	Penalty friction interface	300	200; 150; 100; 50; 1. N.B. the 300MPa case was executed in the interface study	Penalty Friction $\mu=1$	Central	5mm
Single variable analysis: Eccentric plug (Model B)	2.5mm lateral offset, friction interface	300	300; 200; 150; 100; 50; 1.	Penalty Friction $\mu=1$	2.5mm eccentric	5mm
	2.5mm lateral offset, tied interface	300	300; 200; 150; 100; 50; 1.	Tied	2.5mm eccentric	5mm
Single variable analysis: Reduced depth beneath the apex. (Model C)	2.5mm medialised, friction	300	300; 200; 150; 100; 50; 1.	Penalty Friction $\mu=1$	Central	2.5mm
	2.5mm medialised, tied	300	300; 200; 150; 100; 50; 1.	Tied	Central	2.5mm

Method

All three geometry models were run with lesion moduli of 300MPa (this was the original model configuration run in the previous study), 200MPa, 150MPa, 100MPa, 50MPa and 1MPa (described in Table 22). The latter was intended to replicate an empty lesion without changing the assembly. The model geometry was as described in Section 3.2.3.

3.3.2 Multivariate analysis

Introduction

The parametric sweep described in Section 3.3.1 highlighted interactions between lesion position and material properties. A design of experiments (DoE) based parametric study (refer to Appendix C for a description of this methodology) was performed to identify interactions between the individual factors.

In the experimental disease models, the mean horizontal offset between the centre of load application and the centre of the plug was 1.4mm (S.D. 1.9mm, range 0-4mm). The mean depth below the apex of the head was 4.75mm (S.D. 0.89mm, range 4-6mm) and the maximum eccentricity always coincided with a deeper plug position. As the full-factorial design used in this multivariate analysis included all possible combinations of position, the ranges for eccentricity and depth beneath the apex were limited to ensure that the plug did not penetrate that surface of the femoral head. The range of horizontal and vertical positions was therefore smaller than that measured in the experimental disease models, dictating the need for a follow-on study to generate experimental disease model-specific geometries.

The final experimental design is summarised in the case list in Table 23. A full factorial DoE matrix was developed and the levels chosen based on the experimental disease models evaluated in Chapter 2. In this design, every possible permutation of the four factors (head modulus, plug modulus, plug horizontal location and plug depth beneath the apex) was tested.

Table 23. Case list for multivariate analysis. The parameters for each case were dictated by a full factorial DoE matrix meaning that every possible combination of the four factors evaluated was tested.

Study	Case	Head Modulus (MPa)	Plug Modulus (MPa)	Plug horizontal location (mm)	Plug depth beneath the apex (mm)
Design of Experiments	1	450	225	0	2.5
	2	450	225	0	5.0
	3	450	225	2.5	2.5
	4	450	225	2.5	5.0
	5	450	75	0	2.5
	6	450	75	0	5.0
	7	450	75	2.5	2.5
	8	450	75	2.5	5.0
	9	150	225	0	2.5
	10	150	225	0	5.0
	11	150	225	2.5	2.5
	12	150	225	2.5	5.0
	13	150	75	0	2.5
	14	150	75	0	5.0
	15	150	75	2.5	2.5
	16	150	75	2.5	5.0

By compiling the results of each test using the DoE methodology, the interactions between the factors were established. Both elastic modulus and RR scores were evaluated as outcomes to allow the difference between the responses to be analysed.

This study highlighted interactions between the factors and confirmed that the trends identified in the single-variable analysis were genuine and not the result of confounding factors. It also demonstrated that the RR score was more sensitive to the factors considered in the models than elastic modulus.

Method

The levels for eccentricity were chosen to be 0mm (concentric) and 2.5mm; the levels for depth beneath the apex at 2.5mm and 5mm (Table 24). The low level for each factor was defined as the one likely to reduce the magnitude of the response based on the results of the parametric sweep study (Section 3.3.1). The combination of a maximum eccentricity of 2.5mm and minimum depth below the apex of 2.5mm resulted in a single thickness shell of elements between the top of the plug and outside of the head. This represented an area of poor mesh geometry because a single thickness of elements cannot adequately represent a beam in bending. However, it maintained a smooth spherical outer surface and as this region was isolated from the centre of load application, it was excluded from the calculation used to establish RR.

The levels for the head and plug modulus were defined using the results of the experimental testing carried out on plugs taken from porcine femoral heads and from bovine lateral epicondyles (Sections 2.2.3 and 2.3.3). A mean head modulus of 300MPa and a mean plug

modulus of 150MPa were defined and a total variation of 100% about these means was used to give sufficient separation between levels (Table 24).

Table 24. Levels for each factor in sensitivity analysis. The factors were chosen because they were likely to influence the response of the *in silico* disease model to an applied load. The levels for the head and plug moduli were chosen based upon the experimental results (Sections 2.2.3 and 2.3.3). Low levels were defined in each case as the level most likely to reduce the magnitude of the response.

Factor	Level	
	Low	High
Head Modulus	150 MPa	450 MPa
Plug Modulus	75 MPa	225 MPa
Plug Lateralisation	2.5 mm	0 mm
Depth beneath the apex	5 mm	2.5 mm

A verification study was performed using linear regression analysis to link the effect of each variable to the elastic modulus and compare the result of the mathematical model to results obtained from the FE simulations. Pearson product-moment correlation coefficient (r) was used to evaluate whether the mathematical and computational results for each case were similar. The closer the correlation coefficient is to one, the greater the correlation between the two sets (Stephen and Hornby, 1997).

3.3.3 Experimental disease model simulations

Introduction

The purpose of this stage of the investigation was to evaluate whether a link between the RR score defined in Section 3.2.4 and the experimental results could be established.

The *in vitro* experimental disease models were constructed from porcine femoral heads by replacing a plug of native bone with a conforming plug of bone taken from the lateral epicondyle of a bovine femur. They were compressed between two flat platens under displacement control to obtain a load-displacement plot. This load condition was re-created in two-dimensional *in silico* simulations and the effect of plug position relative to the load vector and apex of the femoral head, head material properties and plug material properties was evaluated systematically in the parametric study (Section 3.3). This investigation showed that the modulus of the head and plug dominated the elastic modulus of the construct and the RR score associated with each configuration. However, it also highlighted the effect that plug location had on the RR score, with eccentric plugs located close to the surface obtaining the highest score. Geometry and material property-specific models (Table 25) were generated for each of the experimental disease models described in Section 2.4. Geometry was established by direct measurement (Section 2.4.6) and an approximate bone mineral density (BMD)-modulus power-law relationship was established to generate elastic moduli for each head and plug.

Table 25. Case list of experimental disease model-specific simulations. This list identifies the disease model subset from the full list of disease models and controls listed in table 2.

Study	Case	Head modulus (MPa)	Plug modulus (MPa)	Plug eccentricity (mm)	Plug depth beneath the apex (mm)
Disease model specific simulations	I	329	131	0	4
	IV	506	146	4	6
	X	348	105	4	6
	XI	524	206	0	3
	XVI	330	84	0	4
	XVII	301	70	0	6
	XIX	268	124	3	4
	XX	231	114	0	5

Method

The geometry of the disease-model specific simulations was based on the experimentally derived horizontal and vertical plug locations established in Section 2.4.6. To maintain consistency with the previous studies, all experimental disease models were assigned a 50mm diameter as described in Section 3.2.1. While this did not reflect the measured diameter of the experimental models (mean 34mm), flattening at the dome occurred in all cases and modelling unique diameters would have introduced a further variable that was likely to confound the effect of lesion location without improving the accuracy with which the *in vitro* disease models were represented.

The disease model femoral heads and donor plugs were CT scanned prior to testing using a MicroCT100 scanner (Scanco Medical AG, Switzerland). The scanning protocol and protocol for obtaining BMD are described Appendix B. Bone mineral density was obtained for the entire plug and for a cylindrical volume of interest centred within the femoral head, oriented axially and bounded 5mm below the subchondral surface. The minimum, maximum and arithmetic mean values for the femoral heads and donor plugs were identified.

Repeated loading of the experimental disease models and controls resulted in varying magnitudes of change to the derived elastic modulus. Therefore, although establishing a value for the elastic modulus of bone plugs is not destructive, the result derived may not have been representative of the properties of the plug during the next loading cycle rendering the value of such a test uncertain. In addition, the bone plugs tested in Section 2.3 were not CT scanned prior to testing so it was not possible to obtain a BMD-modulus relationship directly. An estimated BMD-modulus relationship was obtained by pairing the maximum, minimum and mean BMD obtained when characterizing the components of the experimental disease model with the maximum, minimum and means values of elastic modulus for the samples taken from an equivalent location tested in Section 2.3.

The resulting paired data (three for porcine femoral heads and three for samples from the bovine lateral epicondyle) were plotted and a power-law trend line was fitted through each set (Figure

49). This resulted in the conversion factors for the femoral head and substituted bone shown in Equation 10 and Equation 11.

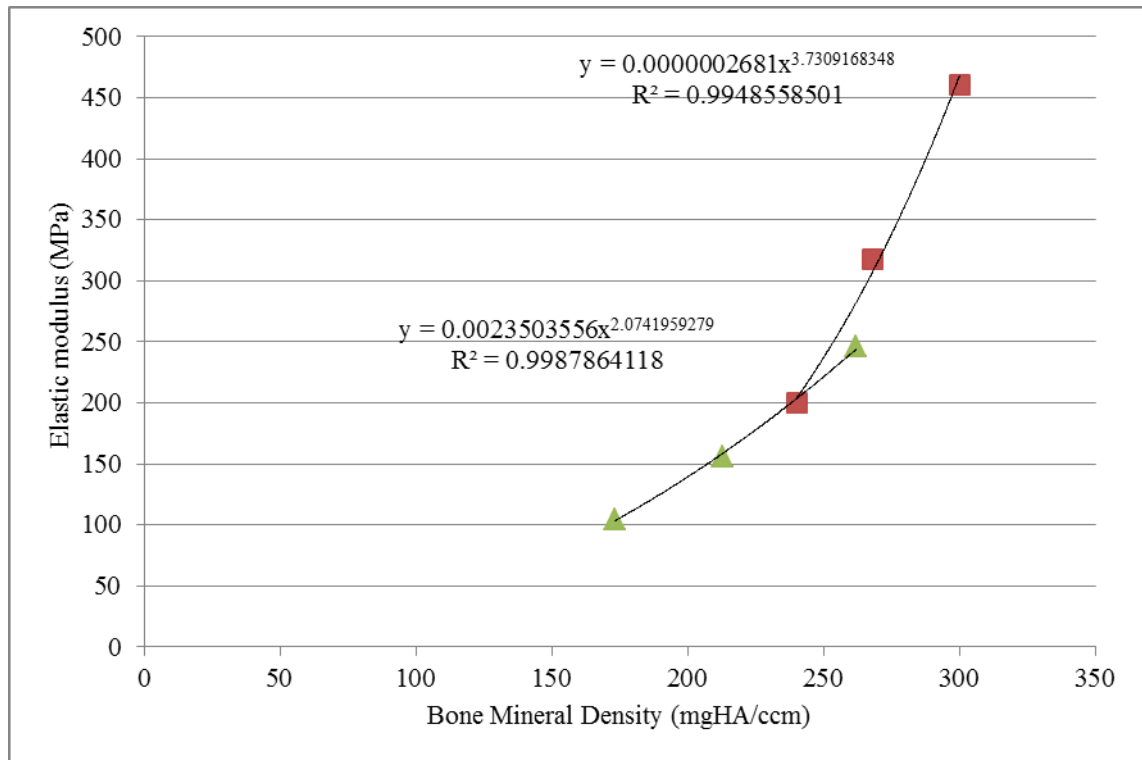


Figure 49. A plot of bone mineral density (BMD) versus Young’s modulus for plugs of bone taken from bovine lateral epicondyles (triangles) and for plugs of bone taken from the central load bearing portion of porcine femoral heads (squares).

Equation 10
$$E_{plug} = 0.002350(BMD)^{2.0749}$$

Equation 11
$$E_{head} = 0.0000002681(BMD)^{3.73091}$$

Models were constructed as described in Sections 3.2.1 and 3.2.3. The head and plug were assigned a Young’s modulus derived using Equation 10 and Equation 11 respectively. The assigned values are recorded in Table 26. The interface between the head and plug was tied. Although this was not the most representative interface condition of the experimental scenario, the relationship between the results of tied and friction interfaces had been shown to vary directly (Section 3.2.3) meaning that relative comparison between the disease models remained consistent regardless of interface condition.

Table 26. Plug and Head moduli derived from equations 10 and 11 for each disease model.

Disease model	Head Modulus (MPa)	Plug Modulus (MPa)
I	294	171
IV	452	186
X	311	142
XI	468	244
XVI	295	120
XVII	269	104
XIX	239	163
XX	206	153

3.3.4 Results

Parametric sweep study

As expected, the results for models with both tied boundaries and friction boundaries were similar and varied in a similar and predictable way: increasing the plug modulus increased the elastic modulus of the construct. When the lesion was assigned a modulus of 1MPa the boundary constraint had no effect. A tied constraint consistently resulted in a stiffer construct than using a friction boundary condition for all other plug moduli (Figure 50).

When the depth of the plug below the surface was reduced from 5mm to 2.5mm, the construct became less stiff overall and more sensitive to the modulus of the plug because the plate of stiffer material above the plug was thinner and so more of the load was carried by the plug itself (Figure 51). The tied interface model tended towards the same apparent stiffness as the original construct (approximately 270MPa) when the plug and head modulus were both set at 300MPa (Figure 52).

Moving the plug laterally had the effect of reducing its impact on the apparent stiffness of the construct because more of the load was carried by the stiffer head material. Similarly, there was a direct relationship between the depth of the plug beneath the apex and the apparent stiffness of the construct.

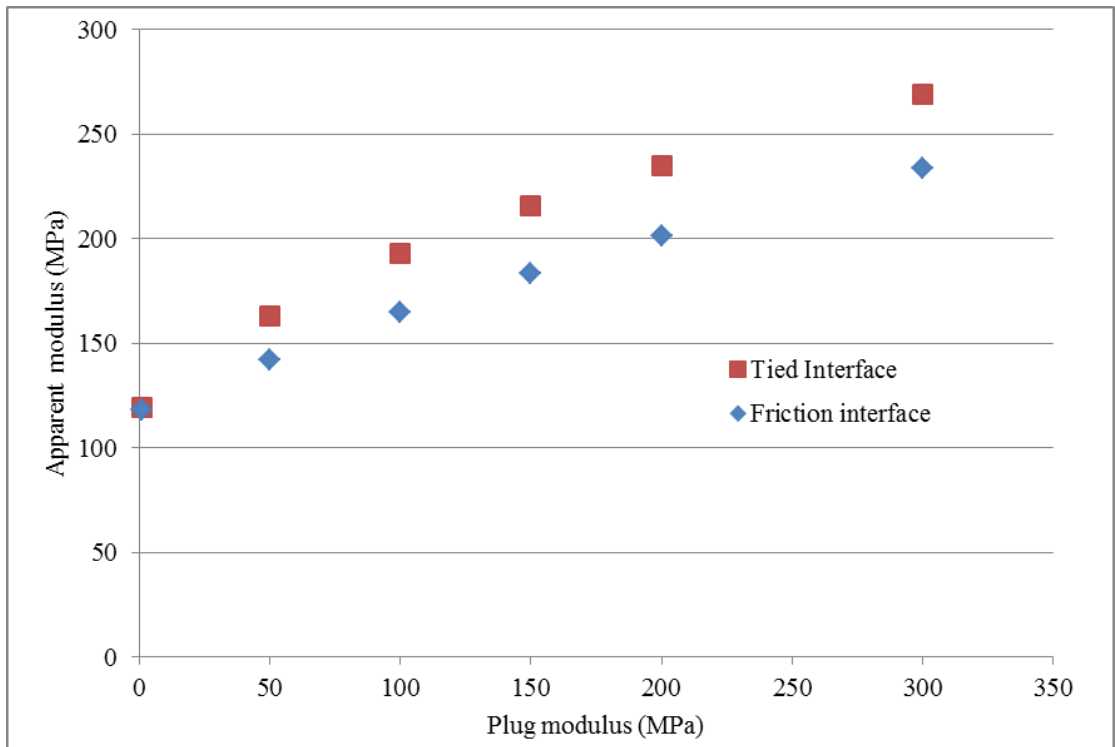


Figure 50. The relationship between plug modulus and the elastic modulus of the construct when the plug was concentric to the applied load and 5mm below the surface is shown. Using a friction boundary condition resulted in an elastic modulus that was lower than when a tied constraint was used at the interface between the plug and head.

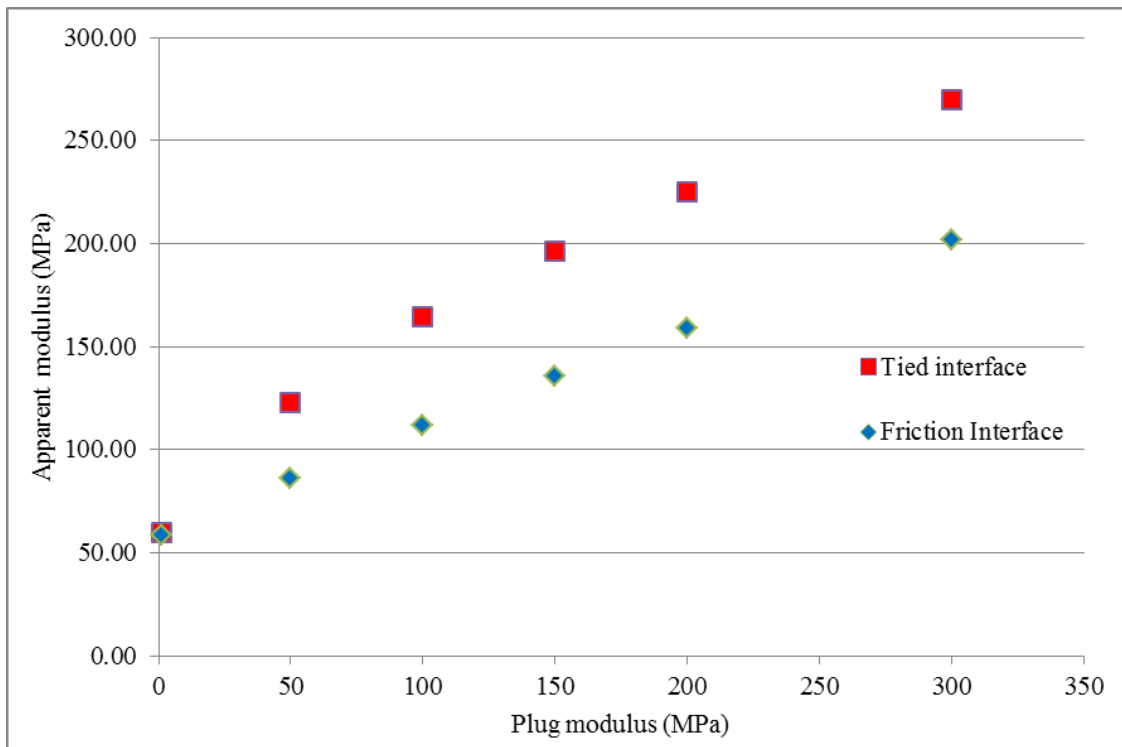


Figure 51. Relationship between plug modulus and elastic modulus when the plug was positioned concentrically and 2.5mm below the apex of the head. Compared to when the plug was positioned 5mm below the apex (Figure 50), the empty plug condition was approximately half as stiff. When the friction interface was applied, the homogenous model was 16% less stiff than when the plug was 5mm below the surface.

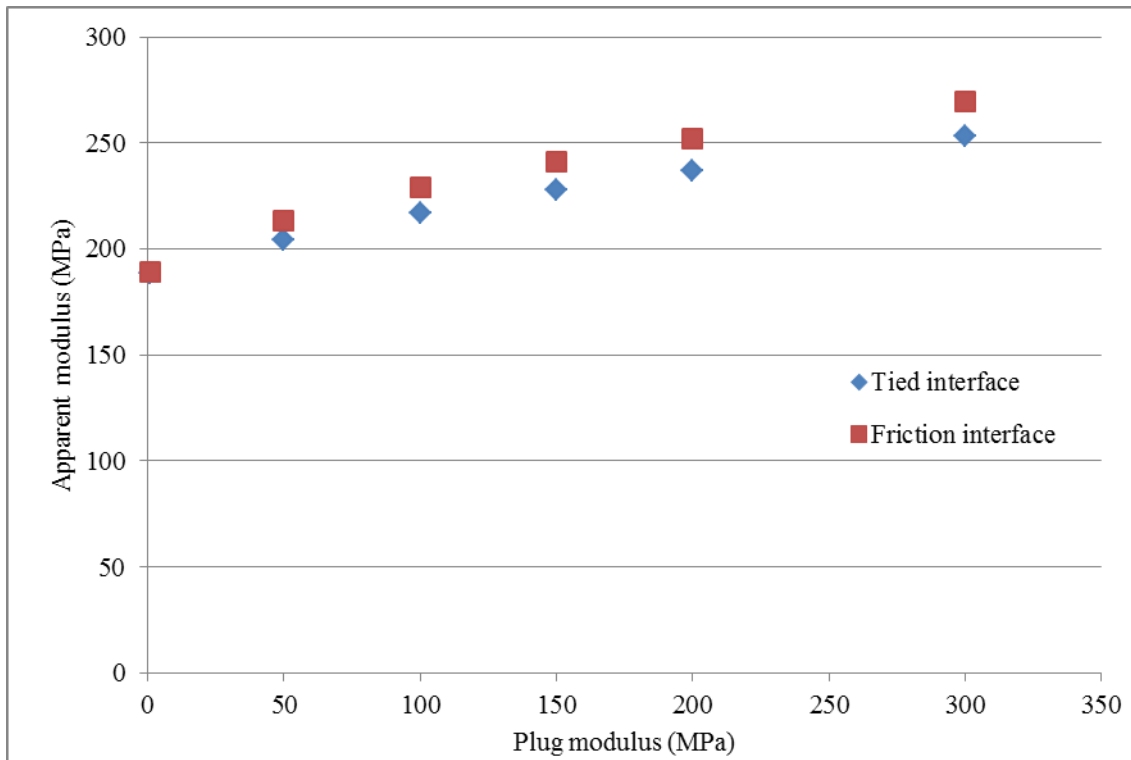


Figure 52. The relationship between plug modulus and elastic modulus when the plug was lateralised by 2.5mm and positioned 5mm below the apex is shown. Compared to the results when the plug was concentric with the applied load (Figure 50), there was substantially less difference between the two boundary conditions, and the effect of changing plug modulus was also less.

Multivariate analysis

Elastic modulus and RR scores were calculated for each case. The main effects plots for elastic modulus and RR_D are shown in Figure 53 and Figure 54 respectively. The interactions plots are shown in Figure 55 and Figure 56.

The plots in Figure 53 and Figure 55 indicated that head modulus had an over-riding effect on the elastic modulus. Plug modulus also had a minor effect, as did eccentricity. Depth beneath the apex in isolation did not drive a main effect but it interacted with eccentricity to invert the relationship between modulus and eccentricity.

To evaluate whether the RR scores for one side of the surface correlated with the magnitude of the difference, Pearson product-moment correlation coefficients were calculated between each response (Table 27). RR_D was strongly correlated with the outcome for the outer surface (RR_O). This was expected as in a strain-controlled test the magnitude of the stress in the entire head will be governed by its modulus and the magnitude of the difference in stress between the two surfaces varies directly with this factor. Although the variation in head modulus was proportional in terms of a percentage change to the other factors, it had the greatest difference between its high and low levels.

Table 27. Pearson product-moment correlation coefficients between each response.

Response	RR _O	RR _I
RR _I	0.32	
RR _D	0.92	0.03

The RR_D value calculated for each of the models is shown in Figure 57. The RR_D score was negative in four cases (9, 10, 11, 16) indicating that the inner surface was more highly stressed than the outer. All four of these were models where the head modulus was low (150MPa). In three cases (9, 10, 11) the plug modulus was higher than the head modulus. In case 16 however, the plug modulus was also low indicating that material properties alone could not fully predict which side of the interface was most highly stressed.

The main effect plots for the RR_D scores (Figure 54) indicated that head modulus had the largest impact on RR_D. Plug modulus and depth beneath the apex had negative t-statistics indicating RR_D increased with low plug modulus and concentric location.

The interaction plots (Figure 56) indicated that the responses to plug modulus and eccentricity were affected by head modulus. The response to eccentricity was also affected by plug modulus. The response to changing depth beneath the apex was not strongly affected by the level of the other factors.

Six interaction pairs were found to cause large changes to the response.

1. When plug modulus was low, a high head modulus represented a significantly higher risk score than a low head modulus: RR_D = 63.9 versus 4.5.
2. When head modulus was high, an eccentric plug location was associated with a higher risk than a concentric plug location: RR_D = 80.8 when eccentricity was high versus 15.8 when the plug was concentric.
3. When eccentricity was high, the effect of head modulus was significant: RR_D = 80.8 when head modulus was high versus negative 3.9 when head modulus was low.
4. An eccentric plug location in a high modulus head was significantly different from a concentric plug location in a low modulus head (RR_D=80.8 compared to 3.0).
5. When the plug was deep to the surface, head modulus had a significant impact: RR_D= 41 when head modulus was high compared to negative 4.6 when head modulus was low.
6. High head modulus plus central plug location was associated with a higher RR_D than a low head modulus with an eccentric plug (55.6 versus -4.6).

Cases 5 and 6 were identified as the worst cases with RR_D values of 92 and 126 respectively. Both had eccentric plugs of low modulus in a head with high modulus. The relative risks for these cases were in the region of 60% higher than the next-worst case. Cases 5 and 6 were both eccentric, bringing one side of the surface close to the centre of load application (Figure 58). While the size of the regions identified were close to the mean of the set (14 and 19 elements respectively), the magnitude of the difference in stress between the two surfaces was in the upper quartile for the set (approximately 6.6MPa in both cases).

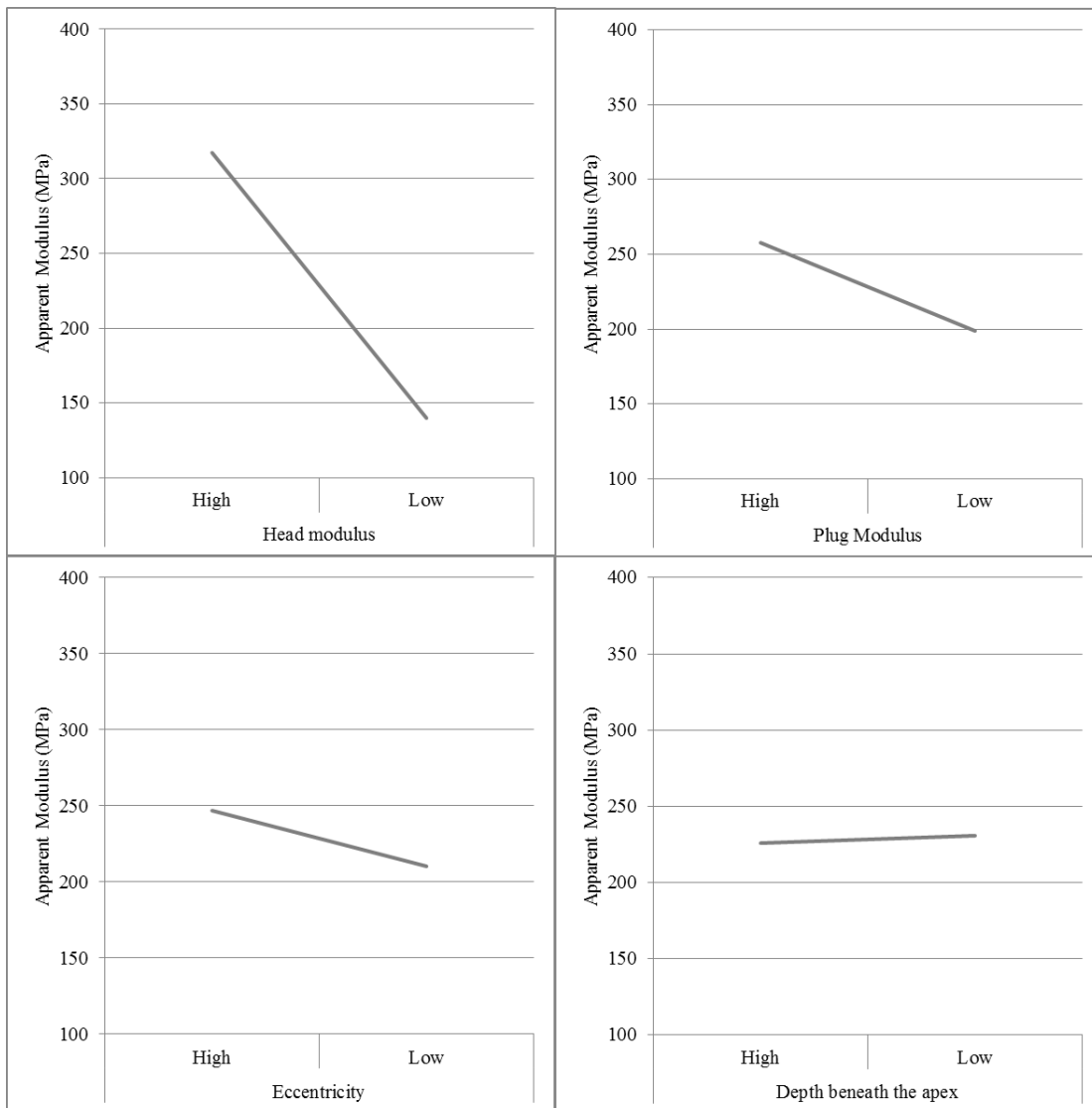


Figure 53. Main effects plots showing change in elastic modulus in response to head modulus, plug modulus, eccentricity and depth beneath the apex.

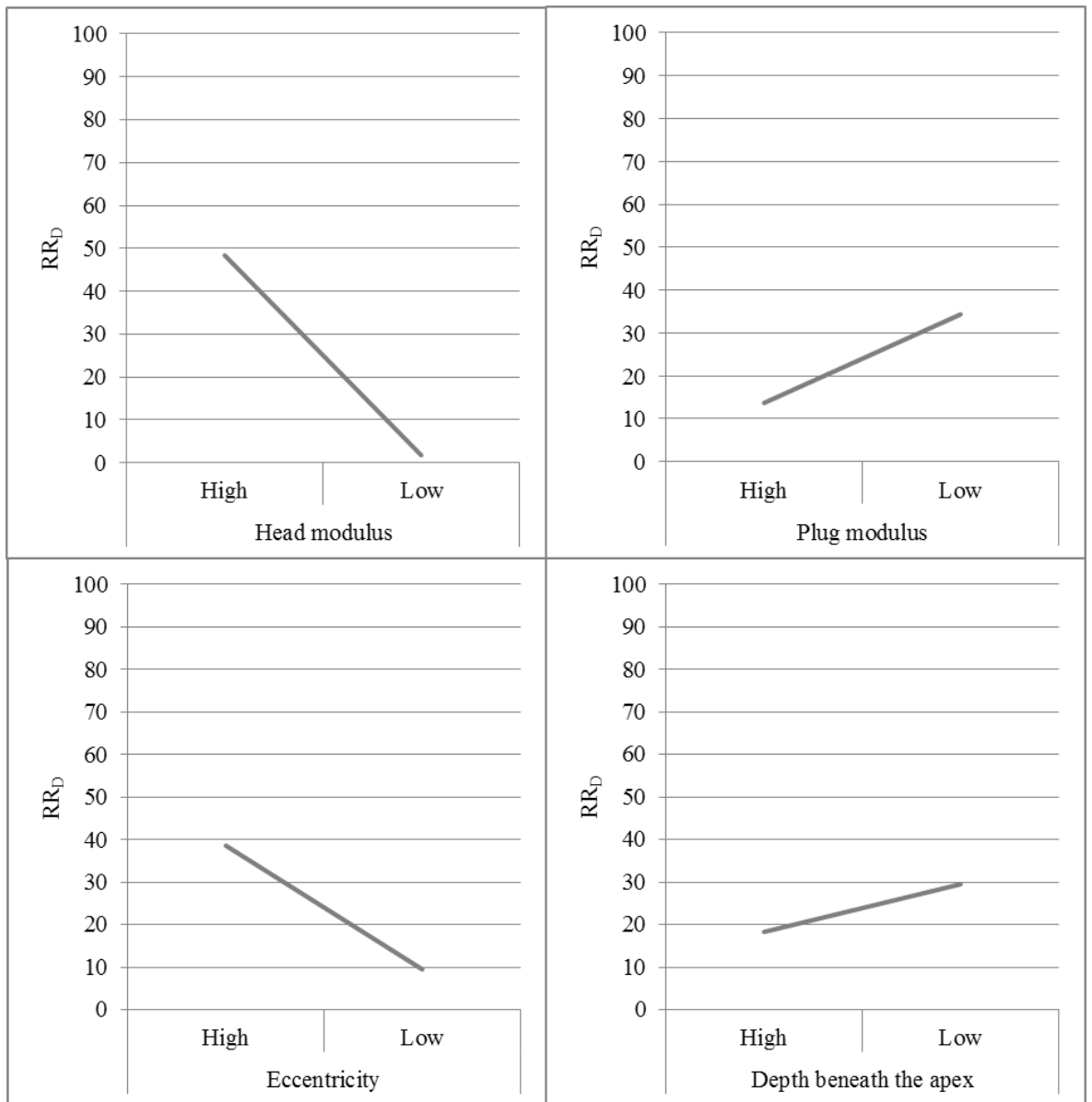


Figure 54. Main effect plots for relative risk (difference) response.

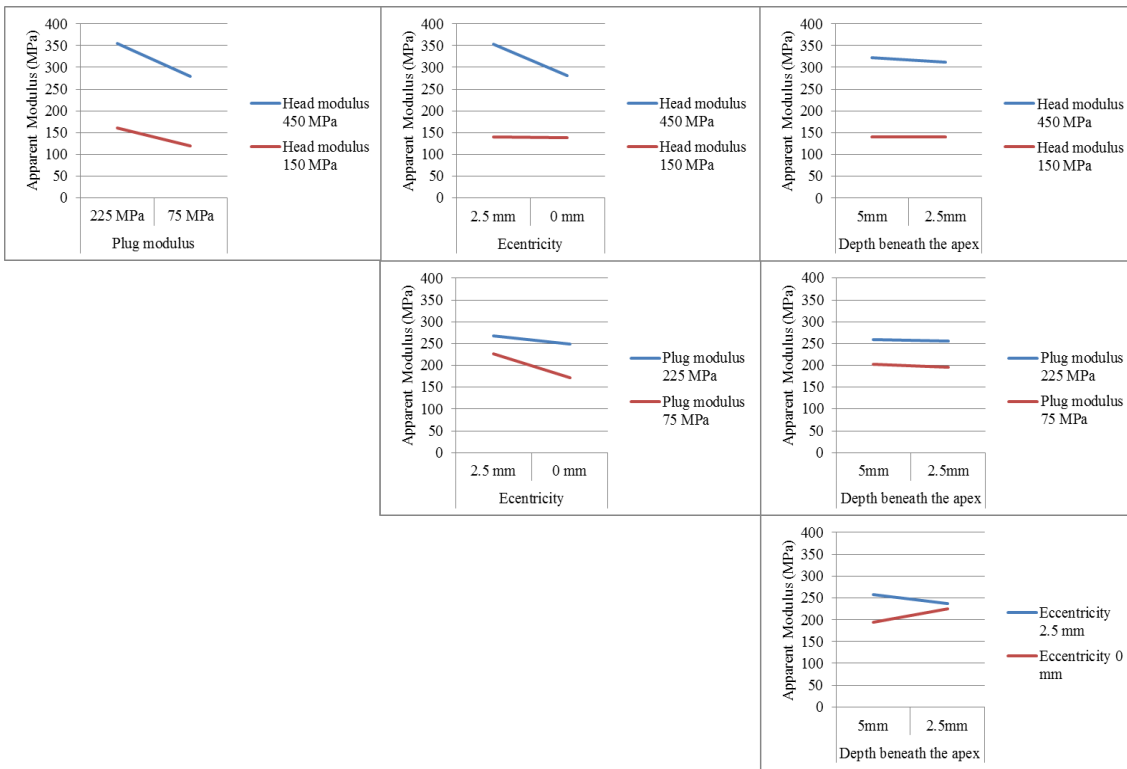


Figure 55. Interaction plot showing change in elastic modulus in response to interactions between head modulus, plug modulus, eccentricity and depth beneath the apex.

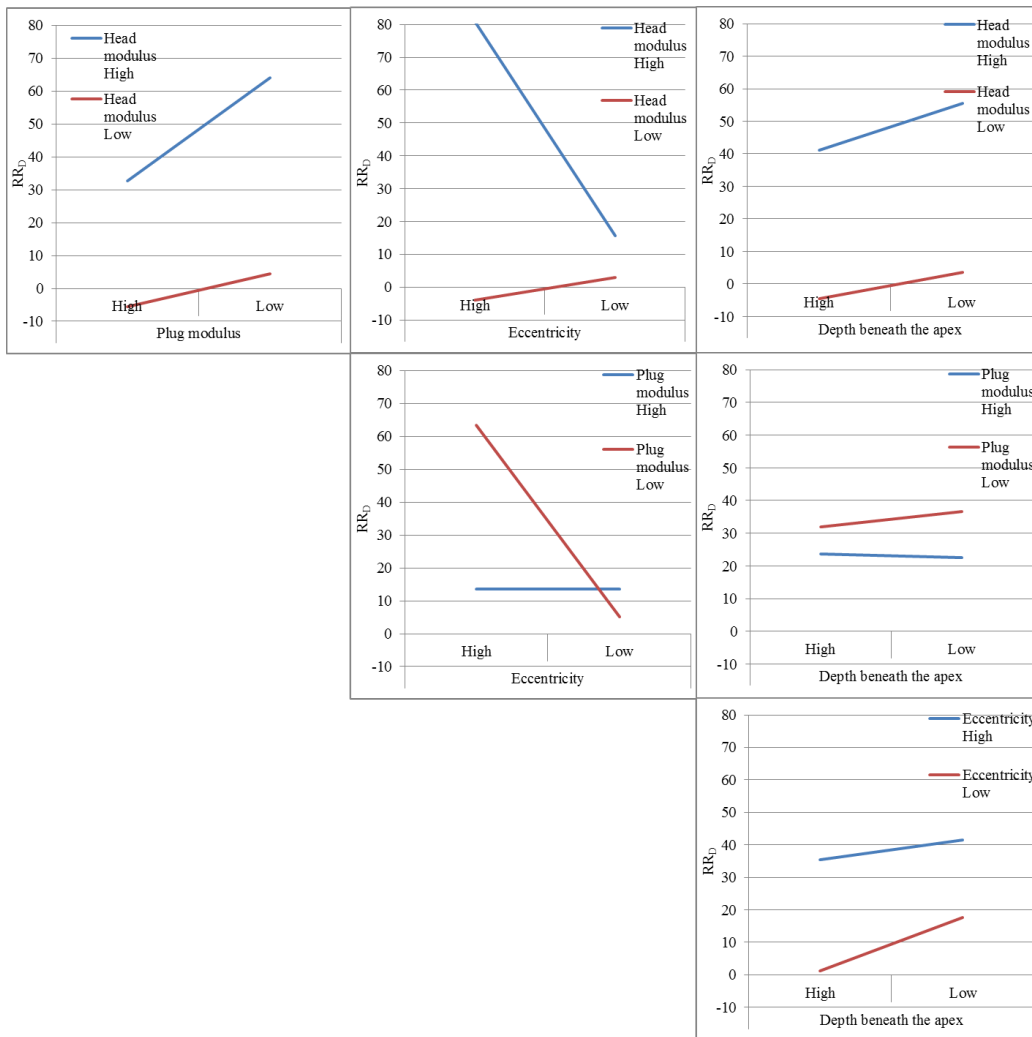


Figure 56. Interaction plots for the relative risk (difference) response

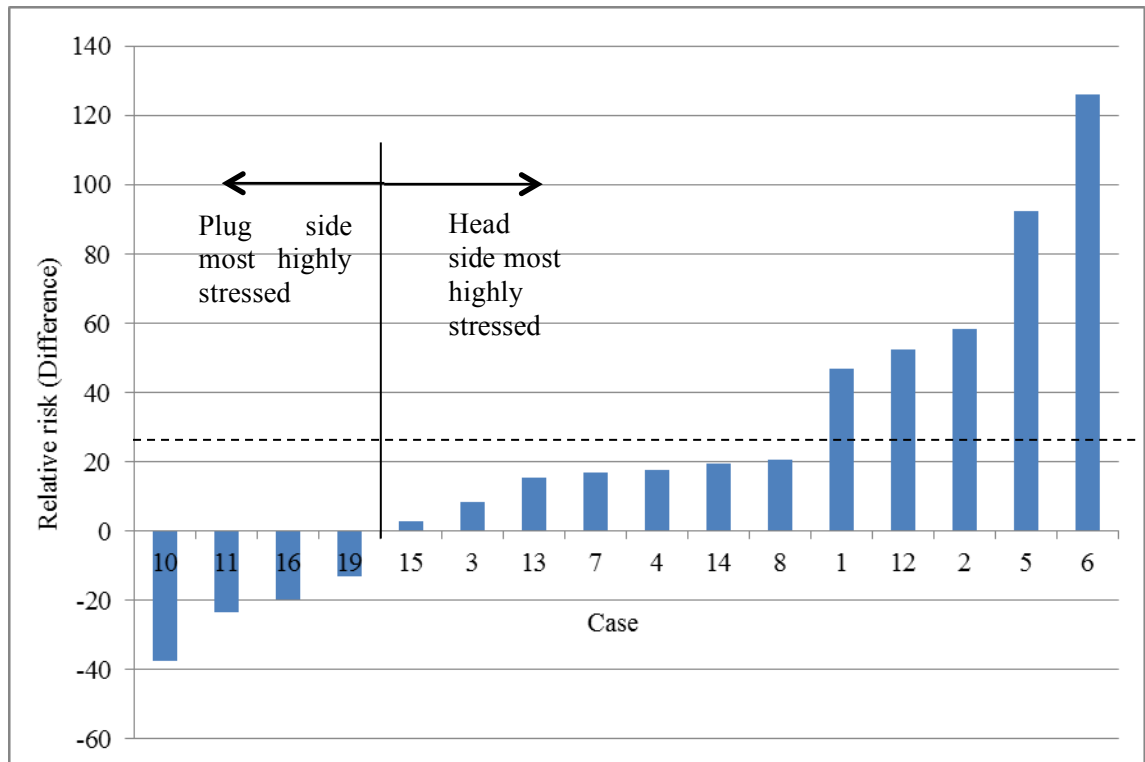


Figure 57. Bar chart of relative risk (difference) (RR_D) for each configuration, arranged in ascending order. The RR_D score for the first four configurations was negative indicating that the plug side of the surface was most highly stressed. The mean RR was 24 (standard deviation 43, range -37 to 126). This is indicated by the broken line on the plot.

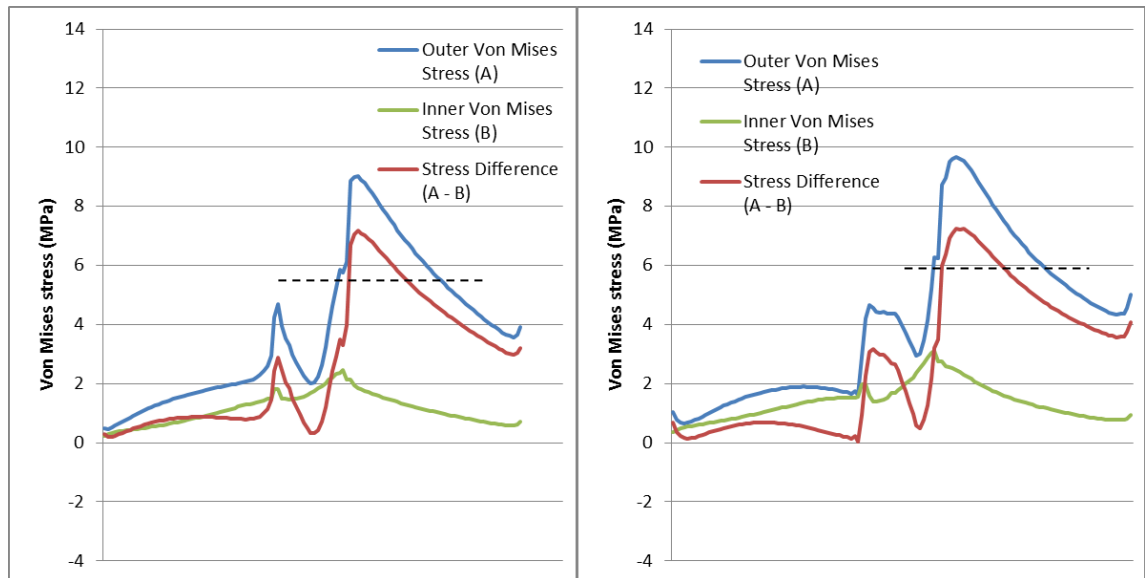


Figure 58. Stress distribution plots for cases 5 and 6. The broken line in each plot indicates the approximate threshold (5.8MPa) above which elements were included in the relative risk calculation. The x-axis is the sequential element location, starting at the bottom left edge and moving clockwise around the surface.

There was a relatively poor ($r=0.6$) correlation between the FE derived elastic modulus and RR_D score. The former is an indication of the global effect of a lesion being present whereas the latter represents a local phenomenon and it is reasonable to assume that a head with a relatively

high elastic modulus could also have significant stress discontinuities if a lesion of less stiff bone was present.

The regression model correlated strongly with the FE simulation results ($r = 0.96$) (Figure 59). Error between the value predicted by the regression analysis and the value derived from the FE simulation directly varied from <1% to 35%. There was no correlation between factor levels and the magnitude of the error. This means that the trend identified for variation in elastic modulus derived from the FE simulation with these parameters can be considered predictable and reproducible.

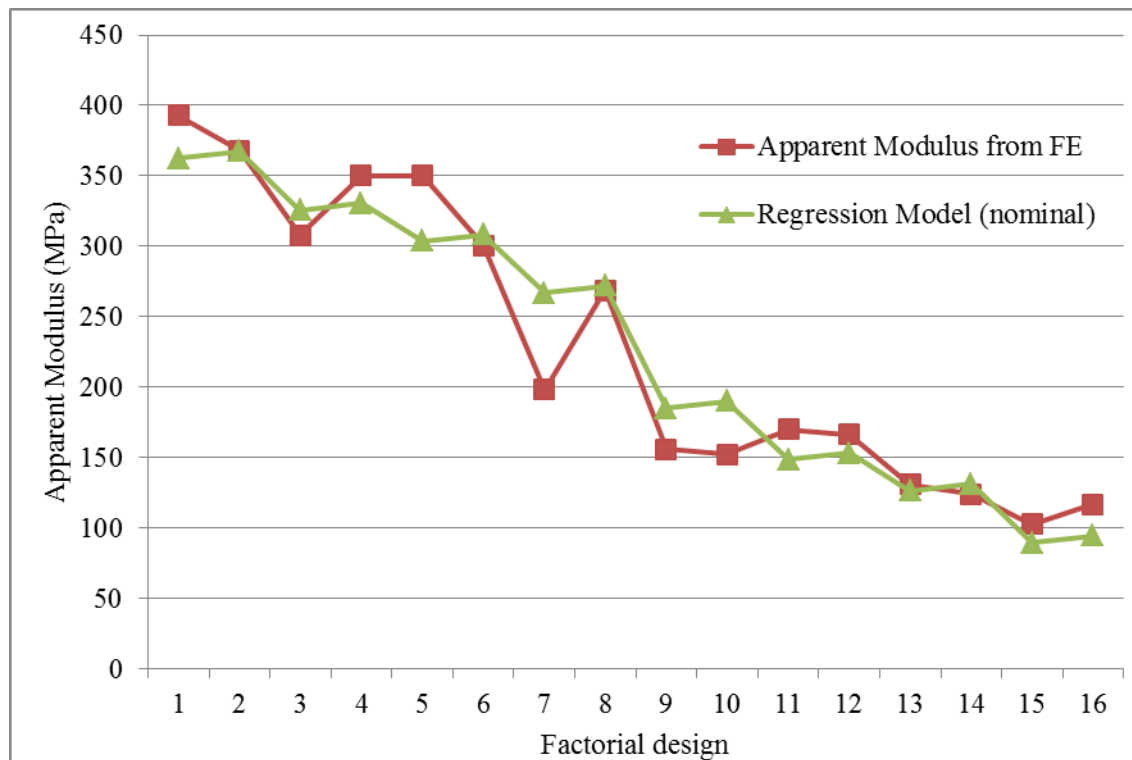


Figure 59. Plot of elastic modulus derived from the FE simulations for each factorial design compared to the regression model derived from the same data.

Experimental disease model simulations

The relationship between bone mineral density and elastic modulus was challenged by comparing the spread of the data to the experimentally derived results described in Section 2.3.3. This was performed for both the simulated healthy bone and simulated necrotic bone and the data sets are compared in Figure 60. While this confirmed that the range was similar between the two groups, there was significant spread in all data sets due in part to the natural variation in material properties of bone but also due to the relatively small sample size ($n=12$ for bone samples taken from porcine femoral heads and $n=17$ for samples taken from bovine lateral epicondyles).

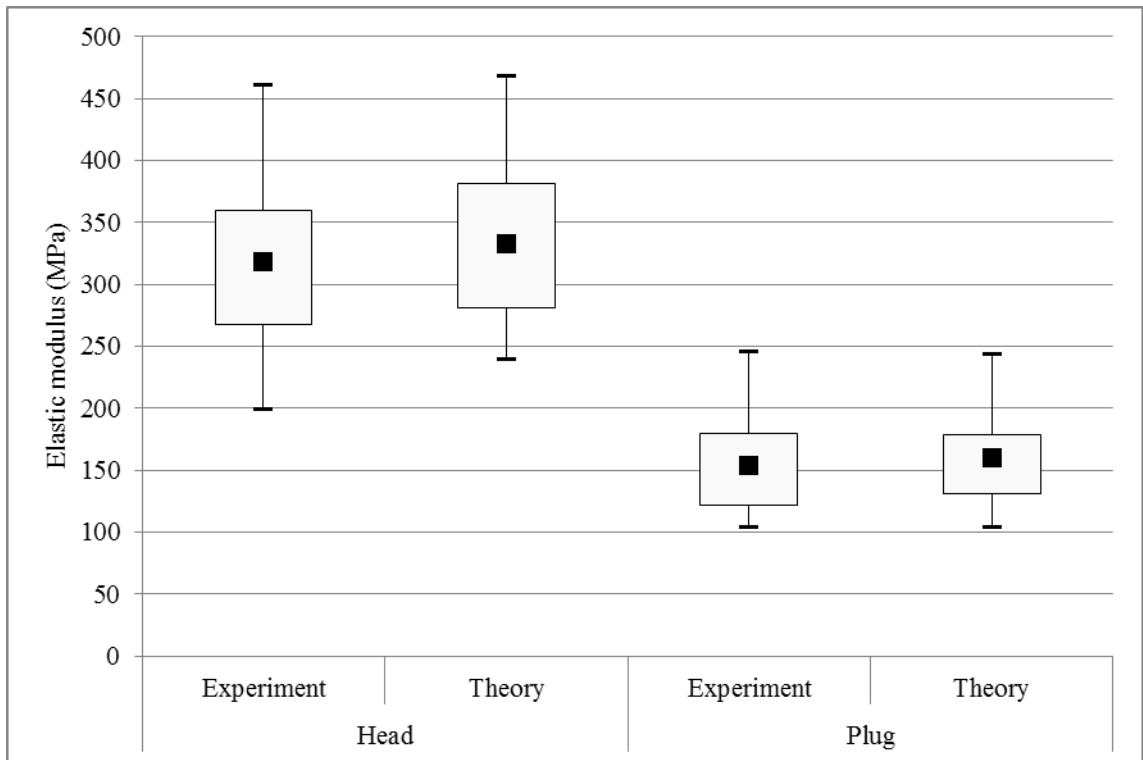


Figure 60. Comparison between theoretical and experimentally derived moduli for porcine femoral heads and donor bone taken from the lateral epicondyle of bovine femurs.

The experimental disease model specific simulations were processed as described in Section 3.2.4 to derive relative risk scores relating to the outer surface (RR_O), inner surface (RR_I) and the difference between the surfaces (RR_D).

The relative risk outcomes are reported in Figure 62. There was no correlation between either the experimentally derived elastic modulus or occurrence of fracture and any of the three relative risk scores ($r = 0.0004$, 0.0889 and 0.1595 for RR_O , RR_I and RR_D respectively). Comparing the maximum VM stress in the outer and inner surfaces, or the maximum difference between the two yielded a similar lack of correlation (Figure 63 and Table 29).

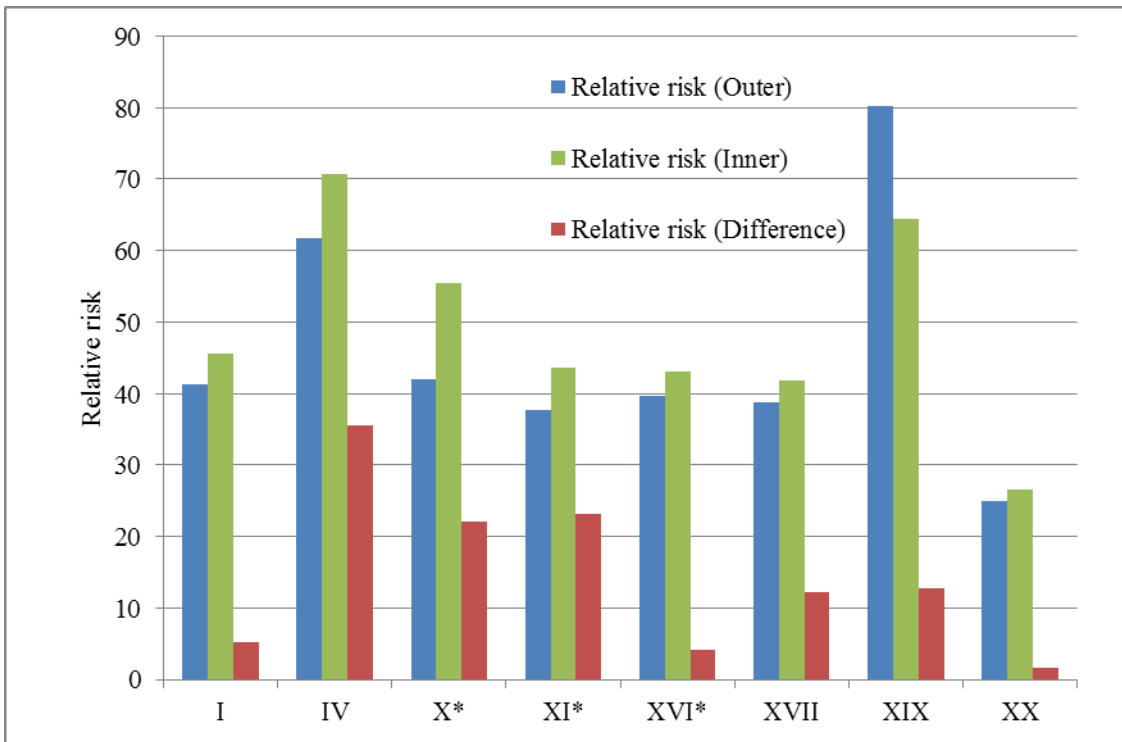


Figure 61. Relative risk scores derived for each of the experimental disease model specific simulations (Section 3.3.3). The experimental disease models are identified by roman numerals; the three disease models that fractured are identified by an asterisk

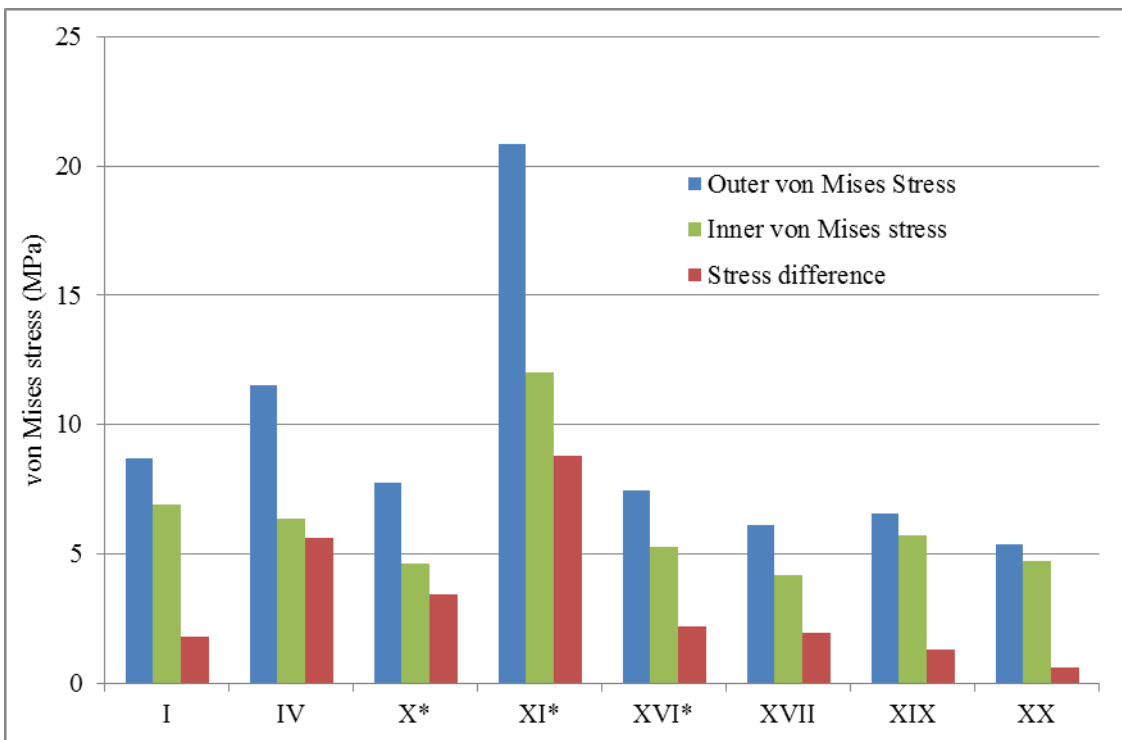
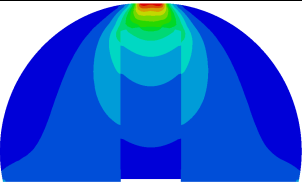
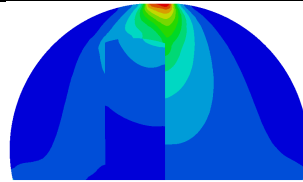
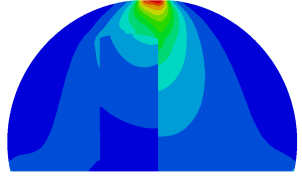
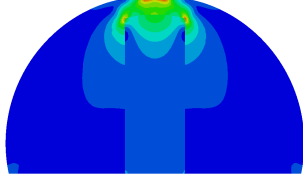
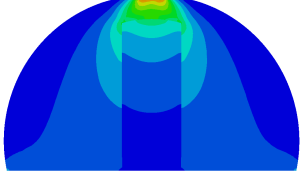
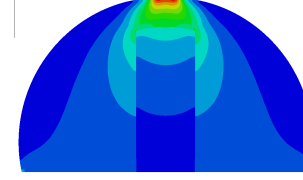
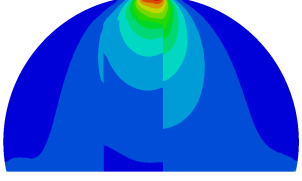
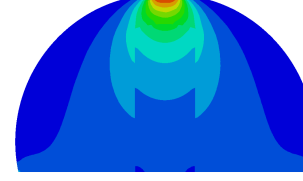


Figure 62. Peak von Mises stress in the outer and inner surface and the difference between each surface for each of the experimental disease model specific simulations. The experimental disease models are identified by roman numerals; the three disease models that fractured are identified by an asterisk

Table 28. Von Mises stress distribution for the eight experimental disease model-specific FE simulations and the associated maximum stress in the outer surface, inner surface and the maximum difference.

I			IV		
	Surface	von Mises stress (MPa)		Surface	von Mises stress (MPa)
	Outer	8.7		Outer	11.5
	Inner	6.9		Inner	6.4
	Diff.	1.8		Diff.	5.6
X			XI		
	Surface	von Mises stress (MPa)		Surface	von Mises stress (MPa)
	Outer	7.8		Outer	20.9
	Inner	6.4		Inner	12.0
	Diff.	3.5		Diff.	8.8
XVI			XVII		
	Surface	von Mises stress (MPa)		Surface	von Mises stress (MPa)
	Outer	7.5		Outer	6.1
	Inner	5.3		Inner	4.2
	Diff.	2.2		Diff.	1.9
XIX			XX		
	Surface	von Mises stress (MPa)		Surface	von Mises stress (MPa)
	Outer	6.6		Outer	5.4
	Inner	5.7		Inner	4.7
	Diff.	1.3		Diff.	0.6

3.3.5 Discussion

Parametric sweep

Lesion material property had a significant effect on the elastic modulus of the construct. This is consistent with the findings of Brown *et al.*, 1992. The magnitude of the effect was influenced by the horizontal and vertical location of the plug relative to the point of load application. A tied interface always resulted in a stiffer construct because in models with a friction boundary condition the outer surface was able to separate from the inner surface, increasing the apparent Poisson's ratio by allowing more horizontal displacement for a given vertical load. Deformation of the superior plate above the plug separated the edges of the domed end of the plug from their mating surfaces, effectively reducing the load-bearing width of the plug and reducing its efficiency as a supporting pillar (Brown *et al.*, 1992). Separation of the two surfaces is akin to the opening of a subchondral fracture (Motomura *et al.*, 2011) and potentially offers a simple method of evaluating the effect that the presence of a crack has on the construct without initiating a complex crack growth model such as that implemented by Taylor and Lee, (2003).

More of the load was carried by the stiffer head material when the plug was deep to the surface compared to when it was in a more superficial position. The role of the necrotic bone subjacent to the subchondral plate was highlighted in a previous FE study (Brown *et al.*, 1992). In this study the authors demonstrated that preservation of normal material properties in the subchondral bone reduced the risk of bone fracture but that the material properties of the underlying lesion were a more critical factor in dictating structural failure. The current investigation confirmed this finding but also suggested that there may be a minimum thickness of bone above the lesion above which the lesion will not contribute significantly to the structural integrity of the femoral head because the subjacent bone carries the majority of the joint load independently. It is likely in such cases that the distance will be a function of both head and lesion material properties.

Multivariate analysis

The sensitivity of simulations of an experimental disease model of AVN to geometric and material variability was evaluated by varying the material properties of the head and plug (representing a lesion of necrotic bone), the eccentricity of the plug relative to the centre of load application and the proximity of the top surface of the plug to the apex of the femoral head using a systematic DoE-based approach.

The multivariate analysis showed that the difference between the head and plug modulus had a significant effect on the relative risk. It also influenced which side of the surface was most highly stressed. This finding is particularly important when one considers the results of Brown

et al., (1981) who observed that both the modulus and compressive stress of necrotic bone were reduced compared to healthy bone.

Eccentricity and location beneath the apex also played a role: the significance of that role depended on the material properties and similar stress magnitudes and distributions could be associated with geometries other than what was tested. The conclusion drawn from this finding is that lesion geometry: size, shape and the location of the transition between healthy and necrotic bone within the head will all play a role in defining the relative risk of failure.

The sensitivity analysis identified a worst case: A model with a high head modulus containing a plug with a low modulus that was positioned eccentrically and close to the surface. The next worst case was similar but deep to the surface. In these cases the stress at the interface was high and there was a relatively large peak in difference between the two surfaces with the majority of the load being carried by the head rather than the plug. It was noted that in both cases the most highly stressed section of boundary aligned closely to the centre of load application.

There was a positive trend for increasing elastic modulus as the depth of the plug beneath the apex increased in the experimental data. This was confounded in the experimental results by the densities (and therefore elastic moduli) of the femoral head and plug and variations in eccentricity and the FE simulation showed that the relationship between elastic modulus and depth beneath the apex was not strong. The effect of proximity of the plug to the apex on RR_D was also insignificant. However, this factor interacted with others to alter the response. Of note is the fact that the highest stress may be inside or outside the lesion depending on the depth beneath the surface.

There was a weak trend for increasing stiffness with eccentricity in the experimental results ($r = 0.45$). However, the influence of confounding factors was high. The FE sensitivity analysis indicated that eccentricity did tend to increase elastic modulus but again, this was not significant. Eccentricity was a significant factor affecting RR_D . As eccentricity increased, the edge of the lesion moved closer to the centre of load application and RR_D increased dramatically. The influence of eccentricity was affected by the ratio of head modulus to plug modulus.

High lesion material stiffness also significantly reduced the effect of eccentricity on RR_D . It is reasonable to assume that a lesion that has the same stiffness as the rest of the femoral head will have a negligible effect on the natural joint whereas the boundary between healthy bone and a low-stiffness lesion will be strongly affected by its location relative to the point of load application.

Experimental disease model simulations

Experimental disease model XI had the lowest derived modulus (94MPa) of any of the experimental disease models and a fracture was identified post-test. It had the highest peak VM stress and RRD scores but model X, which also fractured, had the lowest RR_D score. The magnitude of the VM stress in this model was consistent with other samples tested (Table 29). No correlation between the proposed relative risk score and the occurrence of fracture could be identified. One possible reason for this could be the use of homogenous material properties within both the femoral head and plug components. Another factor is the use of simplified geometry in the FE simulations compared to the organic shapes present in the experimental disease model. The experimental disease models were also loaded multiple times and the cracks could be a result of cumulative failure rather than an acute event.

In the experimental disease models, the aim was to remove a plug of bone from the central portion of the porcine femoral head: the location generally associated with the highest density bone within the femoral epiphysis. The post-test analysis of the experimental disease models (Section 2.4.6) showed that the location of the plug relative to the target position (central, 5mm below the subchondral surface) varied. The FE simulations highlighted the sensitivity of the experimental disease model to plug location. It is feasible that this effect would be magnified if the location of the substituted bone included an area of relatively low density.

The results of the multivariate analysis (Section 3.3.2) indicated that elastic modulus was strongly correlated to the modulus of the femoral head and another possible reason for the inability to identify cases that fractured is lack of correlation between the actual material properties and those applied to the *in silico* simulations.

Finally, the outcome measure used, RR_D , assessed stress magnitude only at the boundary between the head and plug volumes. It is possible that this was not the most highly stressed region in the experimental disease models.

3.4 Conclusions

In this chapter a series of studies designed to systematically evaluate the effect of different modelling strategies and physical parameters on the relative performance of finite element simulations that represented the experimental disease models described in Chapter 2 were presented.

The parametric studies confirmed the logical effect of these parameters on the stiffness of the disease model. The risk score was demonstrated to be sensitive to all factors considered within the parametric studies and to be a more sensitive outcome measure than stiffness. It was concluded that the risk score was a more clinically relevant outcome measure than stiffness as it

had the potential to identify the location at highest risk of fracture rather than providing an ambiguous surrogate measure.

The interface study highlighted the sensitivity of the head-lesion construct to the interface between the healthy bone and necrotic lesion: Using a friction interface resulted in a construct that was less stiff than one with the same material properties that used a tied interface. It is concluded that the former, which allowed separation at the interface, was analogous to the presence of a crack within the femoral head and offered an insight into the rapid progression of the disease after fracture occurs. However, as the focus of this thesis was on the pre-fracture phase of AVN, a tied interface that was intended to simulate the continuum between healthy and necrotic bone was used in subsequent studies.

Two parametric studies were conducted. These showed that the outcome measures associated with the construct was affected primarily by head modulus but that lesion modulus and location also had an effect. The performance was characterised using two outcome measures: Elastic modulus and relative risk. The latter performance measure was shown to be more sensitive to variations within each model than the former and has the advantage of being independent of the method of load application.

Limitations to the relative risk score were highlighted when it was used to assess experimental disease model specific simulations. Thus, while it appears to be a sensitive measure, it must be treated with caution and will be explored further in Chapter 4.

Chapter 4. Finite element analysis based evaluation of lesion size, shape and orientation

4.1 Introduction

Current classification systems for AVN are based on lesion size and location and have limited prognostic value, making it difficult for the surgeon to choose the most appropriate treatment. Therefore there is an unmet clinical need for a better means of quantifying the risk of disease progression to improve the stratification of patient care. Stress concentrations at the lesion boundary may contribute to the formation of fractures clinically and an aim of this thesis was to establish whether a risk score that quantified the stress distribution at the lesion boundary offered an improved means of stratifying patients.

In Chapter 3, a novel approach that quantified both the magnitude of the stress discontinuity at the lesion boundary and the size of the region most severely affected was evaluated using simulations of an experimental disease model. Although the simulated disease model used simplified loading and geometry compared to reality, the analysis confirmed the sensitivity of the risk score to variation in material properties and lesion location.

The broad aim for the studies recorded in Chapter 4 was to reduce the magnitude of the gap between the simulated experimental disease models that were tested with a simple load regime and the physiological scenario. Two objectives were planned to achieve this. The first was to develop and evaluate a method of loading the simulated disease model in a way that controlled the distribution of applied stress on the surface of the femoral head. The approach was not intended to recreate the physiology of the natural hip joint. Its aim was to better represent load transfer through the relatively soft, conforming articular surfaces of a natural hip joint during a single static loading condition. The second objective was to analyse the sensitivity of the risk score to lesion size and alignment relative to the load vector.

Three studies were planned to meet the objectives:

1. Development and evaluation of a conforming contact model (introduced in Section 4.3.1).
2. Simulation of experimental disease models using conforming contact (introduced in Section 4.4.1).
3. Simulation of cone-shaped lesions (introduced in Section 4.5.1).

The sequence in which the studies were performed and link to Chapter 3 is shown in Figure 63.

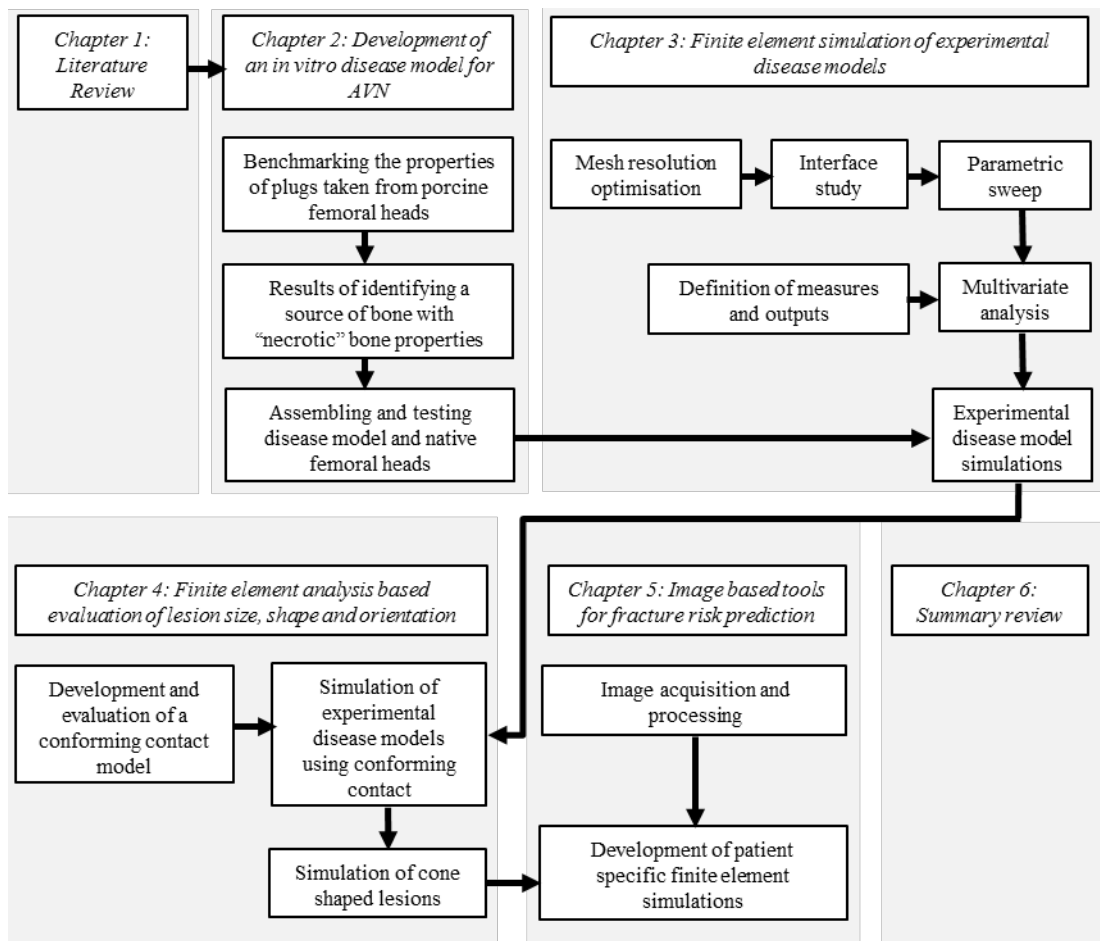


Figure 63. Flow chart summary of the studies performed in each chapter.

The first study defined a methodology used to apply load indirectly to the femoral head via a soft conforming medium intended to distribute stress more evenly across the surface of the head compared to direct compression via a flat platen. As the aim was to generate a more diffuse load pattern, it was anticipated that a larger proportion of the lesion boundary would be loaded.

This methodology was used in the rest of Chapter 4 and in Chapter 5. The methodology was refined to achieve a target displacement of 0.5mm at the apex of the femoral head. This allowed direct comparison back to the results of the mesh resolution optimisation study (Section 3.2.2) and showed the difference between direct compression using a flat platen and indirect compression via a relatively soft conforming filler

It was hypothesised that displacement at the apex of the femoral head would be increased by the inclusion of softer material within the femoral head (e.g. a lesion). Evaluation of this hypothesis was included in the second and third studies in this chapter.

The second study allowed the effect of the new method of load transfer to be compared to the results presented in Section 3.3.4. It demonstrated the sensitivity of the experimental disease model to the method of load application and highlighted opportunities for developing future *in vitro* experimental disease models for AVN.

The effect of lesion size, shape and orientation were evaluated in the third study. This study showed that the relative risk score was sensitive to all three factors and also that the factors interacted.

4.2 Standard methods for FE model generation

The literature review highlighted a range of potential methods of load application. It confirmed that the magnitude and orientation of the joint reaction force vector varies substantially depending on activity. It also confirmed that the articular surfaces remain intact in pre-collapse hips with AVN, dictating the need to reproduce the effect that soft tissue and joint conformity would have on the stress distribution within the simulated disease model. Recreating the physiology of the natural hip joint would introduce another source of variability to the experiment and was not the focus of this thesis. Therefore the aim of the improved method of physiological loading was not to recreate a specific activity, but to generate a physiologically representative method of applying load.

The literature review also confirmed that physiological lesions vary significantly in size and shape but are often generalised as having a cone-like morphology. Simulating conical lesions in an *in silico* disease model gives a better approximation to physiological shapes than the experimental disease models but still allows them to be geometrically defined. This is an important consideration when performing parametric studies to investigate the effect of lesion shape and orientation on the risk score.

All two-dimensional simulations were constructed using the same standard methods as were described in Section 3.2.1. The material properties used for each study are summarised in Table 29. A target element edge length of 0.5mm was used in all two-dimensional assemblies. Interactions at each interface are described in Table 30. The results of the parametric sweep (Section 3.3.4) confirmed that the simulations behaved the same regardless of friction coefficient used, therefore a high friction coefficient, nominally representing the interference fit between the pin of bovine bone and native porcine femoral head in the experimental disease models was used throughout.

Table 29. Young's modulus assigned to the model components for each study using the conforming contact load configuration shown in Figure 64.

Study	Platen modulus (GPa)	Filler Modulus (MPa)	Head Modulus (MPa)	Lesion Modulus (MPa)
Conforming contact development (Section 4.3)	100	Model specific. Refer to Table 32	300	N/A
Experimental disease models with conforming contact (Section 4.4)	100	50	Model specific: refer to table 17	Model specific: refer to table 17
Conical lesions (Section 4.5)	100	50	300	150

Table 30. Interactions for each interface in the conforming contact simulations (Figure 64) were consistent throughout the studies described in this chapter. The interfaces are described with the master surface listed first. All contact parameters are described in Section 3.2.1. Tied contact is defined as an interaction that restricts all relative motion at the interface between the two surfaces.

Interface	Interaction
Platen to filler	Contact (Tangential: Friction, $\mu=1.0$; Normal: Hard contact)
Filler to head	
Head to lesion	Tied
Filler to filler (Patient-specific simulations only)	

4.3 Development and evaluation of a conforming contact model

4.3.1 Introduction

The region of contact between the cartilage of the femoral head and that of the acetabulum *in vivo* varies with age and pathology (Dorr *et al.*, 2000) making it difficult to predict the exact contact conditions between the acetabulum and a necrotic femoral head. For the purpose of this investigation, the following assumptions were made:

1. In pre-collapse femoral heads the femoral and acetabular cartilage is unaffected and will act as a cushion between each bone surface, distributing the joint forces over a greater area than would be predicted by Hertzian theory.
2. The location of failure in the femoral head will be in regions where an abnormal stress distribution is present regardless of whether the failure event is acute or as a result of fatigue.

Based on these assumptions, a model that applied a focussed load to the femoral head through a relatively soft, conforming interface was generated. Loading under displacement control was used to maintain consistency with the simulations performed in Chapter 3. While the load pattern may not have represented the true size of the contact region and magnitude of the stress *in vivo*, it provided a consistent method of assessing the relative performance of different model geometries while eliminating unrepresentative discontinuities at the edge of the contact area and distributing the load over a larger proportion of the head.

In the concept design for conforming contact, the flat platen was replaced with a stiff semi-circular platen. This was in conforming contact with a compliant body (the filler) that in turn conformed to the femoral head (Figure 64). Load application through a semi-circular platen was preferable because loading under displacement control via a flat platen was shown to generate uniform stress throughout the femoral head (Figure 69).

The stress distribution within the femoral head was affected by the radius of the platen, the stiffness of the filler and the distance between the femoral head and platen. The aim of this method development study was to generate a configuration that would allow consistent comparison across different simulated AVN cases. The objectives for this study were to

identify how the different parameters affected stress and to choose a single configuration in which to challenge the cases in the rest of this chapter.

A preliminary parametric sweep was performed to identify trends in the response to changes in platen radius, separation between the head and platen and filler modulus. This demonstrated that the peak stress caused by conforming contact tended to be lower than that found in simulations of direct contact between a flat platen and the femoral head. Design of Experiments (DoE) was used to evaluate the interactions between the parameters and identify a configuration that would be used in subsequent studies. The parameters for each of the simulations in the parametric sweep and design of experiments are recorded in Table 32. A final refinement to the methodology was performed to achieve a displacement of 0.5mm at the apex of the femoral head using the parameters defined in the DoE.

Both peak von Mises (VM) stress in the head component and displacement at the most superior node were recorded as outcome measures.

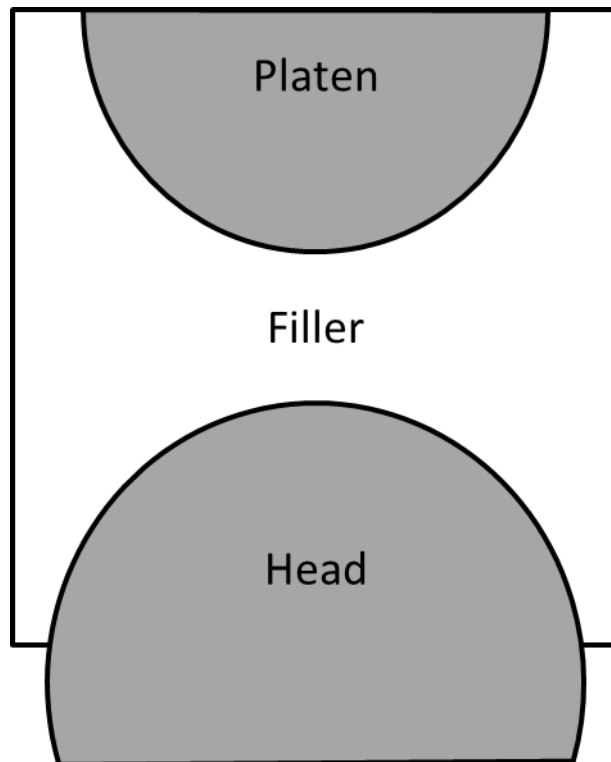


Figure 64. Schematic diagram of the conforming contact concept assembly. The assembly consisted of a relatively stiff, hemispherical platen, a filler of relatively low modulus and a simulated femoral head. The simulated femoral head had a diameter of 50mm and extended 10mm beyond the hemisphere. In the design of experiments the diameter of the platen, the distance between the platen and head and the modulus of the filler were varied.

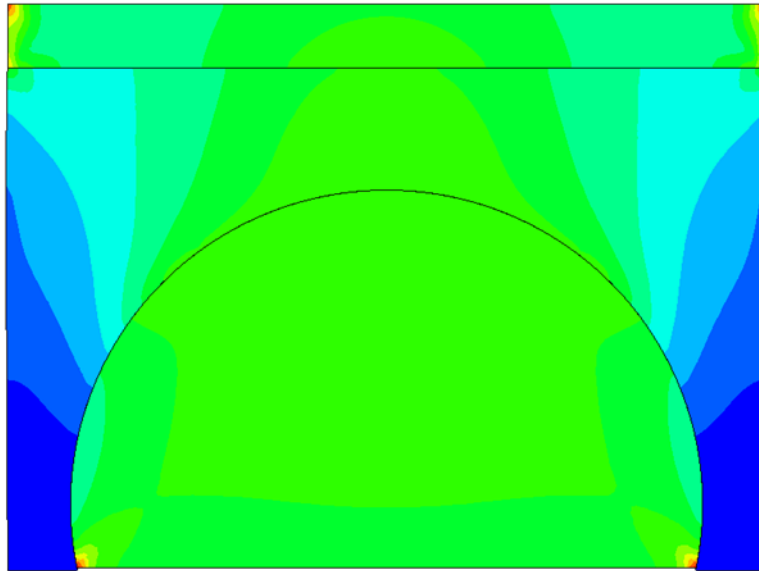


Figure 65. Distribution of von Mises stress in the femoral head caused by loading the filler component using a flat platen until a displacement of 0.5mm at the apex of the femoral head was achieved. The concept geometry shown in Figure 63 was chosen because loading via a flat platen was found to generate near-uniform stress throughout the head.

Table 31. List of parameters used in the study performed to develop a strategy for loading disease models through a conforming contact. The study was broken into three stages: a parametric sweep (n=25); a formalised Design of Experiments (n=8) and a final refinement stage (n=2).

Study	Filler modulus (MPa)	Platen radius (mm)	Separation (mm)	Applied displacement (mm)	Target element edge length at interfaces (mm)				
Parametric sweep	500	20	20	0.5	0.5				
	150			1.7					
	300		15	15		1.7			
						1.1			
						1.0			
						0.5			
						0.5			
						0.5			
	600		10	10		0.5			
	900					0.5			
	1200	0.5							
	100	10				10	0.5		
							0.5		
							1.0		
							1.4		
	150	10				10	1.0		
	150						1.1		
	300						10	10	1.0
			0.8						
			0.5						
			0.9						
	150		10	10			1.0		
	100						10	10	1.2
									1.0
									1.6
50	10	10	1.0						
50			10	10	1.0				
					1.6				
					2.6				
Design of experiments	50	20	15	1.0					
	10	20	15	1.0					
	50	20	10	1.0					
	10	20	10	1.0					
	50	5	15	1.0					
	10	5	15	1.0					
	50	5	10	1.0					
	10	5	10	1.0					
Displacement refinement	50	20	10	1.67					
	50	20	10	1.68					

4.3.2 Method

In this study a methodology for applying a distributed load across the surface of the head-lesion assembly was developed based upon the concept design shown in Figure 64. This study refined the concept design by defining the platen geometry, separation between the head and platen, the filler modulus and the displacement applied to the platen.

Friction interaction criteria with a co-efficient of friction of 1 were used for the platen-filler and filler-head boundaries. A friction interaction was used because of the large deformations expected at the upper and lower edges of the relatively soft filler.

The inferior surface of the head was pinned to maintain consistency with the previous studies and represent the experimental disease model.

Upon selection of the optimum configuration and refinement of the applied displacement, the geometry of the filler was adapted to remove stress concentrations in the surface of the femoral head. The final configuration was used for the rest of the studies in Chapter 4 and Chapter 5.

Four factors that would influence the magnitude and distribution of the stress within the femoral head were identified:

1. The displacement applied to the rigid platen.
2. The radius of the rigid platen.
3. The distance between the apices of the platen and femoral head.
4. The modulus of the filler material.

A parametric sweep was used to establish trends in the way that these parameters affected two outcome measures: Peak VM stress in the head and displacement at the apex of the head. Four geometry models were generated and the modulus of the filler and displacement applied to the platen varied according to the parameters defined in the parametric sweep section of Table 30. The parametric sweep confirmed that each factor influenced the outcome and that their effects were approximately linear. A DoE evaluation was then performed to explore the relationship between each factor.

The relationship between displacement of the platen and stress or displacement in the head was shown to be direct and linear during the parametric sweep investigation so this was not included in the factorial design. Therefore, a three factor full factorial design (Table 32) was used to evaluate the influence of each of the other factors. The full matrix is shown in Table 33. The DoE study identified the main effects of each parameter and interactions. The configuration that gave the highest stress within the set of cases evaluated was identified and defined as the configuration that would be used in the subsequent studies. It is noted that higher stresses could have been achieved, and the DoE provided information that would help define such a configuration. However, no further attempt was made to increase peak stress because the aim was to use data generated with this methodology to compare between cases and not to draw conclusions based on absolute outcomes.

Upon completion of the DoE study, two further simulations were performed with the chosen configuration to establish the platen displacement that would cause a 0.5mm displacement at the apex of the head/lesion construct.

Table 32. Factorial design used to evaluate the effect of platen radius, separation between apexes and filler modulus on the stress distribution and displacement in the femoral head.

Factor	Platen radius (mm)		Separation (mm)		Filler Modulus (MPa)	
Level	Low	High	Low	High	Low	High
Value	5	20	10	15	10	50

Table 33. Design of experiments matrix used to investigate the effect of varying platen radius, separation between the platen and head and filler modulus on the peak von Mises stress in the head and the displacement of the most superior node in the head. The value attributed to each level is shown in Table 32.

Case	Platen radius	Separation	Filler modulus
1	High	High	High
2	High	High	Low
3	High	Low	High
4	High	Low	Low
5	Low	High	High
6	Low	High	Low
7	Low	Low	High
8	Low	Low	Low

4.3.3 Results

This study refined the original concept design for a method of simulating the application of load to the femoral head through a soft conforming medium. The interaction between each factor in the design was also established. Case three in the DoE was chosen as the preferred design: a large platen radius (20mm) combined with low separation (10mm) and high filler modulus (50MPa). These parameters were chosen as the standard for the remaining work.

The results associated with each case described in Table 33 are recorded in Table 34. Filler modulus had the most significant effect on both displacement (Figure 66) and VM stress (Figure 67). Separation distance had the second most significant effect on peak VM stress followed by platen radius. In terms of the magnitude of the change in response, separation distance and platen radius had an equal but opposing effect on displacement.

The responses were inter-related but the relationship was not perfectly linear due to the interactions between the three input factors. This was highlighted by comparing the responses for Case 1 to Case 7 (both high filler modulus) and Case 2 to Case 8 (both low filler modulus): The same displacement was measured for each of these pairs but the peak VM stresses were different.

This was attributable to two factors:

1. For the displacement response (Figure 68) the effect of platen radius was of equal magnitude to and the inverse of the effect of separation so the displacement when both variables were high was equal to the displacement when both variables were low.

2. The peak VM stress response (Figure 69) was more sensitive to separation than to platen radius so there was a difference between the responses when both variables were high compared to the response when both variables were low.

The interactions plots for displacement at the apex of the femoral head (Figure 68) and peak VM stress (Figure 69) showed that none of the factors interacted strongly but confirmed that the combination of high separation and platen radius was confounded with the combination of low separation and low platen radius for the displacement response.

Two further cases were run with the same configuration as case 3 but with displacements of 1.67 and 1.68mm applied to the platen. These iterations confirmed that the displacement at the apex of the head varied linearly with displacement applied to the platen and resulted in a 0.5mm displacement at the apex and a peak VM stress of 6.4MPa in the same location. It was noted that this ratio of applied displacement to measured displacement was only valid for the particular head configuration used and the relationship between applied and measured displacements was evaluated further in Sections 4.4.3 and 4.5.3.

The stress distribution for Case 3 was compared to the stress distribution in the equivalent head geometry when it was compressed using a flat platen in Figure 70. The stress in the head compressed using conforming contact was less concentrated at the apex than in the flat contact case and there was no evidence of flattening.

However, stress concentrations coinciding with the edge of the filler were observed the filler material was extended to cover the whole surface of the head and to move these to the inferior corners of the simulated head. These regions were remote from that considered in the RR score calculations (Figure 71). The magnitudes of the displacement and peak stress in the apex of the head were re-evaluated and found to be unchanged and the configuration shown in Figure 71 (right) was defined as the standard for all subsequent studies. This configuration resulted in a distributed load being applied to the simulated head over an arc of approximately 140°.

Table 34. Results associated with each case described in Table 33. These results were used to identify the configuration that would be used in subsequent studies and to identify interactions between each factor.

Case	Platen radius	Separation	Filler modulus	Peak von Mises stress at apex (MPa)	Displacement at apex (mm)
1	High	High	High	2.70	0.20
2	High	High	Low	0.65	0.05
3	High	Low	High	3.70	0.30
4	High	Low	Low	0.98	0.08
5	Low	High	High	2.30	0.16
6	Low	High	Low	0.53	0.04
7	Low	Low	High	3.40	0.20
8	Low	Low	Low	0.83	0.05

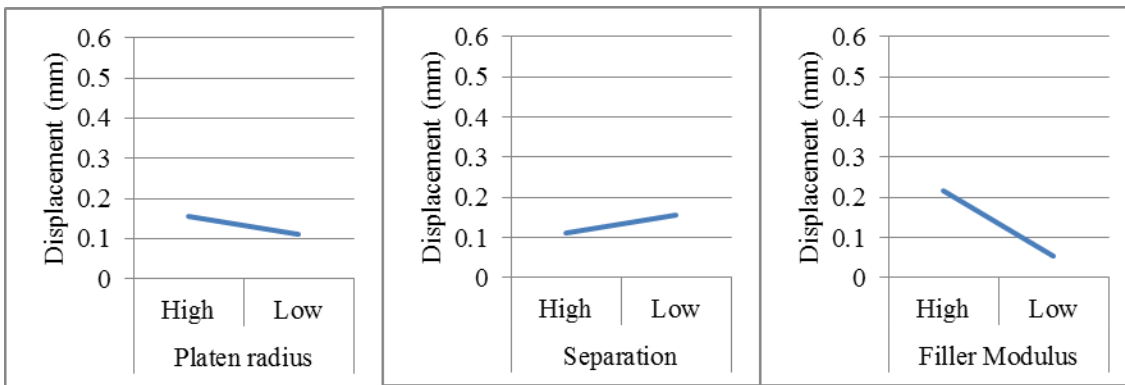


Figure 66. Main effect plots for DoE evaluation of the effect of platen radius, separation and filler modulus on displacement at the apex of the head. Filler modulus had the largest effect on VM stress followed by separation. The responses to changes in platen radius and separation were of equal magnitude but inverted.

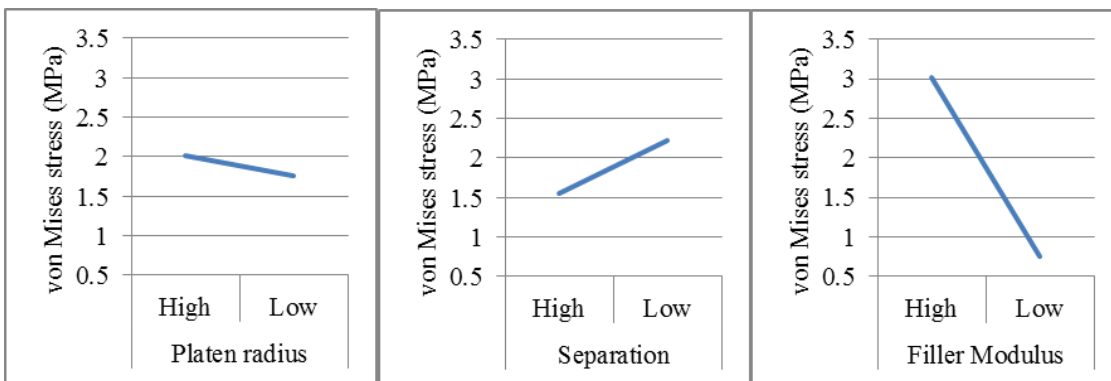


Figure 67. Main effect plots for DoE evaluation of the effect of platen radius, separation and filler modulus on the peak VM stress at the apex of the head. Filler modulus had the largest effect on VM stress followed by separation. The effect of platen radius on VM stress was negligible compared to the other two factors.

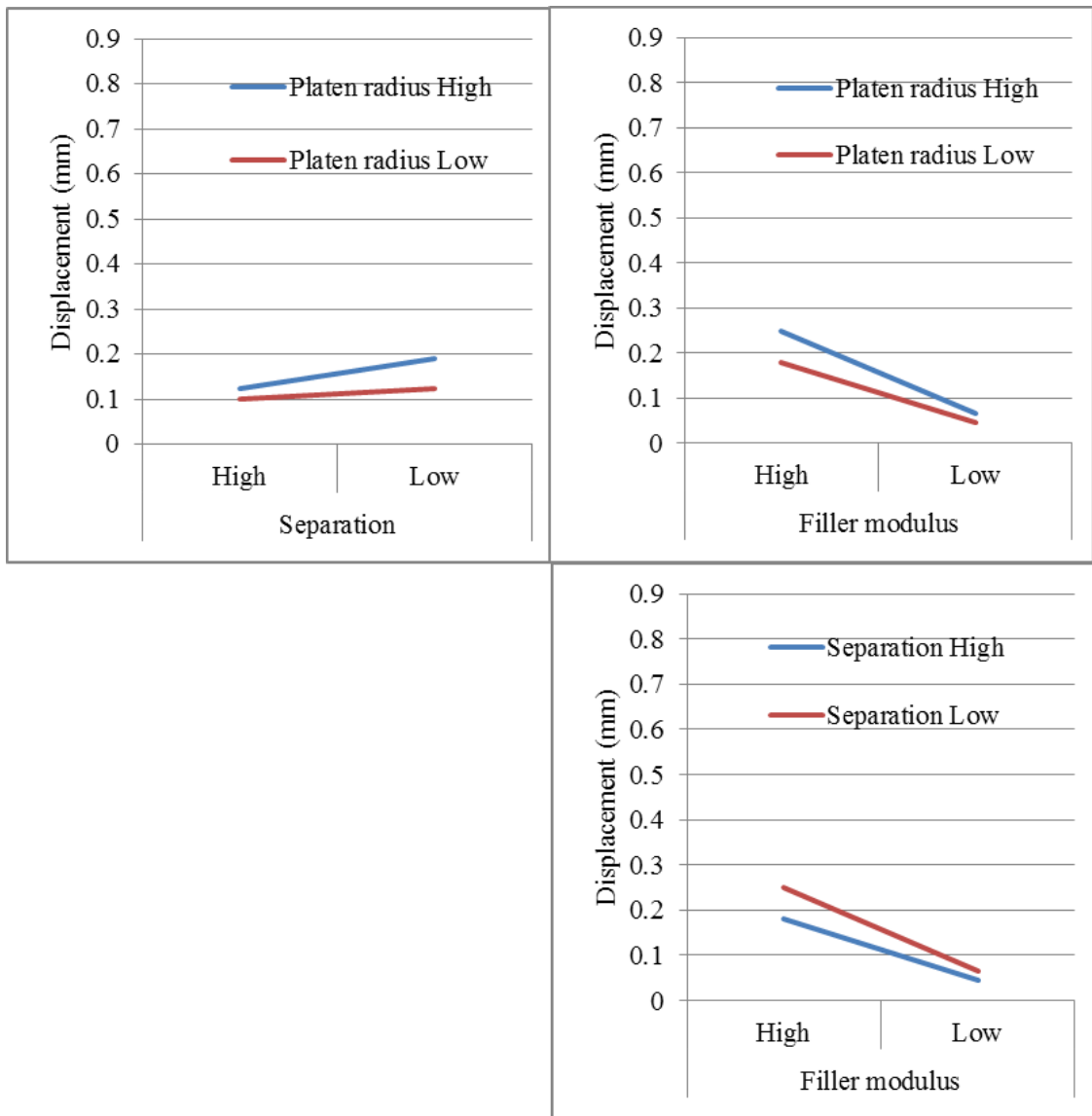


Figure 68. Interaction plots for DoE evaluation of the effect of platen radius, separation and filler modulus on the displacement at the apex of the head. The plots indicate that none of the factors interacted strongly but that the combination of high separation with high platen radius resulted in the same displacement as the combination of low separation with low platen radius. No other combination of the three factors resulted in the same confounded result.

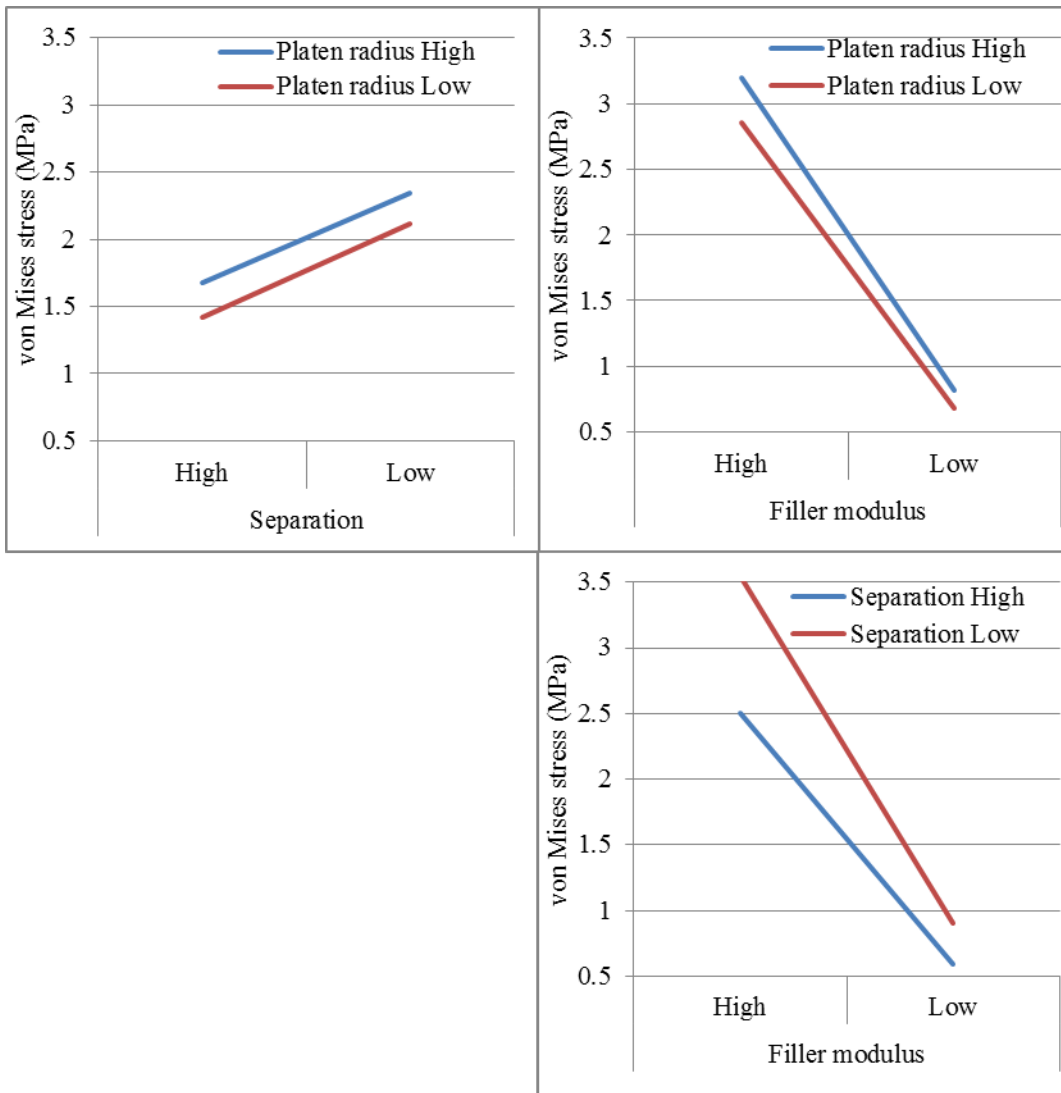


Figure 69. Interaction plots for DoE evaluation of the effect of platen radius, separation and filler modulus on the peak VM stress at the apex of the head. The plots indicate that none of the factors interacted strongly and that the combination of high platen radius, high filler modulus and low separation gave the highest peak VM stress. This equates to case three.

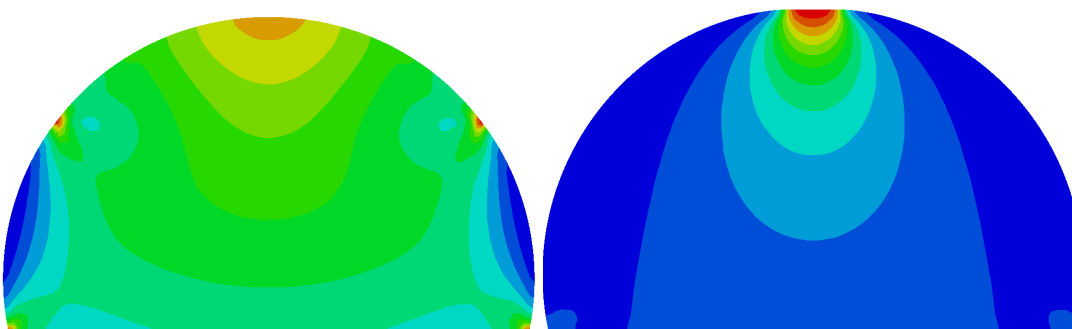


Figure 70. Left: Plot of von Mises stress distribution in a femoral head for the conforming contact methodology defined by this study. Right: Plot of von Mises stress distribution in the same head under direct compression using a flat platen. The stress under conforming contact was less concentrated at the apex and there was no flattening. However, it was noted that two areas of high stress, located at approximately 45° to the apex, were present in the left hand image.

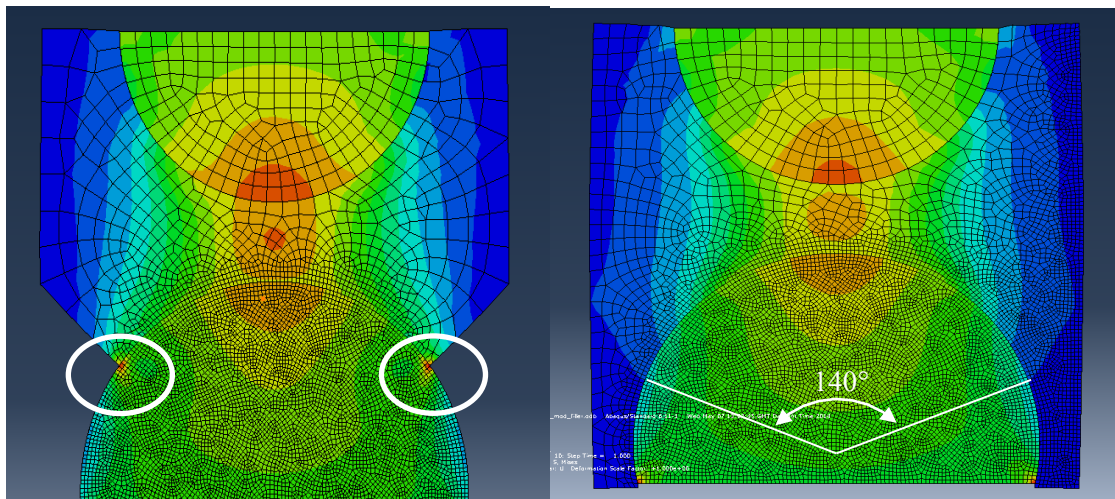


Figure 71. Left: Initial assembly for case three with white ovals indicating the undesirable stress concentrations; Right: Final model configuration showing the filler extended to encompass the entire head, thus moving the stress concentrations found in the initial design to the bottom edge of the simulated head. This location was outside the region considered in the RR evaluations. The platen had a radius of 20mm and was separated from the head by 10mm. This configuration exerted a surface load over an arc of approximately 140°.

4.3.4 Discussion

A more physiologically representative load distribution was achieved by loading the simulated femoral head via a relatively soft conforming body to generate a contact region without stress concentrations. The size of the contact region and magnitude of the applied load could be adjusted independently by varying the parameters of the loading mechanism. This study confirmed the sensitivity of the risk score to the method of load application and it was concluded that a more physiologically representative method of loading the experimental disease models would be required in future *in vitro* studies. Using the chosen configuration, load was applied over approximately 140° of the surface of the femoral. This is larger than the affected region caused by the approach used by Yang *et al.*, (2002) but the previous method used an abbreviated surface similar to that shown in Figure 72 (Left). In the current work, such an approach was found to produce unrealistic stress concentrations in the region of the lesion boundary and it is concluded that the revised approach offers an improved method of creating a physiologically relevant load pattern.

This study defined a standard methodology for all subsequent studies in this thesis and provided an insight into the effect of each of the model parameters on the response. The conforming contact simulation strategy was not intended to provide a validated means load transfer that recreated the natural hip in terms of stress distribution and magnitude. It provided a means of comparing between different simulated lesions using a more physiologically representative means of load transfer onto the femoral head than direct load transfer via a flat platen.

The head was deformed by 0.5mm in the simulations where load was applied via a flat platen (Figure 38). The same displacement was achieved on a solid femoral head with a modulus of 300MPa in the final conforming contact model design (case 3) by applying a displacement of

1.7mm to the semi-circular platen. This resulted in a peak VM stress of 6.4MPa which was in the region of the UCS established for the surrogate bone used in the experimental disease model (Section 2.3) but in the lowest quartile of the peak VM stresses in the FE simulation using a flat platen. The observation that stress distribution was affected by the method of load application warranted further investigation and defined the focus of the second study in this chapter (Section 4.4).

There are some limitations to this methodology. A fixed displacement to the platen was applied and while this resulted in a displacement of 0.5mm at the apex of the simulated solid femoral head, the parametric study performed in Section 3.3 showed that the elastic modulus of the femoral head was affected by the location and material properties of a simulated lesion. It was therefore hypothesised that heads with a lower elastic modulus would experience greater displacements when these parameters were used. However, femoral heads with a necrotic lesion are less stiff than healthy femoral heads and are more likely to fracture so the increase in displacement (or strain) with reducing elastic modulus is physiologically relevant.

Another limitation is that although the configuration chosen caused the highest stress in the head compared to the other configurations tested, the magnitude of the stress was driven by the input variables used and the final methodology does not represent an optimised configuration. The aim of this study was not to generate a physiologically relevant load condition, but to develop a method that would allow comparison between cases in each study. The result of the DoE showed the trends associated with each variable and would facilitate optimisation in future studies where a target stress magnitude was required. A target VM stress could be achieved by varying the filler modulus and the separation between the platen and apex of the femoral head. The displacement at the femoral head was shown to vary linearly with displacement at the platen. The confounding effect of platen radius and separation on displacement is logical: A large platen will displace a greater area of filler and therefore a larger proportion of the surface of the femoral head will be displaced. However, increasing the separation between the platen and head will tend to reduce displacement at the head because more of the applied displacement will be absorbed through elastic deformation of the filler itself. This is a useful observation as it highlights the potential to vary the stress caused in the head and displacement at its apex as independent variables.

4.3.5 Conclusion

A simple FE methodology that simulated compression of a femoral head via a soft conforming body was developed and the effect of varying its key parameters was investigated. This is a more physiologically representative method of load application with scope for further refinement both *in silico* and *in vitro*.

This is a novel approach for transferring load in a physiologically representative way. Although only evaluated computationally in 2D, the method could be re-created and therefore validated in 3D *in vitro*. It offers the potential to vary the applied stress and displacement independently. This potential was highlighted and explained by results of the DoE study which showed that different peak stresses could be obtained for the same measured displacements.

4.4 Simulation of experimental disease models using conforming contact

4.4.1 Introduction

In Section 3.3.3 the geometry and material properties specific to the experimental disease models (Chapter 2) were recreated *in silico*. The RR scores for each of the experimental disease model specific simulations were distinct from each other but it was found that the contact between the flat platens and heads caused high stress in a relatively concentrated area and that this would influence the relative risk score when the boundary was very close to the contact region. For example the plug in case XI was close to the surface and directly beneath the part of the head in contact with the rigid platen (Table 25). This model had the highest stress at the interface between the head and lesion compared to the other models (Figure 62). However, because the load was concentrated over a small area the RR scores were indistinguishable from several of the other cases (Figure 61).

The effect of changing the method of load application from a solid, flat platen to the conforming contact configuration developed in Section 4.3 on the peak stress and RR scores was evaluated in this study. The aim was to establish whether a link existed between the two methods of load application. The same head and pin geometry (Table 15) was used but the flat platen was replaced with the conforming contact geometry shown in Figure 71 (right).

In addition to comparing the two methods of load application, this study allowed the effect that the stiffness of the femoral head had on the displacement at the apex of the femoral head to be evaluated.

4.4.2 Method

Simulations of experimental disease models compressed using flat platens were described in Section 3.2. The models used in the current study were modified by removing the flat platen and replacing it with the filler and semi-circular platen defined in Section 4.3: A platen with a 20mm radius, separated from the head / lesion assembly by 10mm with the space between occupied by a filler component with a modulus of 50MPa. The platen was displaced by 1.7mm to maintain consistency with all other conforming contact studies. The RR scores defined in Section 3.2.4 were used to compare the results of this study to the results reported in Section 3.3.2. In addition, the maximum VM stress in the outer and inner surfaces, the maximum

difference in VM stress and the displacement at the apex of the femoral head were also measured.

Comparison between the flat and conforming contact results was made by testing for correlation using the Pearson product-moment correlation coefficient.

4.4.3 Results

The maximum VM stress tended to be lower in the conforming contact cases than in the equivalent cases under direct compression (Figure 72, Figure 73 and Figure 74). This result was consistent with the findings of the method development study (Section 4.3). Despite the lower VM stresses, the magnitude of the RR scores (inner, outer and difference) tended to be higher in the conforming contact cases (Figure 75, Figure 76 and Figure 77). The increased RR scores were the result of a significantly higher number of elements identified as having stress above the threshold (Table 34).

Table 35. Number of elements identified as having stress above the threshold in the relative risk calculations for simulations of the experimental disease models using flat and conforming contact.

	Average number of elements		
	Outer	Inner	Difference
Flat	6	9	5
Conforming	19	16	27

Von Mises stress

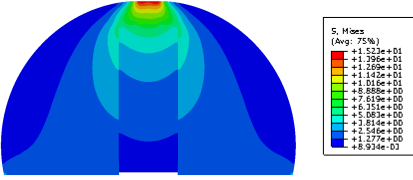
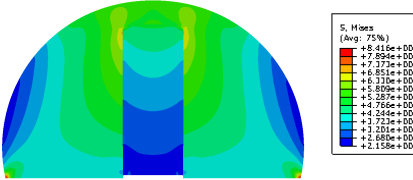
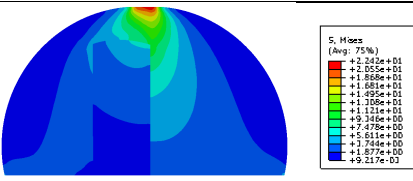
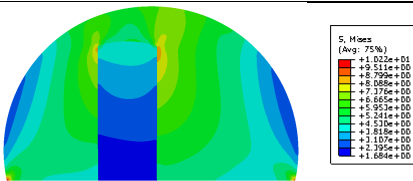
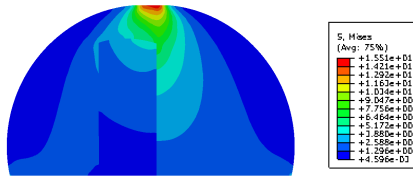
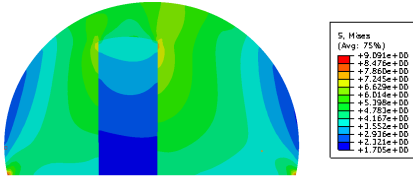
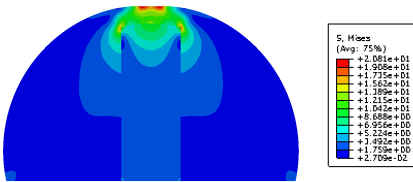
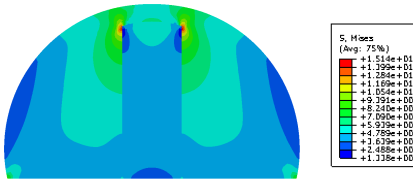
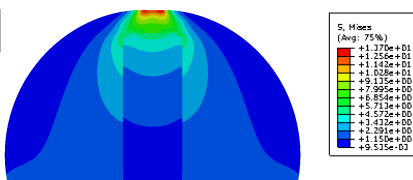
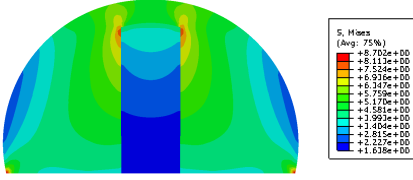
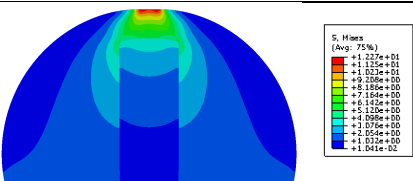
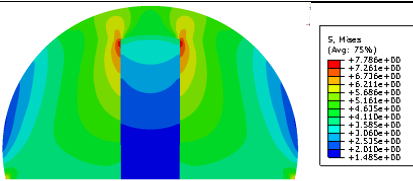
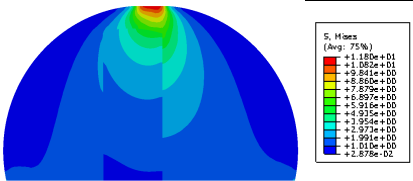
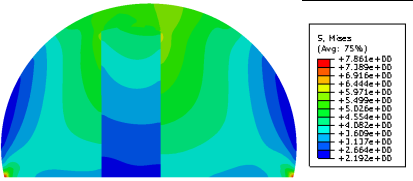
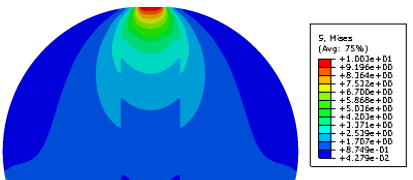
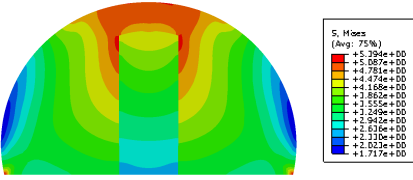
The stress distribution was evaluated qualitatively in Table 36. This highlighted that the magnitude and location of the peak VM stress at the interface changed not only with plug position within the experimental disease model but also with the method of applying load.

The maximum differences in VM stress between the two surfaces in each case were positively correlated between both loading regimes ($r=0.90$) (Figure 72).

The maximum VM stresses measured in the outer surfaces were also positively correlated ($r=1.0$) (Figure 73). In all instances except case XVII the stress under direct compression was higher. The magnitude in case XVII was almost the same under both load conditions.

The maximum VM stress measured in the inner surfaces was also positively correlated ($r=1.0$) (Figure 74). With the exception of case XIX, the results for the conforming contact cases were all within 1MPa of each other compared to a range of 9MPa under direct contact. The results of the significance and correlation tests are summarised in Table 37.

Table 36. Visual comparison of the von Mises stress distribution in the experimental disease model specific simulations loaded via a flat platen or through a conforming contact. Dark blue indicates areas of lowest stress; red indicates the areas of highest stress.

Experimental disease model	Flat platen	Conforming contact
I		
IV		
X		
XI		
XVI		
XVII		
XIX		
XX		

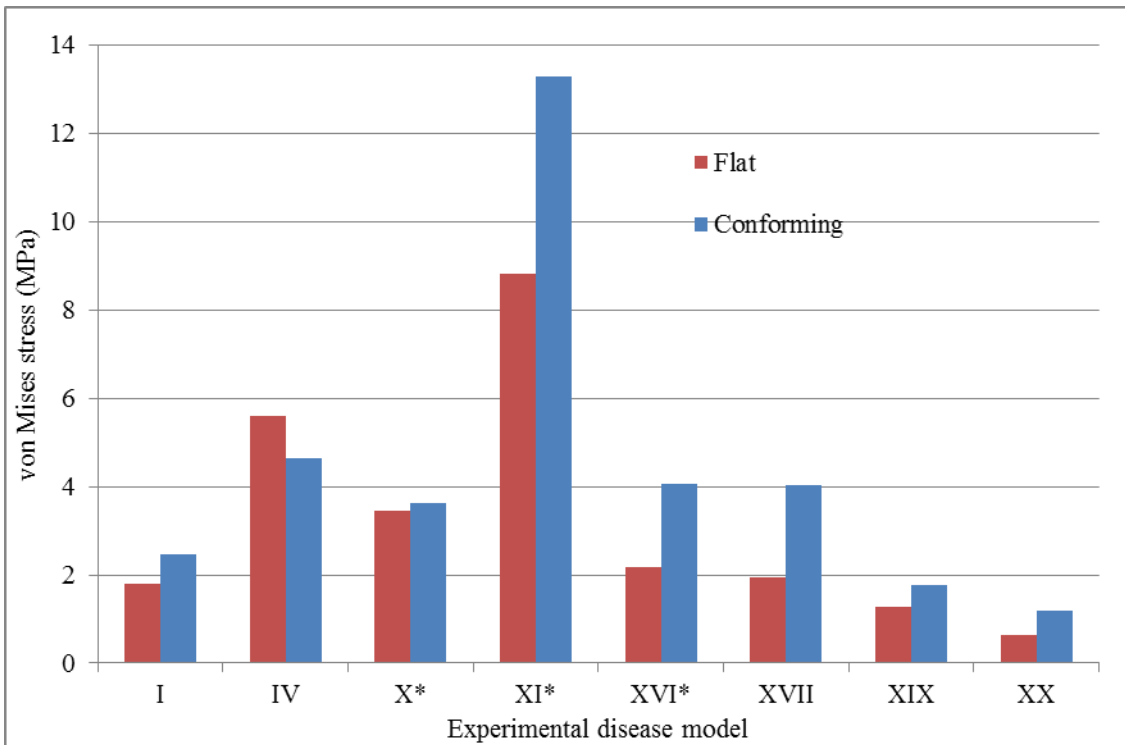


Figure 72. Maximum difference in von Mises stress measured between the inner and outer surfaces for the simulated experimental disease models under flat and conforming load cases. The results were highly correlated ($r=0.95$).

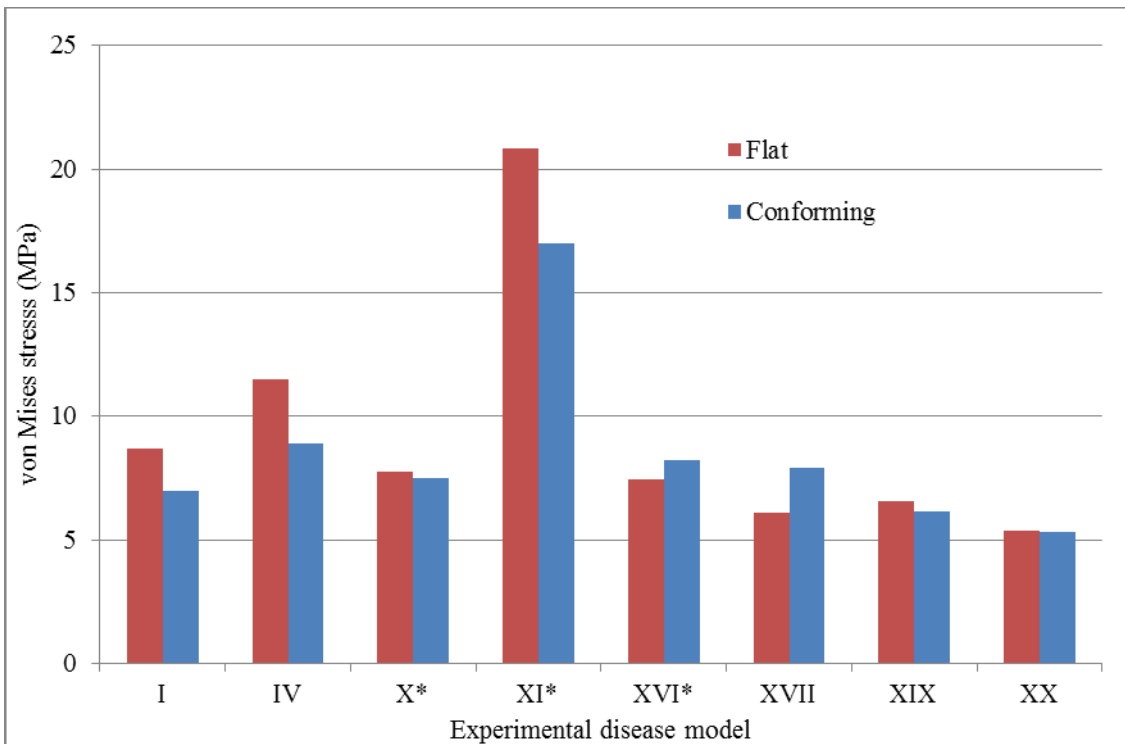


Figure 73. Maximum von Mises stress measured in the outer surface for the simulated experimental disease models under flat and conforming load cases. The sets were highly correlated ($r=0.95$).

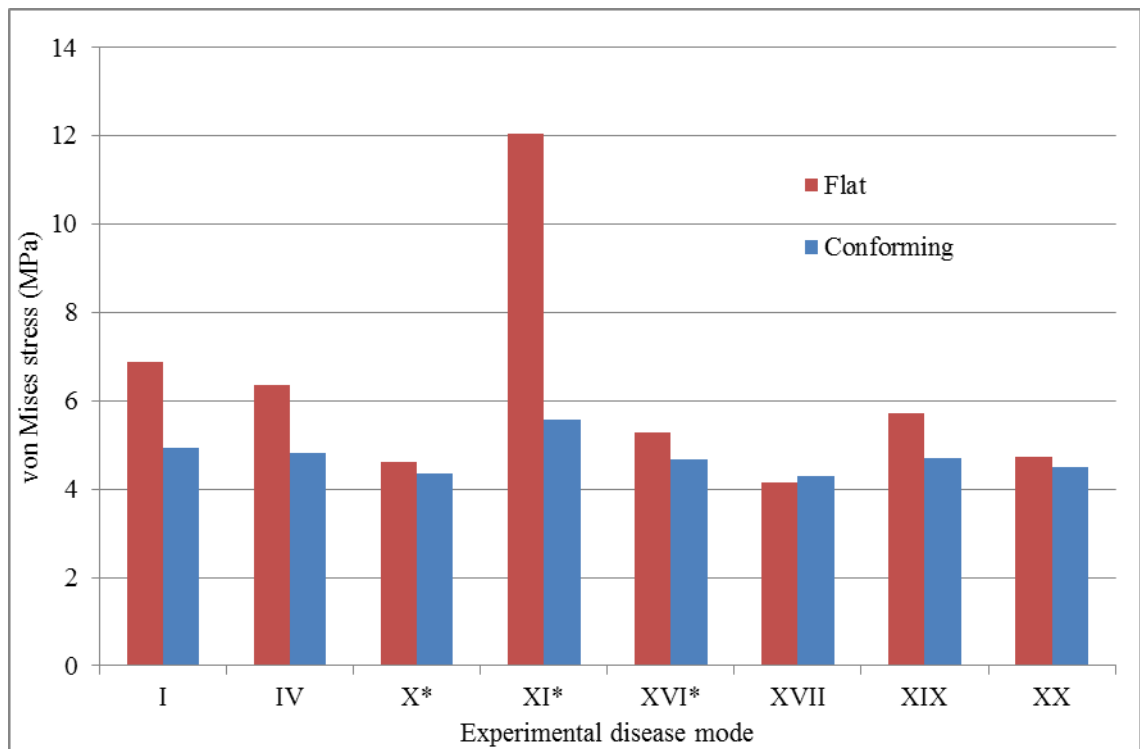


Figure 74 Maximum von Mises stress measured in the inner surface for the simulated experimental disease models under flat and conforming load cases. The results were poorly correlated ($r=0.36$).

Table 37. Tests for correlation between the maximum von Mises stress values obtained at the outer and inner surfaces and the difference between the two obtained using two load conditions were performed by calculating a Pearson product-moment correlation co-efficient. The results for all three measures were highly correlated.

Outcome: Max. von Mises stress	Difference	Outer	Inner
Correlation coefficient ($r=$)	0.9	1.0	1.0

Relative risk

The RR_D scores obtained using the two methods of load application were poorly correlated ($r=0.26$). There was greater variation between the cases in the conforming contact set than between the cases in the set compressed by a flat platen (Figure 75).

The RR_O scores were also poorly correlated ($r= 0.35$). This lack of correlation was noteworthy because the peak VM stress in the outer surface was highly correlated ($r=1$) so the differences in RR_O scores obtained using each methodology were driven by the change in the area identified by the RR score algorithm. The variation in RR_O scores within the conforming contact set was also greater than between the cases in the set compressed by a flat platen (Figure 76). The RR_I scores were poorly correlated ($r=-0.1$).

The results of the correlation tests for each RR score are summarised in Table 38.

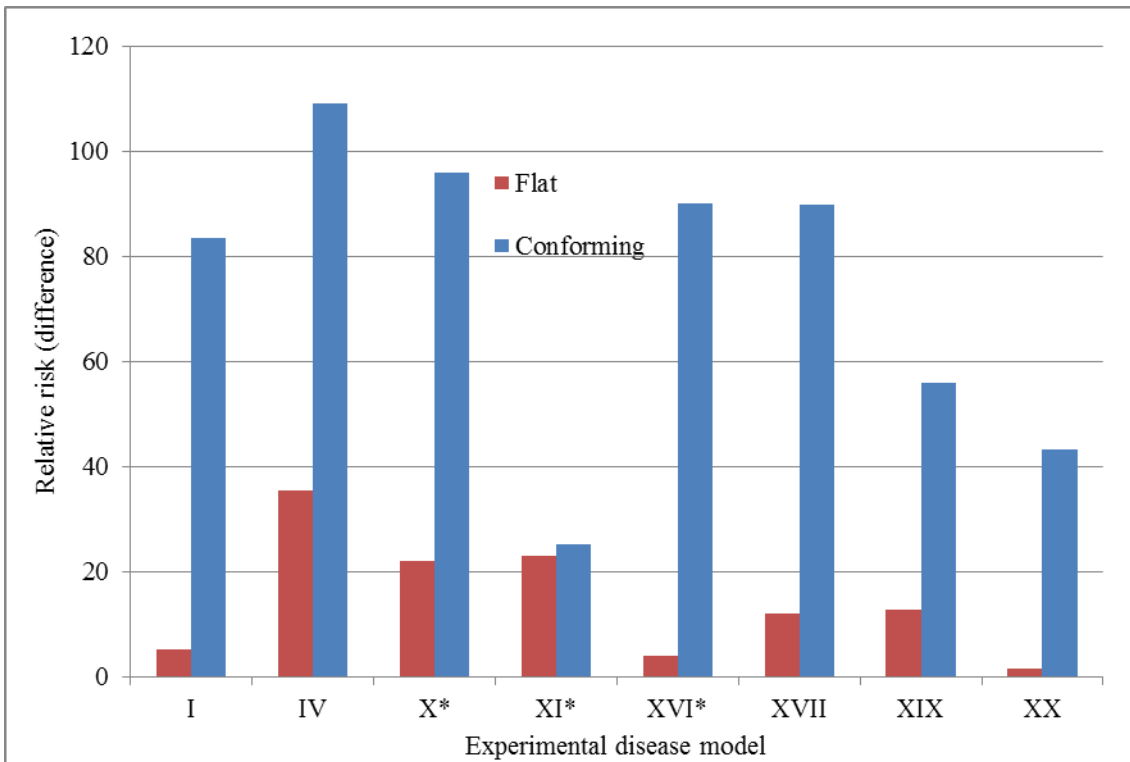


Figure 75. Relative risk score calculated for the difference between the inner and outer surfaces for the simulated experimental disease models under flat and conforming load cases. The experimental disease models marked with an asterisk were found to have fractured during the test. The results for the flat and conforming load cases were not correlated ($r=0.3$).

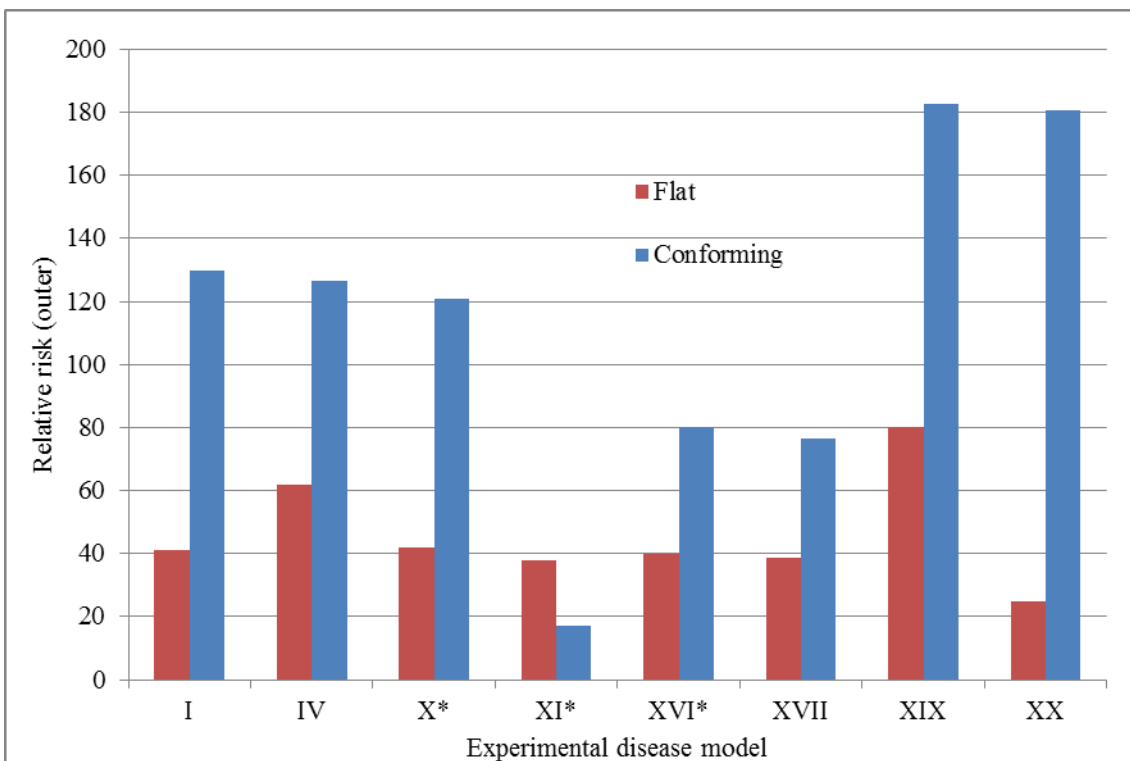


Figure 76. Relative risk score calculated for the outer surface for the simulated experimental disease models under flat and conforming load cases. The experimental disease models marked with an asterisk were found to have fractured during the test. The results for the flat and conforming load cases were not correlated ($r= -0.01$).

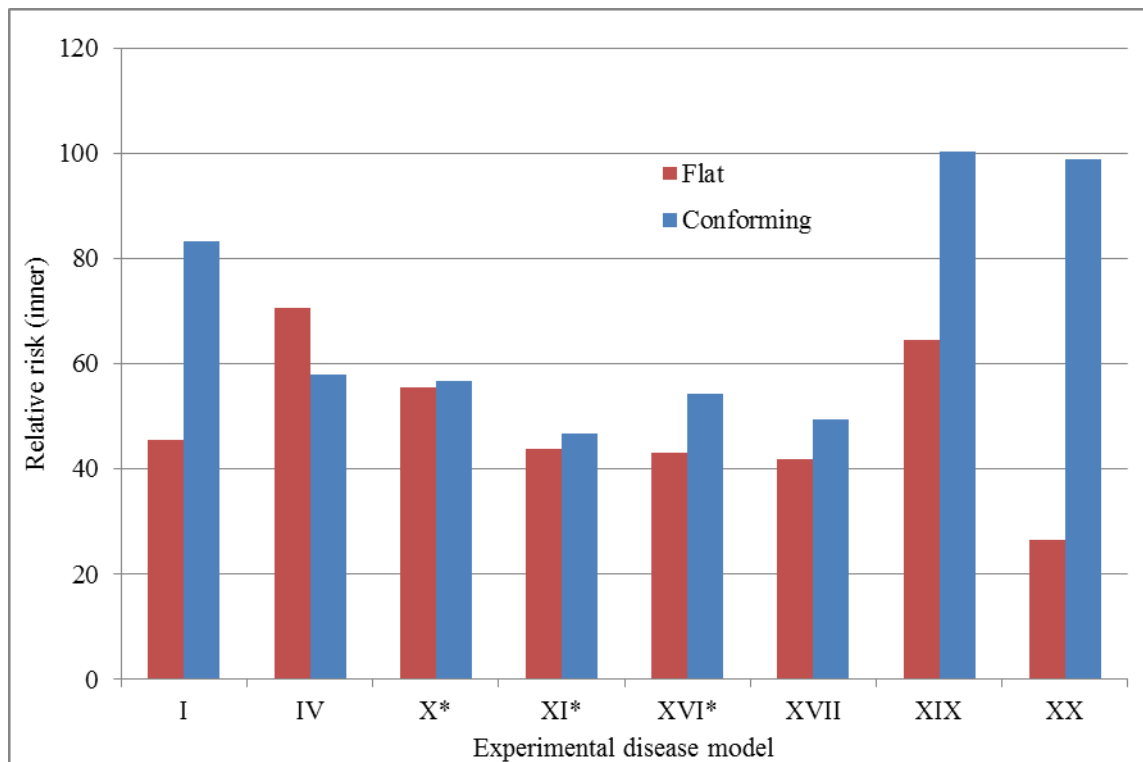


Figure 77. Relative risk score calculated for the inner surface for the simulated experimental disease models under flat and conforming load cases. The experimental disease models marked with an asterisk were found to have fractured during the test. The results for the flat and conforming load cases were not correlated ($r=0.18$).

Table 38. Tests correlation between the three relative risk outcome measures obtained using two load conditions indicated that there was poor correlation in all three outcome measures.

Outcome: Relative risk	Difference	Outer	Inner
Correlation coefficient ($r=$)	0.26	0.35	-0.1

Displacement at the apex

Displacements measured at the apex of the femoral head caused by application of a 1.7mm displacement to the semi-circular platen are recorded in Table 40. The multivariate analysis in Section 3.3.4 demonstrated that head modulus had the strongest influence on elastic modulus in the experimental disease models. The relationship between head modulus and displacement at the apex is shown in Figure 78. There was a strong negative correlation between these factors ($r=-0.9$). The multivariate analysis showed that the plug modulus and its location also influenced the elastic modulus of the femoral head but only weak correlations between these factors and the measured displacement were observed (Table 40).

Table 39. Displacements measured at the apex of the femoral head in the experimental disease models simulations. These displacements are the result of a displacement of 1.7mm being applied to the hemispherical platen during the simulation.

Experimental disease model	Displacement at the apex (mm)
I	0.59
IV	0.45
X	0.57
XI	0.49
XVI	0.63
XVII	0.66
XIX	0.64
XX	0.68

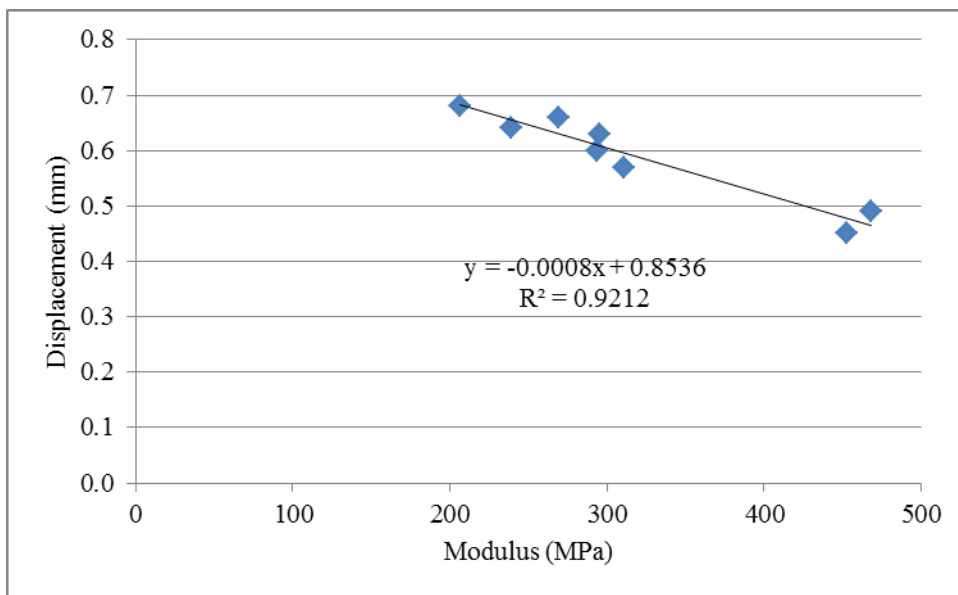


Figure 78. The relationship between the modulus of the femoral head in the simulated experimental disease model and the displacement at the apex of the femoral head caused by applying a displacement of 1.7mm to the semi-circular platen in the conforming contact simulations was shown to have a strong negative correlation ($r=-0.96$).

Table 40. Pearson product-moment correlation coefficients (r) for the relationship between displacement at the apex of the femoral head caused by applying a displacement of 1.7mm to the semi-circular platen in the conforming contact simulations and head modulus, plug modulus (Table 26), distance between the top of the plug and apex of the head and eccentricity (Table 15). Only head modulus showed a strong (negative) correlation.

Variable	r
Head modulus	-0.96
Plug modulus	-0.70
Distance between top of plug and apex of head	-0.10
Eccentricity	-0.44

4.4.4 Discussion

The comparison between simulations of experimental disease models compressed directly using a flat platen or indirectly via a conforming filler showed that, in general, the conforming contact scenario resulted in lower peak VM stresses but, because the load was distributed over a larger area, a larger region of the lesion boundary was involved and hence a higher overall relative risk score was obtained for the conforming contact cases.

The importance of simulating the applied load in a physiologically relevant way was highlighted by cases IV, XVI and XVII. In each case the magnitude and extent of the peak stresses and the extent of the stress discontinuities changed depending on the method of load application. This was reflected most obviously by the change in the RR scores (Table 41). Both the magnitude of the risk scores and ranking of the cases were affected by the change in method of load application. In comparative studies, the magnitude of the score is unimportant but ranking is critical. Although the conforming contact methodology was not validated, it was a closer approximation of load transfer within a hip joint than direct compression using a hard, flat platen and is recommended for future experimental and computational disease models. This observation highlighted the need to further explore the relationship between the load vector and the location and orientation of the lesion boundary. This became the subject of the third study in this chapter.

Table 41. Comparing the relative risk scores obtained using flat and conforming contact simulations for cases IV, XVI and XVII highlighted the sensitivity of both the experimental disease model and relative risk score to the method of load application. The scores obtained using the conforming contact protocol were higher and the cases were ranked differently than when direct compression using a flat platen was used.

Case	RR _D		RR _O		RR _I	
	Flat	Conforming	Flat	Conforming	Flat	Conforming
IV	35.5	4.2	61.8	126.5	70.6	57.9
XVI	4.1	90.1	39.7	80.0	43.1	54.4
XVII	12.1	89.8	38.7	76.4	41.9	49.3

Comparing cases XIX and XX provided an example of the need for a RR score that considered both the size and magnitude of stress concentrations caused by lesions within the femoral head.

Case XIX had an eccentric pin resulting in a relatively large region (6mm) of high stress at one corner of the plug. Case XX was concentric so the highest stresses were in the central dome of the plug over a smaller region (3mm).

Under direct compression, both cases had similar peak VM stress in the outer surface (6.6MPa and 5.4MPa respectively) and inner surface (5.7 and 4.7 MPa respectively) making it difficult to differentiate between them. The difference between the inner and outer surfaces for case XIX was higher (1.3MPa) than for case XX (0.6MPa) because the interface was in shear and the peak VM stresses on the inner and outer surfaces were in different locations. This was not apparent

in case XX because load was transferred between the head and plug directly and the stress maxima were therefore co-located in each surface. The regions of greatest stress difference were significantly larger for case XIX (5.5mm) than for case XIX (1.5mm). The size of the discontinuity is important (Prendergast and Taylor, 1994) and there is a risk that these two cases would not be differentiated by measures of VM stress in the interface alone.

The RR scores for cases XIX and XX under direct compression are summarised in Table 42. Case XIX had the highest RR scores. This was consistent with the findings of the multivariate analysis study (Section 3.3.2) which demonstrated elevated scores when the head-plug interface was brought closer to the load vector. There was a greater than two-fold difference between RR_O and RR_I , and a fourteen-fold difference in RR_D . Although these scores have not been validated clinically, the increased sensitivity to lesion location compared to using peak stress alone was promising. The outcome measure most sensitive to a change in the method of load application was RR_D . This agreed with the findings of the multivariate analysis (Section 3.3.2).

Table 42. Comparing relative risk scores for cases XIX and XX showed that there was a greater than two-fold difference between the cases using RR_O and RR_I , and a fourteen-fold difference using RR_D .

Case	RR_D	RR_O	RR_I
XIX	12.9	80.2	64.4
XX	1.7	25.0	26.5

The sensitivity of the relative risk scores was again highlighted by this comparison as case XIX had the highest scores under direct compression but case XX had the highest scores under conforming contact.

In the introduction to this chapter (Section 4.1) the hypothesis that compression at the apex of the femoral head would vary inversely with its stiffness in the conforming contact simulations was posed. The results of the parametric study reported in Section 3.3.4 highlighted that the modulus of the femoral head had the strongest influence on elastic modulus of a head with a simulated necrotic lesion but that the other factors also contributed. The results of the current study showed that there was a strong inverse correlation between the modulus of the femoral head and the displacement measured at its apex and therefore the hypothesis was upheld.

4.4.5 Conclusion

This study demonstrated the importance of using a physiologically representative method of load transfer to compress femoral heads and confirmed that direct compression using a flat platen cannot be used as a simulation of physiological load transfer. It also confirmed the hypothesis that the displacement at the apex of the femoral head was inversely correlated to its stiffness and highlighted the improved ability to differentiate between cases when the RR scores were used compared to comparing peak VM stress directly. The outcome measure that was most sensitive to changes in both lesion location and the method of applying load was RR_D .

4.5 Simulation of cone shaped lesions

4.5.1 Introduction

The previous study (Section 4.4) demonstrated the sensitivity of the relative risk scores to the method of load application. Based on this finding, the hypothesis that the orientation of the lesion boundary relative to the applied load would also influence the relative risk score was posed. A study was designed to investigate the influence of lesion geometry and orientation on peak VM stress and RR scores. New, more clinically representative conical lesion geometries were developed to provide insight that could not be obtained using the parallel-sided plug models used in Chapter 3 and the study reported in Section 4.4.

This study was split into three evaluations:

1. Effect of lesion size.
2. Effect of lesion edge location relative to the centre of load application.
3. Effect of non-radial orientation of the surface between the head and lesion.

The case list for this study is shown in Table 43.

Lesions have been referred to as having a conical morphology in clinical descriptions of AVN of the femoral head (Michael A Mont *et al.*, 1998). The first evaluation was used to generate baseline data that related the size of the lesion to the RR score. Three conical lesion geometries, defined by their included angles of 15°, 30° and 45° and symmetrical about the centre of load were generated (Figure 79).

The second evaluation tested the 45° lesion in multiple orientations to separate the effect of lesion size from the effect of the location of the boundary of the lesion relative to the centre of load.

Two additional geometries were developed in the third evaluation. In one configuration the lesion boundary flared outwards in the subchondral region and in the other it closed inwards (Figure 80). The aim was to show the effect that introducing a non-straight lesion boundary had on the relative risk score. These geometries were also tested in multiple orientations.

Table 43. List of parameters for the cases evaluated in the conical lesion study. Five geometries were evaluated: 15°, 30° and 45° cones with radial boundary geometry, a 45° cone that flared outwards at the surface (acute boundary geometry) and a 45° cone that closed inwards at the surface (obtuse boundary geometry). The 45° variants were evaluated at different orientations relative to the load vector.

Evaluation	Cone angle (°)	Orientation relative to load vector (°)	Boundary geometry	Head Modulus (MPa)	Lesion Modulus (MPa)	Target element length (mm)
Lesion size	15	0	Radial	300	150	0.5
	30	0	Radial			
	45	0	Radial			
Lesion orientation	45	7.5	Radial			
	45	15	Radial			
	45	22.5	Radial			
Non-radial boundaries	45	0	Acute			
	45	7.5	Acute			
	45	15	Acute			
	45	0	Obtuse			
	45	7.5	Obtuse			
	45	15	Obtuse			

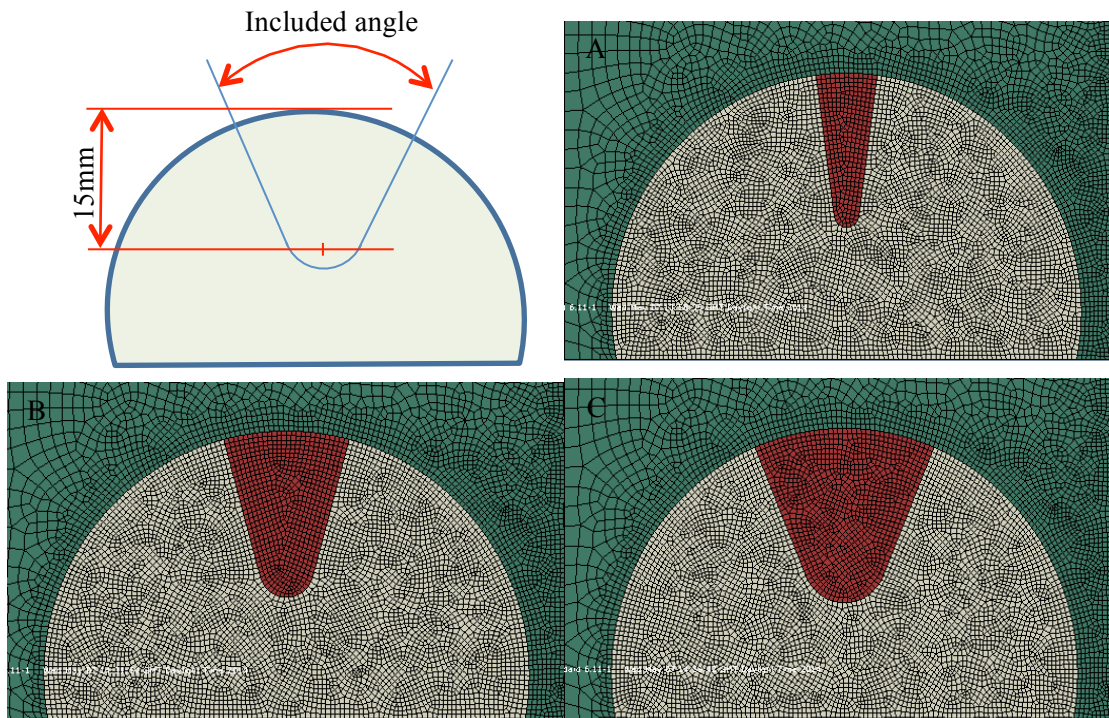


Figure 79. Representations of conical lesions with (A) 15°, (B) 30° and (C) 45° included angles. The straight edges were aligned radially and the depth to which they extended below the surface of the head was maintained at 15mm below the apex. Note that the semi-circular rigid platen has been cropped from these images.

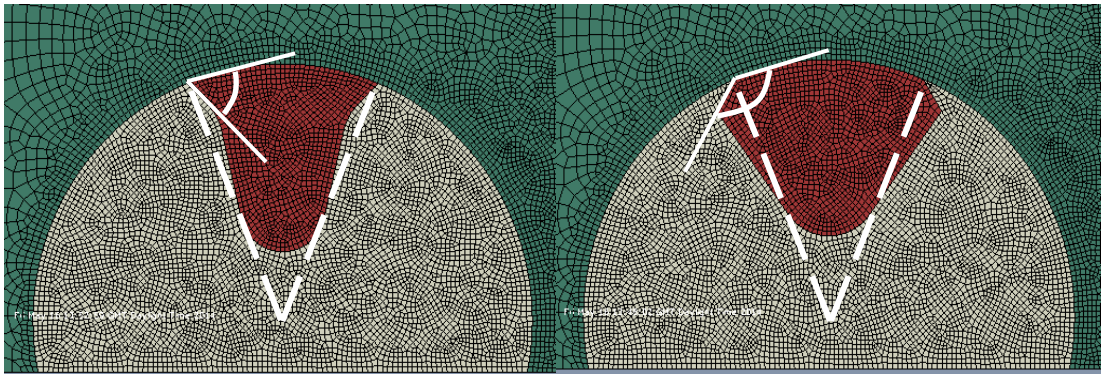


Figure 80. Left: A simulated lesion with a 45° included angle (indicated by the broken lines and intersecting at the head centre) and an acute angle between the internal surface and the circumference (indicated by the solid line). Right: A simulated lesion with a 45° included angle and an obtuse angle between the internal surface and circumference.

4.5.2 Method

The conforming contact parameters defined in Section 4.2 were used as a basis for these simulations. Lesion and head material properties were kept constant as their effect was established in Chapter 3.

Effect of lesion size

Three cone-shaped lesions were simulated: One with a 15° included angle, one with a 30° included angle and one with a 45° included angle (Figure 79). The straight edges were aligned radially and extended 15mm below the apex of the head where they were joined with a tangentially aligned radius. Load was applied vertically through the centre of the head-lesion construct by applying a displacement of 1.7mm to the semi-circular platen.

The peak VM stress at the lesion boundary and RR_D values were calculated for each scenario using the method described in Section 3.2.4. The calculation included only the right-hand half of each lesion boundary in Figure 79.

Effect of lesion orientation

The head with a 45° lesion was rotated in 7.5° increments so that the angle between the centre of load application and edge of the lesion reduced from 22.5° (a symmetrical 45° lesion) to 15° (replicating the edge angle of a 30° lesion), 7.5° (replicating the edge angle of a 15° lesion) and 0° (aligning the edge to the load vector) (Figure 81). The inferior surface of the head was pinned in all cases and load was applied vertically through the centre by applying a displacement of 1.7mm to the semi-circular platen. As discussed in Chapter 3, the region of contact extended from the centre of load application approximately 70° in each direction. The edge of the head was approximately 100° from the apex so rotating the femoral head was an efficient approach to generating the simulation and the inferior surface remained remote from the edge of the load bearing zone in all cases

The peak difference in VM stress at the lesion boundary and RR_D values were calculated for each scenario using the method described in Section 3.2.4 . The calculation included only the right-hand half of each lesion boundary in Figure 81.

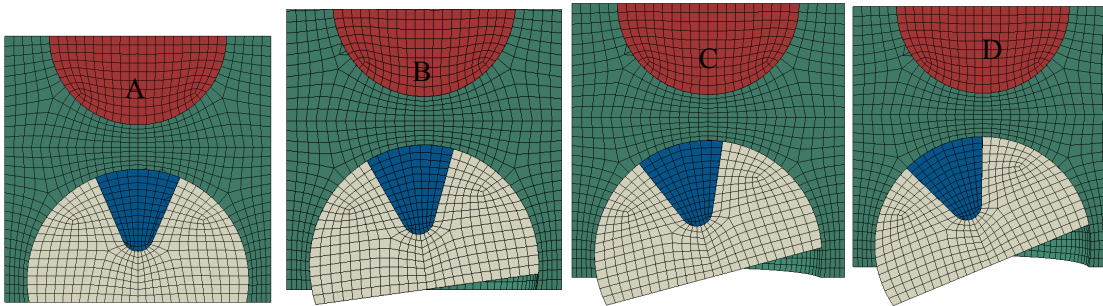


Figure 81. Cross-sections through the simulations using conforming contact with conical lesion models. The lesion was simulated with a 45° included angle. It was oriented neutrally (A) and rotated by 7.5° (B), 15° (C) and 22.5° (D) respectively.

Effect of lesion shape

In the evaluations of lesion size and orientation, the surface that represented the transition between healthy and necrotic regions was oriented radially. Two alternative configurations were developed to evaluate the effect that the shape of the surface had on the relative risk score. The first configuration was modified so that the boundary between the lesion and head flared outwards and the resultant angle between the lesion surface and subchondral circumference was acute. The lesion boundary in the second model closed inwards and therefore had an obtuse edge (Figure 80). Both maintained a 45° included angle about the head centre when measured at the surface of the head to maintain the surface area in contact with the filler. This meant that the acute-angled version had a smaller total area than the obtuse-angled version.

The peak difference in VM stress at the lesion boundary and RR_D values were calculated for each scenario using the method described in Section 3.2.4. The calculation included only the right-hand half of each lesion boundary in Figure 80. The 45° lesion case tested in the previous evaluation was used as a baseline against which these results were compared.

4.5.3 Results

Evaluation of the effect of lesion size

The purpose of this evaluation was to evaluate the relationship between the size of a conical lesion and the associated relative risk score. Both the peak VM stress in the outer surface and difference between the two surfaces varied inversely with included angle. The stress at the inner surface was unaffected (Figure 82). No cases were identified where the stress was higher on the inner surface than the outer surface because the head modulus was higher than that of the plug in all cases.

The magnitude of RR_D was reduced by 30% when the included angle was increased from 15° to 30°. The 45° lesion case had a four-fold lower RR_D value than the 15° lesion (Figure 83). These reductions were attributable to both a reduction in stress and a reduction in the length of the area identified by the relative risk scoring algorithm (Table 45).

The displacement at the apex increased with increasing lesion size because more of the applied load was supported by the lesion rather than the higher modulus femoral head (Table 46).

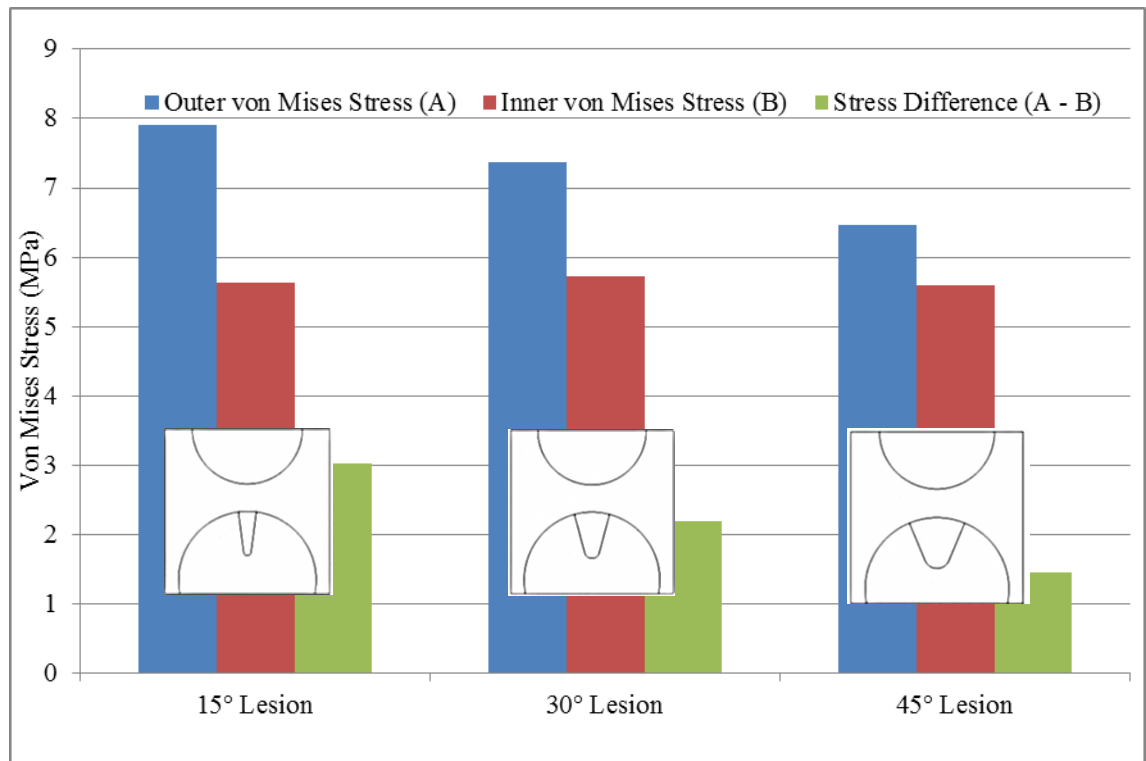


Figure 82. Variation in peak von Mises stress associated with the difference between the surfaces for the three cone angles considered. The diagrams in the chart show the lesion size and orientation for each case considered.

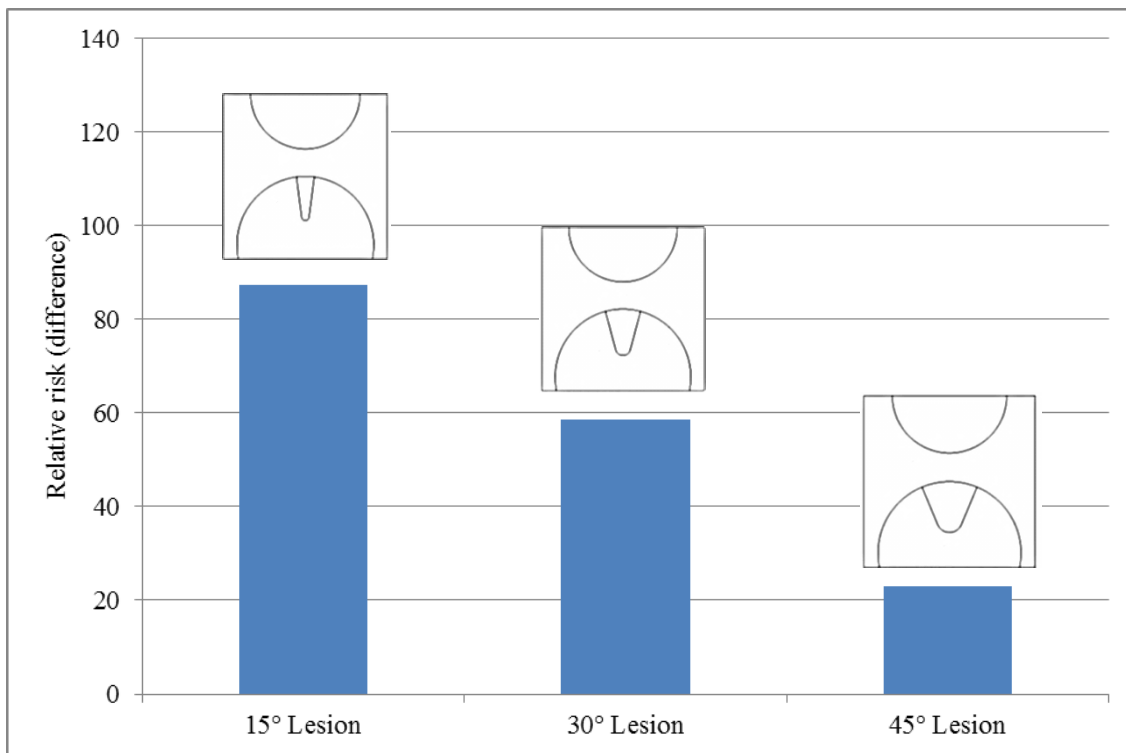


Figure 83. Variation in relative risk (difference) associated with the difference between the surfaces for the three cone angles considered. The diagrams in the chart show the lesion size and orientation for each case considered.

Table 44. The maximum von Mises stress difference and number of elements identified both varied inversely with the included angle of the simulated lesion.

Case	Maximum stress difference (MPa)	Number of elements identified (n)
15° Lesion	3.0	31
30° Lesion	2.2	28
45° Lesion	1.5	17

Table 45. Displacements caused at the apex of the head by displacing the platen by 1.7mm for different conical lesion sizes. Displacement varied directly with lesion size because more of the applied load was carried by the lower modulus lesion rather than the femoral head

Case	Displacement at the apex (mm)
15° Lesion	0.58
30° Lesion	0.62
45° Lesion	0.64

Evaluation of lesion orientation relative to the centre of load

This evaluation aimed to isolate the effect of lesion size from the effect of orientation of the lesion boundary relative to the load vector.

The peak difference in VM stress between the inner and outer surfaces for each configuration is shown in Figure 84. The results for the rotated 45° lesion were between 1% and 2.4% lower than for the symmetrical lesions.

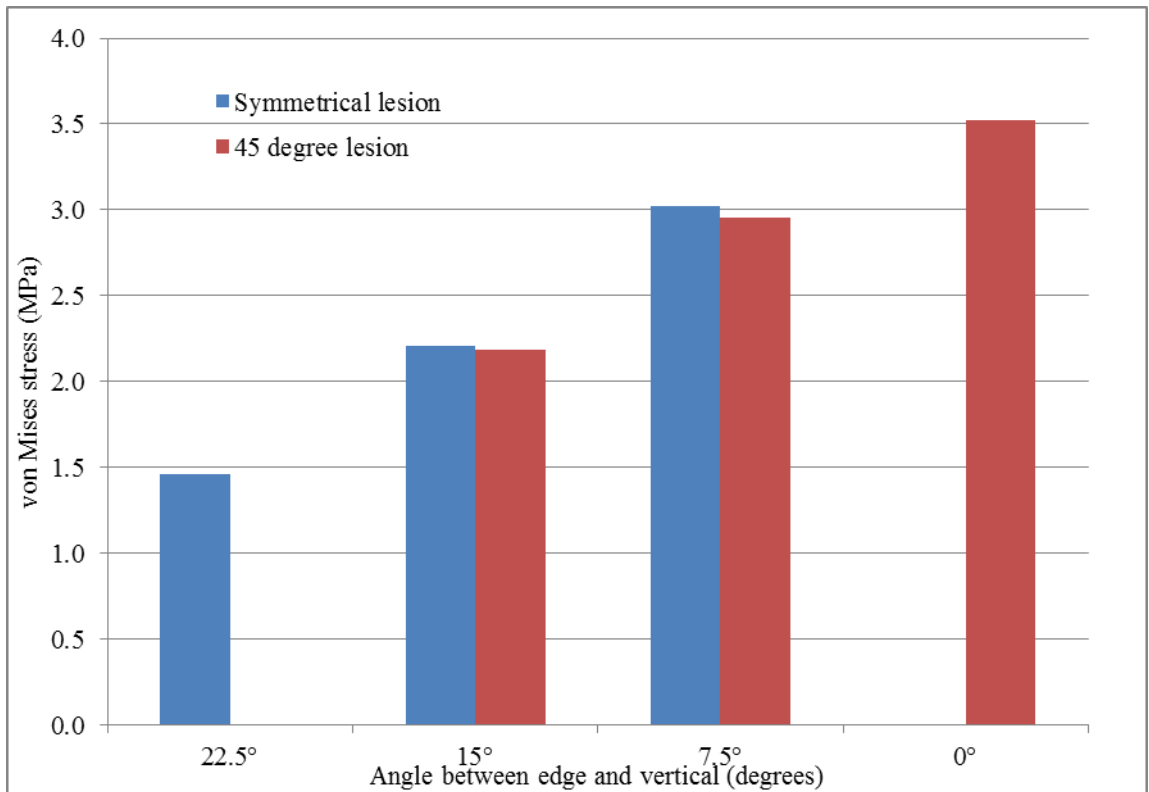


Figure 84. The peak difference in von Mises stress between the inner and outer surfaces increased as the angle between the edge of the lesion and vertical reduced. The results for the rotated 45° lesion were within 2.5% of the symmetrical case for the 15° and 30° centre-vertical angles.

The RR_D value calculated for the rotated 45° lesion was between 5% and 6% lower than for the symmetrical lesions (Figure 85) because between 1 and 2 fewer elements were identified in these cases by the algorithm used to calculate relative risk.

The displacement at the apex of the lesion-head construct was constant regardless of orientation of the 45° lesion (Table 47) suggesting that the elastic modulus of the femoral head was not affected by its orientation.

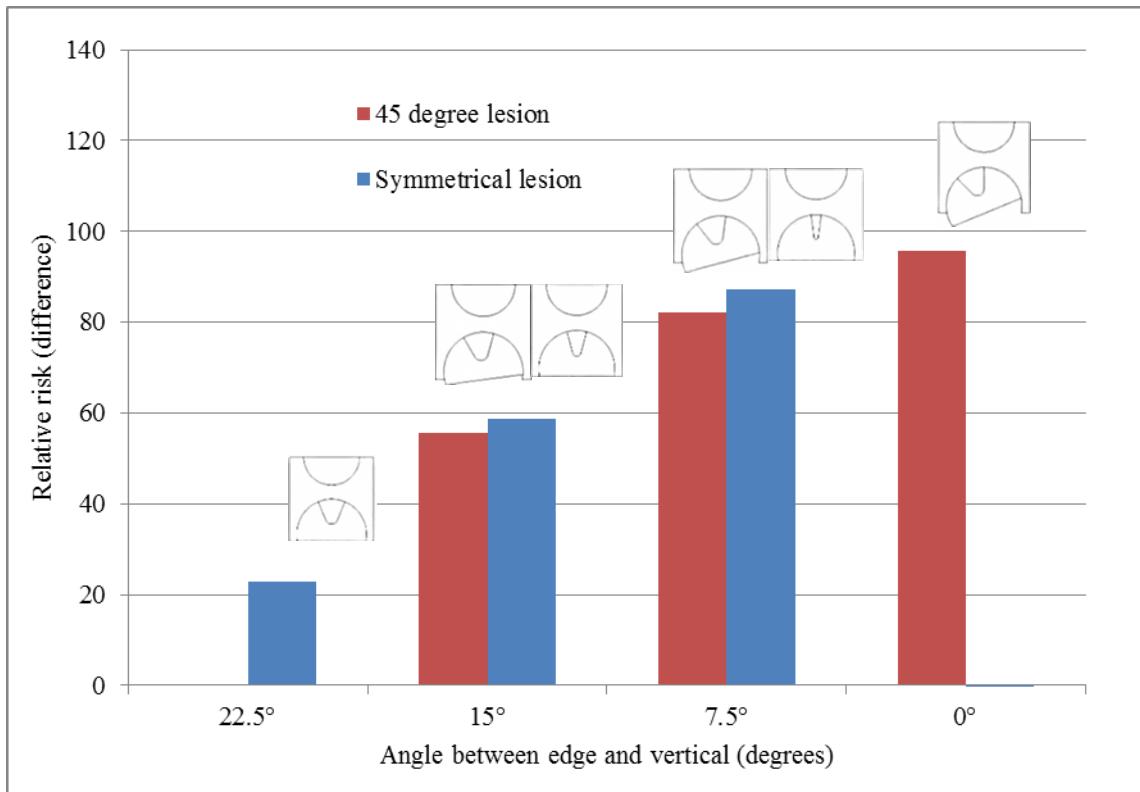


Figure 85. RR_D values calculated for symmetrical lesions with included angles of 45°, 30° and 15° compared to the results for a 45° lesion rotated to achieve the same centre-edge angle. The diagrams show the size and orientation of the simulated lesion in each case.

Table 46. Displacements at the apex of the femoral head with a 45° lesion in caused by displacing the platen by 1.7mm for different orientations. No difference in displacement was measured suggesting that the elastic modulus of the femoral head was not affected by its orientation.

Angle between edge and vertical	Displacement at the apex (mm)
22.5°	0.64
15°	0.64
7.5°	0.64
0°	0.64

Evaluation of the effect of lesion shape

In this evaluation the effect that changes in the shape of the lesion boundary had on relative risk was measured. Qualitatively, there was a difference in the appearance of the stress field between the acute and obtuse cases (Figure 86). Peak stress in the acute case was located deep to the outer surface and spread over more of the surface than in the obtuse case. The stress at the top edge of the interface between the head and lesion was homogenous. In the obtuse case, the peak stress was superficial to the outer surface of the head and extended up to the change in orientation of the surface.

Compared to the baseline case where the edge was radially aligned, the peak VM stress in the outer surface of the head-lesion interface was 13% lower in the acute case and 4% lower in the

obtuse case. The peak VM stress in the inner surface of the head-lesion interface was identical to the baseline in the acute case and 16% lower in the obtuse case.

Rotating the acute lesion relative to the load vector caused a progressive increase in VM stress (Figure 87) because both the radially aligned and flared regions of the lesion boundary became more vertical and moved closer to the centre of the applied load (Figure 88).

The results for the obtuse case were less linear: the peak VM stress in the outer and inner surfaces increased when the head was rotated by 7.5° because the lesion boundary moved closer to the centre of the applied load but reduced below the values obtained for the neutrally oriented case when the head was rotated by 15° because the relatively less stiff lesion became progressively more protected by a shelf of stiffer material (Figure 88).

In a neutral orientation, RR_D increased from 23 for the baseline case to 42 with an acute lesion edge but reduced to 17 with an obtuse edge (Figure 89). This change was attributable to the length of the region identified in the relative risk algorithm because, in terms of the peak stress difference between the two surfaces, the acute case was identical to the baseline and the obtuse case was 18% higher.

In the acute case, the internal surface of the lesion deep to the point of load application was oriented more vertically and closer to the load vector than in the baseline case. In the obtuse case the geometric discontinuity in the head-lesion boundary acted to limit the length of the region of elevated stress (Figure 89).

Rotating the acute lesion relative to the load vector caused an increase in RR_D because the magnitude of the stress difference increased from 2.2MPa in the neutral case to 2.9MPa at 7.5° rotation and 3.3MPa at 15° rotation (Figure 87) and also because the number of elements identified by the relative risk algorithm increased from 20 to 22 and 23 respectively.

For the obtuse case, the magnitude of the stress difference was relatively constant, changing from 2.6MPa in neutral orientation to 2.4MPa at 7.5° rotation and 2.7MPa at 15° rotation. The number of elements identified by the relative risk algorithm reduced from 7 in the neutrally oriented case to 5 when the head was rotated at 7.5° and 15° highlighting the limiting effect that this geometry had on the length of the stress discontinuity.

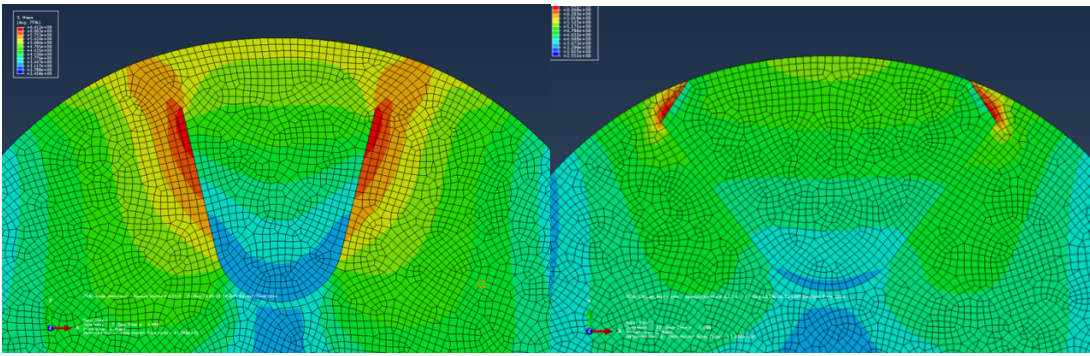


Figure 86. Left: Acute edged lesion; Right: Obtuse edged lesion. The magnitude of the stress was similar to the baseline (a 45° lesion with the edges aligned radially) in both cases. However, the length of the surface identified in the relative risk calculation was significantly shorter in the obtuse case.

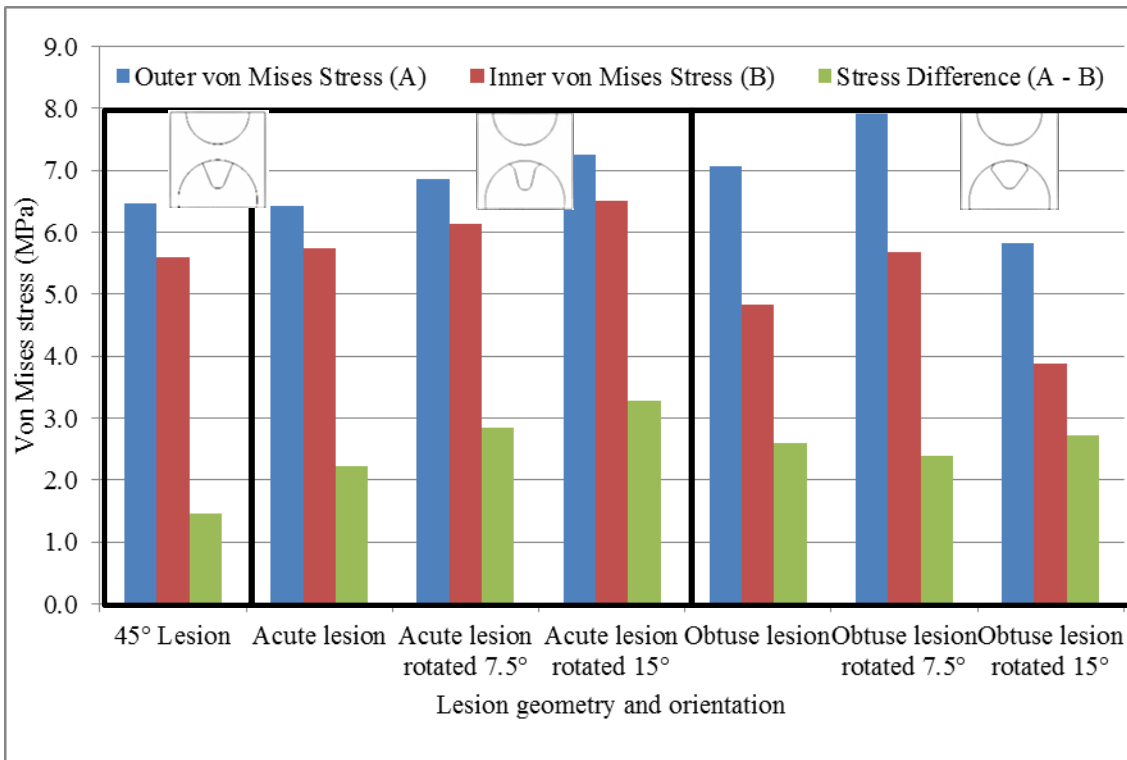


Figure 87. Peak von Mises stress in the inner surface, outer surface and the peak difference between the two surfaces for a radial-edged 45° lesion, an acute lesion at various angles relative to the load vector and an obtuse lesion at various angles relative to the load vector. The diagrams in the plot indicate the geometry used in each case.

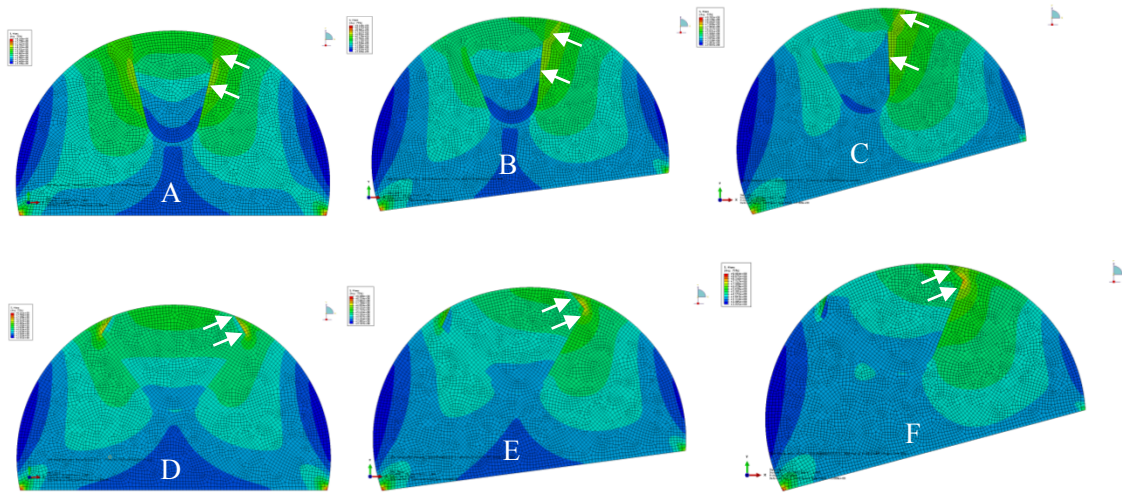


Figure 88: Plots of von Mises stress for the acute and obtuse lesions in three orientations. When the acute lesion was rotated from neutral (A) to 7.5° (B) and 15°(C) the peak von Mises stress increased because both sections of the lesion boundary became more vertical and moved closer to the centre of the applied load. When the obtuse lesion was rotated from neutral (D) to 7.5° (E) the peak von Mises stress increased because the boundary moved closer to the applied load but reduced when it was rotated to 15° (F) because the lesion was shielded by the stiffer material above it.

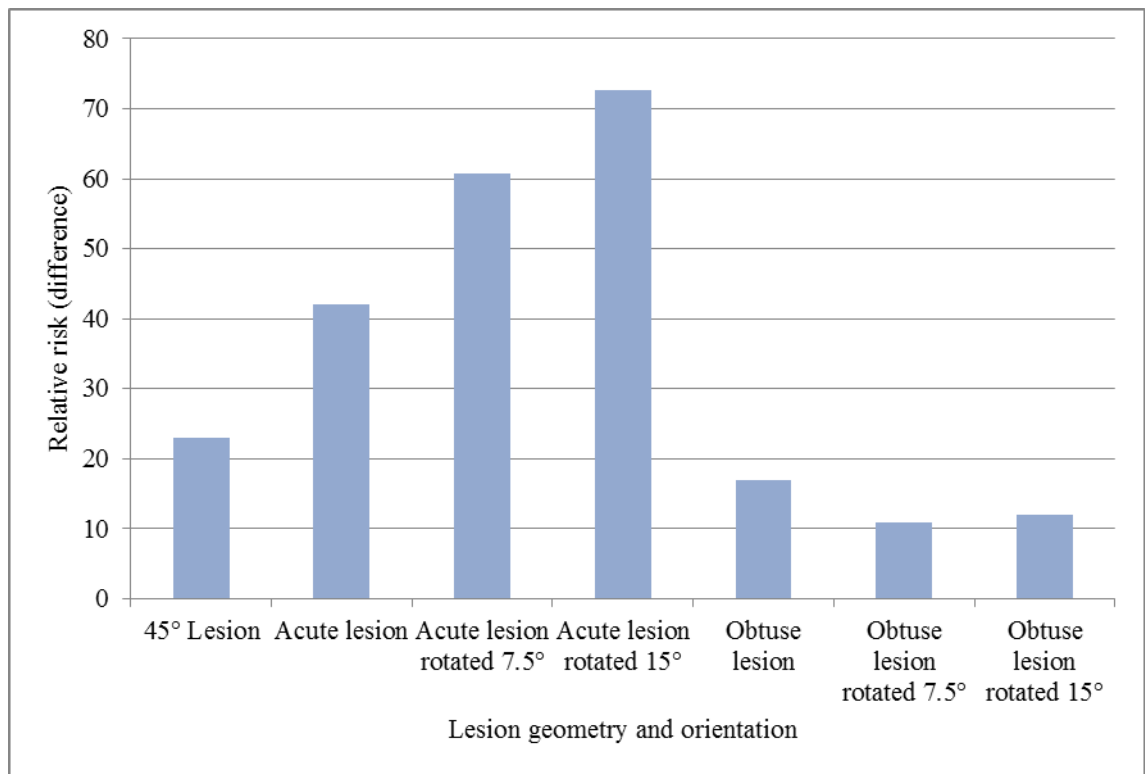


Figure 89. Relative risk (difference) associated a radial-edged 45° lesion, an acute lesion oriented neutrally, at 7.5° and at 15° relative to the load vector and an obtuse lesion oriented neutrally, at 7.5° and at 15° relative to the load vector. The relative risk (difference) score increased linearly with rotation for the acute case because both the magnitude and length of the stress discontinuity increased. It was substantially lower and varied less in the obtuse cases because of the limiting effect that the geometry had on the number of elements identified in the algorithm used to calculate relative risk.

4.5.4 Discussion

The effect of lesion size and shape was evaluated in a series of parametric studies. Conical lesions with different sizes and orientations relative to the load vector were evaluated, demonstrating the relationship between the risk score and boundary orientation. The boundary geometry was then modified so that a portion of it was no longer aligned radially, confirming that local geometry had a significant effect on the magnitude of the risk score. The results of these studies allowed two hypotheses to be developed: The first was that the risk score would be able to discriminate between different lesion geometries. The second was that lesion orientations or femur positions that aligned portions of the lesion boundary to the load vector would increase the risk of fracture originating from this location regardless of the size of the lesion. These hypotheses were tested in Chapter 5.

The cone-shaped lesion study demonstrated that the stress at the boundary between the healthy and necrotic bone was unrelated to lesion size but directly related to the orientation of the lesion boundary relative to the load vector. This showed that the effect of lesion size and orientation have confounding effects on the relative risk score and also that the risk of failure may vary with activity: If a large lesion is oriented directly under the centre of load application then stress discontinuities at the lesion boundary will be less important than the strength of the necrotic bone and failure could occur through direct compression of bone. Conversely, stress discontinuities at the boundary that are large in terms of both the magnitude and area affected may be caused by the combination of the shape and orientation of the lesion boundary even if the lesion volume is small.

Five new lesion configurations were evaluated: 15°, 30° and 45° lesions with radially aligned surfaces and two non-radial lesion configurations: one where the upper portion of the lesion flared outwards and one where the lesion flared inwards.

The first and second evaluations showed that the stress discontinuity at the radially aligned lesion-head boundary reduced with increasing lesion size because as the lesion grew larger, the interface became more distant from the centre of load application. The inverse relationship between included angle and RR_D is logical when one considers that the lesion boundary moved further away from the centre of load with increasing angle and the stress magnitude decreased accordingly.

The inverse relationship between lesion size and stress was negated by rotating the head to re-align the lesion boundary in closer proximity to the centre of load application showing that lesion shape and load vector orientation were confounding factors. Thus it was shown that the relative risk, or more fundamentally the stress at the boundary between the healthy and necrotic bone, was unrelated to lesion size but directly related to the orientation of the surface relative to

the centre of load application. This is an important observation as it supports the hypothesis that size alone does not dictate the risk of failure at the boundary.

This outcome is important because it confirms that the risk of failure or the likely failure mode for a particular lesion geometry and location may vary with the activity undertaken by the patient. For example a small lesion where the boundary lies distant from the load vector during a normal walking cycle may be associated with a low risk of failure at said boundary. However, if another activity of daily living such as deep flexion brings the lesion boundary closer to the centre of load application then the relative risk will increase significantly. This finding has clinical relevance as it may be possible to restrict weight bearing during specific activities to reduce the risk of failure for some lesion geometries. Conversely, if the lesion has an edge in a position that is frequently and unavoidably load bearing, then this patient may be considered to be at a high risk of fracture at the healthy bone-necrotic bone interface.

The third evaluation demonstrated the sensitivity of the simulation to changes in the geometry of the interface between healthy and necrotic segments. Peak stress magnitudes at the interface were relatively insensitive to shape but the location of maxima varied significantly. When the lesion boundary flared outwards (Figure 80 (left)) the location of greatest stress difference was deep to the articulating surface below the flared region; when it closed inwards ((Figure 80 (right)) the region of greatest stress difference was superficial to the subchondral surface. In this evaluation the relative risk was lowest when the lesion flared inwards because the geometric discontinuity limited the length of the region of high stress and the shelf of relatively more stiff bone acted to protect the lesion boundary. The location of this stress discontinuity, and the approximately circumferential alignment of the surface in this location were both consistent with the location of the osteolytic lesions that have been proposed as the origins of circumferential subchondral fractures propagated through a shear mechanism (Motomura *et al.*, 2011). This is an important consideration in the development of future simulations and highlights the need for further evaluation of the relative risk score to explore this potential weakness in the methodology.

Of the three geometric cases, the acute lesion geometry was most sensitive to orientation relative to the load vector, with RR_D increasing as the edge approached vertical. It was noted however, that for the same orientation relative to the load vector, the magnitude of RR_D was lower than the equivalent cases where the lesion boundary was radially aligned. This was attributed to the fact that the non-radial surface truncated the size of the region of elevated stress as it did not reduce the magnitude of the peak stress. It cannot be assumed that the geometry had a protective effect and it is more likely that the case further highlights the need for additional evaluation using patient specific models.

Another potential limitation is that the overall risk of failure may remain high when large lesions are present even if the relative risk score is low. A high risk of failure associated with large lesions was observed clinically by Nishii, Sugano, Ohzono, Takahashi Sakai, *et al.*, 2002. In these cases fracture may be more likely to originate within the lesion itself rather than at the periphery. The current study highlighted the fact that the risk of fracture could be high regardless of lesion volume if the lesion boundary was aligned to the load vector. Thus a more comprehensive approach to ranking lesions in terms of risk of fracture that included both relative risk score and a measure of the volume of the lesion may be required.

The study reported in Section 3.3 showed the effect that offsetting the lesion boundary relative to centre of load application had on relative risk. The cone-shaped lesion study showed the effect that changing the orientation of the boundary relative to the load vector but the combined effect of these two factors was not investigated.

4.5.5 Conclusion

This study confirmed that the stress at the boundary between healthy and necrotic bone varied depending on the shape of the surface and its orientation relative to the load vector. This is an important outcome because it suggests that the risk of fracture at the lesion boundary will vary depending on the size and location of the lesion, the shape of lesion boundary and its orientation relative to the load vector. It also suggests that these factors may influence whether fracture occurs because of direct compression of the necrotic bone within the lesion or because of shear at the lesion boundary.

One limitation of the relative risk score defined in Section 3.2.4 is that it did not consider lesion volume and further work is required to confirm whether inclusion of this factor offers an improved means of assessing the overall risk of fracture.

Another limitation that warrants further investigation is the apparent low risk associated with lesions whose edge aligns approximately to the articular surface. Subchondral fractures have been associated with high shear in these regions, suggesting that such a boundary may be less benign than indicated by the current comparison method. In order to achieve this it may be necessary to improve the resolution of the simulations by including the bone-cartilage interface.

Chapter 5. Image based tools for fracture risk prediction

5.1 Introduction

In this chapter, studies to assess the risk of disease progression in femoral heads with AVN were performed using a morphology-based risk score to rank a series of patient-specific models. The aim was to evaluate whether the risk score offered an improved means of stratifying patients in terms of their risk of disease progression compared to the ARCO grading system. The first objective was to establish whether the risk score would be able to discriminate between different lesion geometries to allow patients to be ranked according to their risk of disease progression. The second was to evaluate the sensitivity of the scoring method to a user's choice of slice and femur orientation to establish whether the approach using 2D cross-sectional geometry was appropriate.

To achieve this, computed tomography (CT) and magnetic resonance (MR) scans of the femoral heads of patients suffering from AVN were used to generate patient-specific geometry models. The CT data was used to identify the external surface of the bone and MR data was used to define the boundary of the lesion. Magnetic resonance imaging is recognised as the standard for confirming suspected AVN of the femoral head because it is often possible to distinguish small lesions or subchondral fractures that are invisible on plane radiographs (Calder *et al.*, 2008).

During construction of the geometry models it became evident that the perceived lesion volume and position could vary significantly depending on the slice selected and it was anticipated that this could affect the relative risk score. An approach that generated simulations from selected 2D slices is preferred because of the reduced segmentation time required and the ease with which the results of an FE simulation can be translated back to the original image. Therefore, the studies described in this chapter (Figure 91) were designed to allow the sensitivity of the relative risk score to slice selection (a measure of sensitivity to user error) to be evaluated. The studies used the conforming contact load configuration developed in Chapter 4 (Figure 64) to challenge the hypothesis that lesion geometry and the joint reaction force vector interacted such that the orientation of the femur associated with the highest risk of fracture was patient-specific. Another aim of this study was to evaluate whether a relative risk score that included lesion volume as a factor would improve the score as a means of assessing the overall risk of fracture.

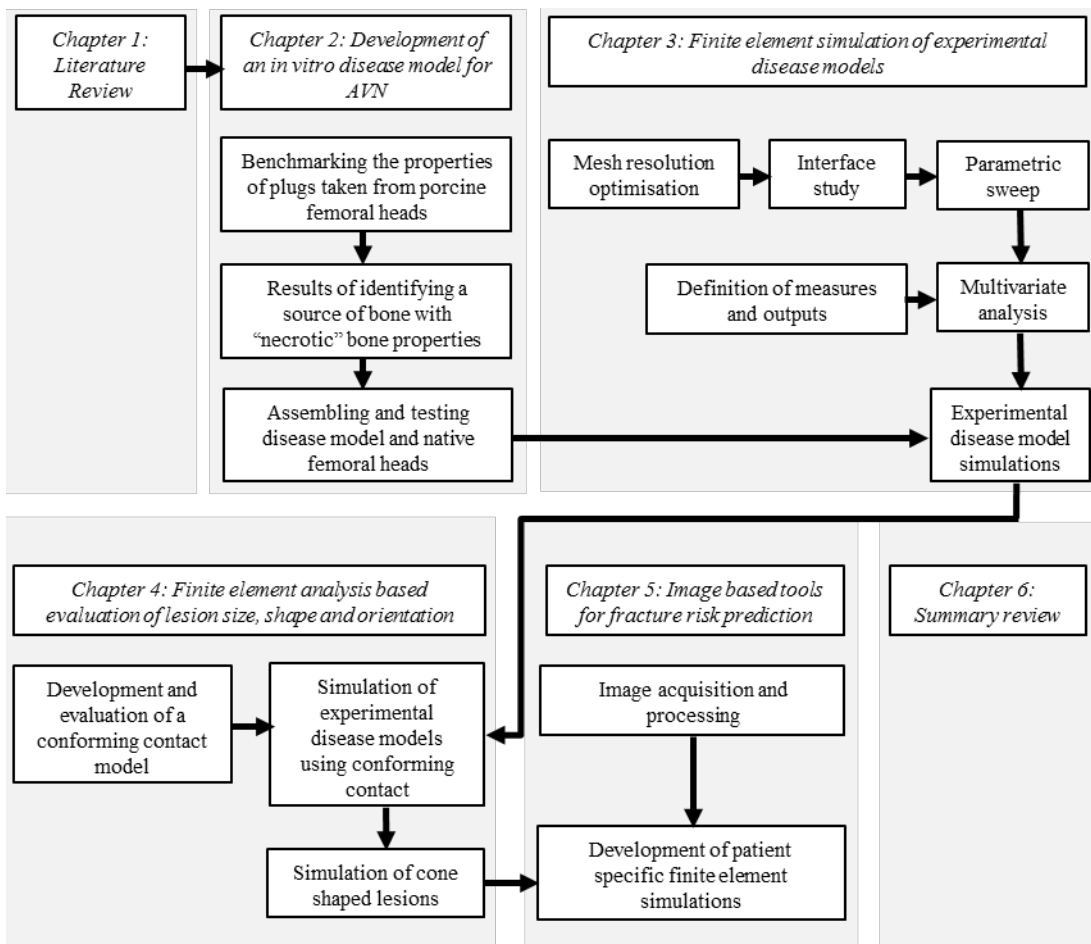


Figure 90. Flow chart summary of the studies performed in each chapter.

Multiple two-dimensional cases were developed from each patient’s unique anatomy. Central anterior-posterior (AP) and medio-lateral (ML) views were chosen to gain an understanding of the three dimensional variation in lesion shape. Two additional cases were generated in an ML orientation because slice selection is a subjective user-defined variable and an understanding of the sensitivity of the relative risk score to user input was required. Finally, the cone-shaped lesion study introduced in Section 4.5 highlighted the effect that orientation had on relative risk score so additional AP and ML cases were generated with the femur oriented in 20° of flexion.

This study was conducted in two stages. In the first stage patient specific images were used to develop geometry models and quantify the necrotic lesion according to the current gold-standard clinical grading system. Of the eight patients that were used in this study, two were identified as having post-collapse AVN (the fracture set) and the remaining six had pre-collapse lesions (the no fracture set). Demographics were compared between pre- and post-collapse patients to identify confounding factors in the second stage of the study.

In the second stage, patient-specific finite element models were evaluated using the relative risk score described in Section 3.2.4 and using a revised score that included the volume of the lesion as a factor. The ability to differentiate between pre- and post-collapse cases and the effect of revising the score on the ranking of the patients was evaluated. Based on the results of this

ranking process, a threshold for the revised score was proposed. The final stage was to assess the sensitivity of the scoring method to user input and femur orientation.

5.2 Image acquisition and processing

5.2.1 Patients

Patients with avascular necrosis of the femoral head were recruited as part of a medical device clinical trial initiated by DePuy Synthes Joint Reconstruction (Leeds, UK). The trial was run in two hospitals in Bangkok (Chulalongkorn Memorial Hospital, Rama 4 Road, Bangkok and Ramathibodi Hospital, Isarapap Min Buri Road, Bangkok), one hospital in Hong Kong (Queen Mary Hospital, Pok Fu Lam Road, Hong Kong) and one in Melbourne (St. Vincent's Private Hospital, Victoria Parade, Melbourne).

The clinical trial protocol was approved by DePuy Synthes and by the independent hospital ethics committees at each site. The protocol and patient consent forms both included the intention to use the information collected on each patient during the trial for further scientific research. Approval to use patient-confidential data at the University of Leeds was obtained from the University of Leeds, Faculty of Engineering Research Ethics Committee (reference MEEC 10-011).

Each patient recruited into the trial received concurrent pre-operative CT and MR scans as part of their normal standard of care. The scans and patient demographic data were uploaded onto a secure server administered by Intelemage (Cincinnati, OH). The administrator's responsibilities included a quality review to evaluate data integrity and conformance to image acquisition protocols. They also provided confirmation of anonymity before the images and demographic data were made available to DePuy Synthes and subsequently this study.

All CT and MR scans were collected following standardised protocols (Appendix D: Clinical data). MR scans were obtained using multiple protocols but only T1 weighted scans with turbo spin echo³ were used in this research.

Eleven patients were evaluated for inclusion in this study. Two patients were excluded because the lesion did not extend into the slices defined in Table 50. A third patient was excluded because multiple lesions were present in the slices making the analysis inconsistent.

5.2.2 Method

Three-dimensional geometry models were generated for each patient using spatially aligned CT and MR scans from each patient. Bone geometry was segmented from the CT scan and the

³ Turbo spin echo is used to shorten scan times compared to a conventional MR scan protocol and was the standard of care at both hospitals in the trial.

lesion boundary was segmented from the MR scan. The native spatial resolutions of the CT and MR scans were 0.5mm x 0.5mm x 0.5mm and 1mm x 2mm x 2mm respectively.

Image acquisition and registration

Three dimensional geometric models of the proximal femur of each patient included in the study were generated in ScanIP (Simpleware Ltd., Exeter, UK). Each patient-specific model was generated from a co-registered pair of CT and MR scans.

Both scans were taken with the patient lying in a supine position. The consistent orientation of the long axis of the femurs relative to the scan co-ordinate systems indicated there was little variation in flexion angle between scan modes, thus flexion in both the CT and MR was assumed to be approximately neutral. The degree of rotation and abduction or adduction varied between modes so co-registration of the images using translation, internal / external rotation and abduction / adduction rotation was necessary. All femurs were oriented in a neutral stance position with approximately 20° of femoral neck anteversion (external rotation) to obtain consistency in orientation across the patient cohort. The diaphysis was aligned to the global Y-axis (vertically upwards) and the medial direction oriented to the global X-axis (Figure 91). For right hips the anterior direction was aligned to the global Z-axis, for left hips the posterior direction was aligned to the global Z-axis.

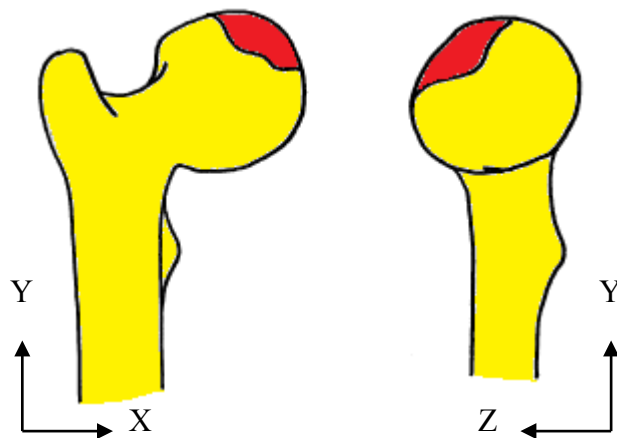


Figure 91. Schematic diagram of a neutrally oriented right femur with a lesion in the anterior-medial quadrant. The diaphysis was aligned to the global Y axis; the medial direction was aligned to the X axis. Approximately 20° of femoral anteversion (external rotation) was applied.

A method of co-registering the CT and MR scans was developed to allow models that represented both the bony geometry and lesion boundary to be developed. CT segmentation was based on a protocol described previously (Buie *et al.*, 2007); MR segmentation was based on the manual process described in a second study (Zoroofi *et al.*, 2001). In addition to generating masks that represented the external geometry of the femur and the lesion, a mask that was the inverse of femur geometry was generated. This equated to the filler used in the conforming contact methodology described in Section 4.3. A summary of the process is shown

in Figure 92. A detailed explanation of each sub-step is shown in Figures 93-97.

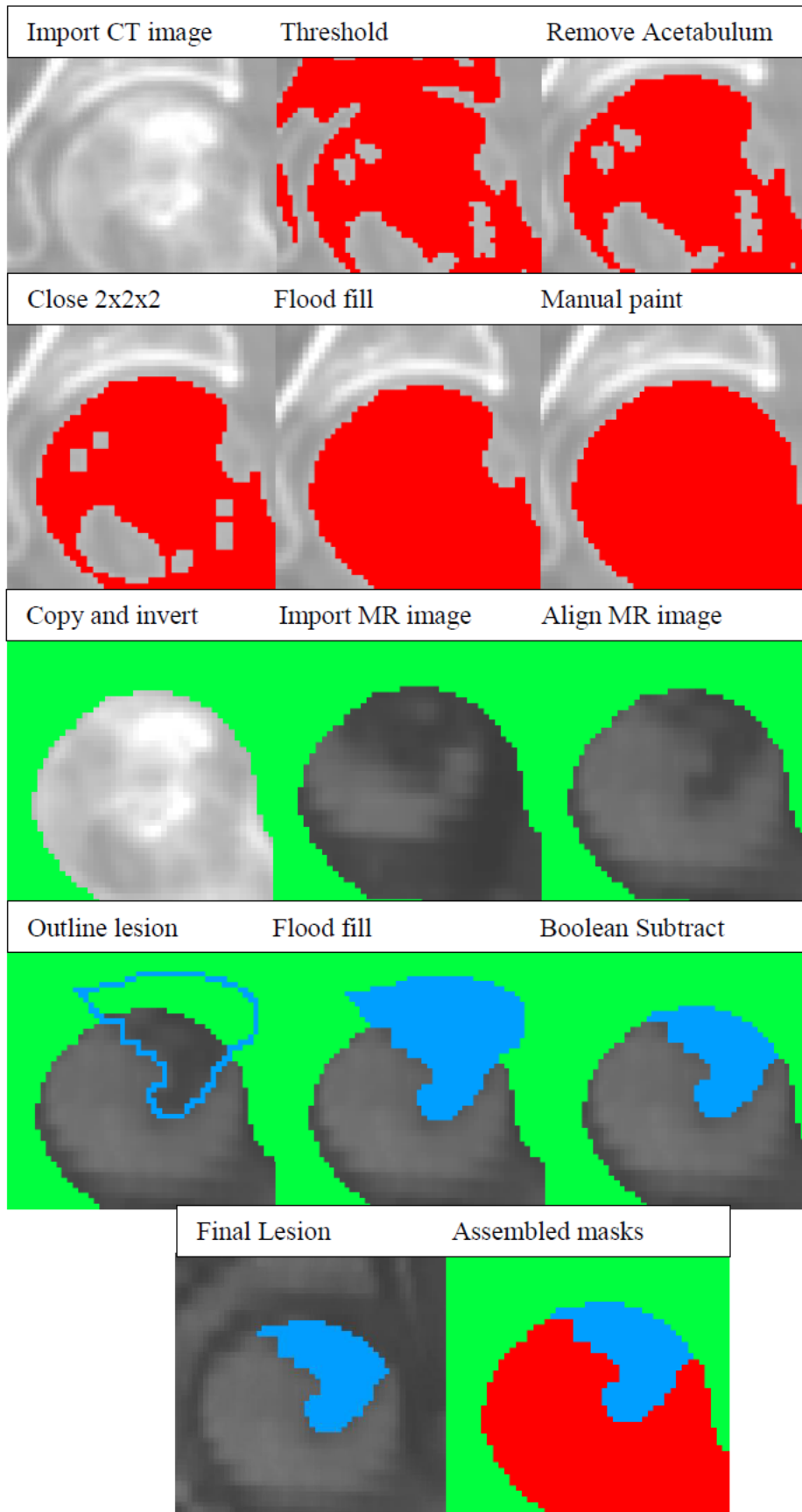


Figure 92. Summary of process used to develop head, lesion and filler masks for patient 01_001. Note that the process is shown in two dimensions for simplicity but the steps were carried out in 3D.

CT data segmentation

CT scans were used to identify the geometry of the proximal femur. They were imported into ScanIP as a stack of images in DICOM format and cropped to generate a volume of interest⁴ (VoI) around the proximal femur, terminating distally below the lesser trochanter and oriented a consistent position (neutral flexion, approximately 20° anteversion) before being down-sampled to a voxel resolution of 1mm³. This resolution was chosen because the re-meshing algorithm described in the following section generated a finer mesh than the native mesh exported from ScanIP and exporting the meshed geometry with a target element edge length of 1mm resulted in a final element edge length of approximately 0.5mm.

An automated method of segmenting cortical and trabecular compartments using two thresholds and a closing function to generate a mask has been described previously (Buie *et al.*, 2007). Developing an automated method was not justified in this study as there were only a small number of samples. A simplified manual approach was possible in this study because a homogenous material was assumed so there was no requirement to differentiate cortical bone from cancellous. The workflow is summarised in Figure 93.

Subchondral fractures were not represented in the geometry models and therefore all eight geometry models simulated intact femoral heads. The presence of a fracture did not alter the external geometry in the two cases where a fracture was present.

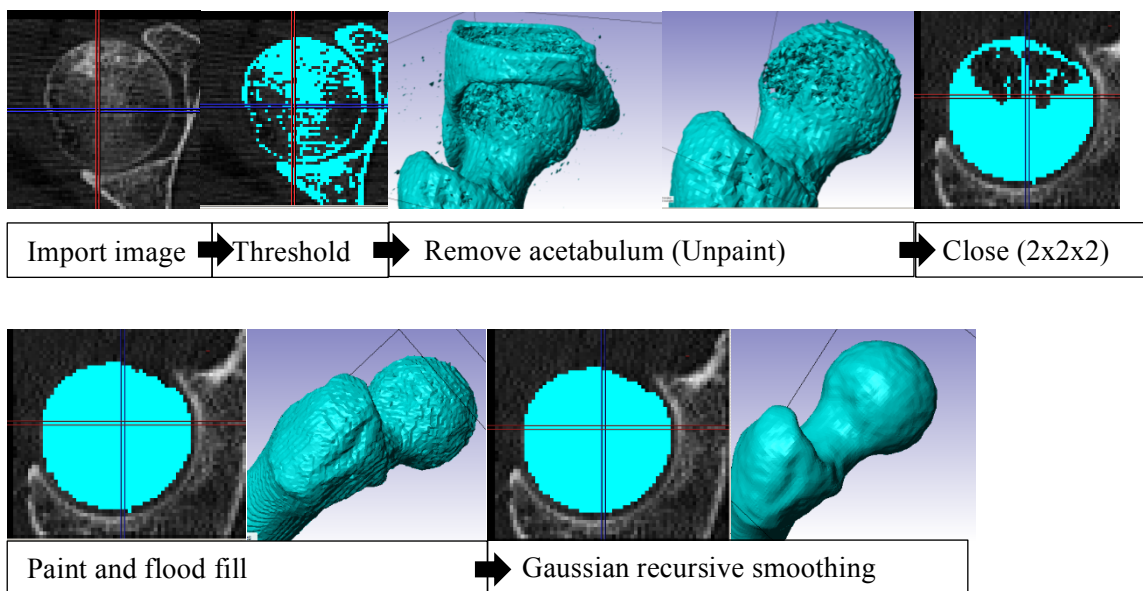


Figure 93. Schematic representation of the workflow used to segment the femur geometry from the CT scan (in this case of patient 01_001) using ScanIP. The process was based on that presented in an earlier study (Buie *et al.*, 2007) and had six key steps: Importing the image and cropping it to establish a volume of interest; thresholding to identify the bone region; manually deselecting voxels (un-painting) associated with the acetabulum; using a closing function to solidify the construct; manually painting any gaps in the external surface that remained after the close function was used and smoothing the final surface.

⁴ The volume of interest is the three dimensional space that contains the borders of an object under consideration. In this study it was a rectangular volume that contained the proximal femur.

The segmented femoral head mask was copied and inverted to generate a negative of the femoral head geometry. This negative mask was used to create the lower half of the filler component in the final FE assemblies. Once the CT image had been completely processed the entire VoI was represented by the combination of these two masks (Figure 94).

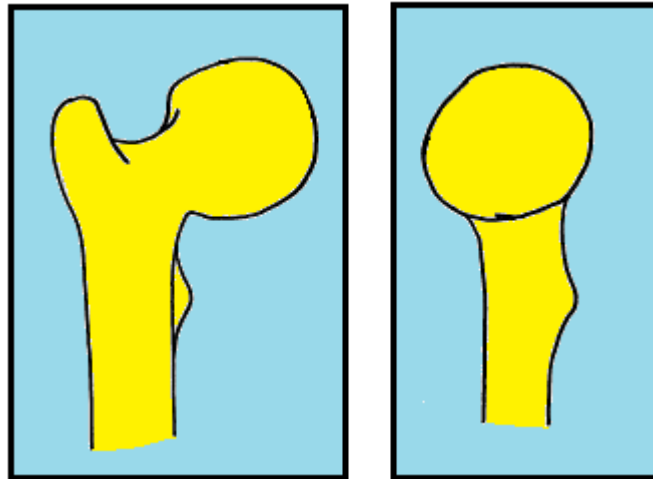


Figure 94. Schematic representation of the completed femur and filler masks in the X-Y and Y-Z orientations. The filler occupied the entire volume of interest.

Registration of the MR image to the CT mask

MR images were used to generate lesion geometry because the inner border between healthy and necrotic bone can be indistinct in CT scans. To generate a model that contained femur and lesion geometry, the MR image had to be spatially aligned to the masks generated from the CT image.

The transition from dense subchondral bone to cartilage is not well defined in a T1 weighted MR image as both tissues have a low fat content. This made the femoral head appear smaller on MR images compared to CT. In the first stage of registration, the MR images were resampled to the same spacial resolution (1mm x 1mm x 1mm) before being manually aligned by translating the MR stack in the X-, Y- and Z-directions. The head centre was maintained as the origin for subsequent rotation adjustments. Landmarks for rotational alignment were the apices of the greater and lesser trochanters and the cortex in the diaphysis. Alignment about the three axes was obtained incrementally as gross changes to one orientation altered the apparent position of the landmarks in the other orientations. Final orientation was verified using both the filler (Figure 95) and femur masks.

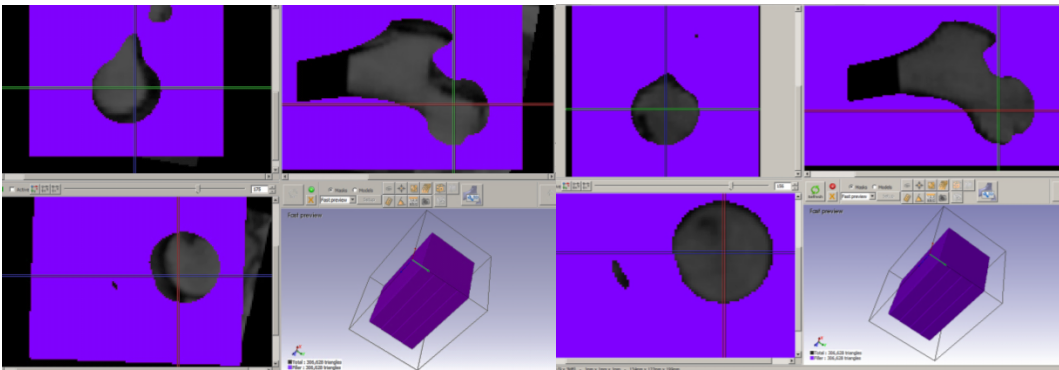


Figure 95. Alignment of the MR scan to the CT derived mask for patient 01_001. Left: the high intensity region of the MR image representing the proximal femur is misaligned relative to the (purple) filler mask; Right: final alignment of the MR image relative to the filler mask. This was obtained by rotating and translating the MR image relative to the filler mask.

The MR image stack was oriented relative to the filler mask using the rotation and translation functions available in ScanIP. Using the filler mask compensated for the lack of information on cortical geometry in the MR scan but required that some assumptions be made regarding the position of the MR image relative to the mask. These assumptions were:

1. The thickness of the diaphyseal cortex was approximately equal in the sagittal and coronal views at each transverse level⁵.
2. The thickness of the cartilage and subchondral bone on the femoral head was symmetrical in the transverse view and the head centres shown in both modalities aligned
3. The thickness of the cortices on the greater and lesser trochanters was uniform in all views.

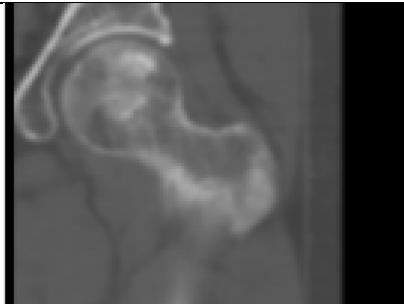

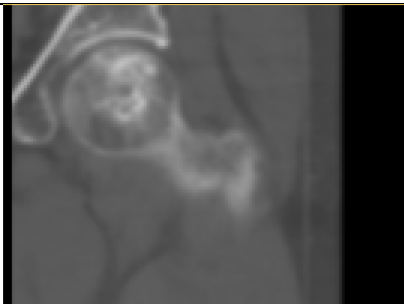
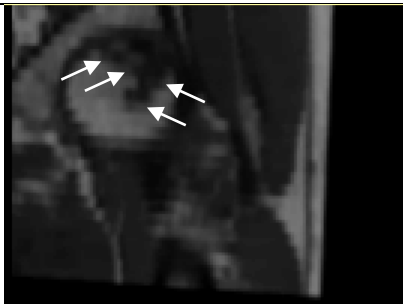
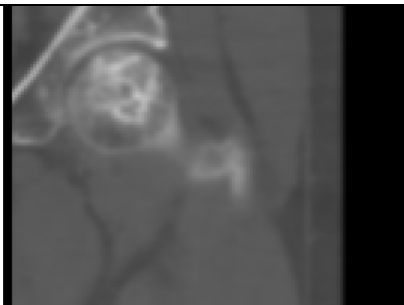

Following these rules enabled each anatomic landmark visible in the MR images to be aligned to the boundary of the equivalent feature in the filler mask.

MR data segmentation

The necrotic lesion was identified by the presence of low-intensity (black) bands on T1-weighted MR images (Sakamoto *et al.*, 1997; Seyler *et al.*, 2008; Takao *et al.*, 2010). An example scan showing the low intensity banding is shown in Table 48. These bands can be an indication of a fibrovascular reactive interface, osteolysis, cysts, reparative tissue or subchondral fracture (Gardeniers, 1993; Kim *et al.*, 2000) and correlate to areas that lack hydrogen-rich marrow fat (Fordyce and Solomon, 1993).

⁵This assumption was verified by checking the alignment of the medullary cavity on the CT scan to the high intensity region representing bone marrow in the MR scan.

Table 47. Anterior-posterior CT- and MR-derived views through a femoral head with AVN (patient 01_001) in ScanIP. The lesion boundary is visible as a low intensity band within the femoral head in the T1-weighted MR images. The boundary is marked with white arrows. It is noted that the high and low intensity bands in this image relate to fat content and are independent of material properties.

Computed Tomography	Magnetic Resonance Imaging
	
	
	

The lesion boundary, used to define the region of bone with reduced mechanical properties, was identified as the outer border of the low intensity band (Takao *et al.*, 2006). This was traced on a slice-by slice basis in all three planes to generate a three-dimensional surface that represented the internal boundary of the lesion. No attempt was made to accurately define the external boundary of the lesion using the MR images. Instead, the lesion mask was deliberately extended beyond the surface of the femoral head. Recursive Gaussian smoothing was used on the lesion mask and then a Boolean subtraction against the filler mask was used to generate the outer surface. This generated a continuous surface between the head and lesion volumes and a conforming surface between the lesion and filler (Figure 96).

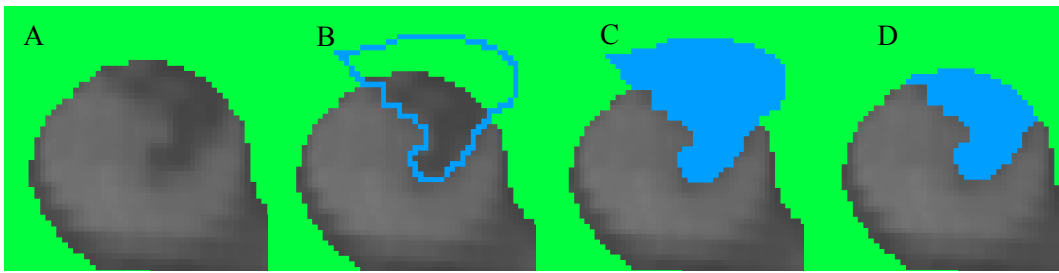


Figure 96. The process of generating a lesion mask: A. The lesion was identified as a low intensity band or region; B. The outer boundary was traced and extended beyond the surface of the femoral head; C. The mask was flood filled and smoothed using recursive Gaussian smoothing and D. Boolean subtraction was used to generate a conforming external surface. Only the anterior-posterior view is shown in this example (from patient 01_001) but the process was repeated in all three orientations

The final step was to perform a Boolean subtraction of the lesion mask from the head mask. The final patient-specific geometry model therefore consisted of three solid masks representing the head, the lesion and the filler (Figure 92).

Quantification of lesion volume and position and clinical grade

Fractures were identified by the author by analysing the CT image stacks: Confirmation of the presence or absence of fracture was obtained through independent clinical opinion as part of the DePuy Synthes clinical trial.

The diameter of each patient's femoral head was measured in ScanIP and used to calculate a spherical volume that was used as an estimate of the volume of the head itself. The volume of the lesion was calculated directly from the mask of the lesion after segmentation by multiplying the number of voxels by the voxel volume (1mm^3). Dividing the lesion volume by the femoral head volume gave a percentage involvement by volume which was converted to an ARCO volume sub-classification (<15% involvement = A; 15-30% involvement = B; >30% involvement = C) (Gardeniers, 1993).

The location of the lesion in the central A-P plane was estimated in accordance with the ARCO grading system sub-classification by identifying whether the lesion occupied the medial, central or lateral quadrants of the femoral head (Figure 97). Although not specified by the grading system, the same approach was implemented in the central medio-lateral view to identify involvement in the anterior, central and posterior quadrants.

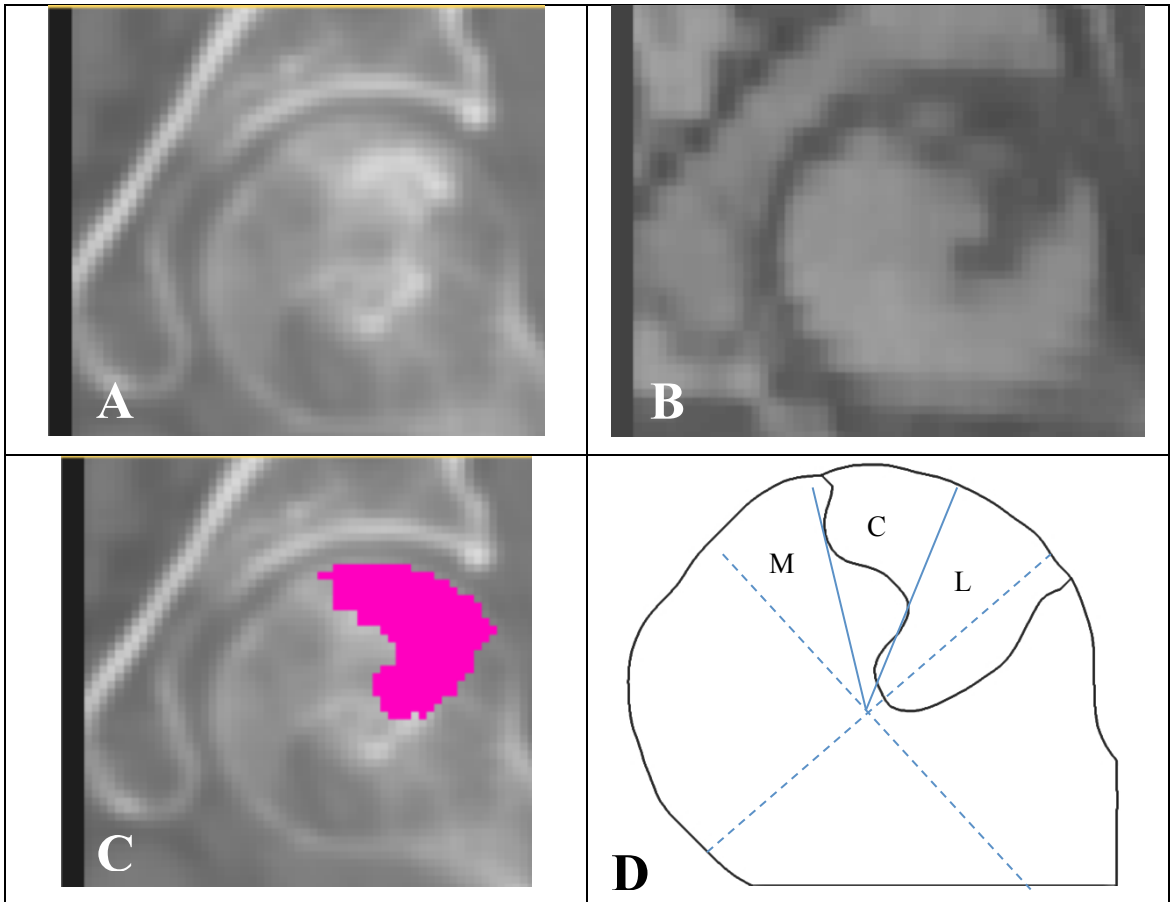


Figure 97. The CT slice is shown in image A. The equivalent MR slice is shown in image B. The lesion boundary is shown overlaid on the CT scan in image C and a schematic representation of the femoral head and lesion is shown in image D. All images are from patient 01_001 in the A-P view. Lesion location was quantified according to the ARCO grading system: The lesion was present in the central (C) and lateral (L) quadrants but not in the medial (M) quadrant)

Evaluation of segmentation repeatability

The repeatability of this method was evaluated by blind re-segmentation of the CT scan for patient 01_001 after a period of approximately 24 months. This scan was chosen because it was the first one to be segmented during the initial model development so was generated when the author had least experience. The original mask (A) and new mask (B) were compared by creating a union of two masks generated using Boolean subtractions: (A-B) and (B-A). The resulting mask (C) contained a set of voxels that represented the absolute difference between the two masks ($C = (A-B) \text{ AND } (B-A)$). Masks A and C are shown in Figure 98. They were converted into FE meshes to evaluate the difference between the first and second processes. Mask A contained 48,220 elements; mask B contained 48,352 (difference 132 elements; 0.27% of mask A).

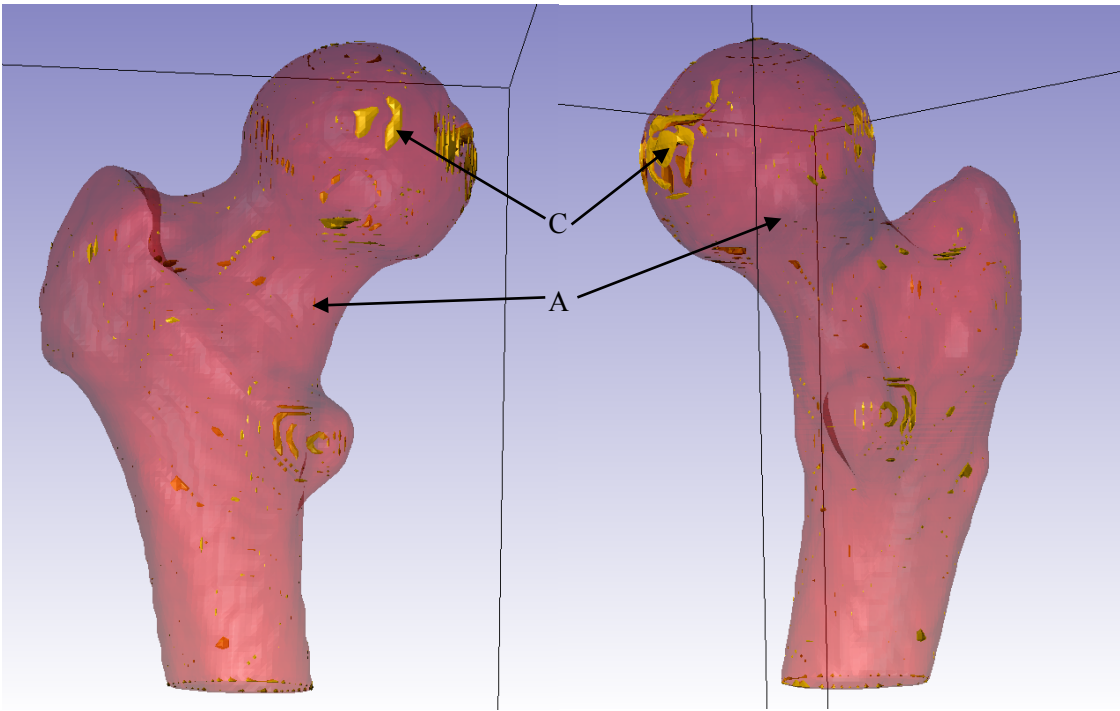


Figure 98. Anterior and posterior views of the original mask (A, shown in red) generated for patient 01_001 overlaid with the mask representing the difference (C, shown in yellow) between the original and blind repeat. The difference in number of elements between the two masks was less than 0.27%.

5.2.3 Results for patient demographics and disease quantitation

Demographics for the eight patients evaluated in this study (three female, five male) are shown in Table 48. The average height and weight were 165.5cm (S.D. 7.5cm) and 66.7kg (S.D. 8.5kg) respectively. Average age was 47.4 years (S.D. 17.2 years). Fractures were detected in patients 01_002 and 02_003. Grade, volume and involvement location are summarised in Table 47. There was no distinction between the fracture set and no-fracture set.

Table 48. Demographics for the eight patients selected for the patient specific geometry model study. Patients 01_002 and 02_003 were identified as having suffered a subchondral fracture prior to image acquisition.

Patient ID	Sex	Height (cm)	Weight (Kg)	Ethnicity	Age
P01_001	Female	162	52	Asian	44
P01_002	Male	173	63	Asian	62
P01_003	Male	172	72	Asian	27
P01_004	Male	173	80	Asian	41
P01_005	Female	156	70	Asian	60
P01_006	Male	157	60	Asian	59
P02_001	Male	171	66	Asian	66
P02_003	Female	160	70	Asian	20

Table 49. Lesion volume and ARCO classification for each patient included in the study. Head volume was estimated by calculating the volume of a sphere with the same diameter, lesion volume was calculated by multiplying the number of voxels in the lesion mask by the voxel volume. The ARCO grade was assigned based on the presence (Grade III) or Absence (Grade II) of fracture – note that all lesions were visible on radiographs and were by definition grade II or higher. The volume classification was dictated by the percentage involvement (<15% = A; 15%-30%=B; >30% = C). Location in the A-P and M-L planes was established by assessing whether the lesion was present in the Medial (M), Central (C) and Lateral (L) (Figure 97); Anterior (A), Central (C) and Posterior (P) quadrants respectively.

Patient	Lesion vol.	Head dia.	Head vol.	Percentage involvement	ARCO Grade	ARCO sub-grade	ARCO Location	
ID	mm ³	mm	mm ³	%	I, II, III	A,B,C	M,C,L	A,C,P
P01_001	3655	43	41630	9	II	A	C,L	A
P01_002	29112	49	61601	47	III	C	M,C,L	A,C,P
P01_003	13635	46	50965	27	II	B	M,C	A,C,P
P01_004	19744	49	61601	32	II	C	M,C	A,C,P
P01_005	5953	38	28731	21	II	B	M,C	C,A
P01_006	4611	44	44602	10	II	A	M,C	C,A
P02_001	19825	44	44602	44	II	C	M,C,L	A,C,P
P02_003	13902	43	41630	33	III	C	M,C,L	A,C

5.3 Development of patient specific finite element simulations

5.3.1 Method

A 2D strategy was employed throughout the studies in this thesis because the most efficient evaluation workflow in a clinical setting would be to derive the simulations directly from 2D image data rather than require segmentation of 3D medical images.

A potential weakness of this approach is that the outcome may be sensitive to slice selection. The orientation of the femoral head relative to the load vector is also highly variable and the studies reported in the previous chapter confirmed that this could affect the risk score. However, the effect that changing orientation would have on the risk score associated with highly variable organic geometries was not known. Therefore, the studies in this chapter were designed to allow patients to be ranked according to an overall risk score, to assess the effect of the user selecting a different slice and to evaluate the difference in score between two femur orientations. The rank was compared to the ARCO grading system because it is the current gold standard for clinical grading of femoral head AVN.

Validation of the score is challenging because the poor prognosis of conservatively treated AVN means that the default treatment for most patients is surgical intervention and altering the

standard of care would be unethical. However, two patients had post-collapse AVN and an important first step in validating the score would be to confirm whether it ranked these patients at highest risk. It is also important to explore alternative methods for interpreting the results and therefore two approaches to deriving a single score for each patient were employed: One based on an overall average score and one based on the number of slices above a threshold. The former is preferable as it ranks patients on a continuum and is not affected by the subjective nature of a threshold-based approach. However, comparing the rank obtained by both approaches allowed the consistency of the outcome to be established.

Preparation of masks for use in FE environment

The most comprehensive means of assessing the risk of disease progression would be to use 3D FE simulations. However, the complexity of using such an approach was highlighted in a pilot study performed using the three-dimensional model of the femur belonging to patient 01_002. This patient was chosen because of the particularly complex lesion geometry (Figure 99). Two simulations were run using a three-dimensional conforming contact model based on the protocol described in Section 4.5. In one simulation the lesion was modelled with half the stiffness of the native bone, in the second the same material properties were used for both segments to simulate a healthy femur. The surface between the healthy and necrotic bone was isolated for both simulations to allow comparison (Figure 100). In the case where material properties were different, regions of high stress corresponding to areas where the surface was approximately aligned to the load vector were visible. These stress concentrations were not visible in the simulation of the healthy femur suggesting that generation of a 3D relative risk score would be viable.

Although implementation of a 3D relative risk score is technically feasible, a major limitation of this approach was that it removed the ability to relate directly between the result of the evaluation and the shape of the lesion on 2D clinical images. While the ability to derive an absolute score for each patient was the principal aim of this study, the ability to provide qualitative guidelines was an important secondary objective and therefore an investigation into the viability of using 2D models was instigated.

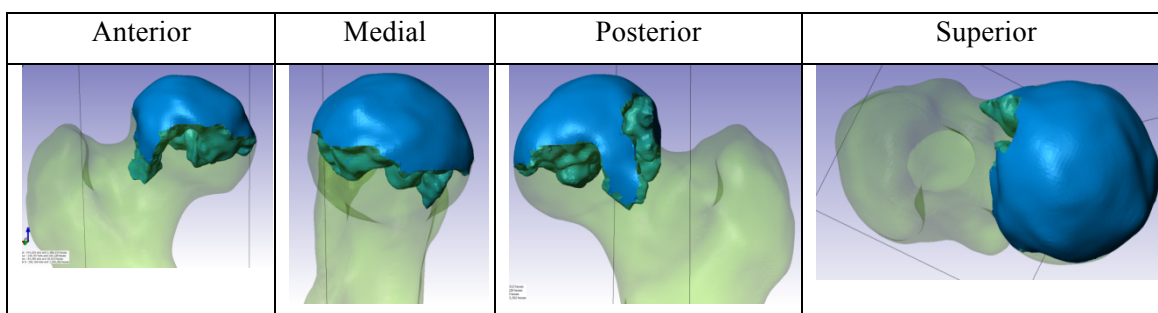


Figure 99. Anterior, medial, posterior and superior views of the femur and lesion geometry models for patient 01_002.

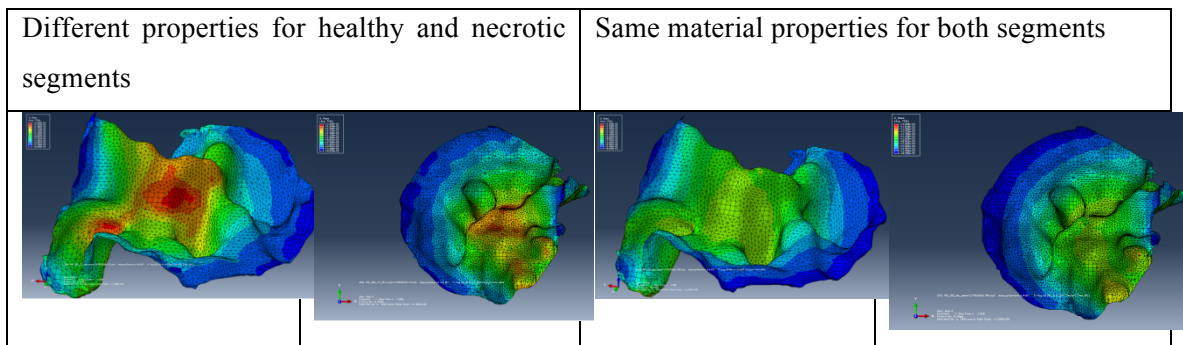


Figure 100. Plots of von Mises stress over the lesion boundary. Left: the boundary when lesion was simulated with half the stiffness of the healthy bone; Right: the same surface from a simulation where the same material properties were used throughout.

This pilot study also showed that the location within the femoral head from which the 2D models were derived was likely to have a significant influence on the stress distribution around the lesion boundary and therefore the relative risk score. Slices from multiple locations were used to evaluate this.

Six one-voxel-thick slices were generated for each patient⁶ (Table 50) from the three-dimensional geometry models: Four were generated with the femur oriented in an approximation of stance (neutral flexion; approximately 20° of anteversion). The remaining slices were generated after 20° of flexion had been introduced. This orientation was used as an approximation of heel strike.

Three of the neutrally oriented slices were aligned to the M-L plane (global Y-Z). These slices were generated through the head centre and 2mm medial or lateral to that location. The aim of including the slices that were medial to and lateral to the central M-L plane was to gain an understanding of the sensitivity of the relative risk score for a patient to the choice of slice through the femoral head. Including A-P and M-L slices in both neutral and flexed orientations was motivated by the results of the previous study (Section 4.5) which showed that orientation of the lesion boundary relative to the load vector was an important consideration.

⁶ Only 5 cases were developed for patient 01_001 as the lesion did not pass through the 20° flexion M-L slice

Table 50. Six two-dimensional slices through the geometry models of each femoral head were generated from the three dimensional geometry model of each patient’s proximal femur, four with the femur in a neutral position and two with the femur oriented in 20° of flexion.

Femur Orientation	Slice name	Slice description
Neutral	A-P	Anterior-posterior passing through head centre
	M-L	Medio-lateral passing through head centre
	Medial	Medio-lateral oriented 2mm medial to the head centre
	Lateral	Medio-lateral oriented 2mm lateral to the head centre
20° Flexion	A-P 20° Flexion	Anterior-posterior passing through head centre
	M-L 20° Flexion	Medio-lateral passing through head centre

The one-voxel-thick three-dimensional masks were extracted from the three-dimensional model and re-oriented to lie on the X-Y plane. The volume of interest was then cropped to contain only two layers in the Z-direction: One layer containing the two-dimensional masks, the other was empty. It was also cropped in the X- and Y- directions to leave 3-6mm of filler around the subchondral surface and to remove the inferior 5mm from the head. The sequence of cropping, extraction, reorientation and cropping is shown in Table 52. Shells between each mask and the Z-minimum plane were generated in the ScanFE (Simpleware Ltd., Exeter, UK) module before each set of single-voxel thick masks was exported from ScanIP into Abaqus CAE for FE analysis using the ScanFE extension settings shown in Table 53. No geometry pre-processing was used before volume meshing because recursive Gaussian smoothing was used during mask generation. Additional smoothing was used during mesh generation to reduce discontinuities between the masks. The target maximum grid size equated approximately to a 1mm mean element edge length in the mixed hexahedral / tetrahedral mesh. Contacts between each surface were generated, as were shells between each mask and the Z-minimum boundary.

Table 51. Schematic representation of the process of extracting and reorienting the 2D slice from the volume of interest (VoI). In this case a medio-lateral slice with the femur in a neutral orientation is shown. It was isolated from the 3D VoI (1) and re-oriented to lie on the X-Y plane (2). The VoI was cropped until it was 2 voxels thick in the Z-direction (3) and to leave 3-6mm of filler around the head remove the inferior 5mm from it.

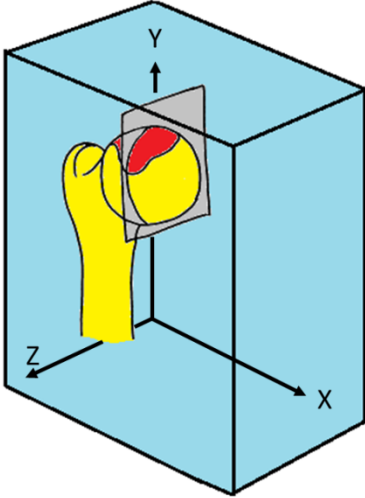
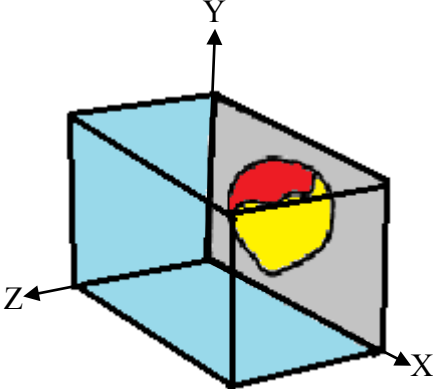
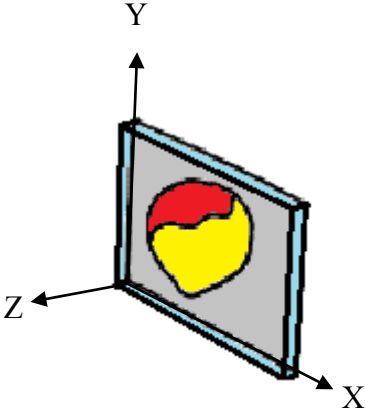
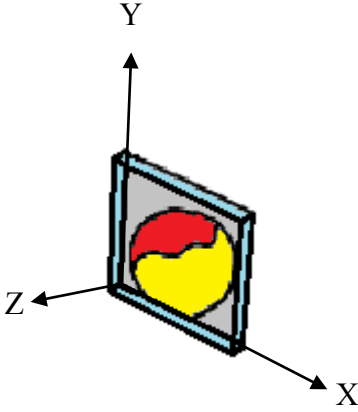
1. The 2D slice was isolated from the 3D VoI	2. 2D slice re-oriented to lie on the X-Y plane
	
3. VoI cropped to 2 voxels thick in Z-direction	4. VoI cropped in the X- and Y-directions
	

Table 52. ScanFE settings used to generate an FE mesh to be exported into Abaqus.

Stage	Setting
Pre-processing	No pre-smoothing
Volume meshing	Additional smoothing: Maximum curvature 0.50; Maximum iterations 5 Optimisation of mesh quality: Minimum quality target 0.05 Target maximum grid size: 1x1x1 Element type: Mixed hexagonal / Tetragonal elements
Contacts	Contact pairs between each mask
Shells	Shell between each mask and the Z-min boundary (X-Y plane)

Conversion to quadrilateral elements

The one-voxel-thick three dimensional geometry models with an additional empty Z-layer were imported into Abaqus from ScanIP as mixed hexahedral/tetrahedral meshes. The intersections between the three masks tended to have a poor quality mesh with small gaps and very thin tetrahedral elements. These areas were manually repaired using the mesh editing tool in Abaqus to generate a mesh with evenly distributed nodes around the periphery of each component (Figure 101). The quality of the revised mesh was unimportant as it was replaced by a two-dimensional quadrilateral mesh using a Python script developed by Dr. Marlene Mengoni, Institute of Medical and Biological Engineering, University of Leeds (Mengoni et al., J. Biomech. Mat. Article in press, accepted March 2015).

The Python script automated the following steps:

1. Deletion of the ScanIP generated mesh.
2. Deletion of all nodes not located at the periphery of each mask and on the “Z” plane.
3. Generation of a sketch for each component (head, lesion and filler), the geometry of which was defined by the peripheral nodes in that component.
4. Generation of a quadrilateral mesh for each component seeded by the peripheral nodes.

After re-meshing, the superior edge of the filler was cropped to produce a horizontal surface between 2mm and 4mm above the apex of the femoral head. A second filler component was generated that mated with this surface and encompassed a semi-circular platen with a 25mm radius. This was added to the assembly to produce a final construct. A schematic diagram of the final construct is shown in Figure 102. The distance between the head and platen was kept constant at 10mm by adjusting the distance between the platen apex and base of the second filler component on a model-by-model basis, thus replicating the conforming contact methodology defined in Chapter 4.

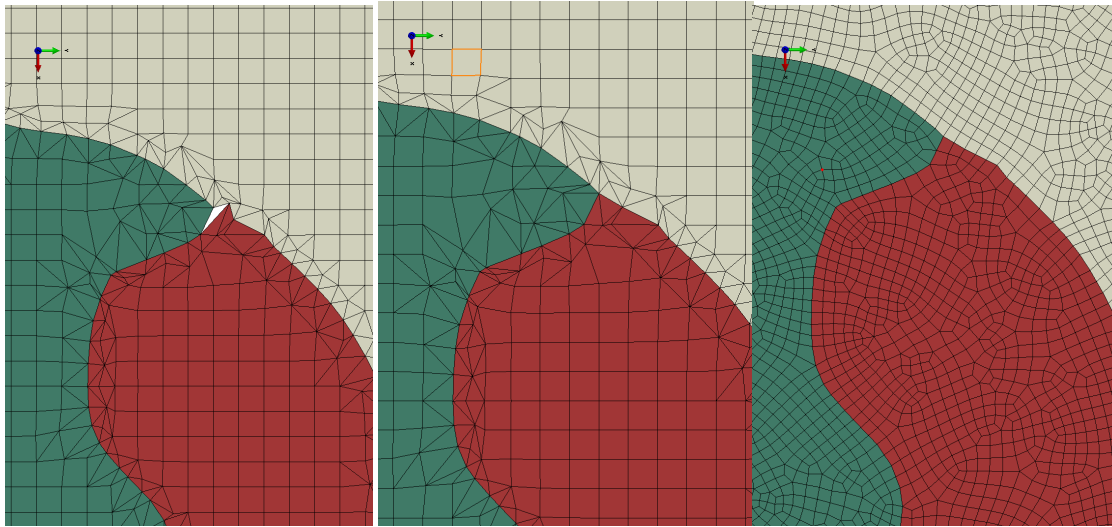


Figure 101. Left: Typical example of the boundary between the head, lesion and filler portions in the model imported from ScanIP. Middle: Manually repaired mesh. Care was taken to maintain an equal element edge length at the surface where possible. Right: Revised mesh generated using the boundary nodes and the method developed by Dr. Marlene Mengoni. The mean element edge length in the original mesh was 1mm. It was 0.5mm in the revised mesh.

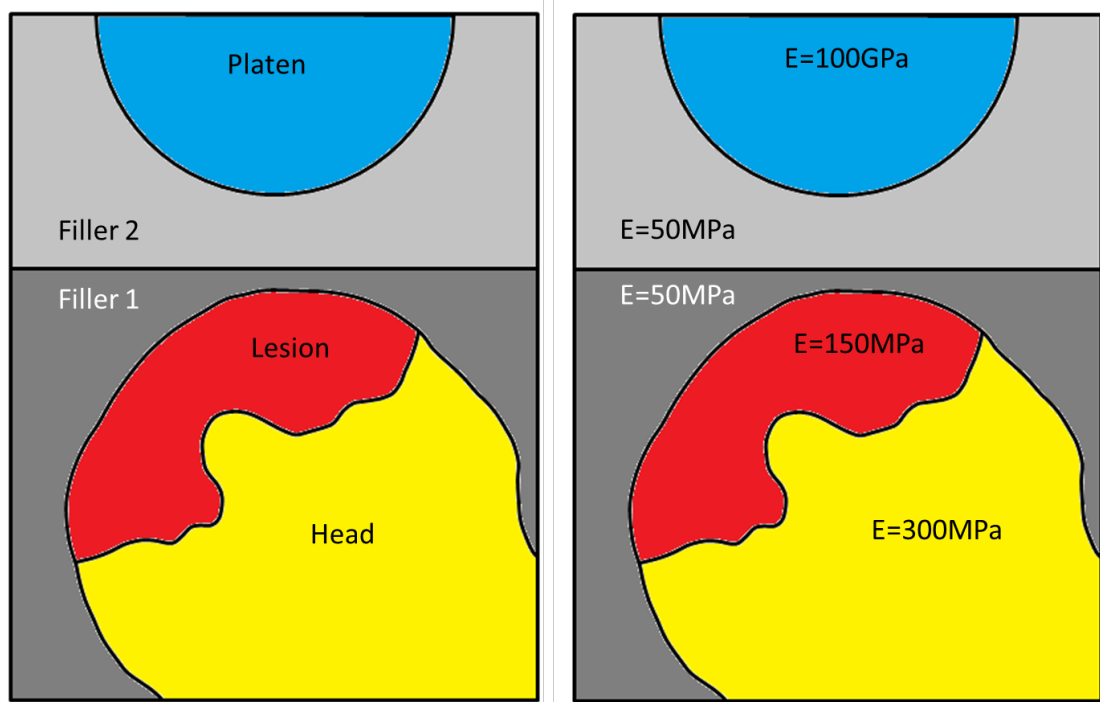


Figure 102. Schematic diagram showing a typical example of the final construct. Left: Labelled by part; Right: Labelled by elastic modulus. The platen radius (20mm), separation between the platen and head/lesion construct (10mm) and filler modulus were defined in the study recorded in Section 4.3.

Mesh, boundary conditions and material properties

The platen and upper section of the filler were assigned a mean element edge length of 1mm. The remaining components all had a mean element edge length of 0.5mm.

The platen was assigned an elastic modulus of 100GPa; the filler 50MPa, the head 300MPa and the lesion 150MPa. All components were assigned a Poisson's ratio of 0.3. The material

properties were kept constant to isolate the effect of shape from differences in the properties of heads from individual patients. It is noted that differences in stiffness would be an important factor to consider in future evaluations of this risk score.

The platen-filler, filler-head and filler-lesion interfaces were defined as a contact interaction with a penalty friction co-efficient of 1 tangentially and hard contact normally. Separation after contact was permitted. The interface between the two filler sections was tied, as was the head-lesion boundary. The inferior surface of the head was pinned. The platen was displaced by 1.7mm over one load step.

Post processing

To evaluate the risk score, 47 2D cross-sectional FE models representing the hips of 8 patients (six with pre-collapse lesions and two post-collapse) were evaluated. The models were generated from 3D geometry models created using CT data to establish the bone geometry and MR data to establish the boundary of the lesion. Once the geometry models were constructed, 2D sections in any orientation could be extracted quickly and consistently. Although potentially more efficient and easier to interpret, there was a risk that this approach would be less sensitive than using a full 3D simulation so multiple cross-sections were generated per patient. This allowed the ability of the score to rank patients and its sensitivity to user input to be evaluated.

Each patient was ranked according to the average of the risk scores obtained for the cross-sectional models of their femoral heads. The rank was compared to the ARCO grading system as this is the current gold standard for quantifying AVN. The risk score rank was consistent with that of the ARCO grading system but offered improved granularity.

When the scores for each cross-section were ranked individually it was discovered that all cross-sections from the post-collapse patients had a risk score above 360. The same patient ranking was achieved by counting the number of slices for the pre-collapse patients with scores above this threshold. This offers an alternative means of assessing risk using a unique interpretation the same data set. It was not possible to confirm whether this threshold assigned would be appropriate in a larger patient cohort: confirmation of this would only be possible through clinical follow-up of patients classified in this way.

Relative risk (difference) was calculated for each case using the method described in Section 3.2.4. Only the most highly stressed half of the boundary was included in the calculation in previous studies where the boundary was symmetrical. In the patient-specific models, the boundaries had an organic form so the entire surface was included. Hence it was not possible to compare results of this study to those presented in Chapter 3 or Chapter 4.

The patient specific finite element models were analysed in the following stages:

1. Analysis of average relative risk scores.
2. Analysis of a revised relative risk score including lesion volume.
3. Case-by-case analysis of revised relative risk score.
4. Analysis of sensitivity to femur orientation and user input.

In the first stage of the analysis an average RR_D score was calculated for each patient to establish whether a difference between the fracture set and the no fracture set could be identified. Two approaches were compared: in the first approach all cases for each patient were included in the calculation; in the second approach only the stance cases were included.

In the next stage, the average scores per patient were re-evaluated using a revised relative risk score that was the product of RR_D and a volume coefficient. Volume expressed as a magnitude (mm^3) and percentage (%) were both evaluated. Again, the average for each patient was calculated using all cases and only the stance cases. At the end of this stage the patients were ranked according to their revised relative risk score.

A case-by-case analysis was performed in the third stage. The aim was to identify whether a threshold for the revised risk score, below which fracture was unlikely, could provide a meaningful assessment of the risk of progression. To achieve this, cases were ranked in order of ascending risk score and the cases from the fracture set identified. A threshold that differentiated the fracture set from the no fracture set was defined and the number of cases per patient above the threshold was identified. This allowed the entire patient group ($n=8$) to be divided into three distinct groups:

Group 1: The patients had no cases above the threshold.

Group 2: The patients had between 1 and 5 cases above the threshold.

Group 3: The patients had all 6 cases above the threshold and were in the fracture set.

Correlation between results obtained using different approaches was evaluated using a Pearson product-moment correlation co-efficient.

During the final stage, sensitivity of the analysis method to femur orientation was evaluated by comparing the A-P and M-L results for cases where the femur was in a stance orientation to the results for cases where the femur was oriented in 20° of flexion. Sensitivity to user selection was evaluated by comparing the results for the three medio-laterally oriented stance cases.

5.3.2 Results

Analysis of average relative risk scores

A general summary of the results of the relative risk calculation for each patient is presented in Table 54. There was a large variation in the intra-patient RR_D score with a typical range of between 19 and 32 points. Within the data set (47 two dimensional cases from eight patients), the overall average relative risk score was 18 (range 3 to 40, S.D. 11).

The average RR_D score for each patient is shown in Figure 104. The average RR_D score was 17.6 (S.D. 3.2; range 10 to 19) in the no fracture set. It was 24 and 29 for patients P01_002 and P02_003 (the fracture set) respectively, indicating that RR_D differentiated between the fracture and no-fracture sets.

Table 53. General summary of relative risk (difference) scores for each case evaluated for each patient. The femur orientation and slice orientation columns describe the slices defined in Table 50. No score was calculated for patient 01_001 for the medio-lateral slice in 20° of flexion because the lesion was not present in this slice. Fracture cases are marked with an asterisk.

Patient	Femur orientation	Slice orientation	Relative risk (difference)	Patient specific statistics	
01_001	Stance	AP	22	Average (n=5)	19
		ML	34	Standard deviation	10
		Medial	14	Range	26
		Lateral	17		
	20° Flexion	AP	8		
		ML	-		
01_002*	Stance	AP	8	Average (n=6)	24
		ML	40	Standard deviation	13
		Medial	27	Range	32
		Lateral	35		
	20° Flexion	AP	10		
		ML	25		
01_003	Stance	AP	21	Average (n=6)	16
		ML	8	Standard deviation	9
		Medial	7	Range	21
		Lateral	19		
	20° Flexion	AP	28		
		ML	9		
01_004	Stance	AP	8	Average (n=6)	17
		ML	25	Standard deviation	11
		Medial	33	Range	25
		Lateral	19		
	20° Flexion	AP	9		
		ML	8		
01_005	Stance	AP	18	Average (n=6)	16
		ML	18	Standard deviation	7
		Medial	8	Range	19
		Lateral	10		
	20° Flexion	AP	27		
		ML	14		

Table 53 continued.

Patient	Femur orientation	Slice orientation	Relative risk (difference)	Patient specific statistics	
01_006	Stance	AP	3	Average (n=6)	10
		ML	10	Standard deviation	10
		Medial	8	Range	28
		Lateral	30		
	20° Flexion	AP	3		
		ML	5		
02_001	Stance	AP	17	Average (n=6)	17
		ML	7	Standard deviation	10
		Medial	21	Range	27
		Lateral	34		
	20° Flexion	AP	11		
		ML	13		
02_003*	Stance	AP	27	Average (n=6)	29
		ML	34	Standard deviation	8
		Medial	34	Range	21
		Lateral	13		
	20° Flexion	AP	29		
		ML	34		

The exercise was repeated using only the four slices obtained in the stance orientation. In this case the average RR_D score was 18.5 (S.D 4.3; range 12.6 to 27.2) in the no fracture set. The RR_D score was identified as 27 for both patient 01_002 and patient 02_003 (the fracture set) (Figure 104). The magnitude of the RR_D score for each patient changed but the relative ranking was unchanged. This indicated that the patient averages were sensitive to slice selection but that, for this particular set of cases the effect was less than the variation between patients.

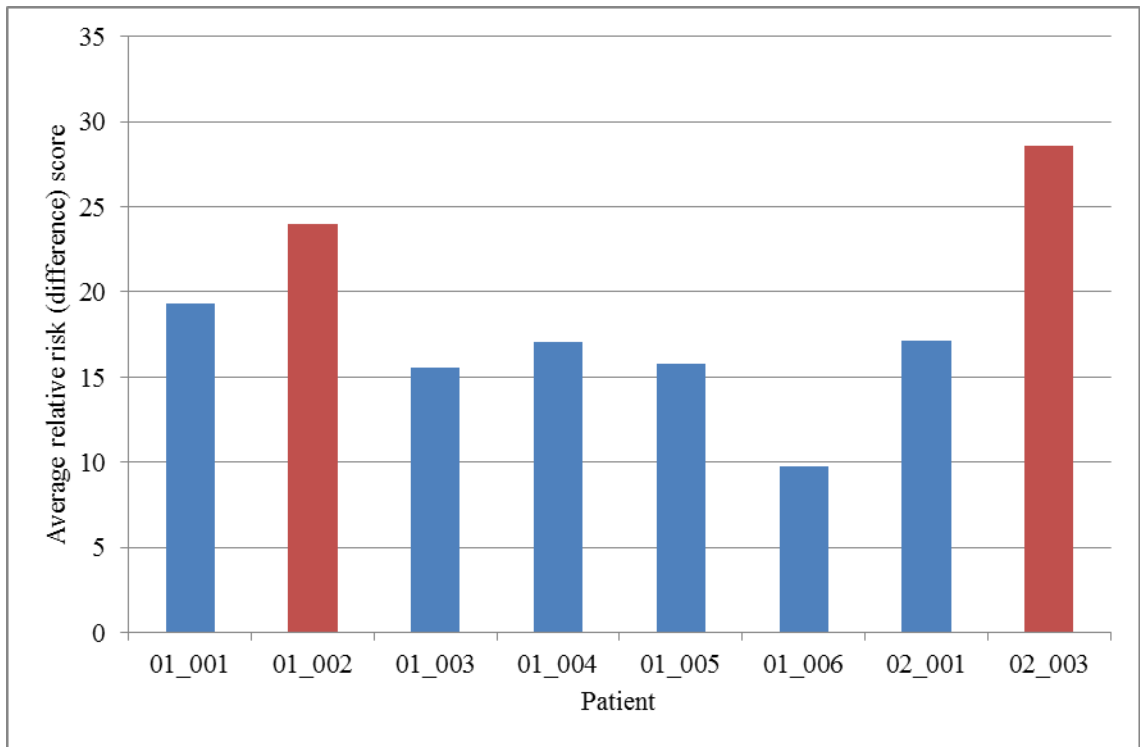


Figure 103. Average relative risk (difference) score calculated for each patient using all slices for each patient. The two patients in the fracture set are shown red; patients in the no-fracture set are shown in blue.

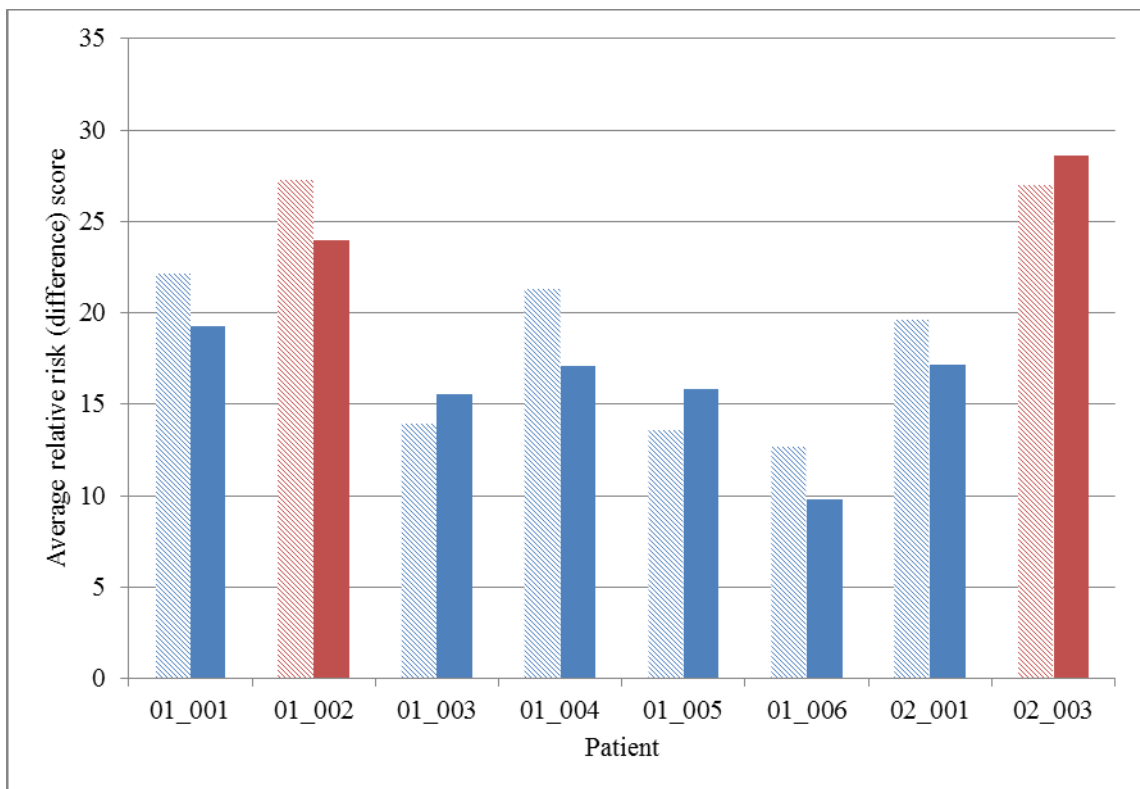


Figure 104. Comparison between average relative risk (difference) scores obtained using only the stance cases (hatched bars) and using slices taken in both stance and 20° of flexion (solid bars). The two patients in the fracture set are shown in red. The patients in the no-fracture set are shown in blue.

Evaluation of a revised relative risk score using lesion volume

The result of multiplying the average relative risk score for each patient by the lesion volume (in mm^3) is presented in Figure 105. A difference was found between the fracture and no-fracture sets but this approach masked the effect of the relative risk score because the relative risk scores were of different orders of magnitude to the volumes: Relative risk scores were of the order 10^1 whereas volume was of the order 10^3 .

A difference between the fracture and no fracture sets was also found when the lesion volume was expressed as a percentage of the volume of the femoral head (v/v %) (Figure 106) and although the rank of the patients did not change, the separation between each patient became more distinct compared to the results when volume was expressed as a magnitude. In particular, patients 01_004 and 02_001 were differentiable in Figure 106 (volume in v/v %) but not in Figure 105 (volume in mm^3). This confirmed that matching the order of magnitude for the components of the revised relative risk score reduced the masking effect that using unequal orders of magnitude introduced.

The evaluations were repeated using only the four cases from each patient taken in stance orientation. The fracture and no fracture sets remained distinctly separated. Comparisons between the two sets of averages are shown in Figure 107 and Figure 108. When volume expressed as a magnitude was used, the rank of patient 01_001 (no fracture) changed relative to patient 02_003 (fracture). There was no change in rank when volume was expressed as a percentage.

In summary, the method where volume was expressed as a percentage offered better differentiation and was less sensitive to slice selection. Henceforth the revised score was calculated as RR_D multiplied by the percentage volume involvement. The patients were ranked from lowest to highest according to the revised score in Table 55. The ranking correlated with the rank attributed to the patients using the ARCO grading. When the ARCO grading system was used, the patients were divided into four clinical grades. When the proposed risk score was used each patient could be allocated a discrete score.

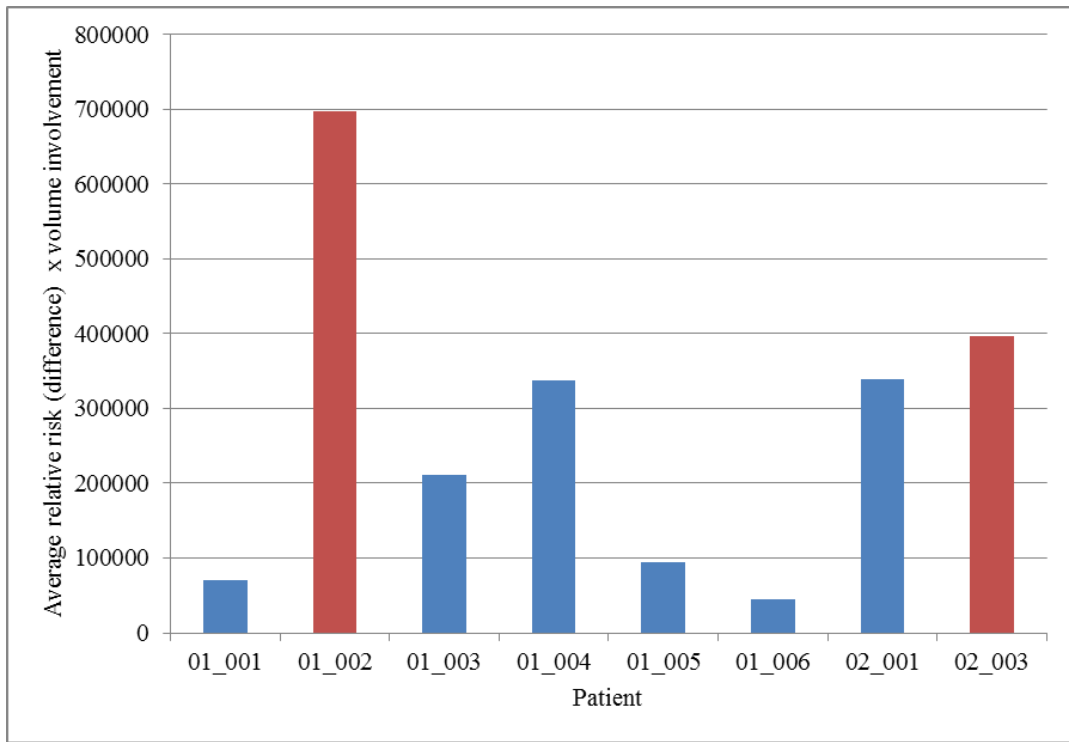


Figure 105. Average relative risk (difference) score multiplied by volume involvement for each patient. The two patients in the fracture set are shown in red and the patients in the no-fracture set are shown in blue. The volume (in mm³) of each lesion was two orders of magnitude higher than the average relative risk score, masking its effect.

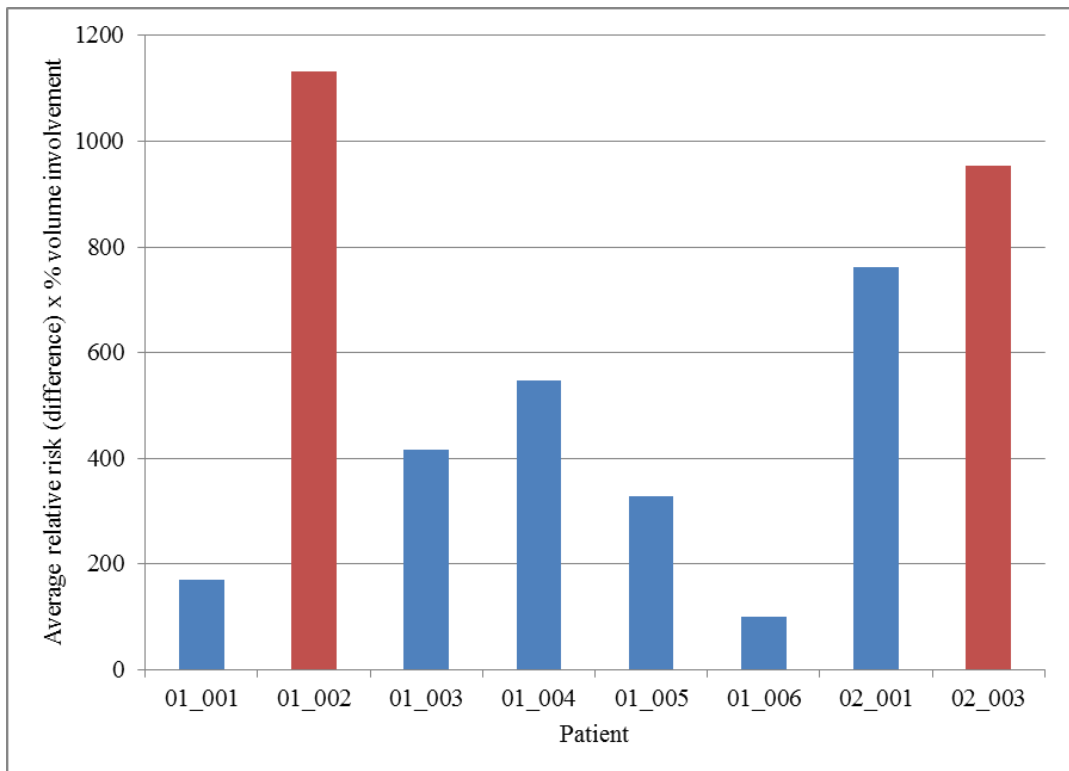


Figure 106. Average relative risk (difference) score multiplied by percentage involvement (v/v %) for each patient. The two patients in the fracture set are shown in red. The patients in the no-fracture set are shown in blue. Describing the volume involvement as a percentage rather than a magnitude reduced the coefficient to the same order of magnitude as the relative risk (difference) scores.

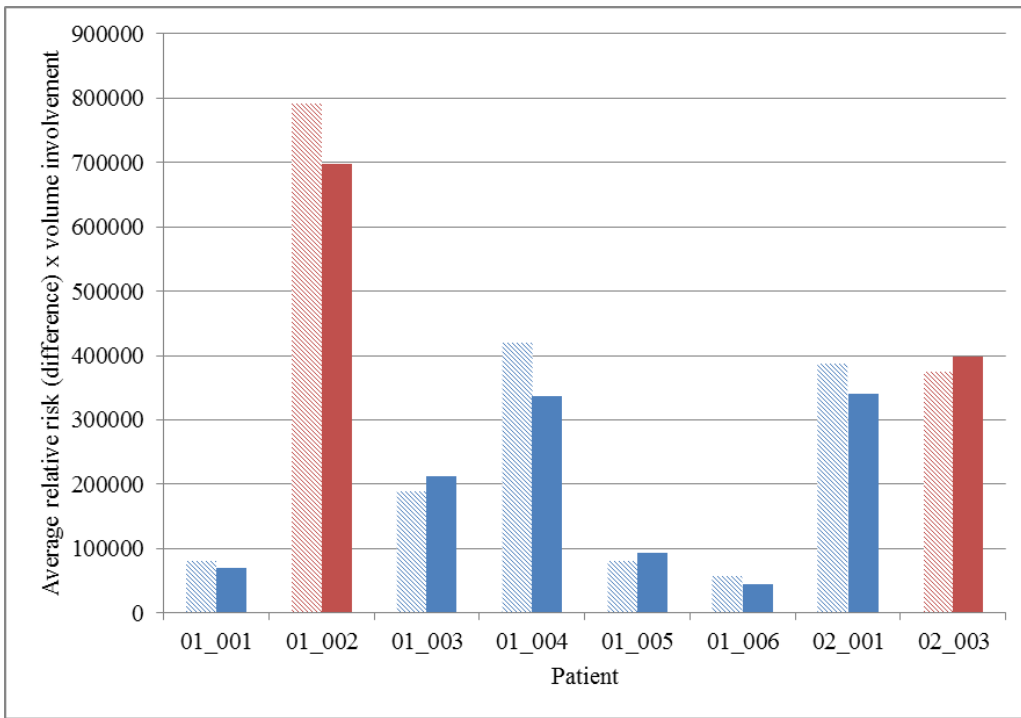


Figure 107. Comparison between average RR_D x volume involvement scores obtained using only the stance cases (Hatched bars) and using slices taken in both stance and 20° of flexion (solid bars). The two patients in the fracture set are shown in red. The patients in the no-fracture set are shown in blue. The volume (in mm^3) of each lesion was several orders of magnitude higher than the average relative risk score, masking its effect.

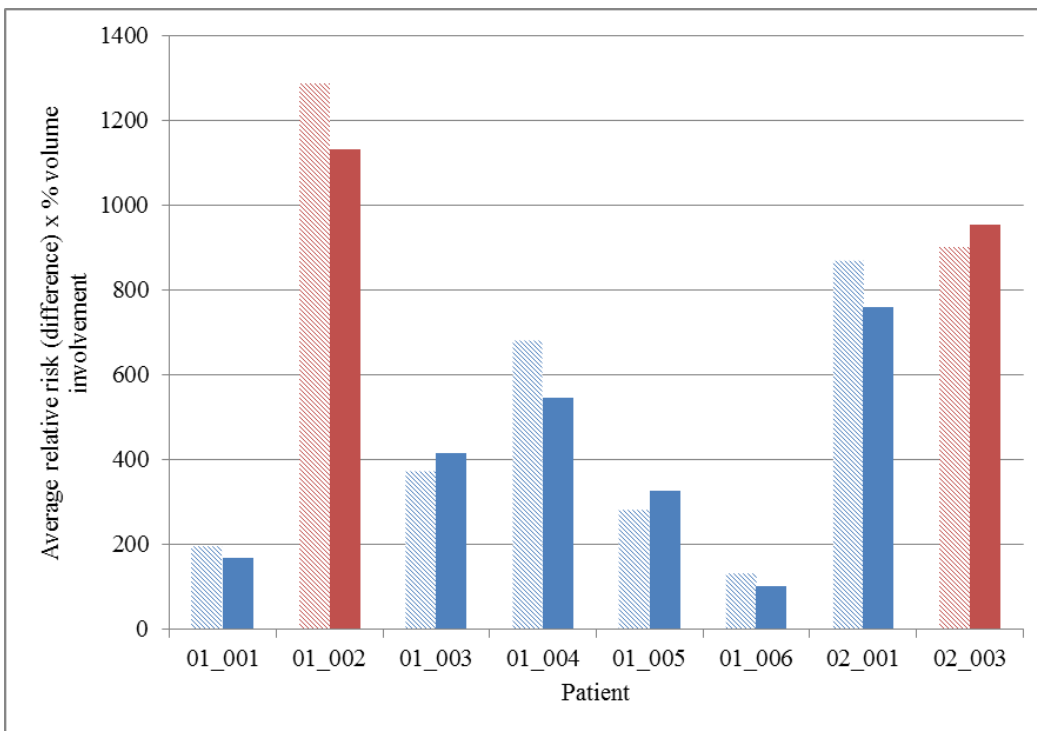


Figure 108. Comparison between average relative risk (difference) multiplied by percentage volume involvement scores obtained using only the stance cases (hatched bars) and using slices taken in both stance and 20° of flexion (solid bars). The two patients in the fracture set are shown in red and patients in the no-fracture set are shown in blue. Describing the volume involvement as a percentage rather than a magnitude reduced the volumetric component of the revised score to the same order of magnitude as the relative risk (difference) scores.

Table 54. The average revised score (using all cases for each patient) was used to rank the patients in ascending order. The ARCO grade and lesion volume are included for comparison. The patients marked with an asterisk constitute the fracture set.

Patient	Revised score	Rank	ARCO grade	Lesion volume (%)
01_006	101	1	IIA	43
01_001	169	2	IIA	44
01_005	328	3	IIB	38
01_003	416	4	IIB	46
01_004	547	5	IIC	49
02_001	762	6	IIC	44
02_003*	955	7	IIIC	43
01_002*	1133	8	IIIC	49

Case-by-case analysis of the revised relative risk score

The next stage of the analysis was to evaluate the revised relative risk score on a case-by-case basis. The 47 cases derived from eight patients were ranked by the revised score in ascending order (Figure 109). The ranked plot showed that the revised score was greater than 360 for all 12 cases from the 2 patients in the fracture set. This value was defined as a threshold against which the cases from the patients in the non-fracture set were evaluated.

The difference in peak VM stress, number of elements identified by the relative risk calculation, relative risk score, percentage volume involvement and the product of RR_D and percentage volume involvement between cases from patients in the fracture and no fracture sets were evaluated. The relative risk, percentage volume involvement and the product of the two were all different between the fracture and no-fracture sets but no difference was found between the two sets in terms of peak VM stress or the number of elements (Table 55). This again confirmed that the revised relative risk score was a better means of quantifying risk than using stress alone.

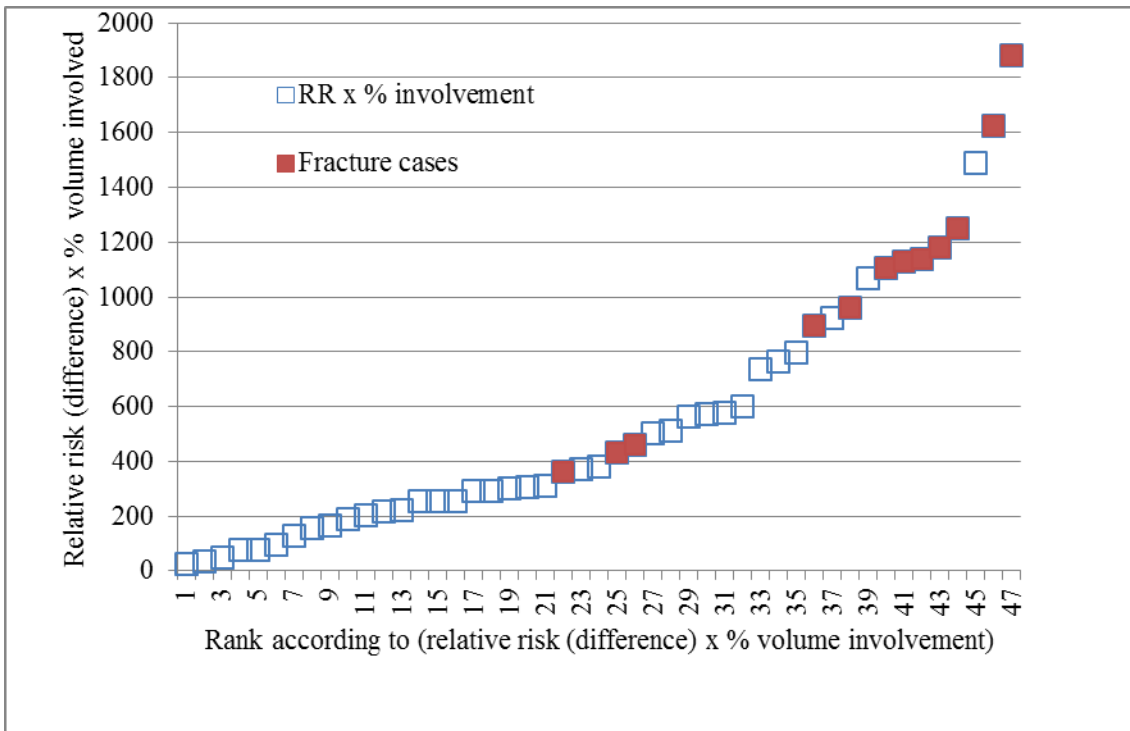


Figure 109. Plot of the revised relative risk scores for each case (n=47 from 8 patients) ranked in ascending order. The solid points represent cases from patients in the fracture set (12 cases from 2 patients). All cases from the fracture set had a revised score of more than 360.

Table 55. Average values for the cases from patients with and without a subchondral fracture and evaluation of the significance of the difference between the two sets for the components of the relative risk (difference) (RR_D), RR_D itself, percentage volume involvement and the product of the score and percentage volume involvement. A significant difference was found between sets for RR_D , percentage volume involvement (V) and the product of RR_D and V.

Measure	Average	
	No Fracture	Fracture
Peak von Mises stress (MPa)	2.8	2.8
Number of elements (n)	10	11
Relative risk (RR_D)	15.7	26.3
Percentage volume involvement (v/v %)	24	40
$RR_D \times V$	393	1035

Thirteen out of 35 cases from 4 out of 6 patients in the no fracture set had a revised score of more than 360. The number of cases identified per patient above this threshold is summarised in Table 56. No cases for patients 01_001 and 01_006 had a revised score greater than 309.

Table 56. Number of cases with a revised score above a threshold of 360 for each patient. Thirteen cases from the no-fracture set were identified as having a revised score above 360. All cases came from four out of the six patients in that set.

Patient	Number of cases above threshold of 360	Cases above threshold
01_001	0	None
01_006	0	None
01_005	2	Stance AP and ML
01_003	3	Stance AP and Lateral; 20° flexion AP
01_004	3	Stance ML, Medial and Lateral
02_001	5	Stance AP, Lateral and Medial; 20° Flexion AP and ML
01_002	6	All
02_003	6	All

The number of cases identified above the threshold was compared to the rank obtained from the average risk scores in Table 55. The resulting relationship was direct and linear (Figure 110) and on this basis the patients were grouped into low, medium and high risk categories based on the revised score. The low risk group contained patients 01_001 and 01_006, both of whom had revised scores of less than 310 for all of their cases. The revised scores for cases in this category (n=11) were lower than the scores for the cases in the medium risk category (n=24). The revised scores were above the threshold of 360 in between two and five cases in the medium risk group (n=24) and the high risk group (which corresponded with the two cases in whom fracture was identified) had all cases above the threshold (n=12).

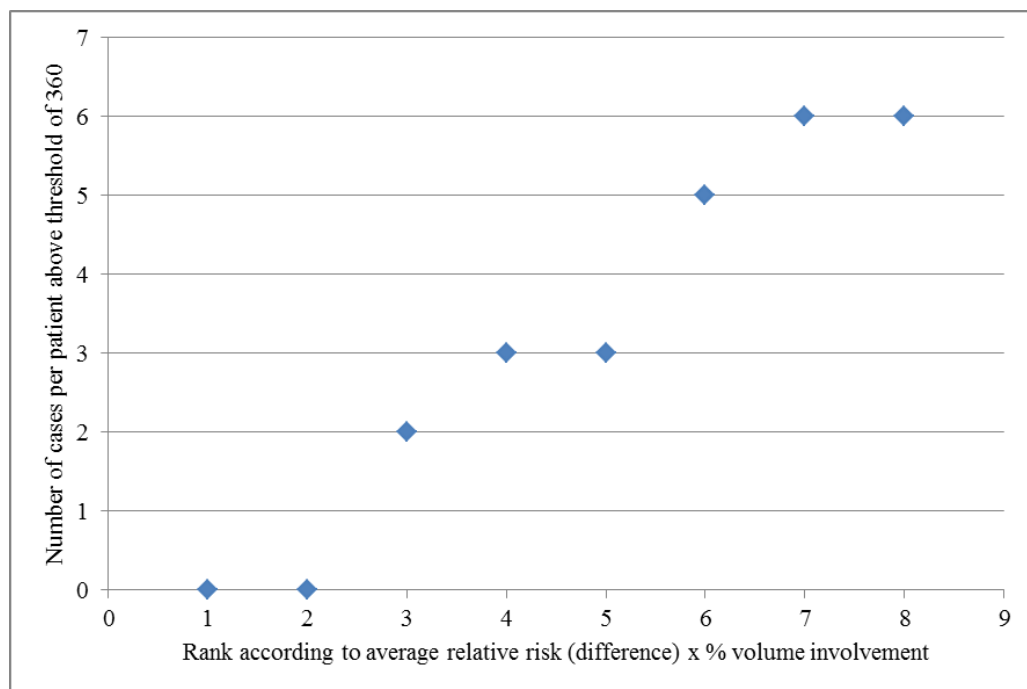



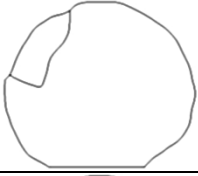
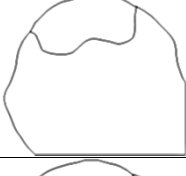
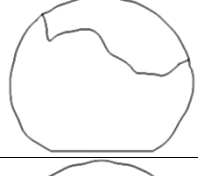

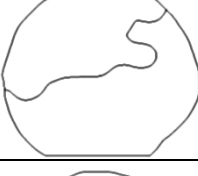

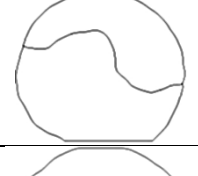



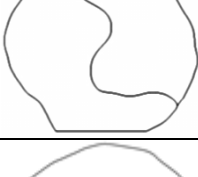




Figure 110. Scatter plot of patient rank according to the revised relative risk score (Table 52) against the number of cases per patient above a threshold value for the revised score of 360 (Table 56). Two patients (01_001 and 01_006) had no cases above the threshold. All six cases from each patient in the fracture set (01_002 and 02_003) were above the threshold.

A qualitative comparison of lesion shape according to patient rank was made in Table 57. There was a trend for increasing lesion size and increasing involvement of the articular surface with rank but this was subjective and not consistent. A further qualitative comparison between the stress plots for a low risk case (Patient 01_001 stance AP, Figure 111) and a high risk case (Patient 02_003 stance AP, Figure 112) was made. The boundary between the lesion and healthy bone was approximately 80 elements longer in the high risk case because the lesion was larger and the surface was more convoluted. Although the peak stress was of comparable magnitude in both cases, the length of the areas where there was a high stress or large stress difference was qualitatively larger in the high risk case. Evaluating the two cases quantitatively showed that the RR_D score was 23% higher in the second cases (27 versus 22) and the volume involvement was more than three times greater (33.4% versus 8.8%) (Table 58).

Table 57. The patients were grouped according to revised relative risk score (relative risk (difference) x % volume involvement) and the presence or absence of fracture. Each patient was ranked in ascending order according to the average revised relative risk score (Table 52). Mid-head AP and ML images of the head and lesion are shown for reference.

RR _D x % volume involvement	Rank (1 = lowest risk)	Patient	Stance AP	Stance ML
<310	1	01_006		
	2	01_001		
>360; no fracture	3	01_005		
	4	01_003		
	5	01_004		
	6	02_001		
	7	02_003		
>360; fracture	8	01_002		

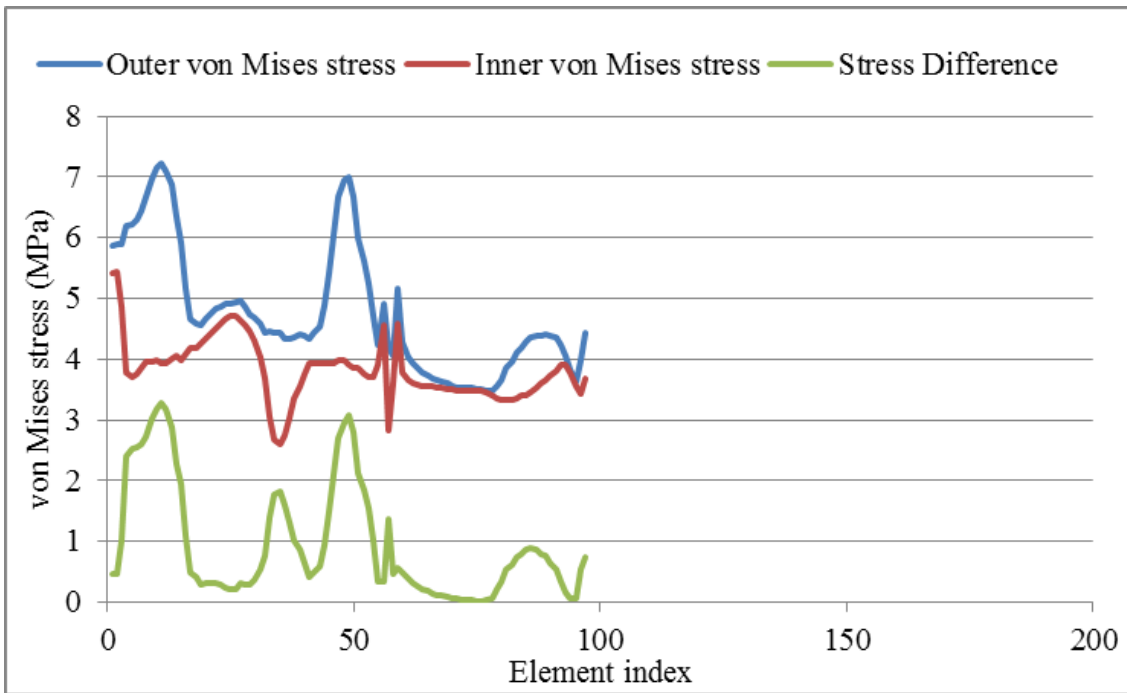


Figure 111. Plot of von Mises stress around the lesion in the stance AP case from patient 01_001. This patient was identified as having the lowest risk of progression according to their revised relative risk score. The x-axis indicates the element index in the ordered set starting at the left-most element in the two dimensional plot. The surface was approximately 80 elements shorter than the equivalent case in the highest risk patient (Figure 108).

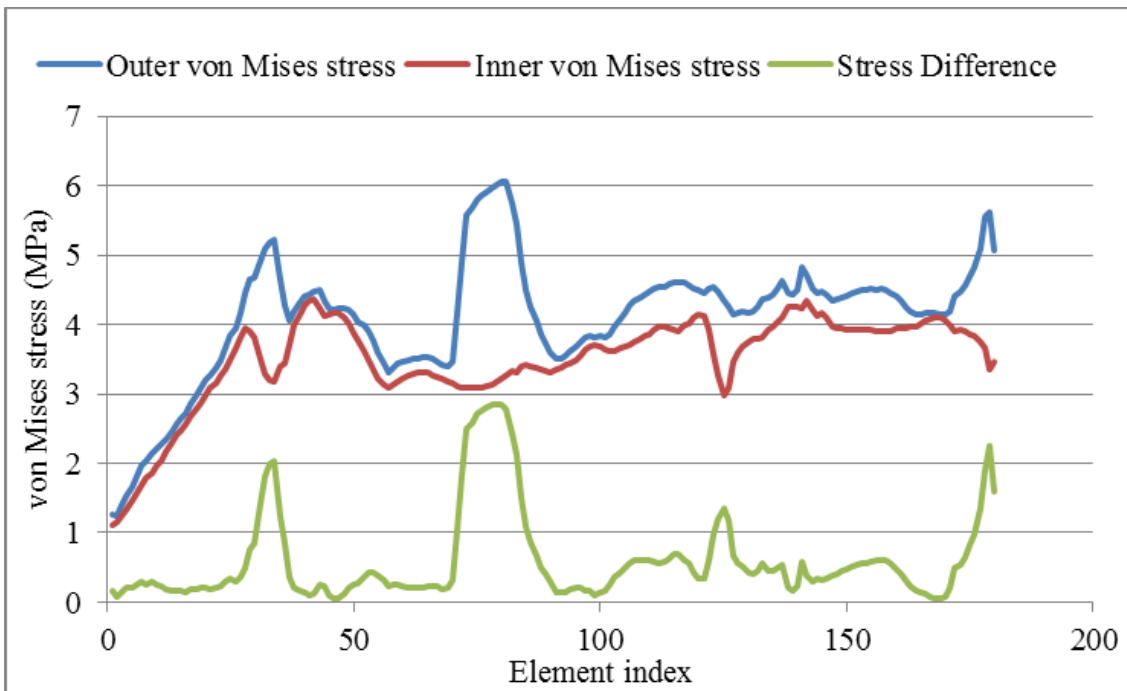


Figure 112. Plot of von Mises stress around the lesion in the stance AP case from patient 02_003. This patient was categorised as having a high risk of progression according to their revised relative risk score. The x-axis indicates the element index in the ordered set starting at the left-most element in the two dimensional plot.

Table 58. Comparison between stance anterior-posterior slice statistics for patient 01_001 and patient 02_003. Patient 01_001 was identified as having the lowest risk of progression; patient 02_003 had the highest risk.

Patient	Maximum VM stress difference (MPa)	Number of elements over threshold	RR _D	Volume (%)
01_001	3.7	7	22	8.8
02-003	2.9	10	27	33.4

Analysis of sensitivity to femur orientation and user input

Sensitivity to orientation was evaluated by comparing the AP and ML results for stance to the results obtained from slices generated in 20° of flexion (Figure 113 and Figure 114). The variation between the scores obtained in the AP planes (average difference 5; S.D 4.6) was slightly less than in the ML planes (average difference 7; S.D. 7.1).

Comparing AP cases, in six out of eight cases the score in stance was lower than the score in 20° of flexion. The exceptions were patients P01_001 and P02_001; there was no pattern in the ML cases. Both AP and ML sets showed some correlation between stance and 20° flexion cases ($r= 0.73$ and 0.76 respectively). Expressed as a percentage of the mean, the overall range of differences between stance and flexion cases was between 1% and 103%. This was larger than the difference between average patient RR_D scores for the fracture and no fracture sets (Figure 103) indicating that this variation could have a significant impact on the risk assessment.

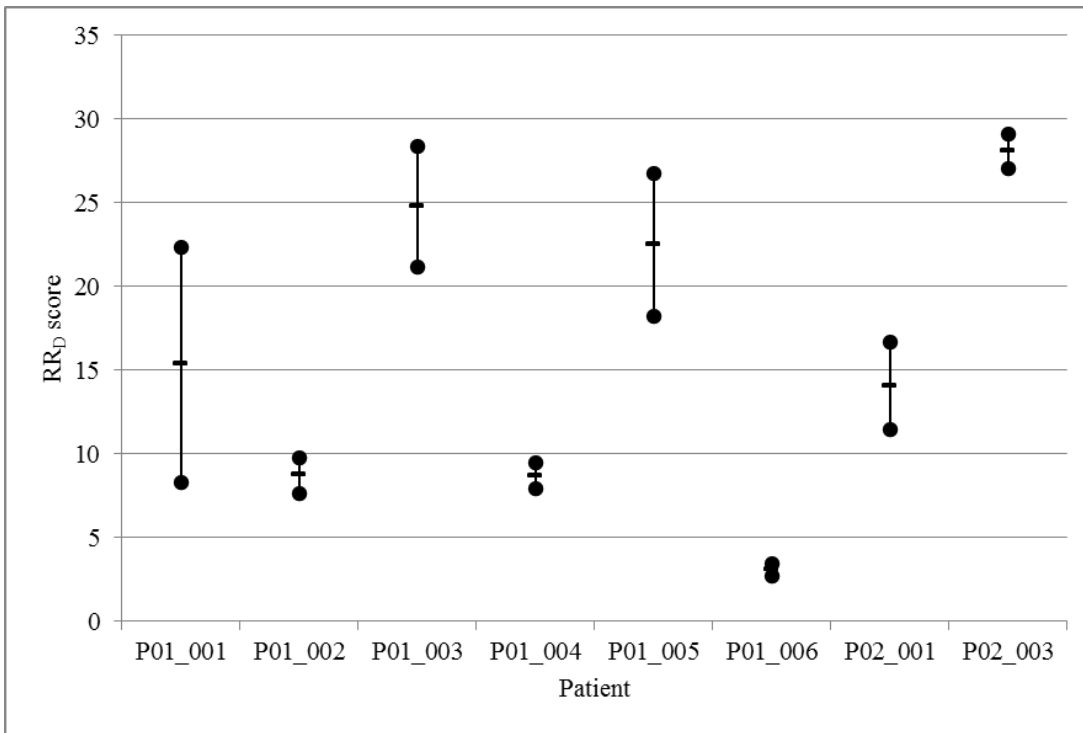


Figure 113. Comparison between relative risk scores derived from anterior-posterior slices taken in stance and 20° of flexion showing the mean, highest and lowest scores obtained for each patient. The bar represents the average of the two values (denoted by the solid circles).

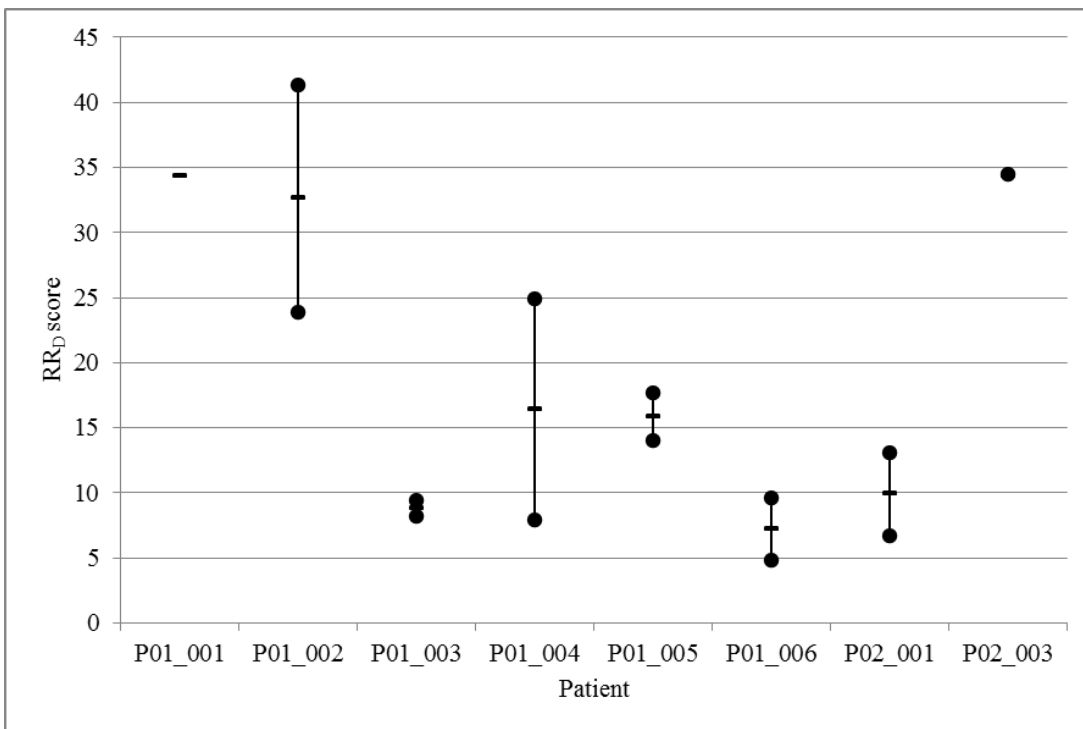


Figure 114. Comparison between relative risk scores derived from medio-lateral slices taken in stance and 20° of flexion. The bar represents the average of the two values (denoted by the solid circles) No ML slice was taken for P01_001 in 20° of flexion as the lesion did not pass through this slice. The score was highest in stance for patients P01_003, P02_001 and P02_003; it was highest in flexion for the other cases.

Sensitivity to the operator's choice of slice was evaluated by comparing the relative risk score for three slices taken in the medio-lateral plane. The results for each case are presented in Figure 115. There was poor correlation between each set (Table 59). Variation due to slice

selection (Figure 116) was between 40% and 144% of the mean. This highlighted the sensitivity of the outcome measure to user input.

The impact of this variation on the ability of the relative risk score to differentiate between the fracture and no fracture patients was evaluated by taking the maximum RR_D score from the three medio-laterally oriented slices for each patient and averaging it with the AP slice for each patient. The resultant scores no longer differentiated between the fracture and no fracture sets.

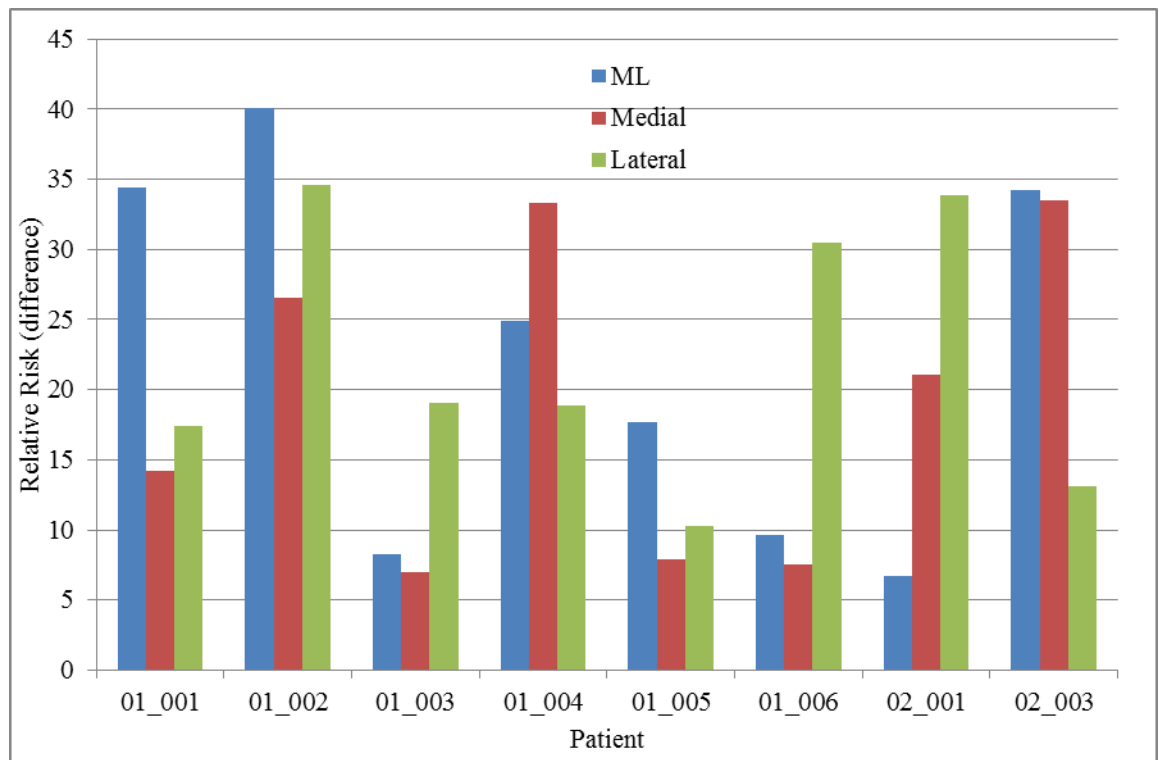


Figure 115. Comparison of relative risk scores obtained for each patient from the central medio-lateral slice and slices taken 2mm medial and lateral to this slice. No trend was established and the intra-patient variation ranged from 44% to 144%

Table 59. Pearson product-moment correlation coefficients comparing the relative risk scores obtained for the medio-lateral, medial and lateral slices for each patient. The correlations were weak indicating that the three data sets were unrelated

Slice	Medial	Lateral
ML	0.6	-0.16
Medial	-	0.05

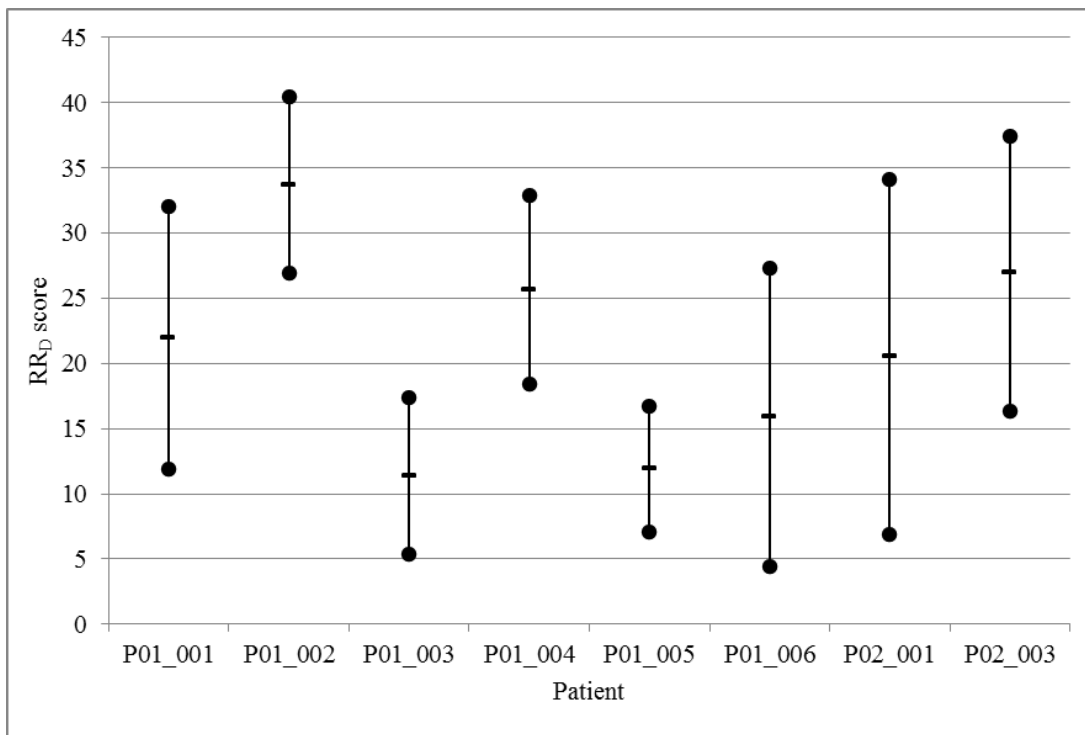


Figure 116. Evaluation of the sensitivity to slice selection using three medio-lateral slices, each 0.5mm apart. The plot shows maximum, minimum and mean scores obtained for each patient.

5.4 Discussion

A total of 47 patient-specific 2D slices were generated from the femoral heads of eight patients with AVN. These were evaluated using the relative risk score first introduced in Section 3.2.4. Two patients had suffered subchondral fractures prior to image acquisition and were classified as having ARCO III AVN; the remaining six were classified as having ARCO II AVN (no fracture present). With the exception of the presence of fractures, there was no significant difference in terms of patient demographics or lesion volume between the two sets.

In the first stage of the study the average RR_D score was shown to differentiate between the fracture and no-fracture sets with statistical significance. To address the limitation highlighted in Section 4.5.5, the score was revised to include lesion volume expressed as a percentage of the volume of the femoral head. The revised relative risk score also differentiated between the fracture and no fracture sets and was used to rank the patients according to risk.

The inclusion or exclusion of cases derived from femurs in 20° of flexion affected the magnitude of the revised relative risk scores but did not change their rank. Re-orienting the femur relative to the load vector aligned different facets of the lesion boundary with the load vector and changed their position relative to the applied load. The relative risk scores were shown to be sensitive to the position and orientation of the lesion boundary relative to the load vector in Chapters 2, 3 and 4 and the current study confirmed that this sensitivity was relevant for organic lesion shapes too. It reinforces the hypothesis that the location around the lesion

boundary at highest risk of fracture will change depending on the orientation of the femur relative to the applied load.

All cases from the fracture set had a revised relative risk score greater than 360. This threshold allowed all eight patients to be classified as having either a low, medium or high risk of progression according to the number of cases from their scans that were above the threshold. There was a difference between the cases assigned to each risk level and the rank according to the number of slices per patient above the threshold also corresponded to the rank according to the averaged revised relative risk scores.

The most significant difference between low and high risk categories was lesion volume. This is consistent with previous studies (Nishii *et al.*, 2002) suggesting that the order derived using the proposed classification is correct. However, the unmet clinical need and limitation common to existing classifications of AVN pathology is the inability to differentiate between patients at medium risk of progression, for whom joint preserving treatment maybe appropriate and high risk patients for arthroplasty is the best choice. Although not clinically validated, the revised relative risk score was shown to be sensitive to lesion size, shape and location and was capable of ranking patients as well as sorting them into three statistically discrete risk levels. The two patients who were identified with post-collapse AVN had the highest relative risk scores. This is an important first step in validating the score that may help to justify future clinical evaluation.

It is noted that although the occurrence of fracture is a binary event, the risk increases incrementally and a linear rank may be more appropriate than discretisation into low, medium and high categories.

The method of risk quantification was shown to be highly sensitive to case selection. There was no correlation between RR_D calculated for adjacent cases and it was possible to confound differentiation between the fracture and no-fracture sets by biasing medio-lateral case selection to the highest scoring case. This demonstrated that a ranking method that used only a small number of cases per patient may have low repeatability and reproducibility but the previous results suggested that averaging a larger number of cases per patient might make the risk assessment less sensitive to user error.

Similar variation in the relative risk score for cases generated in the same plane but with the femur in different orientations was observed. It was not possible to confirm the hypothesis that risk of fracture would vary with femur orientation in this study and further work would be required to evaluate whether this is indeed the case. In a future study to evaluate this, the choice of joint load applied in each orientation should be carefully considered as joint load will vary with orientation and higher loads on one orientation would directly affect the relative risk score. The material properties were kept constant to isolate the effect of shape from differences in the

properties of heads from individual patients. It is noted that differences in stiffness would also be an important factor to consider in future studies.

The ability to differentiate between fracture and no fracture cases and to rank patients relative to a threshold value was a promising outcome. This outcome could be confounded by the small sample size and further work is required to verify the finding and to identify which factor is most significant. It was also impossible to confirm whether the threshold assigned would be appropriate in a larger patient cohort: confirmation of this would only be possible through clinical follow-up of patients classified in this way.

5.5 Conclusion

A method of ranking and classifying patients in terms of their relative risk of disease progression using a systematic risk scoring algorithm was developed. The risk score quantified the volume of the lesion and the effect that its shape, size and location had on the risk of fracture. Although the effect of size and location has been evaluated previously, this is the first study to demonstrate a link between lesion morphology and the risk of fracture progression.

Altering the orientation of the cross-section relative to the load vector affected the risk score. The magnitude of the effect varied depending on the specific geometry confirming that the score was sensitive to both the shape of the lesion boundary and its orientation relative to the load vector.

The results correlated well with the rank attributed to the patients according to the ARCO grading system. Whereas the ARCO grading system only allowed the patients to be grouped into four levels, and could not distinguish between patients in each grade, the relative risk score provided an additional level of resolution that allowed differentiation between each patient.

Further evaluation of this method of ranking patients according to their risk of progression is required before it could be used as a prognostic tool. The sensitivity analysis confirmed that the outcome was sensitive to user input and further work is required to confirm whether this means that the perceived benefits of the 2D approach are outweighed by the benefit, in terms of reducing user influence, of a 3D approach. This would require a larger cohort of patients as well as clinical follow-up. However, general guidelines that may help the surgeon to estimate the risk of fracture can be derived from the current study: The locations at highest risk of fracture were found where the lesion boundary was orientated parallel to the load vector. This risk increased with the proximity of these regions to the centre of load application and also varied for different sections through the lesion meaning that multiple CT or MR views must be evaluated before a prognosis can be developed. Finally, it is noted that the load vector in the natural hip is dynamic and therefore the location at highest risk of fracture may vary depending

on activity and the surgeon and engineer should consider the position of the lesion relative to the joint load in multiple physiologically relevant femur orientations.

Chapter 6. Summary review

6.1 Overall discussion

The overall aim of this thesis was to establish whether the risk of disease progression could be quantified more accurately than is possible using existing classification systems. The studies performed to achieve this are summarised in Figure 117.

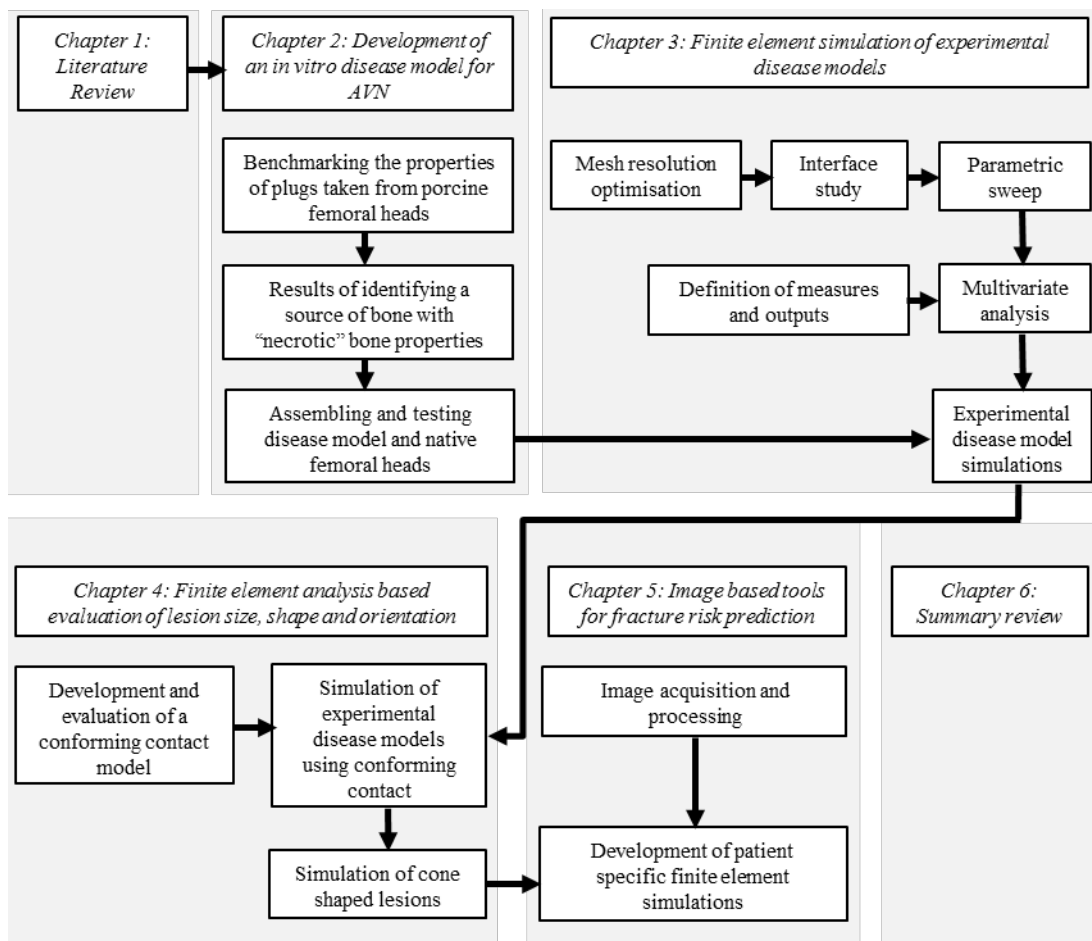


Figure 117. Flow chart summary of the studies performed in each chapter.

The development of an *in vitro* experimental disease model for AVN that allowed the effect of a simulated lesion on the elastic modulus of a femoral head to be established was reported in Chapter 2. The experimental disease model was made by substituting a plug of bone taken from the lateral epicondyle of a bovine femur into the central load-bearing region of a porcine femoral head.

Brown *et al.*, (1981) presented data showing that the strength and elastic modulus of bone taken from a pre-collapse human femoral head was reduced by a 41% and 59% respectively compared to healthy bone. This study proved that it is possible to identify samples of bone with material properties with a similar ratio compared to bone taken from porcine femoral heads.

Compressing experimental disease models and control femoral heads directly using a flat, rigid, platen allowed consistent application of strain to the femoral heads under displacement control and showed that the stiffness of the simulated lesion affected the stiffness of the entire femoral head.

The results of compressing the experimental disease models and native femoral heads over several cycles with increasing displacements showed that the behaviour of the material was approximately linear elastic at loads of less than 1200N and displacements of less than 1mm. The method of deriving the elastic modulus of the samples using Hertzian contact theory was validated by comparison to an analytical solution. These limits and linear-elastic material properties were used in the FE simulations described in Chapters 3, 4 and 5. Although the experimental disease models and FE simulations were based on properties derived from porcine bone, the properties used correlated with those used previously (Table 60).

Table 60. Comparison between previously reported material properties used in FE simulations of human femoral heads and the properties derived or used in the current studies.

Author	Healthy bone		Diseased bone		
	Elastic modulus (MPa)	Ultimate compressive strength (MPa)	Disease	Elastic modulus (MPa)	Ultimate compressive strength (MPa)
Experimental results	318±119	15.2±2.85	Simulated AVN	157±52	6.3±1.4
Parametric FE study	300±150	-	Simulated AVN	150±75	-
Experimental disease model FE study	317±151	-	Simulated AVN	160±84	-
Cone shaped lesion study	300	-	Simulated AVN	150	-
Patient specific simulations	300	-	Simulated AVN	150	-
Brown <i>et al.</i> , 1981(Femoral head)	439±19	19.4±0.3	Pre-collapse AVN	Mean 180	Mean 11.4
Li and Aspden, 1997(Femoral head)	Median 310	Not reported	Osteoarthritis	Median 356	Median 4.3
			Osteoporosis	Median 247	Median 2.5
Haba <i>et al.</i> , 2012(Femoral head)	Not reported	Not reported	Osteoarthritis	232±130	6.1±3.0
Steinhauser <i>et al.</i> , 2006 (Femoral neck)	385.7±SD189.4 361.7±SD300.6	8.5±6.0 6.6±5.2	Not reported	Not reported	Not reported
Öhman <i>et al.</i> , 2007	273±1.06	18.0±6.4	Not reported	Not reported	Not reported

The study simulating compression of experimental disease models using conforming contact in Chapter 4 indicated that a more physiologically representative means of applying load to the femoral head is necessary in future studies. Such an assembly could be reproduced experimentally but several aspects of this design should be considered during its development:

1. The load and displacement applied to the femoral head could be optimised to represent a particular physiological scenario by altering the design of the platen and filler.
2. The displacement induced in the head relative to the displacement applied to the platen is a function of the stiffness of the experimental disease model as well as the design of the platen and filler. A means of measuring the displacement at the surface of the head is required.
3. Orientation of the femoral head relative to the applied load was shown to be an important factor but was not evaluated in the current study. The ability to do so should be considered in future experiments.
4. Anisotropic material properties and Poisson's ratio have not been evaluated. The effect of these should be evaluated in a 3D FE simulation to optimise the fixture design prior to manufacture.

Another aspect of experimental disease models for AVN that must be improved is the generation of more clinically relevant lesion sizes, shapes and orientations. Substituting plugs of bone within the femoral head limited the degree to which shape could be modified and generated two discrete surfaces. Ideally the transition from healthy to necrotic bone would be a continuum with both sclerotic and necrotic regions represented. Furthermore, it was confirmed in Chapter 5 that simulation of organic lesion shapes will be necessary to fully understand the effect that the combination of boundary orientation and location within the femoral head will have on local stress discontinuities.

The sensitivity of the experimental disease model was evaluated *in silico* in Chapter 3. The method of load application and sensitivity of the experimental disease models to geometric variations were explored using a series of parametric studies. These studies showed that head and plug modulus, the eccentricity of the plug and the depth of the plug beneath the subchondral surface all had a significant effect on the elastic modulus of the construct.

An algorithm for establishing a score that quantified the magnitude of the peak stress at the lesion boundary and the size of the region of elevated stress was developed. This was established in the hope that it could rank patients in terms of their risk of disease progression in terms of remodelling or fracture at the lesion boundary. It is acknowledged that there is an indirect and un-validated link between this mechanical measure and the risk of fracture or remodelling but the methodology did highlight areas with the potential to fracture or remodel and proved sensitive to all parameters evaluated in this thesis.

The need for such a score was highlighted by Fardellone (2008), who introduced the concept of an absolute risk score that considered both clinical and mechanical factors in a prognostic measure. This has great significance in the context of avascular necrosis because of its multiple possible aetiologies; rapid and destructive pathogenesis. While the clinical factors were not

considered in the current study, it evaluated the potential for using an interface-stress based relative risk score to differentiate lesion geometries that were associated with a high risk of progression from those that were less likely to progress. This was a novel approach compared to previous studies, which have used direct assessment of peak stress within the femoral head (Brown *et al.*, 1992).

Using this score to evaluate the experimental disease model geometry failed to identify those models that fractured during the experiment. However, such factors as the variation in material properties throughout the femoral head, and the effect of imperfect femoral head geometries were not considered. The score proved to be sensitive to all four factors considered and the trend for reduced disruption in the stress field when the lesion was deep to the subchondral surface correlated to the earlier work by Brown *et al.*, 1992. Daniel *et al.* (2006) evaluated contact stress in the articular surface of a femoral head with a simulated osteonecrotic lesion. They found that contact stress increased with reducing lesion stiffness and that the outcome was sensitive to orientation of the load vector. Although the outcome measures differ, both findings correlate with the results of this study. In addition to this more recent study, previous literature on the effect of load on the natural femur highlighted the need to evaluate a range of physiologically relevant load vectors and magnitudes (Bergmann *et al.*, 2001; Brown *et al.*, 1993; Radcliffe and Taylor, 2007; Yang *et al.*, 2002; Turner *et al.*, 2005). Sensitivity of the relative risk score to the position of the lesion relative to the load vector was reflected in the results of the parametric sweep (Section 3.3) and cone-shaped lesion studies (Section 4.5). Its sensitivity to the method of load application was demonstrated through comparison between the results of the simulations of experimental disease models compressed using a hard platen (Section 3.3.3) and using conforming contact (Section 4.4). Under these two loading conditions the relative risk score proved to be sensitive to angular and lateral orientation of the lesion boundary relative to the centre of the applied load and the method of load application.

A possible improvement that could be implemented in future *in silico* simulations would be to integrate the patient-specific lesion geometries developed in Chapter 5 into whole femur-pelvis constructs such as were used by Daniel *et al.*, 2006. However, the benefit of such a comprehensive physiological model must be assessed against the increased uncertainty that comes with such a complicated simulation. The experimental disease models used organic materials with inhomogeneous material properties but the *in silico* simulations assumed homogenous, linear elastic materials with a macro-scale resolution. There remains a need to understand the role of nano-scale tissue constituents and micro scale tissue organisation (Vaughan *et al.*, 2012) before the effect that alterations to the stress distribution within a femoral head with AVN could have on bone metabolism can be simulated. These nano- and micro-scale parameters are not well understood for AVN and preliminary work to understand the effect of changes to bone mineralisation, trabecular architecture and alterations to the

collagen matrix on stress distribution within the femoral head is necessary before more advanced experimental disease models can be generated.

The conforming contact methodology developed in Chapter 4 was used in Chapter 5 to evaluate *in silico* disease models that were derived from computed tomography and magnetic resonance images of the femoral heads of patients suffering from AVN. Segmentation of the femur and lesion geometry using dual image modalities built upon previous research (Buie *et al.*, 2007; Zoroofi *et al.*, 2004) and took full advantage of the relative strengths of each modality: CT offers fine resolution of the bone structures while MRI clearly defines the lesion boundary.

The algorithm for quantifying the relative risk of fracture was revised to include lesion volume and this revised score was used to rank and categorise patients. This approach was unique in its ability to quantify lesion morphology as well as volume and location. By evaluating the size and magnitude of stress discontinuities at the lesion boundary, location, orientation and shape are all inherently considered. Lesion volume has been previously identified as an important factor (Nishii, Sugano, Ohzono, Takahashi Sakai, *et al.*, 2002) and was shown to be a useful addition to the current method of risk evaluation. The effect of orientation of the femur relative to the load vector has not been fully explored and it was not possible in the current study to conclude whether any of the patients were at higher risk of progression in flexion (e.g. at heel strike) compared to stance. The question of whether a lesion is more likely to cause failure because of a low load, high frequency event such as walking or a high load, low frequency event such as stumbling has clinical relevance because it may dictate whether protective weight bearing or restriction of certain activities is a viable alternative to clinical intervention. The current methodology could be used to answer this question in future by evaluating multiple lesion shapes in multiple orientations. The effect of muscle forces on the bone and load vector has not been considered. In future studies, consideration must be given to applying relevant load magnitudes for each orientation and to how the score for multiple slices for an individual patient is aggregated.

Apparent lesion size, shape and orientation varied significantly between patients but there was also significant intra-patient variability in relative risk scores. This was evident when comparing different slice orientations: for example the scores from the anterior-posterior slices were unrelated to those from medio-lateral slices; the results when the femur was oriented in stance differed from the results when the femur was oriented in flexion. Comparing the results for adjacent slices in the same plane and orientation highlighted the sensitivity of this method to user-defined slice selection.

These observations confirmed that an assessment of the risk of disease progression could not be based on a single slice. Averaging the score for multiple slices per patient differentiated patients in whom a fracture had been previously identified from those in whom no fracture had

been detected. This suggests that an overall risk score based on multiple two-dimensional simulations or three dimensional simulations could be developed. Although not proven by the current study, it also highlighted the potential for such a score to identify the location around the lesion boundary at highest risk of fracture or remodelling and the orientation of the femur which is most likely to cause this event. Significant further investigation is required to confirm this, firstly by evaluating more patients using a larger number of slices and orientations and secondly by validating the results through clinical follow-up. The two patients who were identified with post-collapse AVN had the highest relative risk scores. This is an important first step in validating the score that may help to justify future clinical evaluation.

Evaluating the relative risk score for individual slices was computationally efficient and allowed for transposition of the result from the FE simulation to the source medical image in an unambiguous way. This method showed that all slices from patients in whom a fracture was detected scored above a threshold of 360. Assessing the number of slices per patient that lay above this threshold allowed the patients to be divided into three categories: in the low risk category no individual slice had a relative risk score above 310. In the medium risk category some but not all slices scored above 360 and in the high risk category all slices had a score of greater than 360.

While the relevance of the identified threshold has not been verified and the number of slices included in each analysis requires further optimisation, this outcome suggests that the relative risk score can be used to either rank patients on a linear scale or to categorise them into discrete levels.

A limitation of the current method was its inability to assess patients with multiple lesions. The approach of assessing the size and magnitude of a stress discontinuity within the femoral head remains viable in such cases. However, the problem of automating data extraction and reporting it in a meaningful way becomes more challenging. In this context it must be acknowledged that the healthy bone-lesion interface may not be the most appropriate surface to assess. A more arbitrary reference surface, for example surfaces oriented relative to anatomic landmarks or to the CT scan volume may be more appropriate. In either case, a desirable extension to the current means of assessing risk of progression would be to identify the location within the femoral head at greatest risk of failure. This would be of great benefit clinically as it would provide the surgeon with a target for surgical interventions. To achieve this goal, two important factors must be considered:

1. The entire lesion boundary must be evaluated, either using multiple two-dimensional slices or in three dimensions. The relative risk score was highly sensitive to apparently small differences in lesion geometry and therefore any method that relied on user selection of slices will be prone to inaccuracy. A method that results in the surgeon

being able to review multiple 2D models remains the preferred option, both from the point of view of the speed with which 2D models can be generated and the ease with which the results can be transferred to 2D slices through CT or MR images.

2. A robust method of relating this location back to the surgeon in a way that can be interpreted in the clinical environment is required. Association of the 2D slice relative to the original CT scan would require both models to be aligned using the same coordinate system and the slice from which the FE model was generated identified.

There is scope for further investigation into the effect of lesion shape and orientation on the stress at the lesion-healthy bone interface. The conical lesion studies highlighted the interrelationship between the orientation of the interface and the load vector. It showed that small changes to the orientation over the interface could have the effect of concentrating or limiting the physical size of a discontinuity. This was not fully explored but may improve the accuracy with which qualitative assessments of the risk associated with lesion shape could be made.

The current study only considered stress at the lesion-healthy bone interface. In future studies it will be necessary to consider the risk of fracture within the body of the lesion as well. This will become increasingly important as the complexity of the simulation increases: inclusion of regions of osteolysis, sclerosis and fibrous cysts would allow multiple failure modes to be evaluated and the relative risk for each may need to be assessed using a different outcome.

Finally, there is a need to develop an approach that can be used efficiently in a clinical setting. Whether this can be an algorithmic method based on a set of rules derived from more comprehensive FE simulation or an alternative analytical method remains to be determined but both avenues should be considered.

Validation through clinical follow-up will be necessary regardless of the approach used to further evaluate the methods to predict disease progression. As the validity of the current relative risk score has not been established it would not be appropriate to develop a study that used this score to dictate the standard of care. The study would need to recruit patients with pre-collapse avascular necrosis of the femoral head who opted for conservative treatment. The inefficacy of conservative treatment (Yoon *et al.*, 2001; Parsons and Steele, 2008; Marker, Seyler, McGrath, *et al.*, 2008; Hungerford and Jones, 2004; Musso *et al.*, 1986) may limit the number of patients willing to give informed consent to such a study.

6.2 Overall conclusions

The viability of generating an *in vitro* experimental disease model for avascular necrosis of the femoral head was also assessed. The experimental disease model confirmed that the presence of a lesion with reduced stiffness affected the overall stiffness the femoral head. This effect was recreated *in silico* and a series of systematic studies demonstrated that material properties, lesion location and the orientation of the lesion boundary relative to the load vector all significantly affected the stress field within the femoral head. The method of load application was also shown to be an important consideration and it is concluded that future *in vitro* models should allow load transfer to the articular surface through a conforming surface that better represents the natural joint. Furthermore, lesion geometry and orientation must be recreated in a manner more representative of the clinical situation.

A novel method of ranking different lesion shapes according to the risk of fracture or adverse remodelling at the lesion boundary was developed. The highly irregular morphology of the lesions evaluated was expected to cause significant variation in the relative risk score between patients and between two-dimensional cases derived from each lesion and the relative risk score proved sensitive to both inter- and intra-patient variability. The final refinement of the relative risk score took lesion volume and the magnitude and physical size of the interruption in the stress field at the lesion boundary into account. By averaging this score over multiple two-dimensional slices a single number that quantified the relative risk was derived. In a small cohort it was able to discriminate between fracture cases and cases without fractures. Ranking patients using the revised score showed excellent correlation to the ARCO clinical grade but whereas the ARCO grading system only allowed the patients to be grouped into four levels, the relative risk score provided an additional level of resolution that allowed differentiation between each patient.

This method of assessing the risk of disease progression for an individual patient was time consuming, complicated and relied heavily on specialised engineering software with significant post-processing to derive a final score. These factors mean that even if such a scoring method was proven to be clinically effective, it is unlikely that it could be adopted outside an academic setting. However, this research refined the requirements for *in vitro* experimental disease models for AVN and there is significant scope to develop new, more efficient methods of assessing risk of disease progression using this research as a basis.

Appendices

Appendix A: Method development

The following approaches were evaluated but found to be an unsatisfactory means of differentiating between disease model and native (control) femoral heads.

Work done to a consistent displacement or force

With a view to overcoming the ambiguous inflection point, the data were re-analysed using consistent displacement or force endpoints. Work done to achieve a given endpoint was used as a comparator because this measurement differentiated between two data sets even if the final load and displacement were the same.

Work done was calculated by numerical integration to establish the area under a load-displacement plot.

The displacement records for each test were adjusted to start at zero and the maximum displacement for each test was recorded. This allowed the test with the smallest displacement per cycle to be identified, thus defining the maximum displacement per cycle that was achieved across the entire set. These maxima are shown in Table 61.

Table 61. Maximum displacement for each cycle. These were calculated by adjusting the displacement values for each plot to originate at zero, then finding the highest value that was common across all data sets for a given cycle.

Cycle	Maximum displacement (mm)
1	0.50
2	0.84
3	1.28
4	1.33

The box-whisker plot generated to show the result of this approach is shown in Figure 118. The mean work done on the disease models is between 35% and 45% lower than was done on the controls.

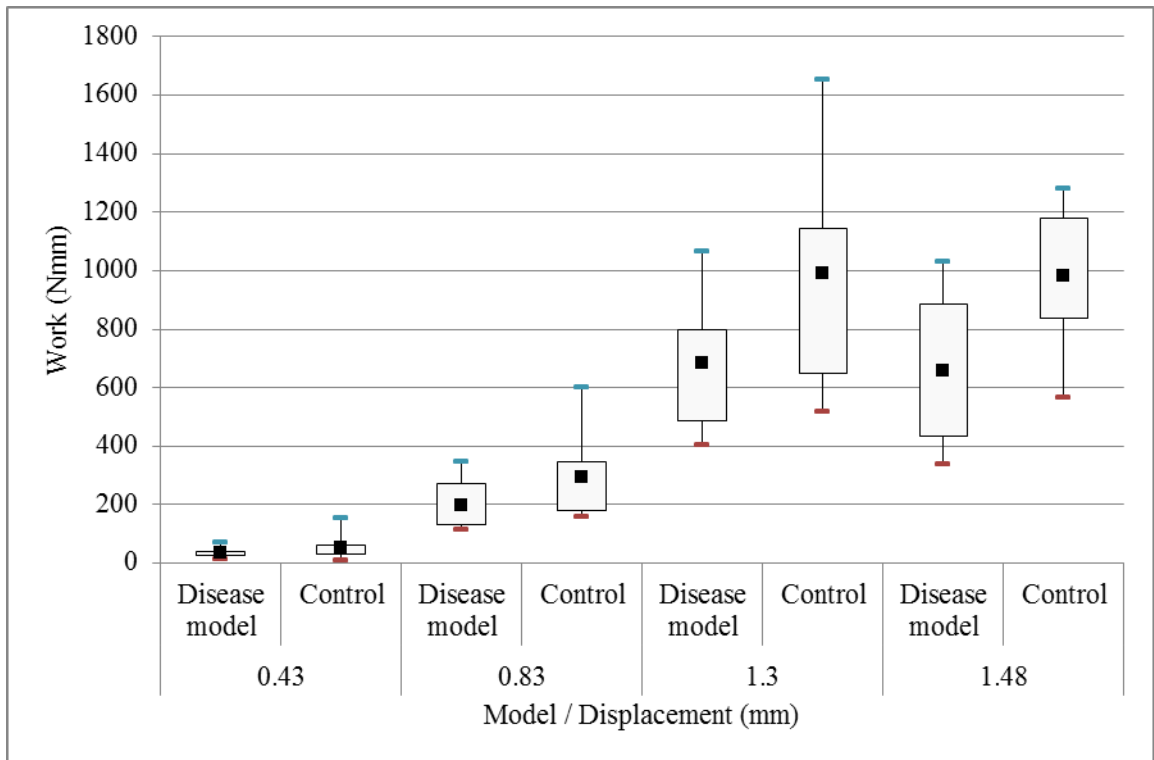


Figure 118. Box-whisker plot of the work to a consistent displacement for disease model and control femoral heads across all repeats of the same cycle. The results were significantly different for the fourth cycle. The mean work done on the disease models is between 45% and 58% lower than was done on the controls

Using the same approach to establish the work done to a consistent force showed that, although not significant, approximately 15% to 32% more work was done on the disease-model femoral heads compared to controls (Figure 119). The majority of this difference was explained by the fact that a greater displacement was required (Figure 120): There was between 14% and 23% difference in the mean displacement at each of the comparison forces.

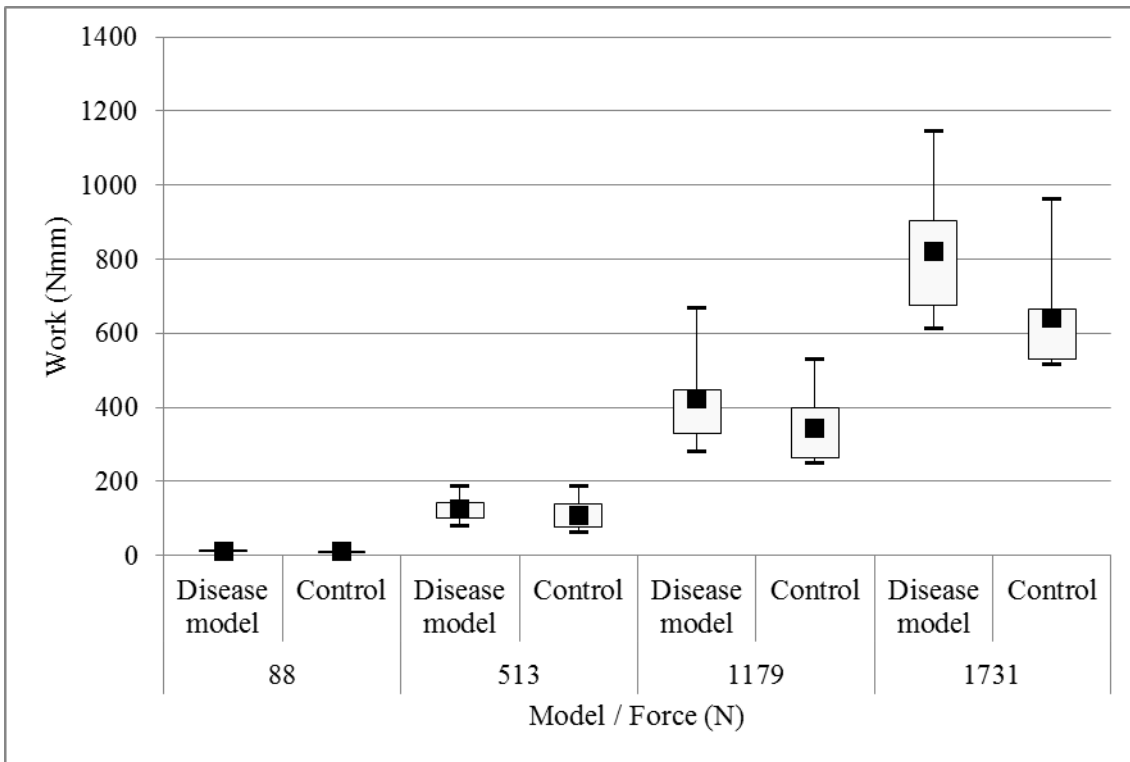


Figure 119. Box-Whisper plot comparing the work done on disease model and control femoral heads to achieve a consistent force. The mean work done on the disease model femoral heads was between 15% and 32% higher in all cases but the difference was not significant.

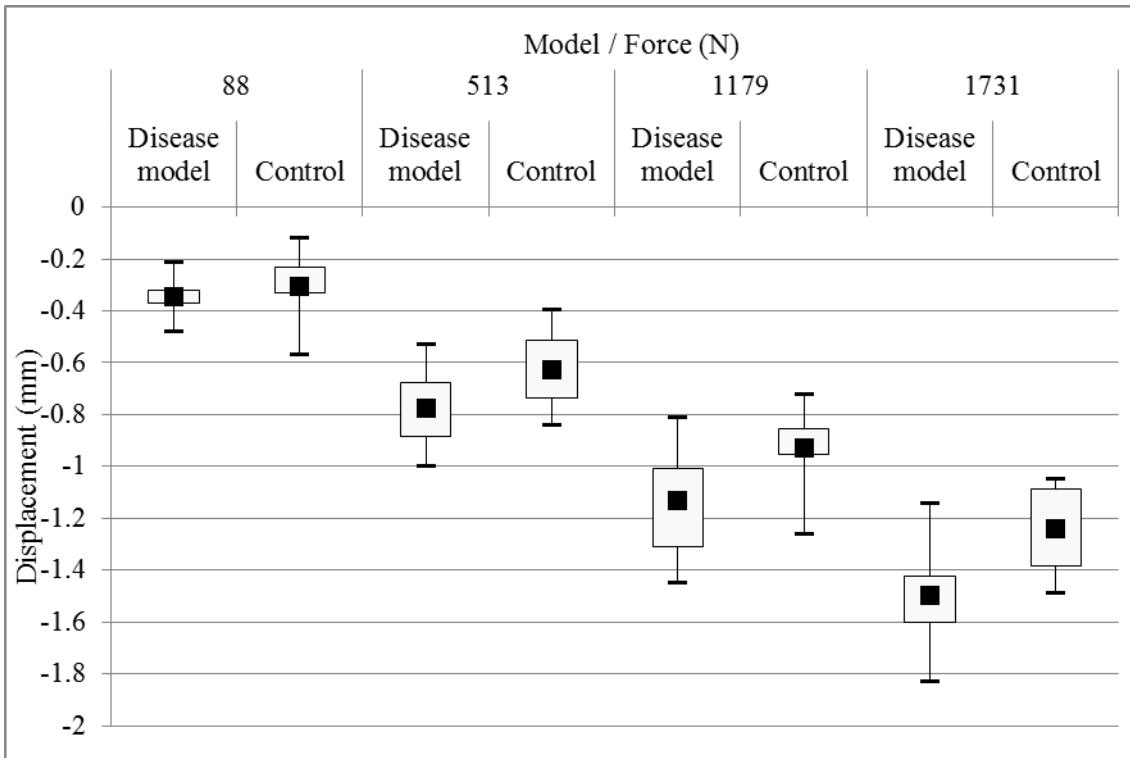


Figure 120. Displacement required to achieve a consistent displacement for disease model and control femoral heads. The displacement for the disease model femoral heads was between 14% and 23% higher but was only significantly different for the fourth load cycle.

Single-modulus based approach

In this approach a single modulus was derived for each femoral head. While this did not account for cumulative plastic damage in the superior femoral head, it did allow a direct comparison between experimental and theoretical results using contact radius as a comparator.

The analysis steps taken were:

1. Measure the largest and smallest contact diameter on each Pressurex film and calculate the mean.
2. Record the largest load and displacement registered for each test cycle.
3. Use the load to derive the Hertzian contact radius and theoretical approach of centres.
4. Minimise the sum of the absolute errors between the derived approach of centres and actual displacement value by varying the modulus of the femoral head.
5. Plot the experimental and derived contact radius for each head.

While good agreement was achieved at small displacements, this approach failed to account for the plastic deformation which occurred at the larger displacements. The cumulative damage resulted in a pre-flattened contact region which reduced the accuracy of the approach of centres calculation. The accumulation of these inaccuracies resulted in poor correlation between actual and predicted contact radii, with the numerical simulation underestimating the final contact radius by approximately 50% in the worst cases. A typical example, generated for control femoral head VI is shown in Figure 121.

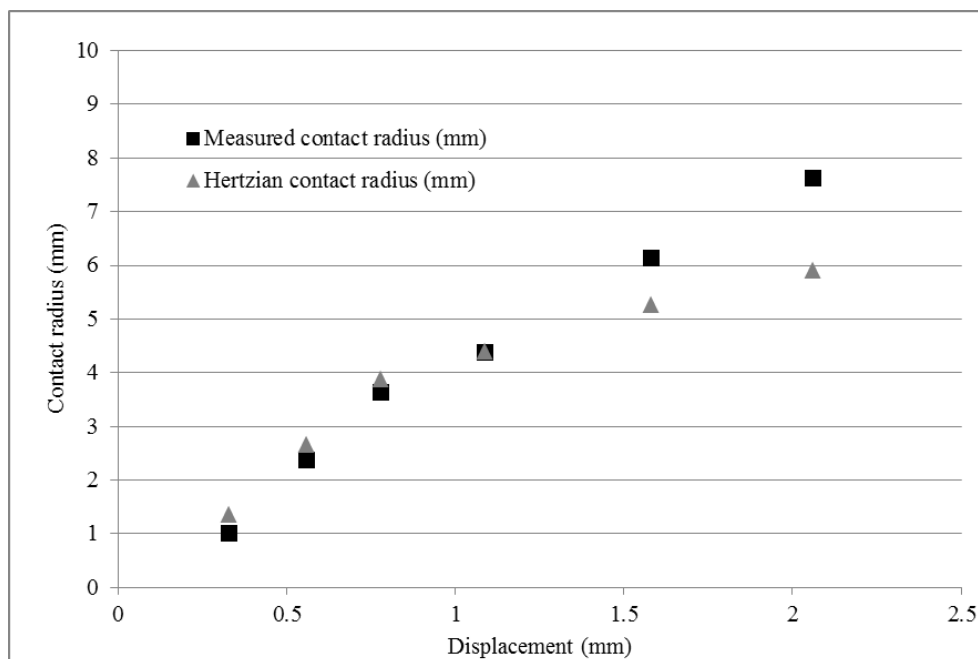


Figure 121. Measured and analytically derived contact radii for femoral head VI (control). The underestimation of contact radius is typical of the results of attempts to derive the bulk modulus by minimising the error between the measured displacement and Hertzian approach of centres.

Similar results occurred for disease model femoral heads. The overall results are presented in Figure 122.

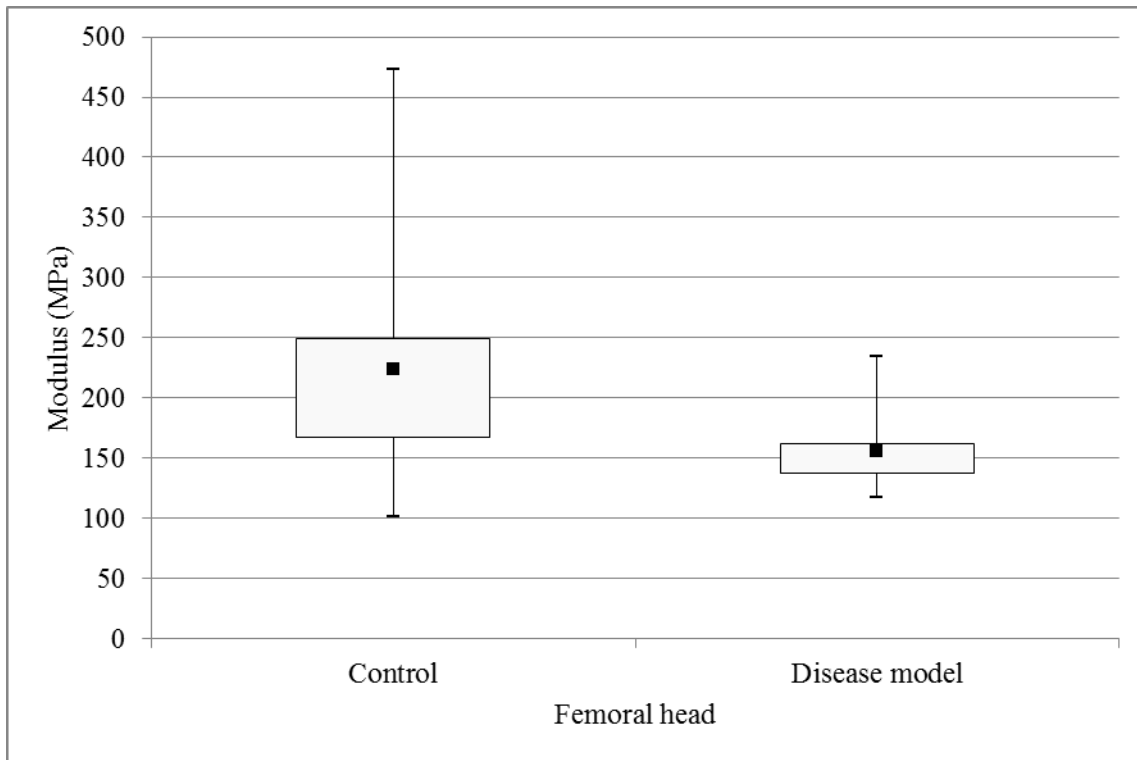


Figure 122. Elastic modulus derived using a single-modulus based approach.

While this method of comparing the native and disease model femoral heads was prone to error, the apparent moduli derived by this approach were in close agreement with the Young's modulus derived for bone plugs used to benchmark the femoral heads (total range 200-450MPa) and surrogate bone used in the disease model (total range 100-250MPa).

Appendix B: MicroCT scanning protocol

All bone samples were scanned using a μ CT 100 (Scanco Medical AG, Switzerland)

Scan parameters

- Resolution: High
- Filter: 0.1mm Aluminium
- Start position: 0mm
- End position: 121.00mm
- Angle: 0°
- Voxel size: 74 μ m
- Interval time 300ms
- Number of slices per sub-set 122
- Calibration (2): 70kVp, 0.1mm Al, BH:1200mg HA/cm³, Scaling: 4096

Three different scanning cylinders were used. The field of view was increased for the largest of the cylinders (Table 62).

Table 62. Fields of view used for each cylinder diameter.

Scanning cylinder diameter (mm)	Field of View (mm)
88	90.1
73	75.4
19	75.4

Post processing

The samples were post-processed using the protocol developed by Ondrej Holub (University of Leeds, Leeds). For porcine femoral heads, a volume of interest was identified by selecting a circle of area 0.75mm² (132 x132 pixels) within each of the porcine femoral heads in the transverse plane. Approximately 80 slices superior to the epiphyseal growth plate were selected giving a cylinder approximately 10mm diameter and 6mm long. The entire volume of the bovine cylindrical samples was selected as the volume of interest.

Bilateral thresholds were used to differentiate bone from tissue and air (Table 63). The bone threshold for bovine bone equated to a lower density than that used for bone from porcine femoral heads. This is consistent with the mechanical test results (Section 2.3) which indicated that the samples of bovine bone were weaker and by inference less dense.

Table 63. Bilateral thresholds used to differentiate bone from tissue and air.

Sample	Bone threshold (mgHA/cm ³)	Air threshold (mgHA/cm ³)
Porcine femoral heads	360	-78
Bovine bone cylinders	276	-85.5

Appendix C: Design of experiments

Design of experiments (DoE) is a systematic methodology that allows the effect of multiple factors on a chosen response to be evaluated. Using this methodology, an experiment is run multiple times with a set of pre-defined input factors set to different levels. The result of each experiment (the response) can be compared to show the effect of individual factors (the main effects) and factors acting in combination (the interactions). This is an important attribute of the methodology as it allows confounding factors to be identified. These are factors that cause the same level of response and therefore their individual effect cannot be distinguished.

While other designs are possible, the simplest permutation is a full factorial experimental design. This defines the case where experiments are run using every possible permutation of factors.

A simple example of a full factorial DoE is an analysis of the force generated by a lever when the length of the lever, the applied force and the position of the pivot are varied (Figure 123). In this case the factors are length, applied force and pivot position relative to the point of load application. The response is the force generated.

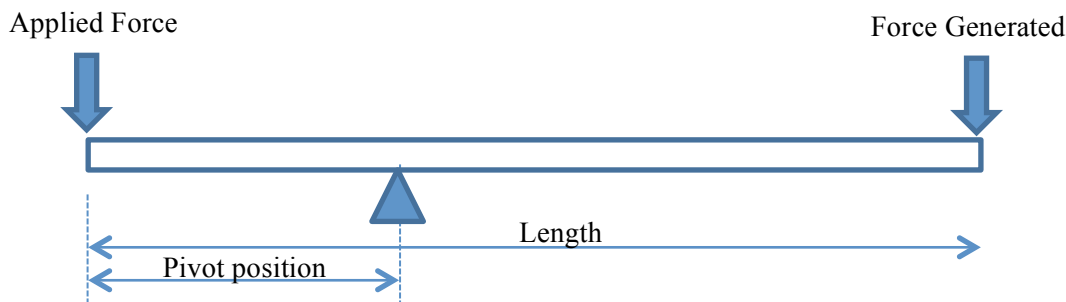


Figure 123. Schematic representation of a lever with three factors that can be varied (applied force, pivot position and length) and one response (force generated).

The levels for each factor should represent a high and low state for the factor in question. Levels are generally chosen to reflect either geometric limits or are defined through parametric sweep studies. The levels for each factor in this example are recorded in Table 64.

Table 64. Factors and levels for example Design of Experiments.

Factor	Level	
	Low	High
Length of lever	2m	3m
Applied force	100N	200N
Pivot location	1m	1.5m

The number of permutations of levels equates to the [number of levels]^[number of factors]. Hence there are eight possible permutations for the experiment as a two-level full factorial design with three factors is being used in this example. The experimental design is shown in Table 65.

In this example the response (Force generated) can simply be calculated as:

$$Force\ generated = Applied\ force \times \frac{Pivot\ location}{Lever\ length - Pivot\ location}$$

The results are also shown in Table 65.

Table 65. The first three columns represent the experimental design. In this Full Factorial example, every permutation of levels is used. The last column is the response.

Length of lever (m)	Applied force (N)	Pivot location (m)	Force Generated (N)
2	100	1	100
2	100	1.5	300
2	200	1	200
2	200	1.5	600
3	100	1	50
3	100	1.5	100
3	200	1	100
3	200	1.5	200

The main effects plots (Figure 124) show the mean of the response at each level of one factor. The first plot shows the change in response when the applied force is 100N versus 300N, the second when the lever is 2m long versus 3m long and the third when the pivot location is 1m from the applied force and 1.5m from the applied force. Two observations can be made from these plots: 1. The force generated varies inversely with the length of the lever and directly with both applied force and the location of the pivot relative to the applied force; 2. Varying the applied load has the least effect on the response (a variation of approximately 130N compared to the 190N range when the other two factors are varied. Note that this outcome would change if the levels for the applied force were changed: an important consideration when developing a factorial design and one factor can mask the effect of the others.

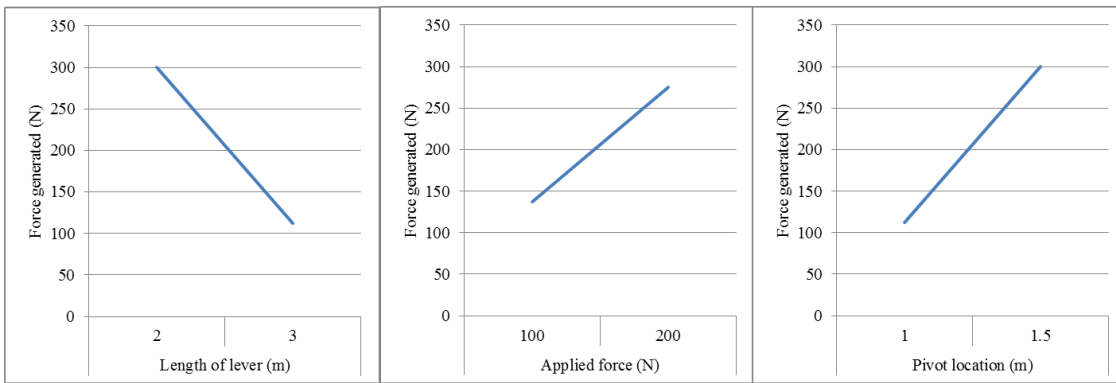


Figure 124. Main effect plots for DoE of the force generated by a lever. These show that the force generated varies inversely with the overall length of the lever; directly with the applied force and directly with the pivot location. The first plot shows the change in response when the Applied Force is 100N versus 300N, the second when the lever is 2m long versus 3m long and the third when the pivot location is 1m from the applied force and 1.5m from the applied force.

The interaction plots (Figure 125) are constructed similarly but show the response when two factors are high or low. While it is possible that one factor will invert the response to another, in this case the response varies directly regardless of the interaction. One line in each plot has a steeper slope. This means that there is a different response to the factor considered in the X-axis depending on the factor considered in the legend. In other words, the factors are interacting to cause a response that is greater than the effect of any one factor on its own.

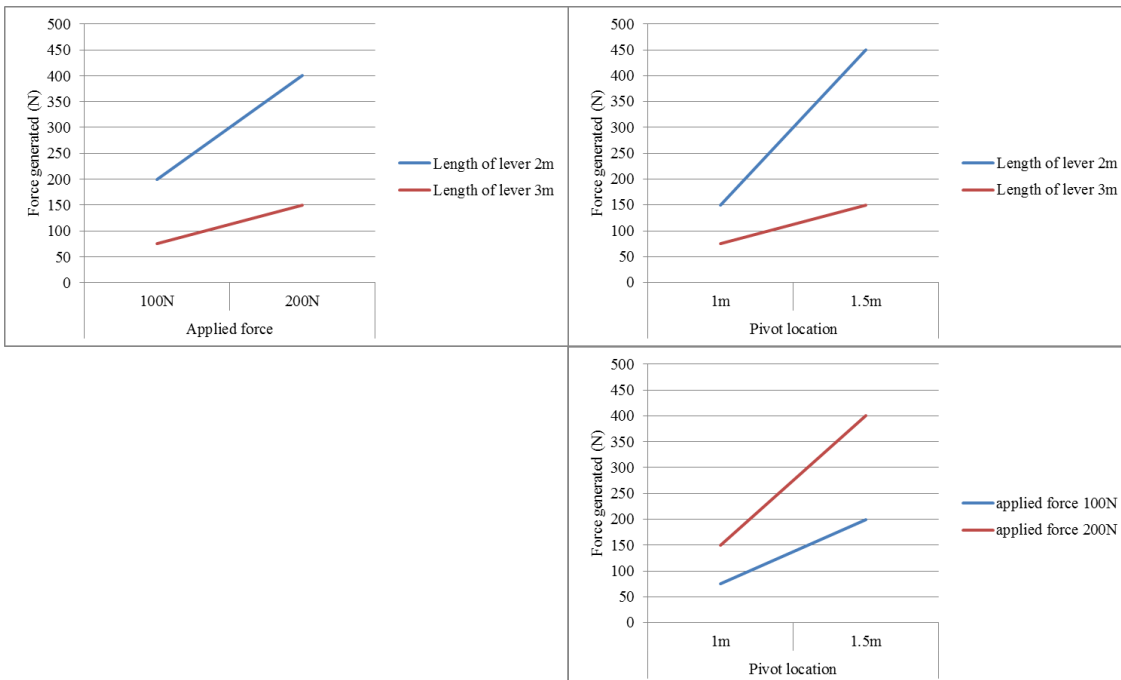


Figure 125. Interaction plots for the DoE example. Two important observations can be made: 1. In some interactions it is possible that one factor will invert the response to another. However, in this case the response varies directly regardless of the interaction; 2. One line in each plot has a steeper slope. This means that there is a different response to the factor considered in the X-axis depending on the factor considered in the legend: the factors are interacting to cause a response that is greater than the effect of any one factor on its own.

Appendix D: Clinical scan parameters

CT scan parameters

All patients were scanned using a 64-row CT scanner with the parameters defined in Table 66.

Table 66. Clinical CT scan parameters

Scout	Length 400mm kVp 120 mAs 30
Scan start	Pelvis ASIS
Scan end	Middle shaft of femur
kVp	120
mA	224mA (250 mAs/Slice)
Rotation time	0.75 sec
Raw slice thickness	1mm
Reconstruction slice thickness	0.5mm
Window width/window level	2000 / 800
Multiplanar reconstruction	Axial, coronal, sagittal : 3mm/3mm Volume rendering: horizontal 12 rotating image

MR scan parameters

Multiple MR imaging sequences were used as part of the clinical trial protocol (Table 67). T1 weighted images were used to generate the patient-specific lesion masks in ScanIP.

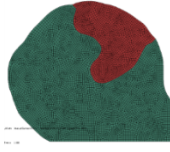
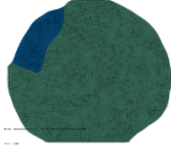
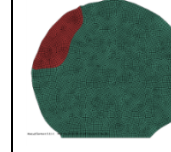
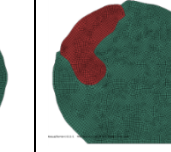
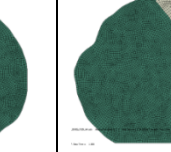
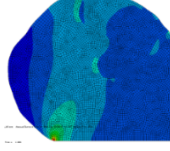
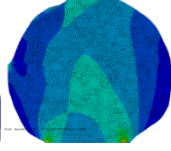
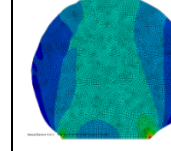
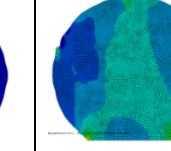
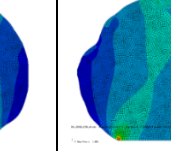
Table 67. MR imaging sequences used in the clinical trial

Sequence number		FOV	Matrix.	Nex.	Slice.	TR	TE	TI	Flip.	ETL	B/W	Slice thic.	Slice gap.
1	T2 SPAIR COR	360*380	288*288	1	40	8807	80		90		162.5	2	1
2	T1 COR	360*380	288*302	1	40	622	20		90		217.8	2	1
3	T2 AXIAL	390*235	460*264	1	30	4871	100		90		217.4	3	1
4	T1 AXIAL	390*235	460*270	1	30	622	20		90		217.4	3	1
5	T1 SAGITTAL	260*207	256*204	1	20*2	497	20		90		218.1	3	1
6	PD SPIR OBL SAGITTAL	200*231	200*194	1	25*2	1800	22		90		217.7	2.5	0

Appendix E: Patient-specific cases

This appendix contains cross-sectional images showing the lesion geometry and von Mises stress distribution for each case described in Chapter 4 (Table 68, Table 69, Table 70, Table 71, Table 72, Table 73, Table 74 and Table 75). In addition, the relative risk scores (Inner, outer and difference) for each patient are plotted in Figure 126, Figure 127, Figure 128, Figure 129, Figure 130, Figure 131, Figure 132 and Figure 133.

Table 68. Geometric representations and von Mises stress plots for each slice generated for patient 01_001.

Stance AP	Stance ML	Stance Medial	Stance Lateral	20° Flexion AP	20° Flexion ML
					N/A, the lesion did not pass through this slice
					N/A, the lesion did not pass through this slice

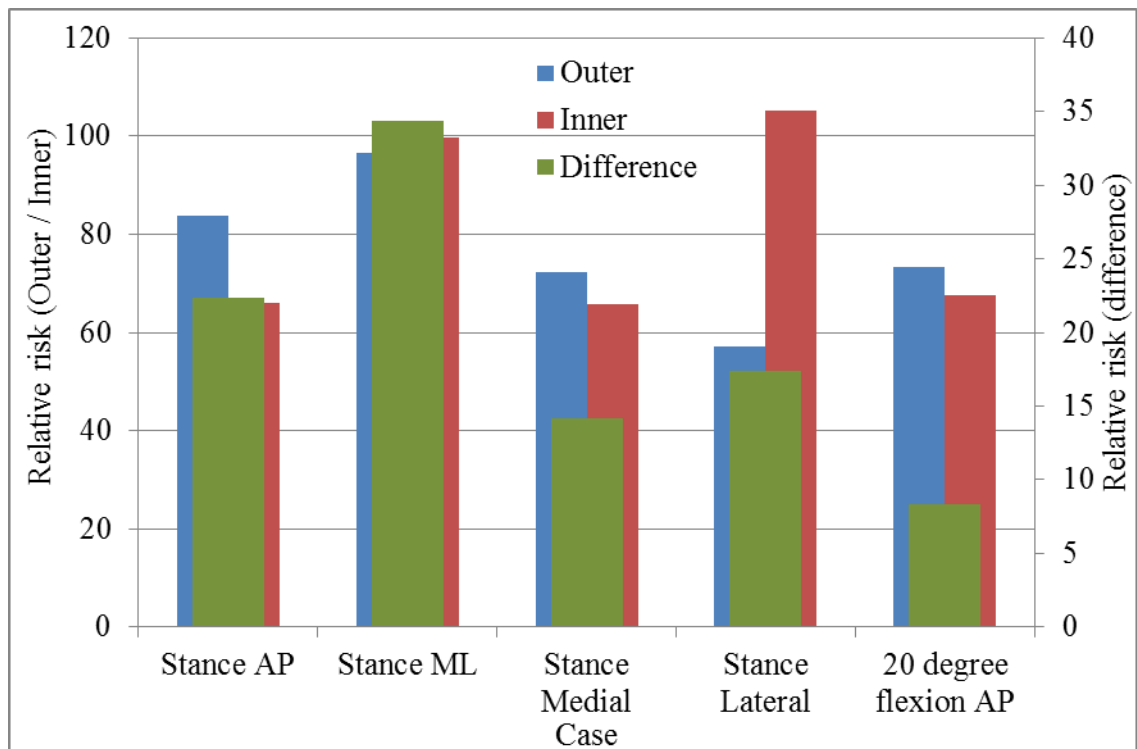
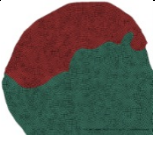
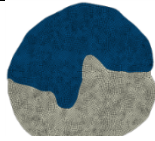
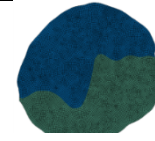
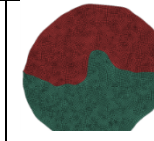
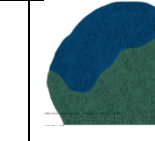
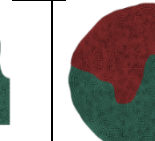
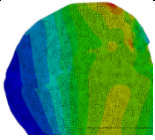
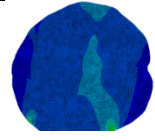
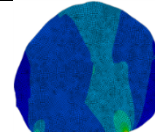
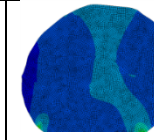
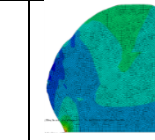
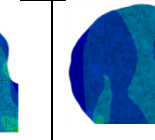


Figure 126. Relative risk scores for each case generated from Patient 01_001.

Table 69. Geometric representations and von Mises stress plots for each slice generated for patient 01_002.

Stance AP	Stance ML	Stance Medial	Stance Lateral	20° Flexion AP	20° Flexion ML
					
					

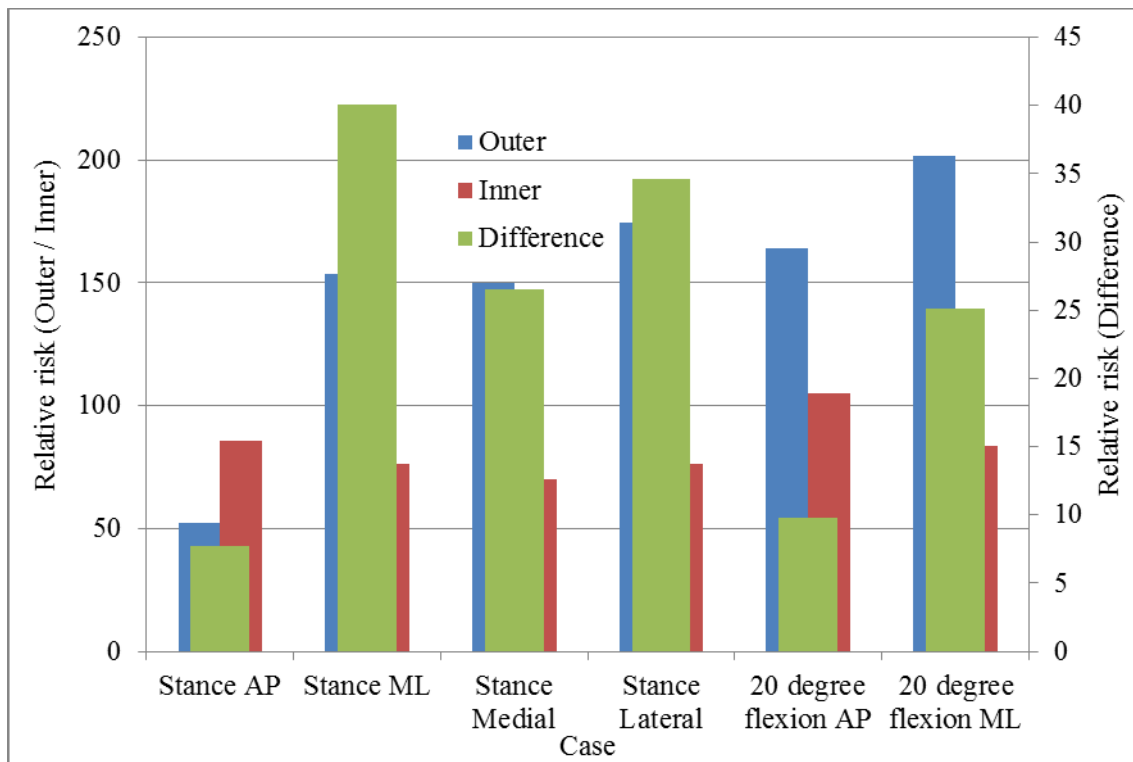
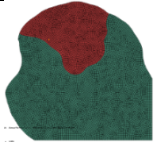
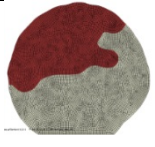
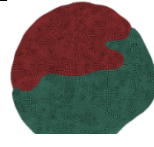
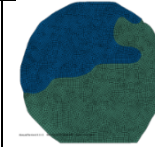
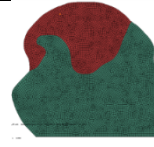
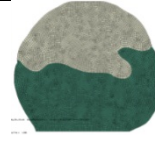
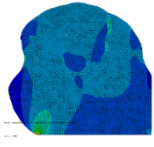
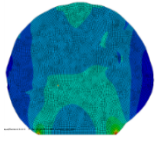
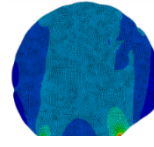
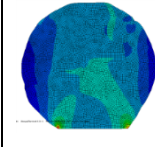
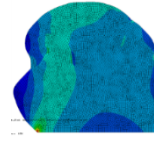
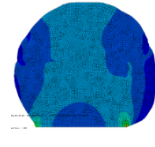


Figure 127. Relative risk scores for each case generated from Patient 01_002.

Table 70. Geometric representations and von Mises stress plots for each slice generated for patient 01_003.

Stance AP	Stance ML	Stance Medial	Stance Lateral	20° Flexion AP	20° Flexion ML
					
					

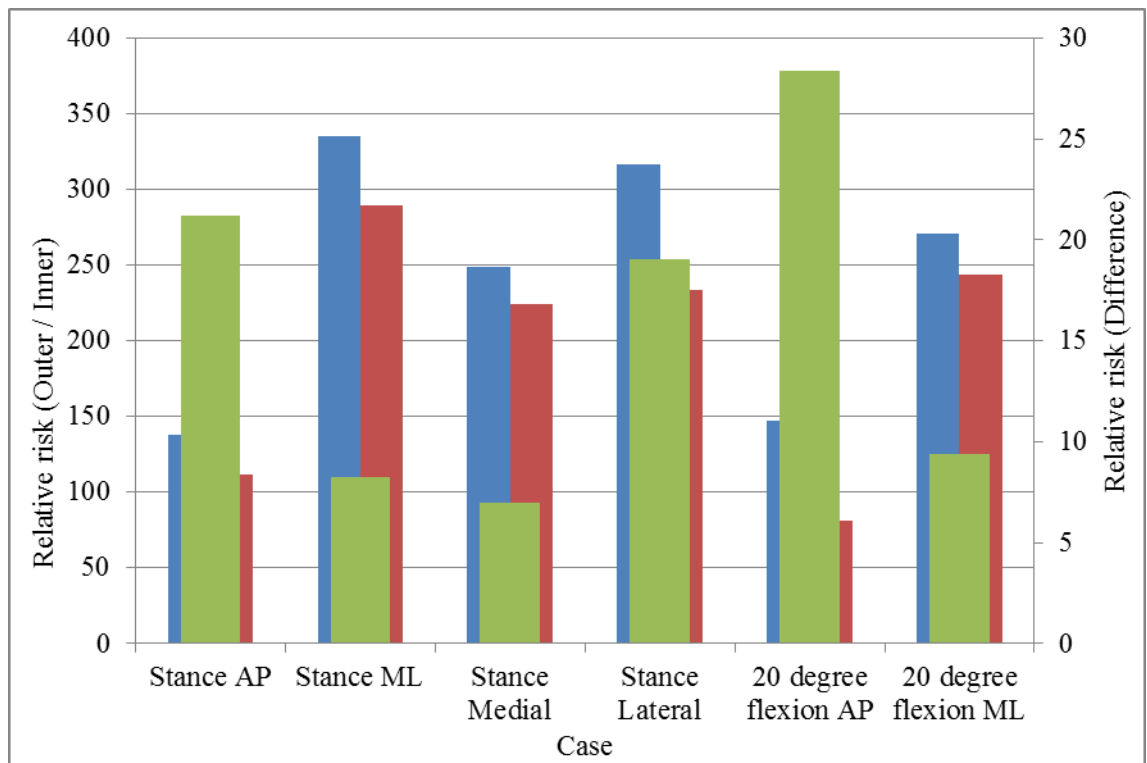
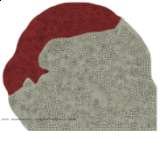
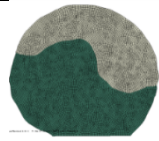
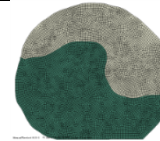
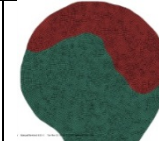
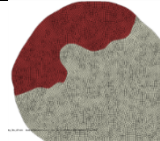
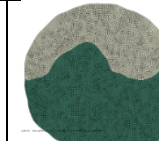
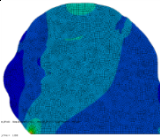
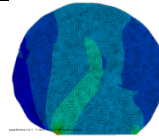
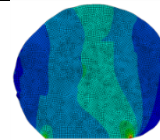
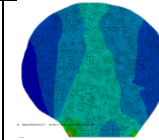
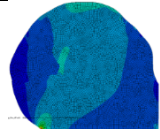
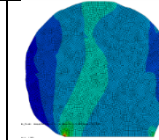


Figure 128. Relative risk scores for each case generated from Patient 01_003.

Table 71. Geometric representations and von Mises stress plots for each slice generated for patient 01_004.

Stance AP	Stance ML	Stance Medial	Stance Lateral	20° Flexion AP	20° Flexion ML
					
					

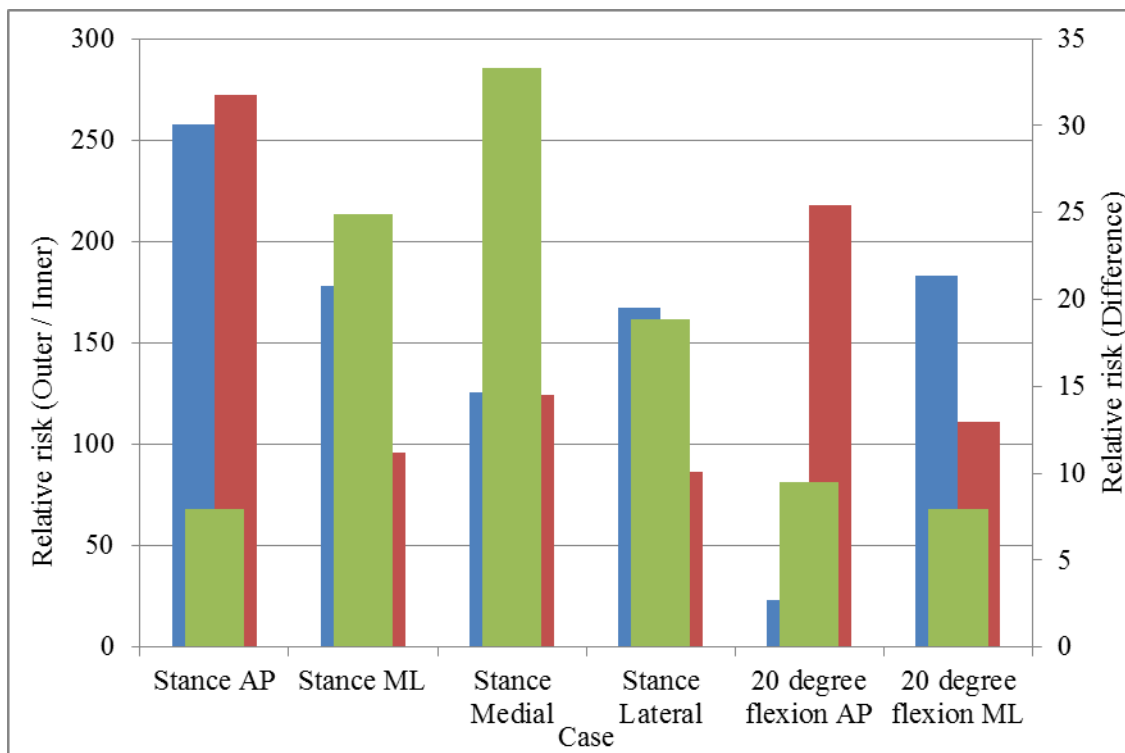
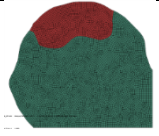
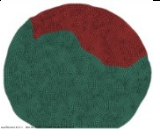
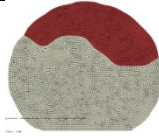
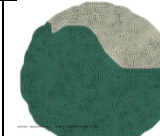
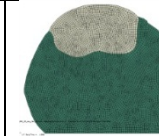
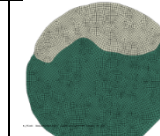
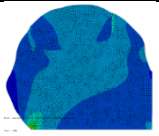
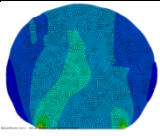
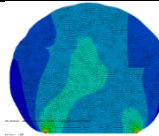
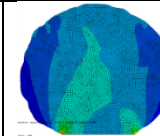
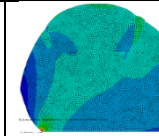
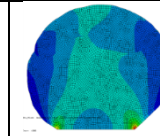


Figure 129. Relative risk scores for each case generated from Patient 01_004.

Table 72. Geometric representations and von Mises stress plots for each slice generated for patient 01_005.

Stance AP	Stance ML	Stance Medial	Stance Lateral	20° Flexion AP	20° Flexion ML
					
					

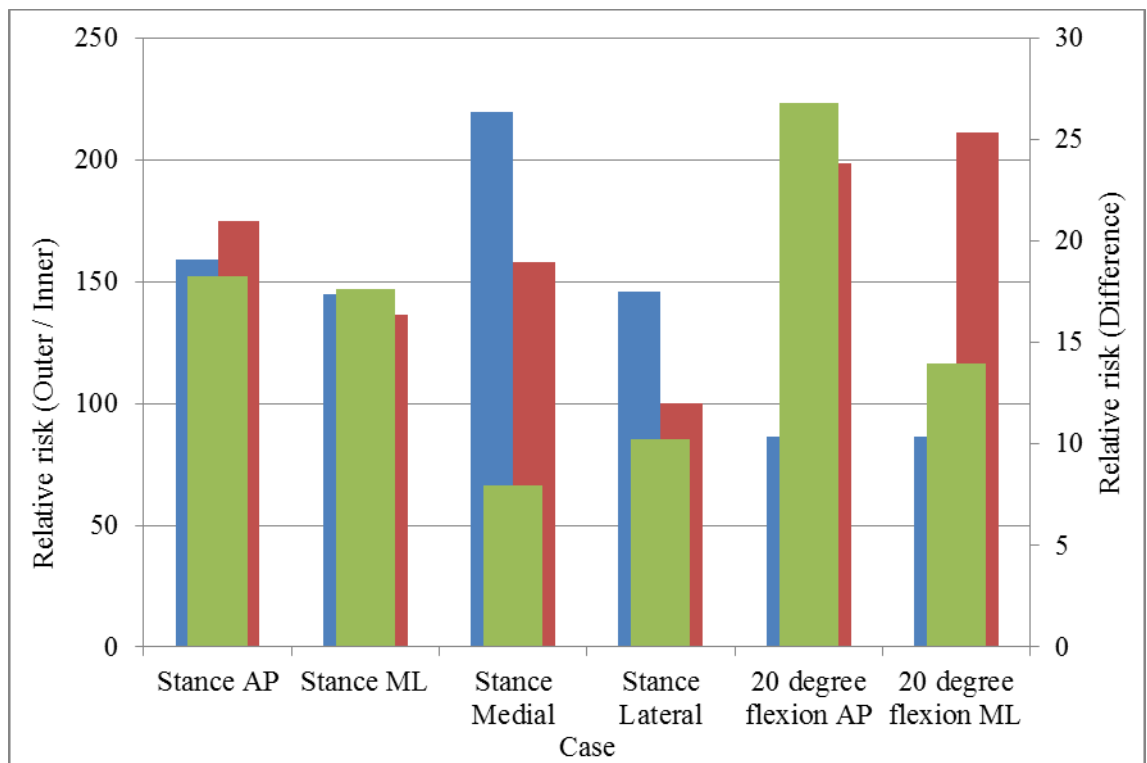


Figure 130. Relative risk scores for each case generated from Patient 01_005.

Table 73. Geometric representations and von Mises stress plots for each slice generated for patient 01_006.

Stance AP	Stance ML	Stance Medial	Stance Lateral	20° Flexion AP	20° Flexion ML

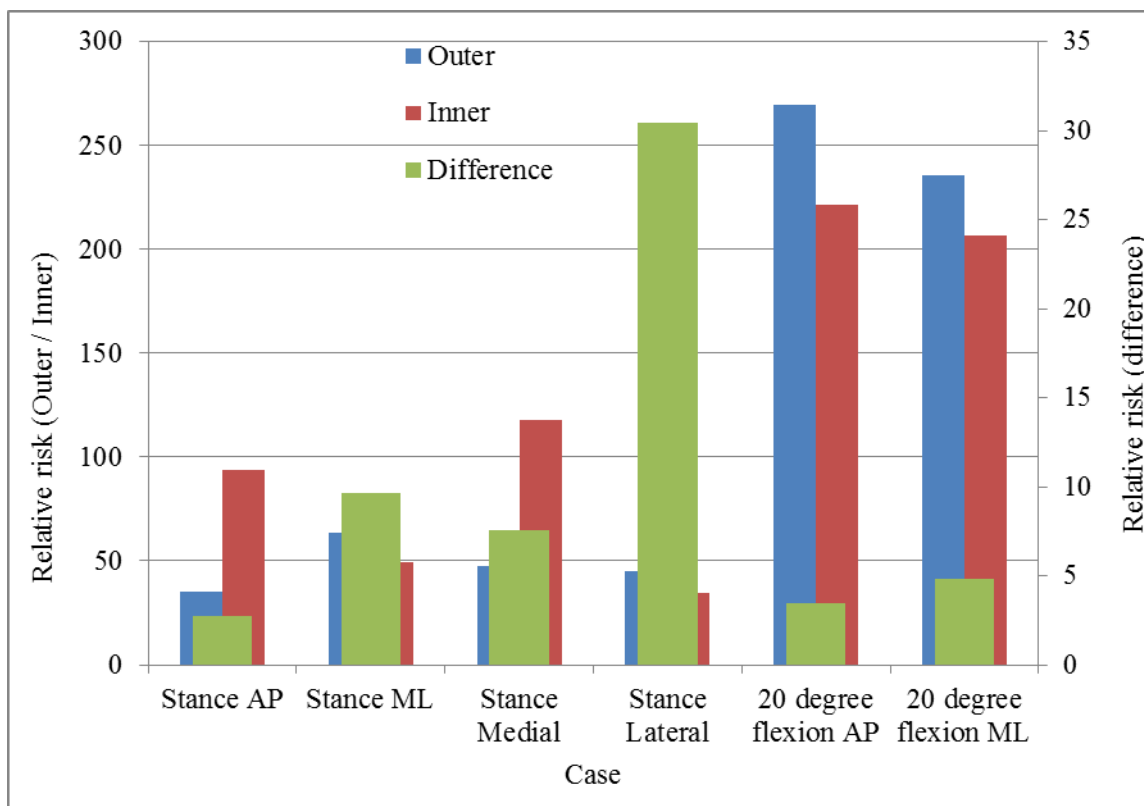
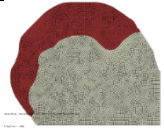
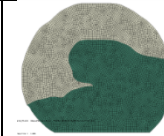
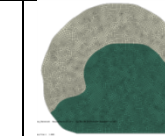
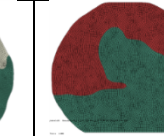
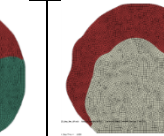
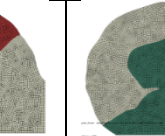
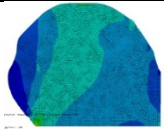
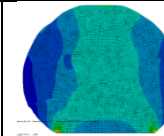
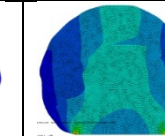
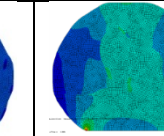
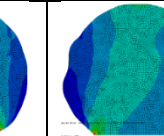
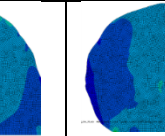


Figure 131. Relative risk scores for each case generated from Patient 01_006.

Table 74. Geometric representations and von Mises stress plots for each slice generated for patient 02_001.

Stance AP	Stance ML	Stance Medial	Stance Lateral	20° Flexion AP	20° Flexion ML
					
					

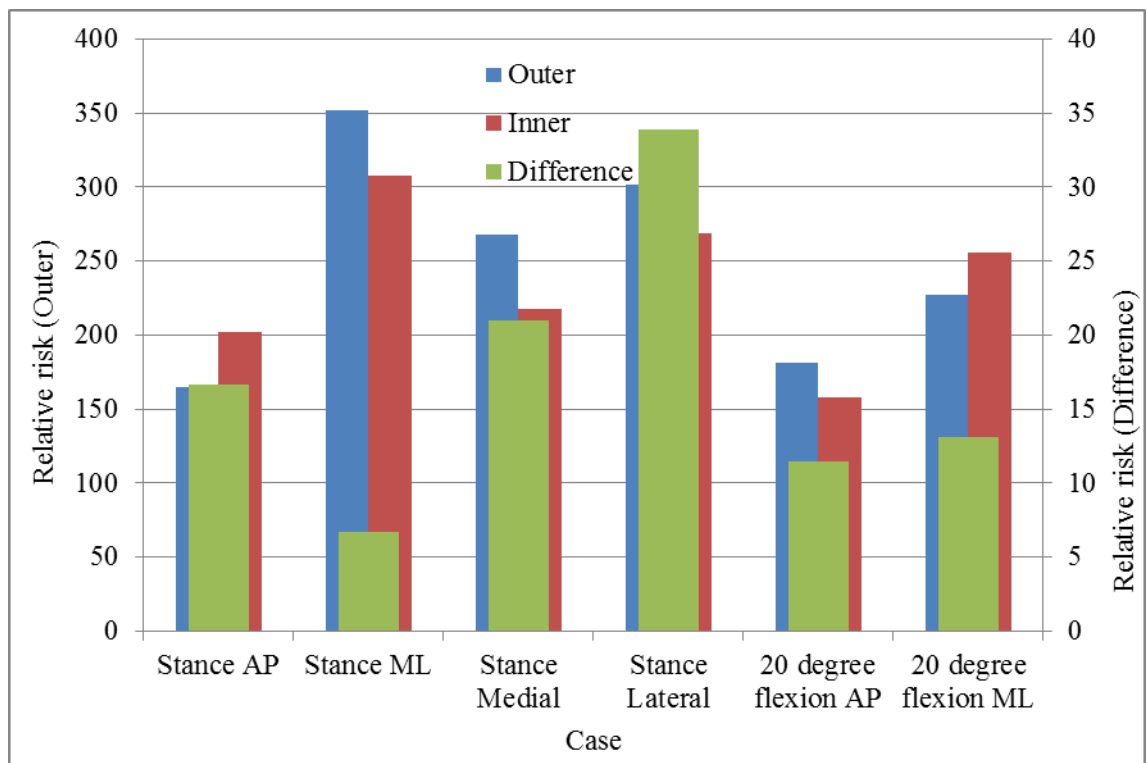
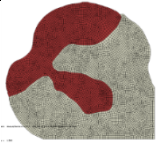
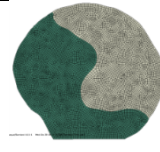
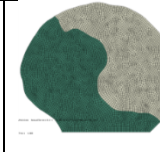
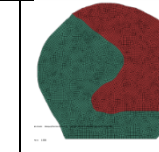
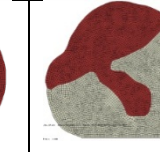
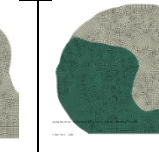
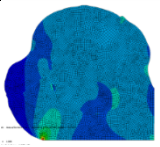
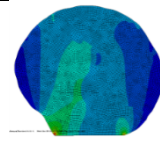
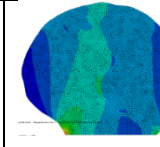
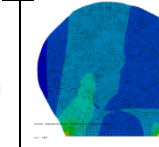
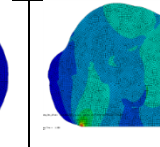
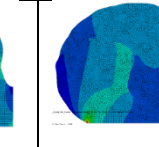


Figure 132. Relative risk scores for each case generated from Patient 02_001.

Table 75. Geometric representations and von Mises stress plots for each slice generated for patient 02_003.

Stance AP	Stance ML	Stance Medial	Stance Lateral	20° Flexion AP	20° Flexion ML
					
					

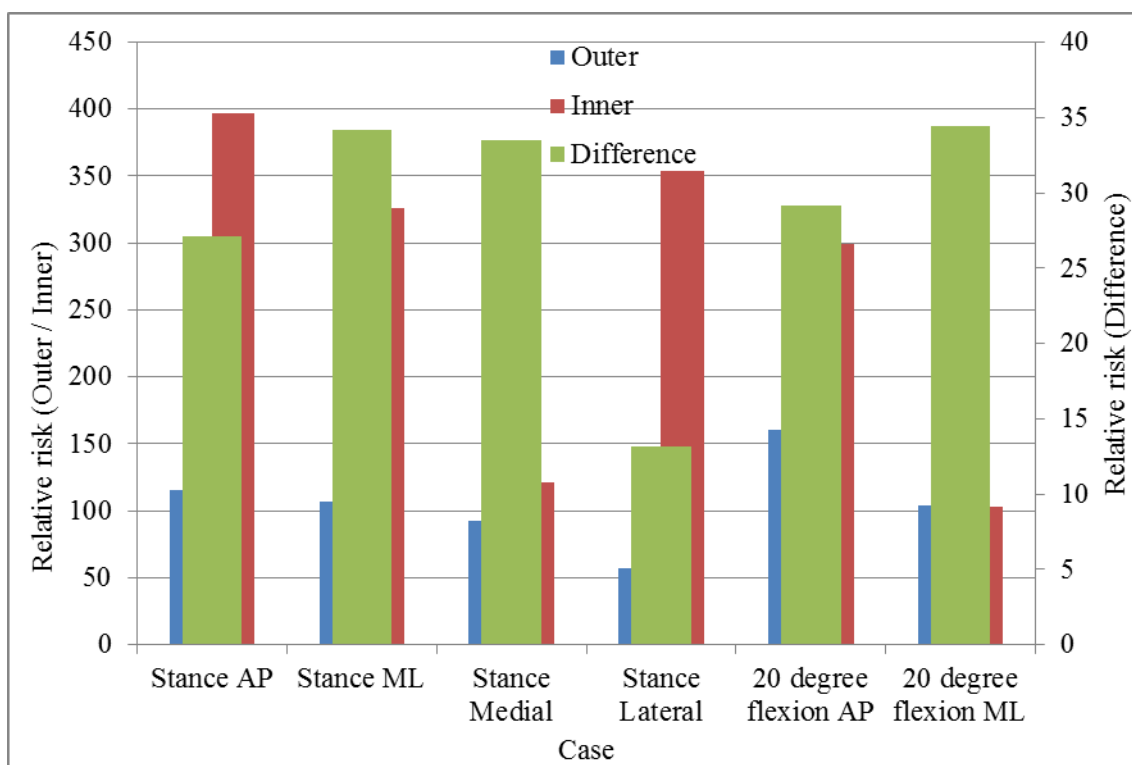


Figure 133. Relative risk scores for each case generated from Patient 02_003.

References

- Aaron, R.K., Lennox, D., Bunce, G.E., Ebert, T. (1989) The Conservative Treatment of Osteonecrosis of the Femoral Head A Comparison of Core Decompression and Pulsing Electromagnetic Fields. *Clinical Orthopaedics and Related Research*. **249**, 209–218.
- Aigner, N., Schneider, W., Eberl, V., Knahr, K. (2002) Core decompression in early stages of femoral head osteonecrosis-an MRI-controlled study. *International Orthopaedics*. **26**(1), 31–35.
- Aldridge, J.M., Berend, K.R., Gunneson, E.E., Urbaniak, J.R. (2003) Free vascularized fibular grafting for the treatment of postcollapse osteonecrosis of the femoral head. *The Journal of Bone & Joint Surgery, American Volume*. **85**(6), 87–101.
- Alvarez-Linera, J. (2008) 3T MRI: advances in brain imaging. *European Journal of Radiology*. **67**(3), 415–26.
- Ambroziak, A., Kłosowski, P. (2006) Survey of modern trends in continuum damage analysis. *Task quarterly*. **10**(4), 437–454.
- Anderson, M.L., Skinner, J.A., Felmlee, J.P., Berger, R.P., Amrami, K.K. (2008) Diagnostic comparison of 1.5 Tesla and 3.0 Tesla preoperative MRI of the wrist in patients with ulnar-sided wrist pain. *The Journal of Hand Surgery*. **33**(7), 1153–1159.
- Arlet, J. (1992) Nontraumatic Avascular Necrosis of the Femoral Head. *Clinical Orthopaedics and Related Research*. **277**, 12–21.
- Arlot, M.E., Bonjean, M., Chavassieux, P.M., Meunier, P.J. (1983) Bone histology in adults with aseptic necrosis. Histomorphometric evaluation of iliac biopsies in seventy-seven patients. *The Journal of Bone & Joint Surgery, American Volume*. **65**(9), 1319–27.
- Aruwajoye, O.O., Patel, M.K., Allen, M.R., Burr, D.B., Aswath, P.B., Kim, H.K.W. (2013) Microcrack density and nanomechanical properties in the subchondral region of the immature piglet femoral head following ischemic osteonecrosis. *Bone*. **52**(2), 632–9.
- Ashman, R.B., Rho, J.Y. (1988) Elastic modulus of trabecular bone material. *Journal of Biomechanics I*. **21**(3), 177–181.
- Assouline-Dayana, Y., Chang, C., Greenspan, A., Shoenfeld, Y., Gershwin, M.E. (2002) Pathogenesis and natural history of osteonecrosis. *Seminars in Arthritis and Rheumatism*. **32**(2), 94–124.
- Atsumi, T., Kuroki, Y., Yamano, K. (1989) A microangiographic study of idiopathic osteonecrosis of the femoral head. *Clinical Orthopaedics and Related Research*. **246**, 186–194.
- Bae, J.Y., Kwak, D.S., Park, K.S., Jeon, I. (2013) Finite element analysis of the multiple drilling technique for early osteonecrosis of the femoral head. *Annals of biomedical engineering*. **41**(12), 2528–37.
- Barille, M.F., Wu, J.S., McMahon, C.J. (2014) Femoral head avascular necrosis: a frequently missed incidental finding on multidetector CT. *Clinical radiology*. **69**(3), 280–5.
- Bathe, K.-J. (1996) *Finite Element Procedures*. W. Stenquist & M. Peterson, eds. Upper Saddle River, New Jersey, USA: Prentice-Hall, Inc.

- Behrens, B.-A., Nolte, I., Wefstaedt, P., Stukenborg-Colsman, C., Bouguecha, A. (2009) Numerical investigations on the strain-adaptive bone remodelling in the periprosthetic femur: influence of the boundary conditions. *Biomedical Engineering Online*. **8**, 7.
- Bejar, J., Peled, E., Boss, J.H. (2005) Theoretical Biology and Medical Vasculature deprivation – induced osteonecrosis of the rat femoral head as a model for therapeutic trials. *Theoretical Biology and Medical Modelling*. **14**, 1–14.
- Belmar, C.J., Steinberg, M.E., Hartman-Sloan, K.M. (2004) Does pain predict outcome in hips with osteonecrosis? *Clinical Orthopaedics and Related Research*. **425**(425), 158–162.
- Bergh, C., Fenstad, A.M., Furnes, O., Garellick, G., Havelin, L.I., Overgaard, S., Pedersen, A.B., Mäkelä, K.T., Pulkkinen, P., Mohaddes, M., Kärrholm, J. (2014) Increased risk of revision in patients with non-traumatic femoral head necrosis. *Acta orthopaedica*. **85**(1), 11–7.
- Bergmann, G., Deuretzbacher, G., Heller, M., Graichen, F., Rohlmann, A., Strauss, J., Duda, G. (2001) Hip contact forces and gait patterns from routine activities. *Journal of Biomechanics*. **34**(7), 859–871.
- Bessho, M., Ohnishi, I., Matsumoto, T., Ohashi, S., Matsuyama, J., Tobita, K., Kaneko, M., Nakamura, K. (2009) Prediction of proximal femur strength using a CT-based nonlinear finite element method: differences in predicted fracture load and site with changing load and boundary conditions. *Bone*. **45**(2), 226–31.
- Bevill, G., Keaveny, T.M. (2009) Trabecular bone strength predictions using finite element analysis of micro-scale images at limited spatial resolution. *Bone*. **44**(4), 579–584.
- Brown, T., Ferguson, A.B. (1980) Mechanical Property Distributions in the Cancellous Bone of the Human Proximal Femur. *Acta Orthopaedica*. **51**(1), 429–437.
- Brown, T.D., Baker, K.J., Brand, R.A. (1993) Mechanical consequences of core drilling and bone-grafting on osteonecrosis of the femoral head. *The Journal of Bone & Joint Surgery, American Volume*. **75**, 1358–1367.
- Brown, T.D., Baker, K.J., Brand, R.A. (1992) Structural consequences of subchondral bone involvement in segmental osteonecrosis of the femoral head. *Journal of Orthopaedic Research*. **10**(1), 79–87.
- Brown, T.D., Way, M.E., Ferguson, A.B. (1981) Mechanical characteristics of bone in femoral capital aseptic necrosis. *Clinical Orthopaedics and Related Research*. (156), 240–7.
- Bryan, R., Mohan, P.S., Hopkins, A., Galloway, F., Taylor, M., Nair, P.B. (2010) Statistical modelling of the whole human femur incorporating geometric and material properties. *Medical engineering & physics*. **32**(1), 57–65.
- Bryan, R., Nair, P.B., Taylor, M. (2009) Use of a statistical model of the whole femur in a large scale, multi-model study of femoral neck fracture risk. *Journal of Biomechanics*. **42**(13), 2171–6.
- Bucki, M., Lobos, C., Payan, Y. (2010) A fast and robust patient specific Finite Element mesh registration technique: application to 60 clinical cases. *Medical image analysis*. **14**(3), 303–17.
- Buie, H.R., Campbell, G.M., Klinck, R.J., MacNeil, J. a, Boyd, S.K. (2007) Automatic segmentation of cortical and trabecular compartments based on a dual threshold technique for in vivo micro-CT bone analysis. *Bone*. **41**(4), 505–515.

- Calder, J.D., Hine, A.L., Pearse, M.F., Revell, P.A. (2008) The relationship between osteonecrosis of the proximal femur identified by MRI and lesions proven by histological examination. *The Journal of Bone & Joint Surgery, British Volume*. **90**(2), 154–158.
- Carter, D., Hayes, W. (1976) Bone compressive strength: the influence of density and strain rate. *Science*. **194**(1), 1174–1176.
- Carter, D.R., Hayes, W.C. (1977) The compressive behavior of bone as a two-phase porous structure. *The Journal of Bone & Joint Surgery, British Volume*. **59**, 954–962.
- Carter, D.R., Spengler, D.M. (1978) Mechanical Properties and Composition of Cortical Bone. *Clinical Orthopaedics and Related Research*. **135**, 192–217.
- Catto, M. (1965) A histological study of avascular necrosis of the femoral head after transcervical fracture. *The Journal of Bone & Joint Surgery, British Volume*. **47B**(4), 749–776.
- Chang, J.K., Ho, M.L., Yeh, C., Chen, C.H., Wang, G.J. (2006) Osteogenic gene expression decreases in stromal cells of patients with osteonecrosis. *Clinical Orthopaedics and Related Research*. **453**(453), 286.
- Chen, W., Zhang, F., Chang, S.M., Hui, K., Lineaweaver, W.C. (2006) Microsurgical Fibular Flap for Treatment of Avascular Necrosis of the Femoral Head. *Journal of the American College of Surgeons*. **202**(2), 324–334.
- Cherian, S.F., Laorr, A., Saleh, K.J., Kuskowski, M.A., Bailey, R.F., Cheng, E.Y. (2003) Quantifying the extent of femoral head involvement in osteonecrosis. *The Journal of Bone & Joint Surgery, American volume*, 309–315.
- Ciarelli, M.J., Goldstein, S.A., Kuhn, J.L., Cody, D.D., Brown, T.M.B. (1991) Evaluation of Orthogonal Mechanical Properties and Density of Human Trabecular Bone From the Major Metaphyseal Regions with Materials Testing and Computed Tomography. *Journal of Orthopaedic Research*. **9**, 674–682.
- Cody, D.D., Hu, F.J., Divine, G.W., Fyhrie, D.P. (2000) Short term in vivo precision of proximal femoral finite element modelling. *Annals of Biomedical Engineering*. **28**(4), 408–411.
- Cotton, J.R., Winwood, K., Zioupos, P., Taylor, M. (2005) Damage Rate is a Predictor of Fatigue Life and Creep Strain Rate in Tensile Fatigue of Human Cortical Bone Samples. *Journal of Biomechanical Engineering*. **127**(2), 213.
- Cui, Q., Saleh, K.J. (2008) Surgical and Molecular Advances in Osteonecrosis. *Clinical Orthopaedics and Related Research*. **466**, 1017–1019.
- Currey, J.D. (1970) The mechanical properties of bone. *Clinical Orthopaedics and Related Research*. **73**, 210–231.
- Daniel, M., Herman, S., Dolinar, D., Iglic, A., Sochor, M., Kralj-Iglic, V. (2006) Contact Stress in Hips with Osteonecrosis of the Femoral Head. *Clinical Orthopaedics and Related Research*. **447**, 92–99.
- Dean, G.S., Kime, R.C., Fitch, R.D., Gunneson, E., Urbaniak, J.R. (2001) Treatment of osteonecrosis in the hip of pediatric patients by free vascularized fibular graft. *Clinical Orthopaedics and Related Research*. **386**(386), 106.

Dopico-González, C., New, A.M., Browne, M. (2010) Probabilistic finite element analysis of the uncemented hip replacement--effect of femur characteristics and implant design geometry. *Journal of Biomechanics*. **43**(3), 512–20.

Dorr, L.D., Bechtol, C.O., Watkins, R.G., Wan, Z. (2000) Radiographic anatomic structure of the arthritic acetabulum and its influence on total hip arthroplasty. *The Journal of arthroplasty*. **15**(7), 890–900.

Edgar, C., Einhorn, T. (2011) Treatment of avascular necrosis of the femoral head with drilling and injection of concentrated autologous bone marrow. *Techniques in Orthopaedics*. **26**(1), 2–8.

Emsley, D., Newell, C., Pickford, M., Royall, M., Swanson, M., Charman, S., Copley, L., van Der Meulen, J., Tse, Y., Young, E. (2009) *National Joint Registry for England and Wales 6th Annual report: 2009*.

Fardellone, P. (2008) Predicting the fracture risk in 2008. *Joint, bone, spine: revue du rhumatisme*. **75**(6), 661–4.

Fayad, L.M., Patra, A., Fishman, E.K. (2009) Value of 3D CT in defining skeletal complications of orthopedic hardware in the postoperative patient. *American Journal of Roentgenology*. **193**(4), 1155–63.

Fordyce, M., Solomon, L. (1993) Early detection of avascular necrosis of the femoral head by MRI. *The Journal of Bone & Joint Surgery, British Volume*. **75**(3), 365–367.

Fukushima, W., Fujioka, M., Kubo, T., Tamakoshi, A., Nagai, M., Hirota, Y. (2010) Nationwide Epidemiologic Survey of Idiopathic Osteonecrosis of the Femoral Head. *Clinical Orthopaedics and Related Research*, Epub ahead of print.

Gardeniers, J.W.M. (1993) Report of the Committee of Staging and Nomenclature. ARCO News Letter, 5:n°2: 79-82, 1993. In *ARCO Committee on Terminology and Staging: Report on the Committee-Meeting at Santiago de Compostela on Thursday the 14th of October 1993*. pp. 79–82.

Glimcher, M.J., Kenzora, J.E. (1977) The Biology of Osteonecrosis of the Human Femoral Head and its Clinical Implications: an abridged communication. *Clinical Orthopaedics and Related Research*. **130**, 47–50.

Glimcher, M.J., Kenzora, J.E. (1979a) The biology of osteonecrosis of the human femoral head and its clinical implications: I. Tissue Biology. *Clinical Orthopaedics and Related Research*. **138**, 284–309.

Glimcher, M.J., Kenzora, J.E. (1979b) The biology of osteonecrosis of the human femoral head and its clinical implications: III. Discussion of the Etiology and Genesis of the pathological squelae; comments on treatment. *Clinical Orthopaedics and Related Research*. **140**, 273–311.

Gold, E.W., Cangemi, P.J. (1979) Incidence and pathogenesis of alcohol-induced osteonecrosis of the femoral head. *Clinical Orthopaedics and Related Research*. **143**, 222.

Goldstein, S.A. (1987) The mechanical properties of trabecular bone: dependence on anatomic location and function. *Journal of Biomechanics*. **20**, 1055–1061.

Golland, P., Grimson, W.E.L., Kikinis, R. (1999) Skeletons : Corpus Callosum Study Shape Representation : Fixed Topology Skeletons. *Corpus*, 382–387.

Guo, K.J., Zhao, F.C., Guo, Y., Li, F.L., Zhu, L., Zheng, W. (2014) The influence of age, gender and treatment with steroids on the incidence of osteonecrosis of the femoral head during the management of severe acute respiratory syndrome: a retrospective study. *The bone & joint journal*. **96-B**(2), 259–62.

Gupta, S., New, A.M.R., Taylor, M. (2006) Bone remodelling inside a cemented resurfaced femoral head. *Clinical biomechanics (Bristol, Avon)*. **21**(6), 594–602.

Haba, Y., Lindner, T., Fritsche, A., Schiebenhöfer, A., Souffrant, R., Kluess, D., Skripitz, R., Mittelmeier, W., Bader, R. (2012) Relationship Between Mechanical Properties and Bone Mineral Density of Human Femoral Bone Retrieved from Patients with Osteoarthritis. *The Open Orthopaedics Journal*. **6**, 458–463.

Hernandez, C.J., Gupta, A., Keaveny, T.M. (2007) A biomechanical analysis of the effects of resorption cavities on cancellous bone strength. *Journal of Bone and Mineral Research*. **21**(8), 1248–1255.

Hernigou, P., Beaujean, F. (2002) Treatments of osteonecrosis with autologous bone marrow grafting. *Clinical Orthopaedics and Related Research*. (405), 14–23.

Hernigou, P., Habibi, A., Bachir, D., Galacteros, F. (2006) The natural history of asymptomatic osteonecrosis of the femoral head in adults with sickle cell disease. *The Journal of Bone & Joint Surgery, American Volume*. **88**(12), 2565–2572.

Hernigou, P., Lambotte, J.C. (2000) Bilateral hip osteonecrosis: influence of hip size on outcome. *Annals of the Rheumatic Diseases*. **59**(10), 817–21.

Hernigou, P., Lambotte, J.C. (2001) Volumetric analysis of osteonecrosis of the femur. Anatomical correlation using MRI. *The Journal of Bone & Joint Surgery, British Volume*. **83**(5), 672–675.

Hungerford, D.S., Jones, L.C. (2004) Asymptomatic Osteonecrosis. *Clinical Orthopaedics and Related Research*. **429**(429), 124–130.

Iorio, R., Healy, W.L., Abramowitz, A.J., Pfeifer, B.A. (1998) Clinical Outcome and Survivorship Analysis of Core Decompression for Early Osteonecrosis of the Femoral Head. *The Journal of Arthroplasty*. **13**(1), 34–41.

Johnson, A.J., Khanuja, H.S., Mont, M.A. (2010) Osteonecrosis of the Femoral Head: Femoral Head Sparing Treatments. *Seminars in Arthroplasty*. **21**(1), 2–4.

Jones, A.C., Wilcox, R.K. (2007) Assessment of factors influencing finite element vertebral model predictions. *J Biomech Eng*. **129**(6), 898–903.

Kang, J.S., Park, S., Song, J.H., Jung, Y.Y., Cho, M.R., Rhyu, K.H. (2009) Prevalence of osteonecrosis of the femoral head: a nationwide epidemiologic analysis in Korea. *The Journal of Arthroplasty*. **24**(8), 1178–83.

Keller, T.S. (1994) Predicting the compressive mechanical behaviour of bone. *Journal of Biomechanics*. **27**(9), 1159–1168.

Keyak, J.H., Falkinstein, Y. (2003) Comparison of in situ and in vitro CT scan-based finite element model predictions of proximal femoral fracture load. *Medical engineering & physics*. **25**(9), 781–787.

Kim, Y.-H., Oh, S.-H., Kim, J.-S., Koo, K.-H. (2003) Contemporary total hip arthroplasty with and without cement in patients with osteonecrosis of the femoral head. *The Journal of bone and joint surgery. American volume*. **85-A**(4), 675–81.

Kim, Y.-M., Oh, H.C., Kim, H.J. (2000) The pattern of bone marrow oedema on MRI in osteonecrosis of the femoral head. *The Journal of Bone & Joint Surgery, British Volume*. **82**(6), 837–841.

Koivumäki, J.E.M., Thevenot, J., Pulkkinen, P., Kuhn, V., Link, T.M., Eckstein, F., Jämsä, T. (2012) Ct-based finite element models can be used to estimate experimentally measured failure loads in the proximal femur. *Bone*. **50**(4), 824–9.

Koo, K., Kim, R. (1995) Quantifying the extent of osteonecrosis of the femoral head. *The Journal of Bone & Joint Surgery, British Volume*. **77**(6), 875–875.

Koo, K., Kim, R., Ko, G., Song, H., Jeong, S. (1995) Preventing collapse in early necrosis of the femoral head. *The Journal of Bone & Joint Surgery, British Volume*. **77-B**(6), 870–874.

Kosmopoulos, V., Keller, T.S. (2008) Predicting trabecular bone microdamage initiation and accumulation using a non-linear perfect damage model. *Medical engineering & physics*. **30**(6), 725–32.

Lai, Y.-S., Wei, H.-W., Cheng, C.-K. (2008) Incidence of hip replacement among national health insurance enrollees in Taiwan. *Journal of Orthopaedic Surgery and Research*. **3**, 42.

Lang, P., Genant, H.K., Jergesen, H.E., Murray, W.R. (1992) Imaging of the hip joint. Computed tomography versus magnetic resonance imaging. *Clinical Orthopaedics and Related Research*. (274), 135–53.

Lau, R.L., Perruccio, A. V, Evans, H.M.K., Mahomed, S.R., Mahomed, N.N., Gandhi, R. (2014) Stem cell therapy for the treatment of early stage avascular necrosis of the femoral head: a systematic review. *BMC musculoskeletal disorders*. **15**(1), 156.

Li, B., Aspden, R.M. (1997) Composition and mechanical properties of cancellous bone from the femoral head of patients with osteoporosis or osteoarthritis. *Journal of bone and mineral research : the official journal of the American Society for Bone and Mineral Research*. **12**(4), 641–51.

Lieberman, J.R. (2004) Core decompression for osteonecrosis of the hip. *Clinical Orthopaedics*. **418**(418), 29–33.

Linde, F., Christian, H., Sorensen, F. (1993) The effect of different storage methods on the mechanical properties of trabecular bone. *Journal of Biomechanics*. **26**(10), 1249–1252.

Lobos, C., Payan, Y., Hitschfeld, N. (2009) Techniques for the generation of 3D Finite Element Meshes of human organs. *Arxiv preprint arXiv:0911.3884*.

Lotz, J.C., Gerhart, T.N., Hayes, W.C. (1990) Mechanical Properties of Trabecular Bone from the Proximal Femur: A Quantitative CT study. *Journal of Computer Assisted Tomography*. **14**(1), 107–114.

Lv, H., de Vlas, S.J., Liu, W., Wang, T.-B., Cao, Z.-Y., Li, C.-P., Cao, W.-C., Richardus, J.H. (2009) Avascular osteonecrosis after treatment of SARS: a 3-year longitudinal study. *Tropical Medicine & International Health*. **14 Suppl 1**(November), 79–84.

- Mahfouz, M., Badawi, A., Merkl, B., Fatah, E.E.A., Pritchard, E., Kesler, K., Moore, M., Jantz, R., Jantz, L. (2007) Patella sex determination by 3D statistical shape models and nonlinear classifiers. *Forensic Science International*. **173**(2-3), 161–70.
- Markel, M.D., Chao, E.Y.S. (1993) Noninvasive monitoring techniques for quantitative description of callus mineral content and mechanical properties. *Clinical Orthopaedics and Related Research*. **293**, 37–45.
- Marker, D.R., Seyler, T.M., McGrath, M.S., Delanois, R.E., Ulrich, S.D., Mont, M.A. (2008) Treatment of early stage osteonecrosis of the femoral head. *The Journal of Bone & Joint Surgery, American Volume*. **90**(Supplement 4), 175–187.
- Marker, D.R., Seyler, T.M., Ulrich, S.D., Srivastava, S., Mont, M.A. (2008) Do Modern Techniques Improve Core Decompression Outcomes for Hip Osteonecrosis? *Clinical Orthopaedics and Related Research*. **466**(5), 1093–1103.
- Matsusaki, H., Noguchi, M., Kawakami, T., Tani, T. (2005) Use of vascularized pedicle iliac bone graft combined with transtrochanteric rotational osteotomy in the treatment of avascular necrosis of the femoral head. *Archives of Orthopaedic and Trauma Surgery*. **125**, 95–101.
- Mazières, B., Marin, F., Chiron, P., Moulinier, L., Laroche, M., Cantagrel, A., Amigues, J. (1997) Influence of the volume of osteonecrosis on the outcome of core decompression of the femoral head. *Annals of the Rheumatic Diseases*. **56**, 747–750.
- Mengoni, M., Luxmoore, B.J., Jones, A.C., Wijayathunga, V.N., Broom, N.D., Wilcox, R.K. Derivation of inter-lamellare behaviour of the intervertebral disc annulus (in press). *Journal of Biomechanical Materials*.
- Meyers, M.H. (1988) Osteonecrosis of the femoral head: pathogenesis and long-term results of treatment. *Clinical Orthopaedics and Related Research*. **231**, 51–61.
- Mont, M.A., Group (1999) Symptomatic multifocal osteonecrosis. A multicenter study. *Clinical Orthopaedics and Related Research*. **369**(369), 312–326.
- Mont, M.A., Hungerford, D.S. (1995) Non-traumatic avascular necrosis of the femoral head. *The Journal of Bone & Joint Surgery, American Volume*. **77**(3), 459–474.
- Mont, M.A., Jones, L.C., Einhorn, T.A. (1998) Osteonecrosis of the Femoral Head. *Clinical Orthopaedics and Related Research*. (355S), 314S–335S.
- Mont, M.A., Jones, L.C., Pacheco, I., Hungerford, D.S. (1998) Radiographic predictors of outcome of core decompression for hips with osteonecrosis stage III. *Clinical Orthopaedics and Related Research*. **354**(354), 159.
- Mont, M.A., Marulanda, G.A., Jones, L.C., Saleh, K.J., Gordon, N., Hungerford, D.S., Steinberg, M.E. (2006) Systematic analysis of classification systems for osteonecrosis of the femoral head. *The Journal of Bone & Joint surgery, American Volume*. **88 Suppl 3**, 16–26.
- Mont, M.A., Ragland, P.S., Etienne, G. (2004) Core Decompression of the Femoral Head for Osteonecrosis Using Percutaneous Multiple Small-Diameter Drilling. *Clinical Orthopaedics and Related Research*. (429), 131–138.
- Mont, M.A., Zywił, M.G., Marker, D.R., McGrath, M.S., Delanois, R.E. (2010) The natural history of untreated asymptomatic osteonecrosis of the femoral head: a systematic literature review. *The Journal of Bone & Joint Surgery, American Volume*. **92**(12), 2165–2170.

Motomura, G., Yamamoto, T., Yamaguchi, R., Ikemura, S., Nakashima, Y., Mawatari, T., Iwamoto, Y. (2011) Morphological analysis of collapsed regions in osteonecrosis of the femoral head. *The Journal of Bone & Joint Surgery, British Volume*. **93-B**(2), 184–187.

Musso, E.S., Mitchell, S.N., Schink-Ascani, M., Bassett, C. (1986) Results of Conservative Management of Osteonecrosis of the Femoral Head A Retrospective Review. *Clinical Orthopaedics and Related Research*. **207**, 209–215.

Nam, K., Kim, Y., Yoo, J., Koo, K.-H., Yoon, K., Kim, H. (2008) Fate of Untreated Asymptomatic Osteonecrosis. *The Journal of Bone & Joint Surgery, American Volume*. **90-A**, 477–484.

Nishii, T., Sugano, N., Ohzono, K., Sakai, T., Haraguchi, K., Yoshikawa, H. (2002) Progression and cessation of collapse in osteonecrosis of the femoral head. *Clinical Orthopaedics and Related Research*. **400**(400), 149.

Nishii, T., Sugano, N., Ohzono, K., Sakai, T., Sato, Y., Yoshikawa, H. (2002) Significance of lesion size and location in the prediction of collapse of osteonecrosis of the femoral head: a new three-dimensional quantification using magnetic resonance imaging. *Journal of Orthopaedic Research*. **20**, 130–136.

Öhman, C., Baleani, M., Perilli, E., Dall'Ara, E., Tassani, S., Baruffaldi, F., Viceconti, M. (2007) Mechanical testing of cancellous bone from the femoral head: Experimental errors due to off-axis measurements. *Journal of Biomechanics*. **40**(11), 2426–2433.

Ohzono, K., Saito, M., Sugano, N., Takaoka, K., Ono, K. (1992) The fate of nontraumatic avascular necrosis of the femoral head: A radiologic classification to formulate prognosis. *Clinical Orthopaedics and Related Research*. **277**, 73.

Parsons, S.J., Steele, N. (2008) Osteonecrosis of the femoral head : Part 2 Options for treatment. *Current Orthopaedics*. **22**(5), 349–358.

Pelker, R.R., Friedlaender, G.E., Markham, T.C., Panjabi, M.M., Moen, C.J. (1984) Effects of freezing and freeze-drying on the biomechanical properties of rat bone. *Journal of orthopaedic research : official publication of the Orthopaedic Research Society*. **1**(4), 405–11.

Petrigliano, F.A., Lieberman, J.R. (2007) Osteonecrosis of the hip: novel approaches to evaluation and treatment. *Clinical Orthopaedics and Related Research*. **465**(465), 53.

Plenk Jr, H., Gstettner, M., Grossschmidt, K., Breitenseher, M., Urban, M., Hofmann, S. (2001) Magnetic resonance imaging and histology of repair in femoral head osteonecrosis. *Clinical Orthopaedics and Related Research*. **386**(386), 42.

Poelert, S., Valstar, E., Weinans, H., Zadpoor, A. a (2013) Patient-specific finite element modeling of bones. *Proceedings of the Institution of Mechanical Engineers. Part H, Journal of engineering in medicine*. **227**(4), 464–78.

Polagar, K., Gill, H.S., Viceconti, M., Murray, D.W., O'Connor, J.J. (2003) Strain distribution within the human femur due to physiological and simplified loading: finite element analysis using the muscle standardized femur. *Proceedings of the Institute of Mechanical Engineers: Journal of Engineering in Medicine*. **217**, 173–189.

Popovic, K.S., Kocar, M. (2010) Imaging findings in bisphosphonate-induced osteonecrosis of the jaws. *Radiology and Oncology*. **44**(4), 215–219.

Porter, M., Beaumont, R., Young, E., Forsyth, O., Swanson, M. (2013) *10th Annual Report*.

- Prendergast, P.J., Taylor, D. (1994) Prediction of bone adaptation using damage accumulation. . *27*(8), 1067–1076.
- Pugh, J.W., Rose, R.M., Radin, E.L. (1973) A possible mechanism of Wolff's Law: Trabecular microfractures. *Archives of Physiology and Biochemistry*. **81**(1), 27–40.
- Radcliffe, I., Taylor, M. (2007) Investigation into the affect of cementing techniques on load transfer in the resurfaced femoral head: a multi-femur finite element analysis. *Clinical biomechanics (Bristol, Avon)*. **22**(4), 422–30.
- Rubin, G.D. (2003) MDCT imaging of the aorta and peripheral vessels. *European Journal of Radiology*. **45**, S42–9.
- Rubin, G.D., Shiau, M.C., Schmidt, A.J., Fleischmann, D., Logan, L., Leung, A.N., Jeffrey, R.B., Napel, S. (1999) Computed tomographic angiography: historical perspective and new state-of-the-art using multi detector-row helical computed tomography. *Journal of Computer Assisted Tomography*. **23**, S83–90.
- Sakamoto, M., Shimizu, K., Iida, S., Akita, T., Moriya, H., Nawata, Y. (1997) Osteonecrosis Of The Femoral Head: A Prospective Study With MRI. *The Journal of Bone & Joint Surgery, British Volume*. **79**(2), 213–219.
- Schmitt, F., Grosu, D., Mohr, C., Purdy, D., Salem, K., Scott, K.T., Stoeckel, B. (2004) 3 Tesla MRI: successful results with higher field strengths. *Der Radiologe*. **44**(1), 31–47.
- Schmitt-Sody, M., Kirchhoff, C., Mayer, W., Goebel, M., Jansson, V. (2008) Avascular necrosis of the femoral head: inter- and intraobserver variations of Ficat and ARCO classifications. *International Orthopaedics*. **32**, 283–287.
- Seeman, E., Delmas, P.D. (2006) Bone Quality — The Material and Structural Basis of Bone Strength and Fragility. *The New England Journal of Medicine*. **354**, 2250–2261.
- Seyler, T.M., Marker, D.R., Ulrich, S.D., Fatscher, T., Mont, M.A. (2008) Nonvascularized bone grafting defers joint arthroplasty in hip osteonecrosis. *Clinical Orthopaedics and Related Research*. **466**(5), 1125–1132.
- Steinberg, D.R., Steinberg, M.E., Garino, J.P., Dalinka, M., Udupa, J.K. (2006) Determining lesion size in osteonecrosis of the femoral head. *The Journal of Bone & Joint Surgery, American Volume*. **88 Suppl.** , 27–34.
- Steinberg, M.E., Bands, R.E., Parry, S., Hoffman, E., Chan, T., Hartman, K.M. (1999) Does lesion size affect the outcome in avascular necrosis? *Clinical Orthopaedics and Related Research*. **367**, 262–271.
- Steinberg, M.E., Brighton, C.T., Bands, R.O.Y.E., Hartman, K.M. (1990) Capacitive coupling as an adjunctive treatment for avascular necrosis. *Clinical Orthopaedics and Related Research*. **261**, 11.
- Steinberg, M.E., Hayken, G.D., Steinberg, D.R. (1995) A quantitative system for staging avascular necrosis. *The Journal of Bone & Joint Surgery, American Volume*. **77-B**, 34–41.
- Steinhauser, E., Diehl, P., Hadaller, M., Schauwecker, J., Busch, R., Gradinger, R., Mittelmeier, W. (2006) Biomechanical investigation of the effect of high hydrostatic pressure treatment on the mechanical properties of human bone. *Journal of Biomedical Materials Research - Part B Applied Biomaterials*. **76**(1), 130–135.

- Stephen, P., Hornby, S. (1997) *Simple statistics for library and information professionals*.
- Sugano, N., Atsumi, T., Ohzono, K., Kubo, T., Hotokebuchi, T. (2002) The 2001 revised criteria for diagnosis, classification, and staging of idiopathic osteonecrosis of the femoral head. *Journal of Orthopaedic Science*. **7**, 601–605.
- Suh, K.T., Kim, S.W., Roh, H.L., Youn, M.S., Jung, J.S. (2005) Decreased Osteogenic Differentiation of Mesenchymal Stem Cells in Alcohol-induced Osteonecrosis. *Clinical Orthopaedics and Related Research*. (431), 220–225.
- Takao, M., Nishii, T., Sakai, T., Yoshikawa, H., Sugano, N. (2010) Repair in osteonecrosis of the femoral head: MR imaging features at long-term follow-up. *Clinical Rheumatology*.
- Takao, M., Sugano, N., Nishii, T., Miki, H., Sato, Y., Tamura, S., Yoshikawa, H. (2006) Longitudinal Quantitative Evaluation of Lesion Size Change in Femoral Head Osteonecrosis using Three-Dimensional Magnetic Resonance Imaging and Image Registration. *Evaluation*. (June), 1231–1239.
- Tanzer, M., Bobyn, J., Krygier, J., Karabasz, D. (2008) Histopathologic retrieval analysis of clinically failed porous tantalum osteonecrosis implants. *The Journal of Bone & Joint Surgery, American Volume*. **90**(6), 1282–1289.
- Taylor, D., Lee, T.C. (2003) A crack growth model for the simulation of fatigue in bone. *International Journal of Fatigue*. **25**(5), 387–395.
- Taylor, M., Verdonchot, N., Huiskes, R., Zioupos, P. (1999) A combined finite element method and continuum damage mechanics approach to simulate the in vitro fatigue behaviour of human cortical bone. *Journal of Materials Science: Materials in Medicine*. **10**, 841–846.
- Tien, W.-C., Kao, H.-Y., Tu, Y.-K., Chiu, H.-C., Lee, K.-T., Shi, H.-Y. (2009) A population-based study of prevalence and hospital charges in total hip and knee replacement. *International Orthopaedics*. **33**(4), 949–54.
- Turner, A.W.L., Gillies, R.M., Sekel, R., Morris, P., Bruce, W., Walsh, W.R. (2005) Computational bone remodelling simulations and comparisons with DEXA results. *Journal of Orthopaedic Research*. **23**, 705–712.
- Turner, C.H., Rho, J., Takano, Y., Tsui, T.Y., Pharr, G.M. (1999) The elastic properties of trabecular and cortical bone tissues are similar: Results from two microscopic measurement techniques. *Journal of Biomechanics*. **32**(4), 437–441.
- Ulrich, D., Van Rietbergen, B., Laib, A., Rueggsegger, P. (1999) The Ability of Three-Dimensional Structural Indices to Reflect Mechanical Aspects of Trabecular Bone. *Bone*. **25**(1), 55–60.
- Varitimidis, S.E., Dimitroulias, A.P., Karachalios, T.S., Dailiana, Z.H., Malizos, K.N. (2009) Outcome after tantalum rod implantation for treatment of femoral head osteonecrosis. *Acta Orthopaedica*. **80**(1), 20–25.
- Vaughan, T.J., McCarthy, C.T., McNamara, L.M. (2012) A three-scale finite element investigation into the effects of tissue mineralisation and lamellar organisation in human cortical and trabecular bone. *Journal of the mechanical behavior of biomedical materials*. **12**, 50–62.
- Viceconti, M., Davinelli, M., Taddei, F., Cappello, A. (2004) Automatic generation of accurate subject-specific bone finite element models to be used in clinical studies. *Journal of Biomechanics*. **37**(10), 1597–605.

- Wehrli, F.W. (2007) Structural and functional assessment of trabecular and cortical bone by micro magnetic resonance imaging. *Journal of Magnetic Resonance Imaging*. **25**(2), 390–409.
- Wehrli, F.W., Song, H.K., Saha, P.K., Wright, A.C. (2006) Quantitative MRI for the assessment of bone structure and function. *NMR in Biomedicine*. **19**, 731–764.
- Wei, H.-W., Sun, S.-S., Jao, S.-H.E., Yeh, C.-R., Cheng, C.-K. (2005) The influence of mechanical properties of subchondral plate, femoral head and neck on dynamic stress distribution of the articular cartilage. *Medical engineering & physics*. **27**(4), 295–304.
- Wirtz, D.C., Schi, N., Pandorf, T., Radermacher, K., Weichert, D., Forst, R. (2000) Critical evaluation of known bone material properties to realize anisotropic FE-simulation of the proximal femur. *American Journal Of Anatomy*. **33**, 1325–1330.
- Wright, D. a, Meguid, M., Lubovsky, O., Whyne, C.M. (2012) Subchondral bone density distribution in the human femoral head. *Skeletal radiology*. **41**(6), 677–83.
- Yang, J.W., Koo, K.H., Lee, M.C., Yang, P., Noh, M.D., Kim, S.Y., Kim, K.I., Ha, Y.C., Joun, M.S. (2002) Mechanics of femoral head osteonecrosis using three-dimensional finite element method. *Archives of Orthopaedic and Trauma Surgery*. **122**(2), 88–92.
- Yoon, T.R., Song, E.K., Rowe, S.M., Park, C.H. (2001) Failure after core decompression in osteonecrosis of the femoral head. *International Orthopaedics*. **24**(6), 316–318.
- Yosibash, Z., Padan, R., Joskowicz, L., Milgrom, C. (2007) A CT-based high-order finite element analysis of the human proximal femur compared to in-vitro experiments. *Journal of Biomechanical Engineering*. **129**(3), 297–309.
- Yosibash, Z., Trabelsi, N., Milgrom, C. (2007) Reliable simulations of the human proximal femur by high-order finite element analysis validated by experimental observations. *Journal of Biomechanics*. **40**(16), 3688–99.
- Young, W.C., Budynas, R.G. (2002) *Roark's formulas for stress and strain: Seventh edition*.
- Zhao, F.-C., Li, Z.-R., Zhang, N.-F., Wang, B.-L., Sun, W., Cheng, L.-M., Liu, Z.-H. (2009) Lesion size changes in osteonecrosis of the femoral head: a long-term prospective study using MRI. *International Orthopaedics*.
- Zhou, G.-Q., Pang, Z.-H., Chen, Q.-Q., He, W., Chen, Z.-Q., Chen, L.-L., Li, Z.-Q. (2014) Reconstruction of the biomechanical transfer path of femoral head necrosis: a subject-specific finite element investigation. *Computers in biology and medicine*. **52**, 96–101.
- Zinn, W.M. (1971) *Idiopathic Ischemic Necrosis of the Femoral Head in Adults*. Georg Thieme.
- Zoroofi, R. a, Sato, Y., Nishii, T., Sugano, N., Yoshikawa, H., Tamura, S. (2004) Automated segmentation of necrotic femoral head from 3D MR data. *Computerized Medical Imaging and Graphics*. **28**(5), 267–78.
- Zoroofi, R.A., Nishii, T., Sato, Y., Sugano, N., Yoshikawa, H., Tamura, S. (2001) Segmentation of avascular necrosis of the femoral head using 3-D MR images. *Computerized Medical Imaging and Graphics*. **25**(6), 511–21.